The role of quartz during deformation of polyphase rocks

Inauguraldissertation

zur
Erlangung der Würde eines Doktors der Philosophie
vorgelegt der
Philosophisch-Naturwissenschaftlichen Fakultät
der Universität Basel

von

Rüdiger Kilian

aus Geisenheim-Johannisberg (Deutschland)

Basel, Januar 2013

Genehmigt von der Philosopisch-Naturwissenschaftlichen Fakultät
auf Antrag von:

Prof. Dr. Renée Heilbronner
(Dissertationsleiterin)

Prof. Dr. Giorgio Pennacchioni
(Korreferent)

Prof. Dr. Holger Stünitz
(externer Experte)

Basel, den 14.12.2010

Prof- Dr. Martin Spiess
(Dekan der Philosophisch-Naturwissenschaftlichen Fakultät)

Contents

Chapter 6

Abstract

In this thesis, the deformation mechanisms, the rheology and the related microstructural evolution of quartz during deformation of polyphase rocks are investigated in natural, small scale shear zones that developed at high temperatures in granitoids. Selected shear zones are from the granodiorite of the Gran Paradiso Nappe, Western Alps, Italy, and the Truzzo granite of the Tambo Nappe, Central Alps, Italy. The microstructural evolution inside strain gradients from non- or weakly deformed hostrocks to ultramylonitic shear zones has been studied by optical microscopy, scanning electron microscopy and image analysis. Crystallographic preferred orientations (CPO) have been studied by means of orientation imaging using computer integrated polarization microscopy (CIP) and electron backscatter diffraction (EBSD).

In both case studies, magmatic quartz grains recrystallize dynamically, and form polycrystalline aggregates that deform by dislocation creep inside a fine grained feldspar-mica matrix, which deforms by diffusion creep. With increasing strain, quartz aggregates form layers and finally disintegrate to form a grain-scale polymineralic mixture with K-feldspar, plagioclase and mica. The disintegration of quartz aggregates marks the transition from a mylonite to an ultramylonite and occurs by intergranular dilatancy, which is related to grain boundary sliding and accompanied by the precipitation of K-feldspar and biotite.

Polycrystalline quartz aggregates form porphyroclasts and deform embedded in a lower viscous matrix at low (5-50 MPa) and constant differential stresses. This situation is approximated by Reuss-bound conditions. Quartz aggregates disintegrate because quartz fails to deform by dislocation creep compliant with the matrix.

In the Gran Paradiso shear zones (lower amphibolite facies, ~500-550°C), a stable quartz grain size forms by a dynamic equilibrium. Subgrain rotation recrystallization and grain boundary migration recrystallization (during synkinematic grain growth) contribute to a grain size decrease and increase respectively. During the formation of the ultramylonite the quartz grain size decreases below the quartz subgrain size and approaches the matrix grains size. It is demonstrated that the dynamic quartz grain size is decreased by a combination of pinning by the precipitated phases and dissolution processes. The constant quartz volume fraction requires quartz precipitation. Pinning eliminates the contribution of synkinematic grain growth, and dissolution permits a quartz grain size below the subgrain size. The ultramylonite deforms by dissolution-precipitation assisted diffusion creep. Quartz in the ultramylonite shows isotropic grain shapes and a random CPO.

Polycrystalline quartz aggregates in the Gran Paradiso mylonites develop a strong CPO consistent with the activity of the basal-<a> slip system. The CPO of each aggregate develops with respect to a local kinematic framework and not to the global (shear zone) reference frame. The local reference frame is defined by the quartz aggregate and its position in the matrix. A strong CPO develops already at low strain, and peripheral [c]-axis maxima reach a stable position at about 70° with respect to the flow plane.

Quartz aggregates show a local shear sense, which, at low strain is systematically opposite to the global shear sense. The inverse shear sense is interpreted to result from flow partitioning between the higher viscous quartz aggregate and the lower viscous matrix in bulk simple shear.

The quartz fabric is in most cases related to the CPO such that the maximum of the surface orientation distribution function is always synthetically rotated with respect to the sense of slip on the basal plane of quartz crystals. This situation implies a crystallographic control of the development of the fabric. Orthorhombic surface fabrics are suggested to form at a high grain boundary mobility, monoclinic surface fabrics from at a lower grain boundary mobility.

In the Truzzo granite shear zones (amphibolite facies, ~550-650°C), dynamic recrystallization of quartz is dominated by grain boundary migration with an increasing contribution of subgrain rotation related microstructures during advanced stages of deformation. The ultramylonite part of the shear zones deforms by diffusion creep, but single quartz grains show a shape anisotropy and a very weak CPO, interpreted to result from a contribution of intracrystalline plasticity.

Subsequent deformation at higher differential stresses leads to a relative hardening of the fine grained phase mixtures in the shear zones with respect to the coarse grained hostrock, resulting in necking of the shear zones.

In the ultramylonite, very local biotite breakdown and subgrain rotation - bulging recrystallization of quartz occurs in thin, newly coalesced layers which represent the very latest structures. This is the consequence of the inversion of the viscosity “contrast” between quartz and the feldspathic material at higher differential stresses and lower temperature.

Theoretical and experimentally derived flow laws from literature are tested with the data obtained in this thesis. The quartz - feldspathic behavior can be simulated at Reuss-bound (iso-stress) conditions, resulting in geologically reasonable strain rates and viscosity ratios.

In the Truzzo granite shear zones, Fourier transform infrared spectroscopy (FTIR) measurements inside single grains reveal that quartz remains dry during recrystallization at the main deformation event. FTIR spectra are flat and the water content is comparable to that of brazil quartz. Fluid inclusions and sub-micron sized white mica inclusions are expelled from magmatic quartz grains during grain boundary migration recrystallization. Deformation of the quartz aggregates took place at water present conditions, and quartz grain size piezometers suggest low differential stresses while dry quartz is considered extremely strong during fluid-absent, experimental deformation. Therefore it is suggested that grain boundary processes contribute to the commonly observed weakening of polycrystalline quartz during fluid present conditions and that the low water concentrations might be sufficient for crystal plasticity at natural conditions.

Kurzfassung

Diese Arbeit behandelt die Verformungsmechanismen, die Rheologie und die damit assoziierten Mikrostrukturen von Quarz bei der Verformung in polymineralischen Gesteinen. Ausgewählte Proben stammen von kleinmassstäblichen, hochtemperierten Scherzonen aus Granitoiden der Gran Paradiso Decke, Westalpen, Italien und der Tambo Decke, Zentralalpen, Italien. Mit Hilfe von optischer Lichtmikroskopie, Raster-Elektronen-Mikroskopie und digitaler Bildanalyse wurde die mikrostrukturelle Entwicklung von unverformtem und leicht verformtem Randgestein bis zu höchst verformten, ultramylonitischen Scherzonen untersucht. Kristallographische Vorzugsregelungen wurden mit Hilfe von computer-integrierter Polarisationsmikroskopie (CIP) und Rückstreuelektronenbeugung (EBSD) gemessen und mit Hilfe von Orientierungskarten analysiert.

In beiden Fallbeispielen rekristallisiert Quarz dynamisch in polykristallinen Aggregaten, die von feinkörniger, feldspatreicher Matrix umschlossen sind. Quarzaggregate verformen durch Dislokationskriechen, die feldspatreiche Matrix durch Diffusionskriechen. Mit zunehmender Verformung bilden die Quarzaggregate zuerst parallele Lagen mit der Matrix um letztendlich zu desintegrieren und eine Mischung auf Kornebene mit Feldspäten und Glimmern zu formen. Die Desintegration der Quarzaggregate markiert den Übergang von Mylonit zu Ultramylonit und findet anhand von intergranularer Dilatanz statt, die in Verbindung mit Korngrenzgleiten steht und durch die Präzipitation von Kalifeldspat und Biotit kompensiert wird.

Die polykristallinen Quarzaggregate bilden Porphyroklasten und fließen in der niedriger viskosen Matrix bei niedriger, konstanter Differenzialspannung (5-50 MPa). Diese Situation kann durch die Reuss-Grenze angenähert beschrieben werden. Die Quarzlagen desintegrieren, da Quarz sich nicht durch Dislokationskriechen kompatibel zur Matrix verformen kann.

In den Scherzonen des Gran Paradiso (untere Amphibolit Fazies, ~500-550°C) bildet Quarz eine stabile, dynamische Korngröße. Subkornrotations-Rekristallisation trägt zur Abnahme und Korngrenzmigration zur Zunahme (durch synkinematisches Kornwachstum) der Korngröße bei. Bei dem Übergang zu dem Ultramylonit wird die Quarzkorngröße kleiner als die Subkorngröße und nähert sich der (Feldspat-) Matrixkorngröße an. Es kann gezeigt werden, dass die Abnahme der Korngröße das Ergebnis einer Kombination aus Korngrenzarretierung (pinning) durch die präzipitierten Phasen und gleichzeitigen Lösungsvorgängen ist. Der Quarz Volumenanteil bleibt konstant, weshalb ebenfalls von der Präzipitation von Quarz ausgegangen werden muss. Korngrenzarretierung unterdrückt synkinematisches Kornwachstum und durch die Lösungsvorgänge wird eine Korngröße unterhalb der Subkorngröße erreicht. Der Ultramylonit fließt durch Diffusionskriechen. Quarz im Ultramylonit hat isotrope Kornformen und keine kristallographische Vorzugsregelung.

Polykristalline Quarzaggregate im Gran Paradiso - Mylonit haben eine starke kristallographische Vorzugsregelung, die durch die basales <a> Gleiten erklärbar ist. Die kristallographische Vorzugsregelung jedes Aggregates entwickelt sich bezüglich eines lokalen kinematischen Bezugssystems und nicht mit Bezug auf das globale kinematische Referenzsystem (Scherzone). Das lokale Bezugssystem wird durch das Aggregat und dessen Interaktion mit der Matrix definiert und durch die Verformung der Matrix und der Kopplung von Matrix und Aggregat kontrolliert. Eine starke kristallographische Vorzugsregelung entwickelt sich bereits bei geringer Verformung und [c]-Achsen - Maxima zeigen eine stabile Orientierung bei 70° in Bezug auf die lokale Fließebene.
Quarzaggregate zeigen einen lokalen Schersinn an, der bei niedriger Verformung systematisch entgegengesetzt zum globalen Schersinn ist. Dies wird als das Ergebnis von Verformungsaufteilung zwischen den höher viskosen Quarzaggregaten und der niedriger viskosen Matrix bei genereller einfacher Scherung interpretiert.
Das Quarzgefüge ist von der kristallographische Vorzugsrichtung abhängig. Das Maximum der Orientierungs-Verteilungs-Funktion der Korngrenzen ist immer synthetisch zu dem Maximum der [c]-Achsen Polfigur rotiert, wobei synthetisch in Bezug auf die Gleitrichtung auf der Basalfläche zu sehen ist. Dieses Verhältnis suggeriert eine kristallographische Kontrolle bei der Gefügeentwicklung. Es wird vorgeschlagen, dass sich orthorhombische Korngrenzgefüge bei hoher Korngrenzmobilität und monokline Korngrenzgefüge bei niedriger Korngrenzmobilität bilden.

In den Scherzonen des Truzzo Granits (Amphibolit Fazies, ~550 -650°) ist die dynamische Rekristallisation von Quarz durch Korngrenzmigration dominiert, wobei bei fortgeschrittener Verformung eine Zunahme von Subkornrotations-Rekristallisation beobachtet wird. Ultramylonitsche Teile der Scherzonen fließen durch Diffusionskriechen, wobei einzelne Quarzkörner eine anisotrope Form und Regelung und eine sehr schwache kristallographische Vorzugsregelung zeigen. Dies wird als Hinweis auf eine Beteiligung von kristallplastischer Verformung interpretiert.
Anschliessende Verformung bei höheren Differenzialspannungen führt zu einem relativen Härten der sehr feinkörnigen Phasenmischungen in den Scherzonen und deren “necking” im umgebenden grobkörnigen Granit.

Als letzte Strukturen im Ultramylonit bilden sich lokal Lagen in denen Biotit instabil ist und Quarz - “Bulging”- und Subkornrotations-Rekristallisation zeigt. Dies wird als Resultat der Inversion des Viskositätskontrastes zwischen Quarz und Feldspat bei höheren Differentialspannungen und niedrigeren Temperaturen angesehen.

Theoretische und experimentell bestimmte Fließgesetze aus der Literatur sind mit den Daten aus dieser Arbeit getestet worden. Das Quarz - Feldspat - Verhalten kann unter konstanter Differentialspannung (Reuss-Grenze) mit geologisch realistischen Verformungsraten und Viskositätsverhältnissen simuliert werden.

Fourier-Transform-Infrarot-Spektroskopie (FTIR) innerhalb von Quarzkörner der Truzzo - Scherzonen zeigt, dass Quarz während der Rekristallisation trocken bleibt. FTIR - Spektren zeigen keine Absorptionsbänder in Verbindung mit intrakristallinem Wasser und der intragranulare Wassergehalt ist vergleichbar mit klarem Quarz (Bergkristall). Primäre Fluideinschlüsse und Sub - Mikrometer - Einschlüsse von Hellglimmer werden durch Korngrenzmigration aus den magmatischen Quarzkörnern entfernt. Die Verformung der Quarzaggregate fand unter der Gegenwart von Fluiden statt. Quarz - Korngrößenpiezometer ergeben niedrige Differentialspannungen, obwohl trockener Quarz bei experimenteller, fluidfreier Verformung eine extrem hohe Fließfestigkeit hat. Es wird vorgeschlagen, dass Korngrenzprozesse an dem generell beobachteten Festigkeitsabfall von Quarz bei der Verformung unter fluidanwesenden Bedingungen beteiligt sind und gegebenenfalls die niedrigen Wassergehalte ausreichen, um Kristallplastizität bei natürlichen Bedingungen zu ermöglichen.

Chapter 1

Introduction

1. Motivation

Deformation in the crust of the earth is usually localized in narrow zones. These zones form in response to plate tectonics and dynamics at various scales. The physical boundary conditions and the rock itself determine the mode and mechanism of deformation (e.g Kohlstedt et al., 1995). At low lithostatic pressures, low temperature and high strain rates, rocks fail by fracturing, and flow is achieved by frictional, pressure dependent processes. At high confining pressures, high temperatures and low strain rates, rocks deform by temperature and rate dependent processes. The crossover of both regimes depends on factors like the geothermal gradient and the imposed displacement rate. Even though his is a interesting subject, the frictional flow of rocks will not be considered further in much detail in this thesis.
Understanding the rheology of the earth crust can help to understand large scale dynamics. Usually a strength of the continental crust is calculated, based on the assumption of a constant strain rate (Kohlstedt et al., 1995). The result is a “strength profile” which often serves as an input for numerical models of crustal scale processes (e.g. Regenauer-Lieb & Yuen, 2006). However, in spite of highly sophisticated algorithms and computational power the experimentally derived flow laws which are used to calculate the crustal strength profiles, are in most cases obtained from pure quartz rocks (e.g. Parrish et al., 1976; Koch et al., 1989; Luan & Paterson, 1992; Gleason & Tullis, 1995; Hirth et al., 2001; Rutter & Brodie, 2004a,b). Despite the criticism of the assumption of constant strain rates and geothermal gradients, it is indisputable that the continental crust does primarily consist of polyphase rocks and not of pure quartz.

The reasons why quartz is often used as a proxy for the continental crust is probably based on the facts that quartz constitutes the second most abundant rock-forming mineral in crustal rocks, that it is one of the most studied minerals in nature and experiments, and that there are very few flow laws of other rock forming minerals (e.g. plagioclase: Rybacki & Dresen, 2000) which can be extrapolated to the variety of natural conditions. It has to be noted that experimental deformation of most polyphase rocks in the ductile field is not possible without melting, because the eutectic point is often lower than the temperature required for experimental strain rates to lie within a human time scale. Melt will have an influence on the rock strength at low percentages and control the strength of the rock above 10-30% (e.g. Arzi, 1978, van der Molen & Paterson, 1979) and therefore melt bearing experiments cannot be extrapolated to melt-free rocks.

Regarding the fact that the crust is principally made up of quartz-bearing polyphase rocks,
it is very important to know to which extend quartz deformation in a polyphase rock deviates from deformation of a monophase quartz rock.

Is it possible to translate inferences made from monophase quartz rocks to quartz in a polyphase rock? Are microstructural concepts (e.g. fabrics, crystallographic preferred orientations) that were established in quartzites transferable to polyphase rocks? What are the deformation mechanisms of quartz in polyphase rocks? How do polyphase rocks scale down from mixtures of polycrystalline aggregates to grain scale phase mixtures? These questions are intended to be answered based on the study of naturally deformed rocks.

2. Setup of this thesis

Granitoid rocks make up large parts of the continental crust. Undeformed granitoids can often be regarded as isotropic. Deformed granitoids either form rather homogenous orthogneisses in broad zones, or mylonites and ultramylonites in highly localized shear zones. This relates to mechanisms supporting localization of deformation.

In the homogeneously deformed granitoids quartz is often recognized to accommodate large parts of the strain (e.g. Vernon et al., 1983). This is probably an additional reason why quartz is regarded as a proxy for crustal rheology. Nevertheless, the strain accommodated by large and homogeneously deformed volumes of orthogneiss is often small compared to zones of localized deformation. Shear zones are found from millimeter scale to planetary scale (e.g. Regenauer-Lieb & Yuen, 2003) and seem to accommodate the major part of displacement generated during plate tectonics.

For that reason shear zones in granitoids have been target to study the deformation of quartz in a polyphase rock.

Samples of small scale shear zones for this thesis were collected from the granodiorite of the Gran Paradiso nappe, the Truzzo granite of the Tambo nappe, the Monte Rosa granite and the Adamello granodiorite (some samples were also kindly provided by Giorgio Pennacchioni).

Durning earlier stages of this work, larger scale shear zones were sampled in Le Chatelard, Aiguilles Rouges massif, the basal part of the Corvatsch nappe and the Ringvasøya shear zones in northern Norway. A set of samples was also collected across the Bergell tonalite with the intention to provide a strain gradient N to S and a temperature gradient E to W (e.g. Berger et al 1996). However, the painful finding that neither the quartz content is constant, nor quartz is present in all samples, renders the Bergell tonalite unsuitable for this study. The shear zone in Le Chatelard seem to have undergone a brittle activity. The rocks sampled from the Corvatsch shear zone show a strong compositional variation. The Ringvasøya shear zones formed in relatively homogenous archaic TTG gneisses, but preliminary inspection confirm a heterogeneous metamorphic overprint.

Even though it might be easier to argue for the geological importance of large scale shear zones, deformation in many large scale shear zones happens within a temperature gradient and flow is often heterogeneous at the shear zone and time scale (e.g. Carter & Norris, 1976; Tapponnier & Molnar, 1977; Guillaume, 1978, Wellman, 1984). Additionally, the larger shear zones are, the higher the probability to encounter compositional heterogeneities due to variable protoliths.

In order to minimize the number of variables, small scale shear zones with only several 10s to 100s of millimeters width have been selected. The temperature and the kinematics across all parts of the shear zone at any given instant of time are likely to be homogeneous, and most small scale shear zones are geologically short lived. Chances are high for a homogenous protolith within the scale of the shear zones. There are two types or scales of polyphase rocks that can be observed: mixtures of polycrystalline aggregates at low strain and mixtures of single grains at the highest strain.

Samples of the small scale shear zones in the Gran Paradiso granodiorite and the Truzzo granite have been studied in most detail and the results are presented in this thesis.

3. Fundamental concepts

In the following a brief review will be given on microstructures related to deformation, crystallographic preferred orientations, deformation mechanisms and flow laws, deformation of polyphase rocks and quartz deformation in polyphase rocks.

Microstructures and deformation mechanisms:
Below the brittle ductile transition quartz is expected to deform either by dislocation creep or diffusion creep.
The presence of a CPO, a monoclinic fabric, a large grain size amongst other criteria have been ascribed to be compliant with dislocation creep (Baker & Wenk, 1972; Hobbs, 1985, Schmid et al., 1987; Stipp et al., 2002). By contrast, a small grain size, a weak or absent CPO and a low fabric anisotropy are usually related to diffusion creep (Boullier & Gueguen, 1975, Stünitz & Fitzgerald, 1993; Fliervoet et al., 1997; Mehl & Hirth, 2006; Kanagawa et al., 2008). Surely there are transitional microstructures because processes of both mechanisms can contribute to the final microstructure.
Dislocation creep related processes in quartz are associated with deformation lamellae, the formation of recovery related structures like subgrain boundaries, and dynamic recrystallization in general (e.g. Passchier & Trow, 1996).
Diffusion creep related processes are associated with the formation of grain boundary alignment, phase mixing, and dissolution-precipitation related structures (Drury & Humphreys, 1988; Kruse & Stünitz, 1998; Wintsch et al., 2002). These criteria are often observed in metals or phase mixtures but diffusion creep in quartz is rarely reported (e.g Behrmann, 1985).

As above mentioned, there is agreement that a CPO is related to intracrystalline deformation. The absence of a CPO is usually attributed to a deformation mechanism where either rigid body rotation of grains or diffusion of vacancies or matter happens at a rate higher than dislocation processes. Anisotropic surface energies have been proposed to contribute to the formation of a CPO during diffusion creep (Bons & DenBrok, 2000). Dissolution-precipitation processes causing a weak preferred c-axis orientation have been suggested for some very low grade rocks (Hippertt, 1994; Stallard & Shelley, 1995). Generally, the rule of thumb would be that rocks undergoing dislocation creep are thought to possess a CPO while rocks undergoing diffusion creep can be expected to lack a CPO.

The relation of particle and surface fabrics with a specific deformation mechanism is not straightforward. Surface orientation distribution functions of experimentally deformed calcite rocks have been shown to switch from strain (orthorhombic) to recrystallization controlled (monoclinic) geometries (Schmid et al., 1987). Nonetheless not every orthorhombic geometry needs not to related to strain. A monoclinic geometry is commonly found in dynamically recrystallized quartz rocks (Knipe & Law, 1987; Stünitz, 1991; Stipp et al., 2002). It has to be kept in mind that fabrics are easily modified by grain growth. Under certain conditions (e.g. Wheeler, 2009) an anisotropic fabric is also found in rocks undergoing diffusion creep (Rybacki & Dresen, 2000; Gomez-Barreiero, 2007; Menegon et al., 2008).

Grain sizes are of twofold importance for the estimate of deformation conditions. During dislocation creep, dynamic recrystallization is the result of recovery. A grain size produced by dynamic recrystallization can be related to the differential stress under which deformation took place (e.g. Twiss 1977, Shimizu, 2008). During diffusion creep, differential stresses are low so dislocation movement is of only minor importance and the grain size is independent of the differential stress. However diffusion lengths scale with the grain size and cause a inverse-nonlinear relation of the strain rate with the grains size. Grain sizes reported for monomineralic quartz rocks, which actually favor the activity of diffusion creep at a geologically significant rate, are usually very small and difficult to attain (e.g. Etheridge & Wilkie., 1979; Rutter & Brodie, 2004b). In a simple model, the grain size needs to be smaller than the subgrain size if diffusion creep should be the dominant deformation mechanism (Langdon, 1994).

The above discrimination of grain sizes into small and large is relative and absolute values depend on the deformation conditions.

While dislocation creep seems to be readily established in natural and experimental conditions (eg. Tullis et al., 1973), diffusion creep seems to be difficult to realize in pure quartz aggregates (Behrmann, 1985; Rutter & Brodie, 2004). In natural rocks the lack of a CPO in medium to high grade quartz rocks has been ascribed to diffusion creep (e.g. Lagoeiro & Fueten, 2008), but actually diffusion creep seems to be rarely realized, probably because grain sizes in the range of few microns are difficult to maintain at high temperature conditions unless grain growth can be suppressed.

Therefore some microstructural properties are good indicators of the deformation mechanism while others are ambiguous or are not exclusive.

Quartz CPOs:

Quartz crystallographic preferred orientation has been extensively studied in naturally deformed quartz rocks (e.g Sander 1934; Behrmann & Platt, 1982; Schmid & Casey, 1986; Mancktelow, 1987; Law et al., 1990; Llana-Funez, 2002) as well as in experimentally deformed quartzites (Tullis et al, 1973, 1977; Dell'Angelo & Tullis, 1989; Schmocker, 2002; Heilbronner & Tullis, 2006).

Historically, quartz c-axis polefigures were intensively studied based on U-stage measurements. CPOs of biaxial minerals were not straightforward to obtain. Modern x-ray or neutron diffraction techniques (e.g Baker & Wenk, 1972; Bunge, 1989) enable the measurement of complete CPOs in a bulk volume of rock. Continuous [c]-axis orientation maps e.g. based on computer-integrated polarization microscopy (CIP) (Panozzo Heilbronner and Pauli, 1993) provide additional information about the spatial distribution of the CPO forming elements (e.g. Heilbronner, 2010). Electron backscatter diffraction (EBSD) is capable of measuring the full CPO as well as producing orientation maps (Venables & Harland, 1973; Adams et al, 1993).

The geometry of a CPO has been used to deduce information of flow like the geometry of the kinematic framework (Schmid & Casey,1986; Law et al., 1990), the degree of non-coaxiality of flow (Behrmann & Platt, 1982; Platt & Behrmann, 1984, 1986), or temperatures of deformation (Kruhl, 1996; Law et al, 2004). The activity of certain slip systems has been attributed to different deformation temperatures (Takeshita, 1996; Stipp et al., 2002) with a transition from basal <a> to prism <a> to prism <c> slip with temperatures increasing from low to medium grade to high grade conditions. Some studies indicate that also a dependency on the accumulated strain or strain rate may influence the geometry of the CPO (e.g Heilbronner & Tullis, 2006; Peternell et al., 2010).

In order to derive kinematic informations from CPOs the reference frame in which the CPO develop has to be known. However, different reference frames are reported. In non-coaxial flow the geometry of a CPO has been observed to be either tied to the global kinematic framework (Van Roermund, et al., 1979, Lister & Hobbs, 1980, Wenk et al, 1989) or the CPO has been observed to rotate with respect to the global reference frame and to be roughly related to a local reference frame close to the finite strain axes (Carreras et al., 1977; Etchecopar & Vasseur, 1987; Heilbronner & Tullis, 2006). Whether one or the other is the case, has been suspected to be related to flow partitioning, a phenomena likely to encounter in polyphase rocks (Lister & Williams, 1979).

Rheology and the type of flow laws:

The stress - strain rate - temperature - grain size relations in experimentally deformed, monophase rocks, can be described in flow laws. Flow laws usually relate the strain rate to the product of the differential stress, grain size, an Arrhenius term and a factor A (Fig. 1).

The differential stress has an exponent n and the grain size has an exponent m. The Arrhenius term establishes the temperature dependence and contains an activation energy Q. The factor A incorporates variables which are assumed to be constant for a certain flow law and condition but in most cases no exact physical relation has been established.

Dislocation creep is thought to be independent of the grain size (m=0) and to depend non-linearly on the differential stress with values of n between 3 and 7 (power-law behavior). The diffusion creep rate is found to be linearly dependent on the differential stress and to depend on the grain size with m=-2 for volume diffusion and m=-3 for grain boundary diffusion. In an isothermal differential stress grain size space separate fields exist for dislocation creep and diffusion creep (Fig. 1). If a material can decrease its grain size, a switch from dislocation to diffusion creep is is possible. While grain growth can easily cause a switch from diffusion creep to dislocation creep, it is disputable if solely dynamic recrystallization is capable to reduce the grain size sufficiently (Etheridge & Wilkie, 1979; Bresser et al., 2001). Therefore, other processes like the inhibition of grain growth, fracturing or reaction are considered to contribute to the grain size decrease (e.g. Kerrich et ., 1980; Fitzgerald & Stünitz, 1993; Newman et al., 1999).

Additional factors influencing the position of the dislocation-diffusion creep fields are e.g. the chemical environment and the availability and state of a fluid phase. For example, during experimental deformation of synthetic, polycrystalline quartz (Luan & Paterson, 1992) a decrease of the stress exponent is observed with the introduction of chemical impurities in the pore fluid while the grain growth is not restricted.

In experiments on quartz undergoing dislocation creep the observation has been made that the strength of the material decreases with increasing confining pressure (Kronenberg & Tullis, 1984). This has been interpreted to display a function of the water fugacity (Hirth et al., 2001) contributing to the pre-exponential factor in the dislocation creep law. Experiments indiacte that quartz under water present conditions shows a decreased strength, compared quartz at water absent conditions or at low water fugacities (Griggs & Blacic, 1965,1966; Kekulawala et al., 1978; Kronenberg & Tullis, 1984, Stipp et al., 2006).

It is obvious that the extrapolation of experimentally derived flow laws to nature is not straightforward because many boundary conditions which can be easily determined in the laboratory are hard to conceive in naturally deformed rocks.

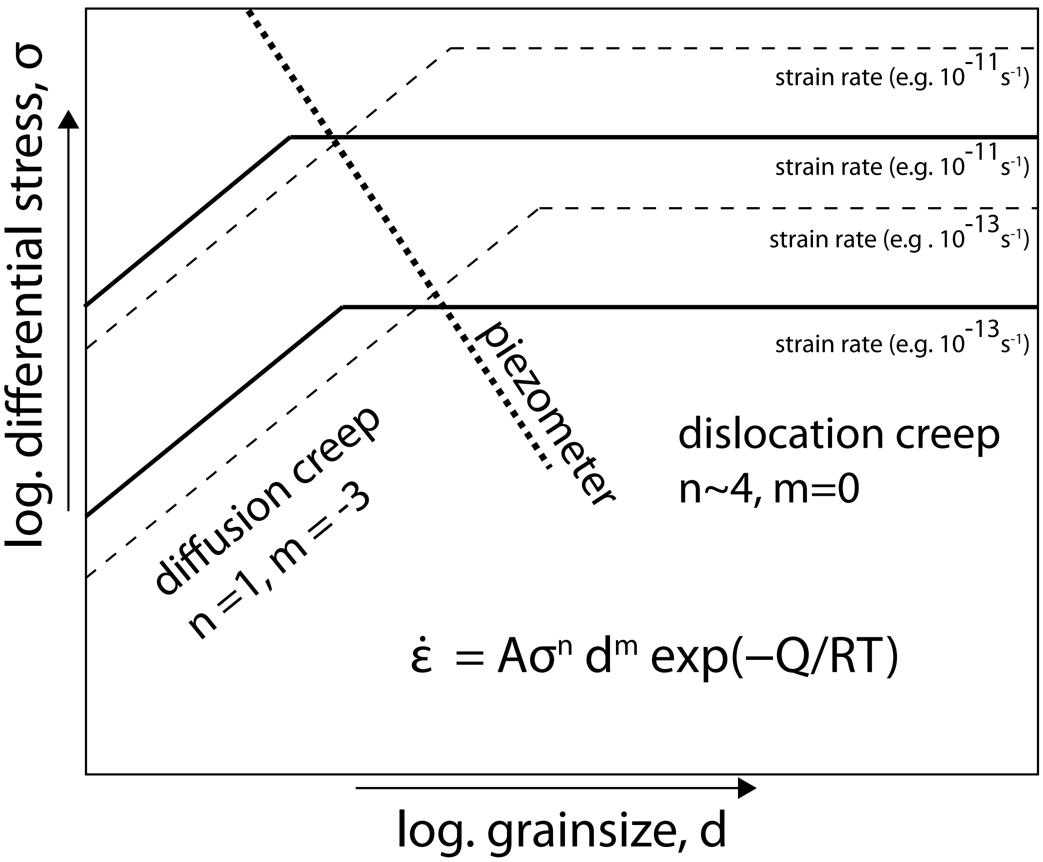

Figure 1: Relation of differential stress, strain rate, and grain size for two hypothetical materials, e.g. quartz (solid line) and e.g. feldspar (stippled line) that deform either by diffusion creep, favored at small grain sizes or by dislocation creep at large grain sizes. The strain rate of dislocation creep is independent on the grain size. In dislocation creep the grain size is related to the differential stress by an empiric, material specific piezometric relation (dotted line for "quartz").

Deformation of polyphase rocks:

Various attempts were made to determine the rheology of polyphase rocks. Experimental rock deformation however is restricted to only few systems with high eutectic melting points (Dimanov & Dresen, 2005). Few experimentally derived flow laws exist for granitoids, but either involve dry and semi-brittle conditions, or low very low strain (Shelton & Tullis, 1981, Hansen & Carter, 1982) as granitoids are usually subject to melting at the experimental conditions required for ductile deformation.

Theoretical considerations suggest that the bulk rheology should depend on the rheologies of the constituting phases, the distribution of phases and their volume proportions (e.g. Handy, 1990; Tullis et al. 1991; Ji et al., 2003). The distribution of phases and their relative strength determines the bulk strength between two bounds (Fig. 2). If the material, which behaves as the weaker phase is interconnected, the bulk material should approach a lower bound in which all phases deform at a constant differential stress (Reuss-bound/ iso-stress). A slight modification of the the Reuss-bound model would be the interconnected weak layer model (IWL) of Handy (1990), which suggests the possibility that the weak matrix may deform at a higher rate than the bulk rock. Generally, the continuous alinement of a weak phase or the formation of layering is believed to reduce the bulk strength of the rock (LeHazif, 1978; Jordan, 1988; Handy, 1990; Bons & Urai, 1994; Zhao & Ji, 1994; Park et al., 2006).

If the material with the lower strength is enclosed in the higher strength material (load bearing framework, LBF, Handy) it can be assumed that the bulk material should approach an upper bound in which all phases deform at a constant strain rate (Voight-bound/ iso-strain rate). It is a frequently encountered situation that a deforming aggregate undergoes a transition from a load bearing framework to an interconnected weak layer by coalescence of the weak phases due to failure of the framework (Arzi, 1978; Rutter & Neumann, 1995; Holyoke & Tullis, 2006a,b).

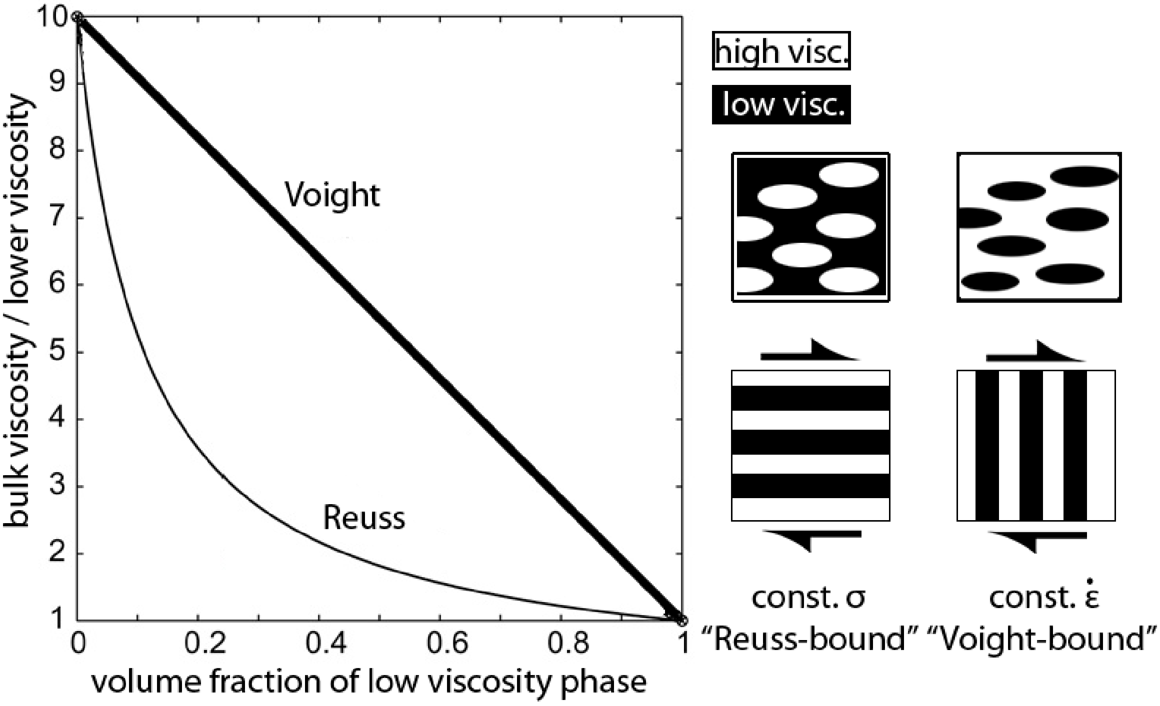

Figure 2: Dependence of the bulk viscosity of a material composed of two phases (with the same stress exponent) as a function of the volume fraction of a low viscosity phase. The value depends on the distribution of both phases. The Reuss-bound is the lower bound, simplified with a system of high viscous inclusions in a low viscous matrix (or layer parallel shear), that deforms at a constant differential stress. The Voight-bound gives an upper bound, simplified with a system of lower viscous inclusions in a load bearing framework (or layer normal shear), that deforms at a constant strain rate (Reuss-Voight curves modified after Pollard & Fletcher, 2005).

However, there are exceptions to that concept. The dispersion of a small fraction of non-connected high strength inclusions in a weaker matrix has been reported to increase the bulk strength (Renner et al., 2007) or contrarily to weaken the bulk material (Bruhn et al., 1999). The former has been attributed to load transfer between the hard phase of the introduction of higher dislocation densities in the surrounding matrix. The weakening effect may relate to a local weakening of the matrix due to stress concentrations in a power-law matrix around the inclusions or enhanced diffusion along phase boundaries compared to grain boundaries (Wheeler, 1992). However, the extrapolation to geological conditions finally depends on the time dependent processes like grain growth (Oolgard, 1990; Renner et al., 2007).

Numerical models have been employed to predict the behavior of polyphase rocks (e.g. Tullis et al., 1991; Johnson et al., 2004; Takeda & Griera, 2006) but the adaption of dynamic microstructural changes is still challenging.

The mixing law is a concept to predict the bulk rheology of a polyphase rock out of the flow laws of the constituting phases within Voight and Reuss-bound behavior (Ji & Xia 2002). However, existing flow laws for many non-quartz rock forming minerals are only valid for certain deformation mechanisms with tight constraints on e.g. orientation conditions (e.g 001 slip in mica: Kronenberg et al., 1990) or water content (e.g. dislocation creep of wet anorthite: Rybacki & Dresen, 2000). Additionally any potential feedback between the constituting minerals , e.g enhanced grain boundary diffusion or effects of stress concentrations are not considered.

In real rocks, the volume proportions of different rheological phases are crucial for the description of the system. The rheologically critical matrix percentage is proposed as a lower limit for a substantial weakening effect (Gilotti,1992) and a stable transition from a load bearing framework to a system controlled by the strength of the weaker phase. Experimental studies on melt bearing systems propose values around 20±10 % (Arzi, 1978, van der Molen & Paterson, 1979, Auer et al., 1981; Dell'Angelo & Tullis, 1988) and values for polyphase rock material are also in the range of 10 to 30 % (Jordan, 1987; Gilotti, 1992; Holyoke and Tullis, 2006).

Strain partitioning:

An effect during flow of a polyphase material with viscosity discontinuities is the partitioning of deformation between the constituent phases (e.g. Lister & Williams, 1980; 1983). This effect of the partitioning of flow has been considered to explain the ambiguous reference frames encountered during CPO development (Lister & Williams, 1979) mentioned earlier in this chapter. The required viscosity discontinuity can exist in a mixture of different mineral aggregates (e.g. a deforming granite) or at the scale of single grains and grain boundaries (e.g. a mineral undergoing grain boundary sliding and coeval intracrystalline deformation).

The partitioning of flow between separate rheological phases in a polyphase rock has to be considered during the interpretations of the CPOs and during the interpretation of deformed markers.

Quartz and deformation of polyphase rocks:
Monomineralic quartz has been studied intensively. There is a good catalogue of microstructural criteria to infer the conditions of deformation, the potential deformation mechanism, information on the boundary conditions (differential stress, temperature) and the deformation history (e.g. Baeta & Ashbee, 1969; White, 1976; Tullis, 1977; Garcia-Celma, 1983; Schmid & Casey, 1986; Law et al., 1990; Hirth & Tullis, 1992; Takeshita, 1996; Stipp et al., 2002).

Previous work on the quartz deformation in polyphase rocks relates to the deformation mechanisms (e.g. Tullis et al., 1990), the CPO development (e.g. Burg & Laurent, 1978) or the influence on the dynamically recrystallized grain size (Song & Ree, 2007).
While in coarse grained polyphase rocks quartz CPOs could be measured with a U-stage (e.g. Burg & Laurent,1978; vanRoermund et al, 1979) fine grained polymineralic rocks deprived investigations prior to the usage of electron beam methods. In more recent studies computer integrated polarization microscopy (Jerabek et al., 2007; Menegon et al., 2008) or EBSD (Peternell et al., 2010) has been used on polycrystalline quartz aggregates in a polyphase rock. There are few studies that suggest a randomness of quartz CPOs in grain scale phase mixtures in highly deformed rocks (Behrmann & Mainprice, 1987; Fliervoet et al., 1997).

According to observations and experiments the relative role of quartz and feldspar - as the main constituents of granites - changes with the metamorphic grade (Vernon & Flood, 1988; Tullis et al., 1990). While feldspar may still behave in a brittle manner and quartz already deforms by intracrystalline plasticity at low grade conditions (Tullis & Yund, 1977a,b; Simpson, 1985; Fitzgerald & Stünitz, 1993; Stünitz & Fitzgerald, 1993), at medium to high grade conditions both deform in a ductile manner. Quartz aggregates may form porphyroclasts if the grain size of the feldspathic matrix is decreased, e.g. due to the formation of fine grained reaction products (Fitzgerald & Stünitz, 1993; Stünitz & Fitzgerald, 1993; Hippertt,1998). Flow by diffusion creep is favored in fine grained feldspar aggregates (Tullis & Yund, 1991).

Studies on deformation of polyphase rocks often either treat grain scale mixture of minerals (e.g. Song & Ree, 2007), or the behavior of mixed polycrystalline aggregates (e.g. Johnson et al., 2004).
Grain scale mixtures have an increased ratio of grain to phase boundaries and therefore a direct influence on the processes related to boundaries. Weakening based on the introduction of a second phase (cc: Oolgard, 1990, Ebert et al., 2007) is often explained with the suppression of grain growth. Enhanced grain boundary diffusion has also been suggested to decrease the rock strength

(Wheeler, 1992, Stünitz & Fitzgerald, 1993). Farver & Yund (1999) measure highly increased diffusion coefficients for oxygen in a natural ultramylonite which also supports a rate increase of diffusion limited processes. Therefore hampered grain growth and increased grain boundary diffusion are in favor of an increasing rate achieved by diffusion creep.

Quartz rich rocks which deform by dislocation creep are reported to show a correlation between a grain size decrease and weakening of a CPO, and an increasing mica content (Song & Ree, 2007). The same effect has been observed in impure calcite mylonites (Ebert et al. 2007) also interpreted as an increase of a diffusion creep component during a combined flow behavior. However the role of diffusion related processes during dislocation creep is not well constrained. Diffusion as well as grain boundary sliding may contribute to the accommodation of grain scale strain incompatibilities (e.g. Zhang, 1996), though combinations of these processes are better known from metallurgy (e.g. Gifkins, 1976; Kottada & Chokshi, 2007). In case of the possibility that the second phase was not initially introduced during deformation cause and effect might be non-ambiguous.

Studies on mixtures of polycrystalline aggregates (e.g. homogeneously deforming granites) rather report effects related to a mechanical aggregate interaction. The deformation mechanism in large aggregates seems not to differ from the one realized in a monophase rock at the same conditions. Strain partitioning is one frequently observed effect (e.g. Johnson et al., 2004, Jerabek, et al., 2007).

The transition between both scales of polyphase rocks - from aggregate scale mixtures to grain scale mixtures - is often related to strain localization (Stünitz & Fitzgerald, 1993; Kleinschrodt, 1994; Fliervoet, 1997; Kruse & Stünitz, 1999, Kenkmann & Dresen, 2002) and coincide with the transition from a mylonite to an ultramylonite. However the processes acting during that transition are often uncertain.

4. Structure of this thesis

Chapter 2 covers the development of microstructures associated with the transition of a mylonite to an ultramylonite in the Gran Paradiso shear zones. Quartz deforms in the mylonite in polycrystalline, monomineralic aggregates, but occurs in a grain scale phase mixture with a smaller grain size in the ultramylonite. The processes involved in aggregate disintegration and grain size reduction are evaluated, and a model for the transition from the mylonite to the ultramylonite is proposed. This chapter is published in a modified form in the Journal of Structural Geology (Kilian et al., 2011a).

Chapter 3 focuses on the development of the microstructures and crystallographic preferred orientations within the strain gradient from a weakly deformed hostrock to a highly deformed mylonite in the Gran Paradiso metagranodiorite. This chapter focuses on the deformation of a polyphase rock which consists of polycrystalline, monophase aggregates.
The development of a quartz CPO, the relation between the CPO, the fabric and shear sense, and the differentiation between a local and a global shear sense are covered. Consequences for the practical determination of shear senses from CPOs or fabrics are emphasized. This chapter is published in a modified form in the Journal of Structural Geology (Kilian et al., 2011b).

The shear zones in the southern Truzzo granite are analyzed in **Chapter 4** with regard to the shear zone formation, localization and propagation mechanisms. The deformation mechanisms of the components in the deformed granite and in the ultramylonitic shear zones are discussed based on microstructures and quartz CPOs. Subsequent changes in the microstructure are related to the rheological evolution of the truzzo granite.
Further, the water content in quartz was measured by FTIR. The influence of the recrystallization processes on the water uptake and the effect of intra- and intergranular water on the strength of quartz are discussed.

The applicability of experimentally and theoretically derived flow laws to natural rocks is discussed in **Chapter 5**. By using the data obtained from the Gran Paradiso shear zones, stress-strain-rate relations are modeled and compared with the observed structures. The flow laws which are most promising for the extrapolation to natural conditions are also tested with data from Chapter 4 and literature.

Chapter 6 provides the summary and general conclusions.

Chapter 2

Quartz grain size reduction in a granitoid rock and the transition from dislocation to diffusion creep

Abstract

In the Gran Paradiso metagranodiorite (Western Alps) small scale lower amphibolite facies shear zones record the transition from a weakly deformed rock composed of polycrystalline mineral aggregates to a homogeneous ultramylonite with a grain scale phase mixture. In the mylonite two different microstructural domains can be distinguished: (1) Polycrystalline quartz aggregates deform by dislocation creep with a constant dynamically recrystallized grain size of 110 μm. (2) Quartz aggregates are embedded in a polymineralic fine grained (~ 15 μm) matrix composed of K-feldspar, plagioclase and biotite which deforms by diffusion creep. Progressive subgrain rotation in quartz aggregates drives grain size reduction (subgrain size ~ 45 μm), whereas concomitant grain boundary migration recrystallization causes a grain size increase.

With increasing shear strain quartz aggregates progressively disintegrate while simultaneously the grain size is reduced. In the ultramylonite the quartz grain size (~25 μm) approaches the matrix grain size and all phases deform by diffusion creep with dissolution-precipitation accommodated grain boundary sliding.

Quartz in the mylonite shows a strong crystallographic preferred orientation (CPO) and a monoclinic surface preferred orientation while in the ultramylonite the CPO is randomized and the surface preferred orientation becomes orthorhombic.

During the initial disintegration of quartz aggregates, K-feldspar and biotite precipitate between quartz grains causing pinning and an associated grain size decrease. Further disintegration is accompanied by the coalescence of K-feldspar precipitates and increased grain boundary sliding. Subsequently, the quartz grain size is further reduced by dissolution.

The precipitation of K-feldspar and biotite between quartz grains deforming by dislocation creep is caused by insufficient grain scale intracrystalline strain of quartz to accommodate heterogeneous

deformation. Heterogeneous deformation can be caused by the limited number of available slip systems in quartz resulting in grain boundary sliding during dislocation creep.

1. Introduction

High strain viscous deformation in natural shear zones frequently produces two types of microstructures: (1) Monomineralic aggregates and (2) Polymineralic mixtures. Both microstructures may occur in the same shear zone in alternating layers.

The monomineralic layers typically deform by dislocation creep as indicated by a strong crystallographic preferred orientation (CPO; e.g. Baker et al., 1972; Hobbs, 1985; Schmid & Casey, 1986), a strong shape preferred orientation (SPO; Schmid et al. 1987, Stipp et al., 2002), and by characteristic dynamic recrystallization microstructures (e.g. Hirth & Tullis 1992, Stipp et al. 2002).

The polymineralic mixtures are often characterized by a fine grain size and a high degree of mixing of phases. Many workers agree that the latter two properties are an expression of diffusion creep and grain boundary sliding (e.g. Boullier & Gueguen,1975; Stünitz & Fitzgerald, 1993; Fliervoet et al, 1997; Mehl & Hirth, 2006; Kanagawa et al., 2008).

Diffusion creep is indicated by a weakening of the crystallographic preferred orientation (CPO) (e.g. Edington 1976, Padmanabhan & Davies 1980, Schmid 1982, Behrmann & Mainprice, 1987), by anticlustering of phases (Kruse & Stünitz, 1998), and characteristic grain boundary geometry and alignment (Drury & Humphreys, 1988). One of the dominant deformation processes in the diffusion creep field is grain boundary sliding, as has been discussed in the context of experimentally determined deformation mechanism maps which predict that diffusion creep is grain size sensitive (Schmid et al., 1977).

A potential switch from dislocation creep to diffusion creep is characterized by grain size reduction. The most important processes for grain size reduction are dynamic recrystallization (Schmid, 1982, Behrmann, 1985, Rutter & Brodie, 1987, Fliervoet et al., 1995), fracturation, neomineralization/mineral reactions (Kerrich et al., 1980, Rubie, 1984, Fitzgerald & Stünitz, 1993; Stünitz & Fitzgerald, 1993, De Ronde et al., 2005) and nucleation and growth of new grains (Kruse

& Stünitz, 1999, Kenkmann & Dresen, 2002). The small grain size can be retained due to impeded grain growth in the phase mixture.

The transition from dislocation to diffusion dominated creep has great consequences for the rheological behavior of the rock. Thus, the questions of what triggers or controls such a transition and which processes are active are essential to understand viscous rock deformation. In order to analyze these aspects, we present a detailed microstructural study on a small scale shear zone in a metagranodiorite covering the progressive transition from monophase polycrystalline quartz aggregates embedded in a polymineralic matrix to an ultramylonitic phase mixture. The main points will be to discuss the processes involved in the transition, such as grain size reduction, phase mixing, and CPO destruction.

In previous studies of strongly deformed granitoids, typical patterns of K-feldspar grains distributed between either plagioclase (e.g. Ishii et al., 2007) or quartz (e.g. Behrmann & Mainprice, 1987) have been described. Similar patterns have also been described for hornblende and plagioclase (Boullier & Gueguen,1975; Kruse & Stünitz, 1999).

In the analyzed shear zone, special attention has been paid to the quartz which constitutes the rheologically stronger phase in the studied rocks. This situation does not appear to be atypical in natural shear zones, despite the fact that quartz is often considered (by experimentalists, theoreticians, and modelers) as a key mineral to estimate crustal strength (e.g Kohlstedt et al.,1995 and references therein).

In this paper we describe natural shear zones which display the entire spectrum of deformation mechanisms from dislocation creep to diffusion creep. The shear zones are narrow and probably rather short lived such that in the region of interest the protolith is rather homogeneous and we do not have to consider a protracted thermal history. The kinematic framework is well constrained; the progressive deformation is assumed to be simple shear and on the scale of the total displacement along shear zones, the protolith is homogeneous. Small scale shear zones also permit a continuous sampling across the strain gradient.

2. Geological setting and sample description

The sampled shear zones are located in the northern part of the Piantonetto valley, in the Gran Paradiso Unit of the Gran Paradiso nappe. These rocks have been studied intensively (mainly by Le Goff & Ballevre, 1990, Brouwer et al., 2002, Menegon et al., 2006, 2008; Menegon & Pennacchioni, 2009). The Permian intrusives (Bertrand et al.,2005) are heterogeneously deformed during the Alpine orogeny (Dal Piaz et al., 1972; Le Bayon et al., 2006) and preserve meter to kilometer scale low strain domains surrounded by granitic orthogneisses (Callegari et al., 1969; Menegon,2006). The low strain domains host coeval straight and planar small scale shear zones in regular, equispaced, subhorizontal (and minor subvertical) groups (Menegon & Pennacchioni, 2009).

The granitoids underwent an early, at least in the low strain domains, static high pressure metamorphism at around 1.0-1.6 GPa and 500-550°C. During the later formation of the shear zones, the pressure decreased to 0.6-0.7 GPa while the temperature remained relatively high at 550+/-50°C (Le Goff & Ballevre, 1990; Brouwer et al., 2002).

Shear zones are regularly spaced, subparallel, up to several centimeters wide, and planar over distances up to several tens of meters (Menegon, 2008; Menegon & Pennacchioni, 2009). The samples investigated are from three small scale shear zones in the Gran Paradiso metagranodiorite, Piantonetto valley, Alpe Drosa area and Lago Teleccio area (GP4: 32T0371554/5037041,GP9: 32T372881 / 5038395 GP11: 32T0371389/5037047) (Fig. 1a). Samples display a strain gradient from weakly deformed metagranodiorite (protolith) to mylonites to fine grained ultramylonites (Fig. 1b). The transition from mylonite to ultramylonite - near the center of the shear zone - occurs over a few mm and can be observed within a single thin section.

The protolith shows a weak initial foliation defined by the preferred elongation and orientation of aggregates of polycrystalline plagioclase and biotite. Elongated K-feldspar crystals (up to 15 mm long) display a weak alignment. Quartz grains of magmatic origin are up to several mm in diameter; in the close vicinity of relatively rigid K-feldspar porphyroclasts, they may recrystallize dynamically along the grain margins (Fig. 3).

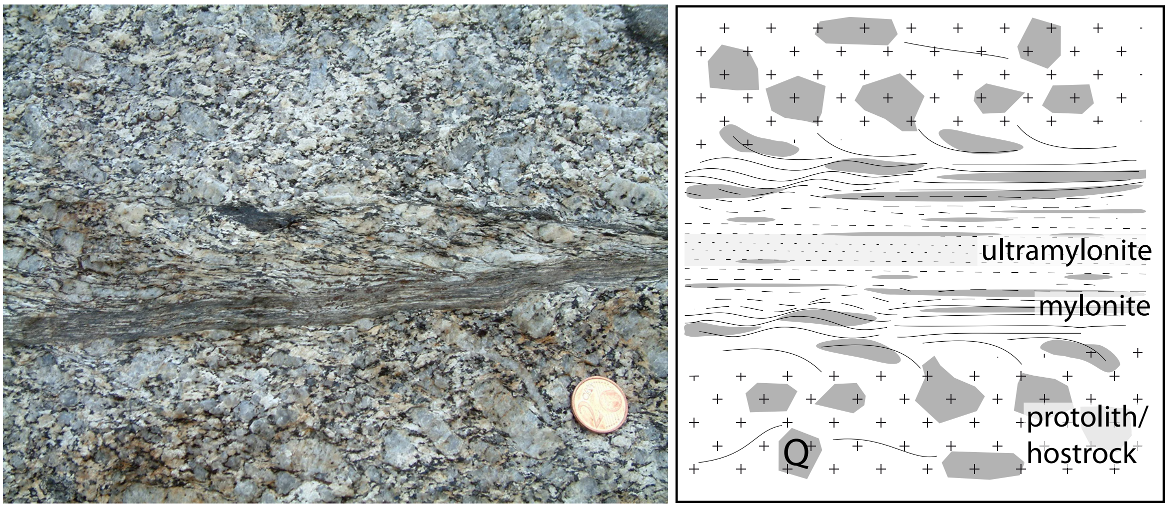

Figure 1: (a) Field view of a small scale sinistral shear zone in the Gran Paradiso metagranodiorite, similar to the sampled shear zones. The coin measures 19 mm. (b) Sketch of a shear zone in the Gran Paradiso metagranodiorite.

In the mylonitic part, the K-feldspar clasts and the biotite are dynamically recrystallized. Together with the plagioclase aggregates they form interconnected layers of varying composition and variable degree of mixing. The magmatic quartz grains are also completely recrystallized and form polycrystalline aggregates. They appear as more viscous domains in the fine grained matrix of K-feldspar, biotite and plagioclase. With increasing deformation, the quartz aggregates elongate until they form continuous layers which can diminish to a thickness of a single grain. As deformation progresses quartz aggregates and layers are converted to quartz - K-feldspar layers.

In the ultramylonite, the quartz layers are disintegrated and mixed into the surrounding matrix. At that point no layering can be observed anymore, all phases are thoroughly mixed. During the disintegration of the quartz aggregates and continued deformation the quartz grain size decreases until all phases have approximately the same grain size in the center of the shear zone (Fig. 2).

In the following, the shear zones will be displayed such that on all micrographs the shear sense is sinistral (except Fig. 14). The shear zone boundaries are horizontal (parallel to the X-Y plane), the transport direction is X, the shear zone normal is Za nd the transverse direction, assumed to be the vorticity axis, is Y. The positive X-axis is 0°, angles are measured counterclockwise.

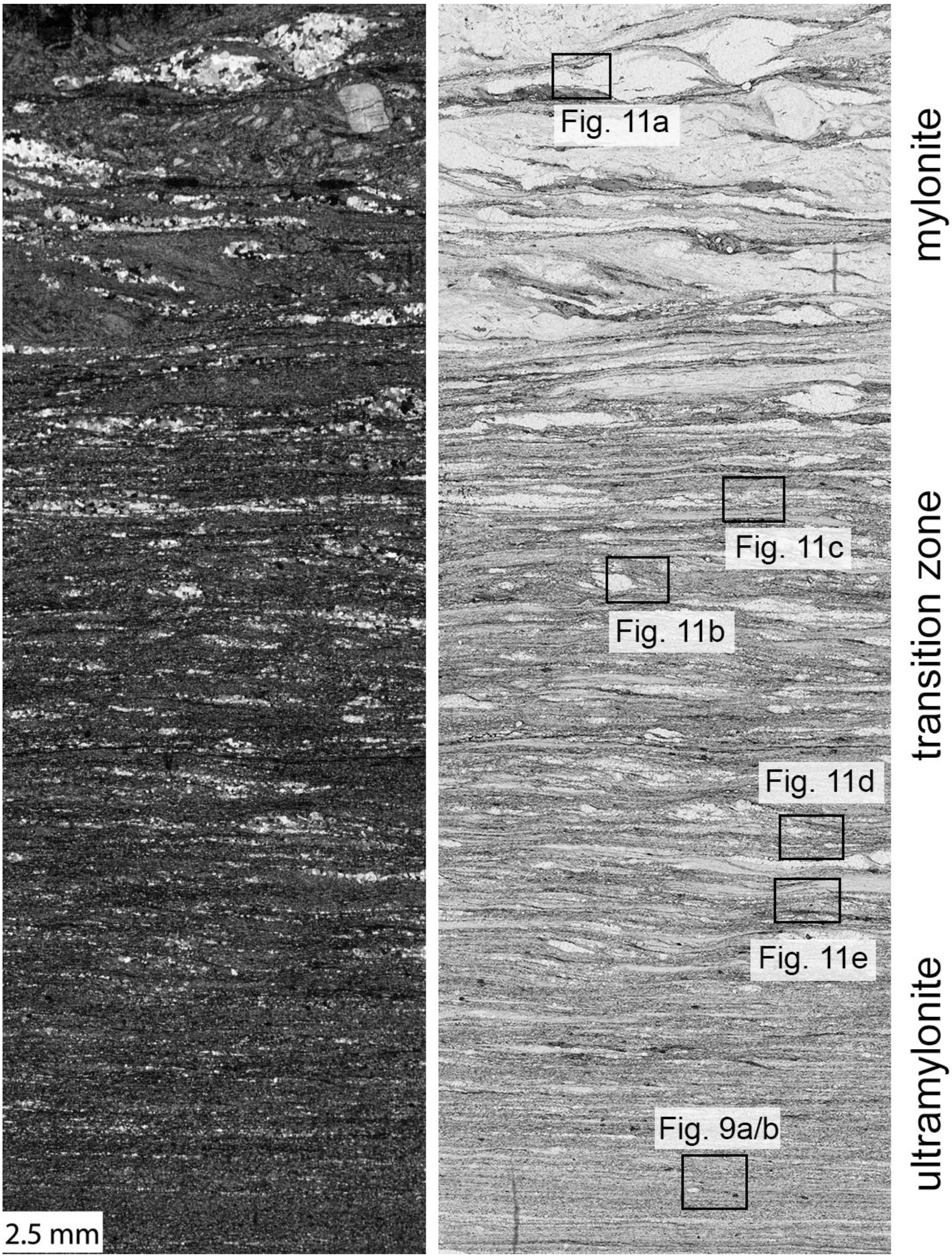

Figure 2: Micrograph of the central part of a sinistral shear zone (scans of thin section, crossed polarizers / plane light). The mylonitic part of the shear zone contains aggregates of recrystallized quartz, a K-felspar porphyroclast, and the fine grained polymineralic matrix. In the transition zone, quartz aggregates are progressively disintegrated. In the center of the shear zone, the ultramylonite consists of a homogeneously mixed matrix and polycrystalline quartz aggregates have entirely disappeared (Sample GP4-3).

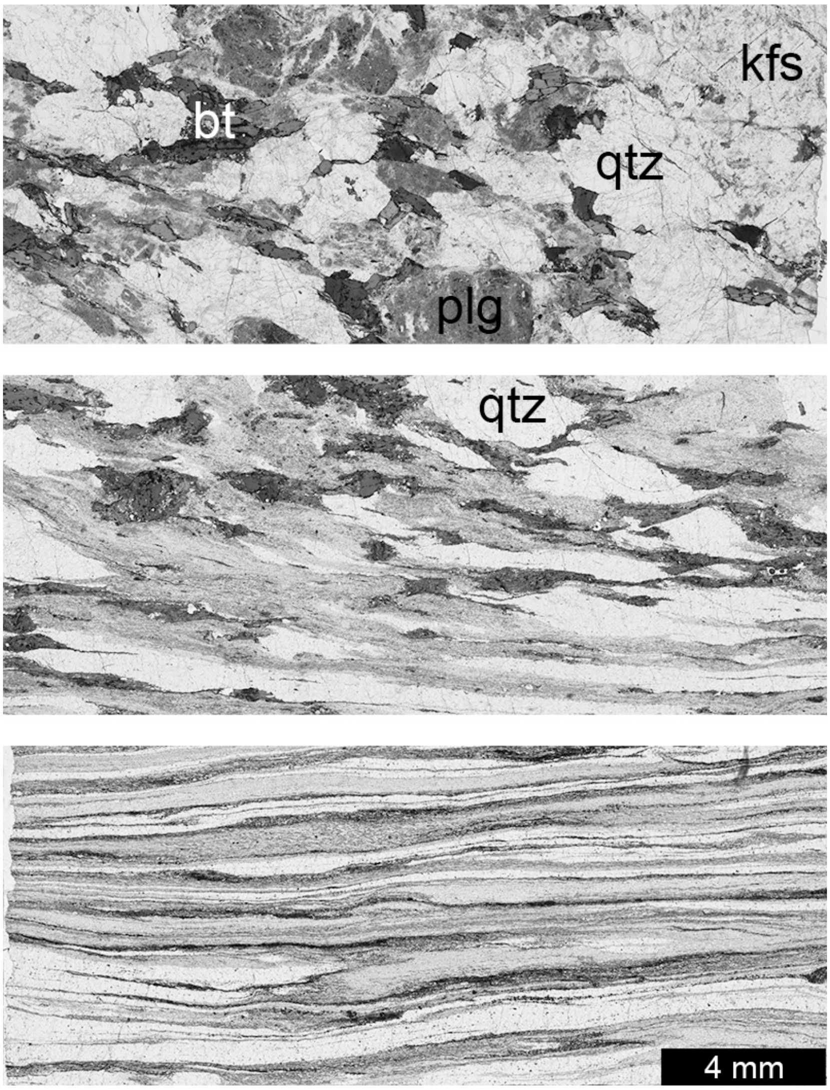

Figure 3: Sequence of weakly deformed hostrock, shear zone margin and highly deformed, mylonitic granodiorite. Quartz aggregates form elongate lenses embedded in the matrix. In the high strain part of the mylonite layers of recrystallized quartz and matrix are parallel to the shear zone zone boundary. Scans of thin sections, plane light.

The foliation is defined by a compositional layering or aligned grains, its overall orientation varies from a dip of approximately -15 to -45° (for sinistral shear sense) in the mylonite to effectively 0° in the ultramylonite. Locally, in particular around quartz aggregates in the mylonite, deviations may occur. An offset along one of the shear zones studied here, was measured to be 0.4 m, producing an local shear strain, γ, of 40. This value is a typical value for sample GP11. For samples GP4 and GP9 it may be much higher.

3. Analytical methods

3.1 Texture analysis and orientation imaging

We used EBSD for the grain size and texture analysis. Polished surfaces and uncovered thin sections were used. Using a ZEISS Evo 50 SEM equipped with a Digiview II EBSD camera and OIM acquisition software, the Euler angles were measured. Samples were polished and lapped with SYTON-fluid (Fynn & Powell, 1979; Lloyd, 1987). The polishing procedure was optimized for quartz to ensure that we got good quality EBSPs for quartz. At same time, the feldspars etched more rapidly and produced a negative relief. The pattern quality of K-feldspar and plagioclase were generally not good enough for reliable indexing. Polymineralic fine grained aggregates were analyzed by EBSD only, because the masking of non-quartz-phases was impossible in the light microscope. EBSP were obtained at step-sizes between 1 and 6.75 μm. During EBSP acquisition,element maps were recorded by energy dispersive spectroscopy (EDS); they were used for the calculation of phase maps and masks that would block all non-quartz-phases from the analysis.

For better visualization the Euler images were transformed to c-axis orientation images.
In addition three principal misorientation images were calculated - the CIP software can be downloaded from http://pages.unibas.ch/earth/micro. CIP misorientation images show the angular deviation of the c-axis (at each pixel) from an external reference direction. The principal misorientation images are calculated with respect to X,Y,Z. Here they served as the basis for image segmentation and grain size determination.

Pole figures were calculated using the MTEX software (Hielscher & Schaeben, 2008) from the raw EBSD output. To evaluate the effect of grain size dependent CPOs, grains were segmented at 7.5° misorientation (using OIM® software) and CPOs calculated for different grain size bins using both the average orientation and the area weighted average orientation of the grain.

The maximum of a pole figure depends on the kernel width, the CPO geometry, and on the number of individual grains that have been measured and only yields a rough estimate of the strength of a CPO. If the full ODF is known, the difference between the uncorrelated misorientation distribution function (e.g Wheeler et al., 2001) and the random distribution for rhombohedral crystal symmetries (Gimmer, 1979) can be calculated. This measure, the so-called M-index is proposed as a robust description of CPO strength omitting the problems associated with the examination of pole figure maxima (Skemer et al.,2005).

3.2 Grain size analysis

Grain sizes were measured from grain maps or obtained from the OIM® software. Two types of source images were used: SEM/BSE contrast images and the three principal misorientation images. Grain maps were obtained by supervised segmentation using the freeware Image SXM (http://www.ImageSXM.org.uk) and the Lazy grain boundaries macro (http://pages.unibas.ch/earth/micro). In the case of OIM calculated grain data, many grains consisted of only few pixels. However, only grains larger 6 square pixels were considered as grains.

On the grain maps, the cross sectional areas were measured and the equivalent diameters, $d_{equ} = 2 \cdot \sqrt{(area/\pi)}$, were calculated. Number weighted histograms, $h(d_{equ})$, were used as input for the STRIPSTAR program and number weighted h(D) and volume weighted histograms, V(D), of the diameters, D, of the calculated volume equivalent spheres were derived. Using a sample size of 120 to 4500, the percentage of antispheres remained below 1 % and hence the derived 3D grain size distributions were considered valid. The basis of the STRIPSTAR program is outlined in Heilbronner and Bruhn (1998); a brief description of its application can be found in Heilbronner and Tullis (2002); sources are available at http://pages.unibas.ch/earth/micro. For both distributions of spheres average grain sizes were calculated: the number weighted mean $\mu_h = \sum (h_i(D_i) \cdot D_i)$ and the volume weighted mean, $\mu_v = \sum (V_i(D_i) \cdot D_i)$ assuming that $\sum V_i(D_i) = 1.00$ and $\sum h_i(D_i) = 1.00$.

3.3 Microstructure analysis

Using subsets of the best resolved grains from the grain maps used for grain size analysis up to ~200 grains were selected. The particle fabric is quantified using the PAROR method (Panozzo, 1983) and the surface fabric by the SURFOR method (Panozzo, 1984). The preferred orientation of the quartz grains is shown as length weighted rose diagrams of long axes and the preferred orientation of grain boundary surface as rose diagrams of surface elements. The axial ratio of each grain, b / a, is determined by the ratio of the projection normal to the longest divided by the longest projection, axperp. / axlong. The average axial ratio of the grains is the mean of the individual axial ratios, b / a, of all the grains.

The bulk properties of the particle fabric as a whole are determined from the projection curves $B(\alpha)$ and $A(\alpha)$. The bulk axial ratio, $(b / a)_{bulk}$, is determined by the ratio of the minimum to the maximum of the projection curves $B(\alpha)$: $B(\alpha)_{min} / B(\alpha)_{max} = b / a$. The bulk preferred orientation of grains is obtained from the angle (α_{min}) at the minimum of $B(\alpha)$: $\alpha_p = 90° - \alpha_{min}$ (Panozzo, 1984). The ratio $(b / a)_{bulk}$ is different from the arithmetic mean of axial ratios of the individual grains since it does not only depend on the axial ratio of the grains but also on the orientation of the grains with respect to one another.

The shape of the individual grains, i.e., the lobateness of the grain boundaries, is described in terms of the PARIS factor (Panozzo and Hürlimann, 1983). The length of the actual perimeter is compared to the perimeter of the convex hull: $PARIS = 2 \cdot (P - PE) / PE$, where P is the perimeter and PE the perimeter of the convex hull (Heilbronner and Keulen, 2006). For perfectly convex shapes - whether round or angular, equant or elongated - the 'excess perimeter' is zero, hence the PARIS factor, expressed as a percentage, is 0%. The more lobate the boundary the higher the PARIS factor - there is no upper bound. For a given fabric, the numerical average of the PARIS factors of the grains is calculated.

PAROR and SURFOR analysis have been used successfully to quantify strain or - in the case of dynamic recrystallization where strain markers are absent - to infer the deformation mechanisms (Schmid et al., 1987; Stünitz, 1991; Stünitz & Fitzgerald,1993; Stipp et al., 2002). Here, we will apply these methods to the deforming quartz aggregates. In combination with texture and grain size information we will use the asymmetry of the rose diagrams to infer the local shear senses. The sources for SURFOR, PAROR and ISHAPES, the software which calculates the PARIS factor, are available at http://pages.unibas.ch/earth/micro.

3.4 Spatial distribution of phases

Phase distribution analysis was used previously to test the randomness of mixtures using the method of Kretz (1969, 2006). A two-phase-mixture of equi-sized grains can be tested for clustering, randomness or anticlustering by a comparison of phase and grain boundary fractions at different volume proportions with the theoretically predicted distributions (Kruse & Stünitz 1999; McKenzie et al., 2009). Because of changing grain size ratios Kretz's method cannot be used. Instead we use the relative frequency of grain boundary and phase boundary contacts. We measured the total length, L_g, of the quartz - quartz grain boundary and the total length, L_p of the quartz - matrix phase boundary. The ratio, R_{gp} is calculated as L_g / L_p. The lower the R_{gp} the more intensive is the mixing of the phases.

3.5 Modal content of quartz

Modal content was determined from SEM/BSE images, from phase maps that were calculated from EDS element counts, or from light micrographs.

The quartz content was measured at different scales. In the weakly deformed to mylonitic part of the shear zone, the composition is homogeneous only in areas of a few cm^2, in ultramylonites, the quartz content could be derived on much smaller areas ($< 1\ mm^2$).

4. Results

The results will be presented in the following sequence: The first two sections will concern the mylonite and the ultramylonite and will be more extensive as they represent the ‘end members’ of the strain gradient across the shear zone. The third section concerns the microstructural transition from the mylonite to the ultramylonite.

4.1 Mylonite

The mylonitic metagranodiorite appears as a rheological bi-phase material consisting of polycrystalline quartz aggregates and K-feldspar porphyroclasts (both of slightly higher viscosity) embedded in a polymineralic matrix of lower viscosity (Fig. 2, 3).

The microstructure and CPO development of quartz from magmatic grains to fully recrystallized aggregates in the low strain part of the shear zones is treated in detail in Chapter 3 (Kilian et al., 2011b); this contribution considers only those parts of the shear zones where quartz is fully recrystallized.

4.1.1 Quartz aggregates

The quartz aggregates are fully recrystallized and appear as elongate objects with a size corresponding to the original grain size (d ~ 3 - 6 mm) and closely aligned with the foliation. In the most highly strained parts of the mylonite they are elongate lenses and, finally, very thin layers parallel to the flow plane of the shear zone (Fig. 4). Throughout the mylonitic part of the shear zone, no relict magmatic quartz grains can be identified in these aggregates. The diameter of the recrystallized grains ranges between 40 and 200 μm; the volume weighted mean $\mu_V(D)$ is 110 μm (Fig. 5a). The mean grain size does not change with increasing finite strain or aspect ratio of the aggregate. Grains have a slightly lobate shape and boundaries are occasionally pinned at second phase particles (Fig. 4b).

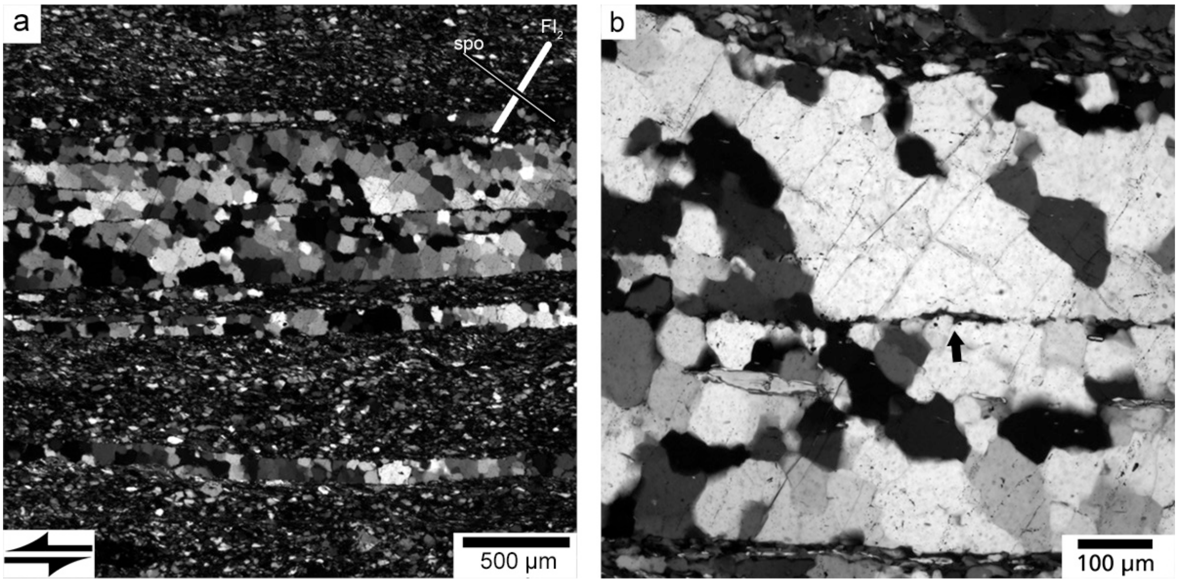

Figure 4: Quartz microstructures. (a) Stretched quartz aggregates embedded in the polymineralic matrix. Cross polarized light. Note weak oblique grain shape preferred orientation (SPO) indicating sinistral shear sense. Fluid inclusion trails and cracks are oriented at right angles (FI). Horizontal discontinuities inside the quartz layers are mostly K-feldspar seams and minor biotite flakes. (b) Detail of quartz in aggregate in a (Circular polarized light). Note protrusion of thin K-feldspar seam between quartz grain boundaries at a high angle to the layer (arrow).

Some monophase quartz aggregates exhibit straight and parallel inclusion trails with a consistent orientation of 50 - 70° to the preferred orientation of the grains (Fig. 4b). They extend across grain boundaries suggesting that fractures formed after the major deformation associated with the shear zone formation and after grain boundary movements had ceased.

Over most of the mylonitic part of the shear zone, the average size of the quartz aggregates as inferred from their cross sectional areas does not decrease significantly along the strain gradient. However, at a certain point, the aggregates become so long that their areas cannot be measured in a single thin section (Fig. 3). The width of the layers can decrease further to a thickness of a single grain. In the most highly strained parts of the mylonites, the layers begin to disintegrate (Fig. 2).

Quartz aggregates show a CPO with a strong peripheral c-axis maximum between 95-110° to the foliation rotated synthetically with the sense of shear (Fig. 6). A weak single girdle is developed and in some aggregates a minor maximum parallel to Y occurs. The <a> axes form a maximum close to the lineation. This CPO-type is attributed to a dominant activity of basal <a> glide (Blacic, 1975; Burg & Laurent, 1978, Schmid & Casey 1986). Subgrain boundaries are found in the partly recrystallized aggregates of the low strain parts of the shear zones but only rarely in recrystallized grains. In most cases, they are parallel to the traces of the {10-10} prism planes, a configuration that is also consistent with the activity of the basal <a> slip system (Trepied et al., 1980).

The PAROR analysis of the recrystallized grains yields a bulk axial ratio, $(b/a)_{bulk}$ of ~ 0.8, and an average axial ratio, b/a, of the grains of ~ 0.6. Thus, there is a weak but consistent shape preferred orientation (Fig. 5a) with a preferred orientation of particle long axes inclined at approx. 125° to 145°, i.e., inclined with the sense of shear. The SURFOR analysis yields rose diagrams of grain surface orientations with an internal monoclinic symmetry. The first maximum is at 160° and the second one at 95°. The second maximum is close to the orientation of the trace of the prism planes and the c-axis maximum (compare Figure 5a - 6). Such a situation is consistent with subgrains forming in this orientation during dynamic recrystallization in basal <a> slip of the monophase quartz aggregates. At higher strains, some quartz aggregates show diamond shaped grain junctions (Drury & Humphreys, 1988).

4.1.2 Matrix

The matrix consists of plagioclase (plg), K-feldspar (kfs) and biotite (bt,), with a minor content of white mica (wm) and accessory epidote, clinozoisite, garnet, titanite, and ilmenite; the grain size of all phases is < 20 μm. The phases are not homogeneously mixed. Instead, a layering can be observed (Fig. 7a). Despite these local variations of the mineral assemblage, the matrix is considered as one single rheological aggregate.

Fine grained plagioclase (An00 and ~An23) layers are mixed to a variable degree with recrystallized K-feldspar and biotite (Fig. 7a). Tails of recrystallized K-feldspar (d ~10 - 20 μm), are mixed into the matrix. K-feldspar clasts are occasionally replaced by myrmekite. Myrmekitization as a source for fine grained plagioclase and quartz in the wall rock matrix has been reported by Menegon et al. (2006).

Minor amounts of white mica, epidote and clinozoisite intergrown with albite and aligned along the former cleavage directions have replaced the magmatic plagioclase. Observations of the pseudomorphic fine grained plagioclase aggregates with the lambda plate inserted reveal a preferred crystallographic orientation. With the onset of deformation, the alignment of white mica and the preferred orientation of plagioclase are randomized.The low content of epidote and clinozoisite (less than 0.1 volume %) is caused by epidote/clinozoisite consumption during the

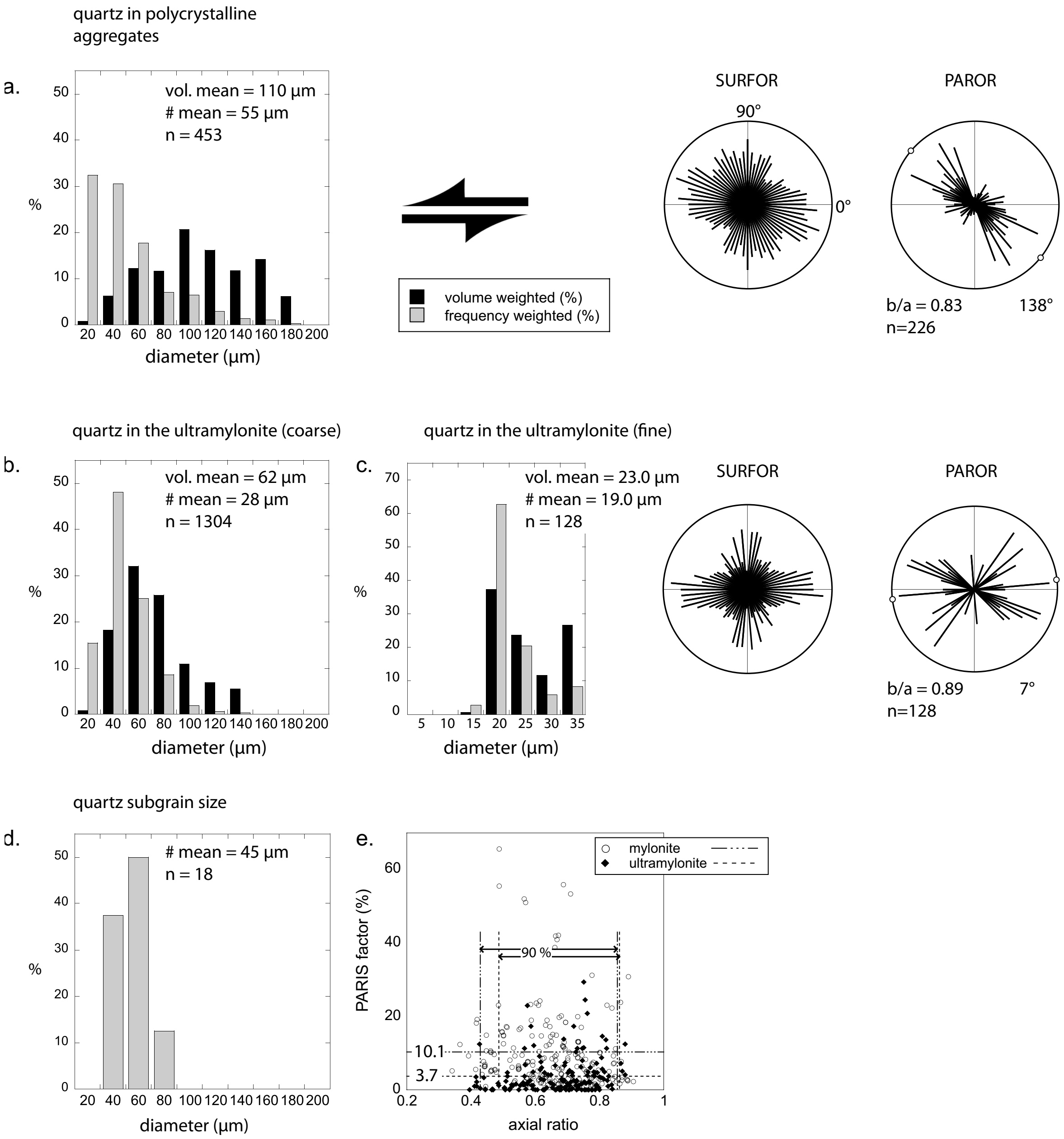

Figure 5: Quartz grain sizes and fabrics. (a) Quartz grain size distribution of recrystallized grains in the mylonite. SURFOR and PAROR rose diagrams. Bulk axial ratio and bulk preferred orientations indicated for the particle fabric. (b) Quartz grain size in the beginning of the ultramylonite after complete phase mixing. (c) Quartz grain size in the finest grained part of the ultramylonite and corresponding SURFOR and PAROR rose diagrams. (d) Subgrain size in recrystallized quartz measured from EBSD maps (boundaries <7.5°). Only subgrains bound by at least 2 subgrain boundaries and non-migrated boundaries are considered. Due to the small number (n= 18)only the frequency distribution is displayed. (e) Grain shape diagram of axial ratio versus the PARIS factor (Panozzo & Hürlimann, 1983). Quartz grains from polymineralic aggregates in the mylonite, plot with slightly higher PARIS factors and a larger scatter in axial ratios.

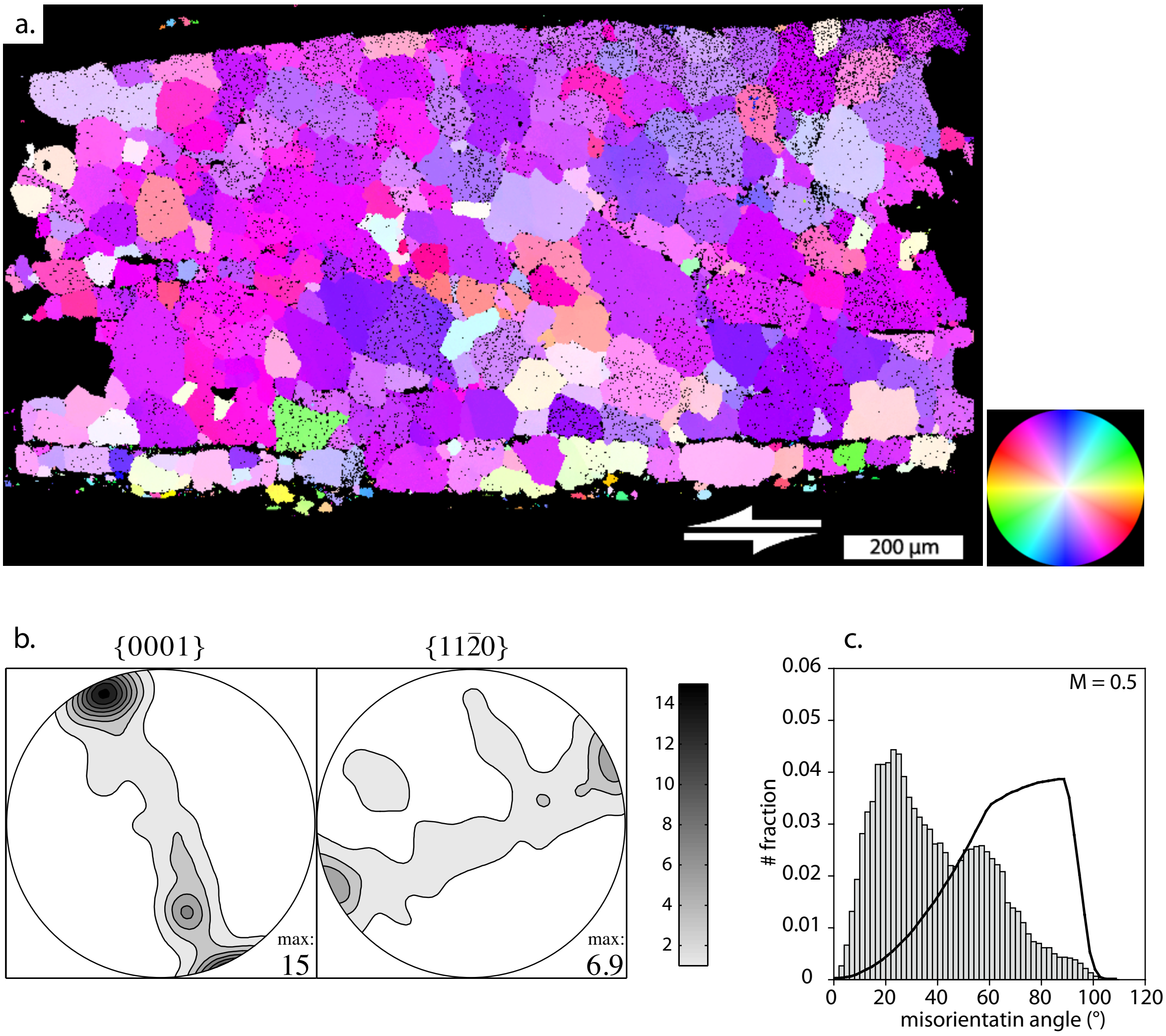

Figure 6: Quartz aggregates in the mylonite. (a) C-axis orientation image of a dynamically recrystallized quartz. The c-axis orientations recalculated from an EBSD-derived Euler angle image. For grain shape and grain size values see Fig. 8c. (b) Polefigures for [c] and <a> axes, calculated from EBSD data at 7.5 degree kernel halfwidth. Upper hemisphere, equal area projection. Contours at 2 times uniform distribution. c) Uncorrelated misorientation of quartz in a polycrystalline aggregate. Solid black line marks the calculated random distribution (see text). M index = 0.5.

formation of oligoclase in the deforming quartz - K-feldspar aggregates (see Menegon et al., 2006). Fine grained biotite results from dynamic recrystallization of primary magmatic biotite (Fig. 7a) and from dissolution and re-precipitation.

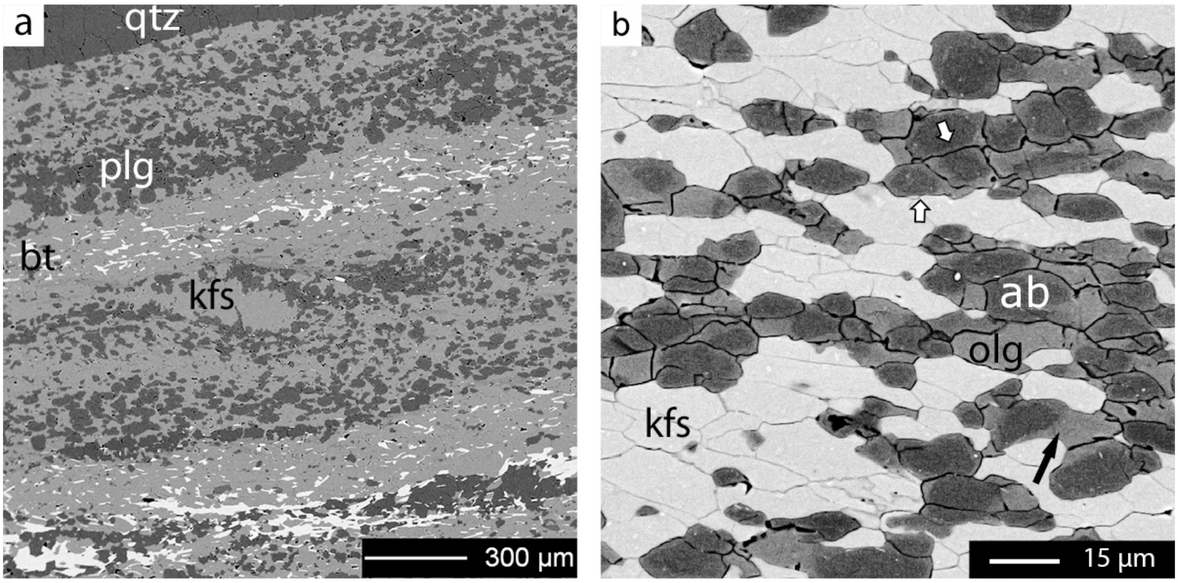

Figure 7: Matrix in the mylonite: (a) Polymineralic matrix showing a compositional layering, consisting of plagioclase (dark grey), K-feldspar (medium grey) and biotite (white). The dark grey layer at the top is a polycrystalline quartz aggregate. (b) K-feldspar - plagioclase aggregate of the matrix. Cores of plagioclase consist of albite, rims of oligoclase. Note preferential growth of rims parallel to the grain shape defined foliation (black arrow)and the truncation of cores of grains against phase and grain boundaries normal to the foliation (white arrows). SEM backscatter electron (BSE) images.

Plagioclase is part of the matrix (see above) appearing in the form of oligoclase grains (Ab16-23), with pure albite cores (Fig. 7b). This change in composition is related to a decrease in pressure or an increase in temperature (LeGoff & Ballèvre, 1990; Brouwer et al., 2002) before or during the onset of the shear zone formation.

In the undeformed host rock, the albite aggregates (d ~ 1-5 mm) contain minor amounts of mica consistently grown along the plagioclase cleavage direction. Albite grains are almost isometric with an average grain diameter μ_v(D) of 14 μm, an average axial ratio b/a > 0.82 and only a weak SPO (Fig. 8a). The fine grained albitic plagioclase is assumed to be a product of the static HP metamorphism and is not related to dynamic recrystallization, because fine grained albite it is also found in lesser or undeformed parts of the rock. The static decomposition of plagioclase into fine grained aggregates which pseudomorphically replace igneous grains has been observed elsewhere in situations where high pressure metamorphism is preserved in low strain domains (e.g. Lenze & Stöckert, 2007, Bucher & Grapes, 2009).

The core-rim transitions are discrete in plagioclase; gradual changes do not occur (Fig 7b). The Ca-rich rims display a variable thickness, growing thicker in direction parallel to the foliation, as described by Menegon et al. (2006).

In the mylonite the volumetric mean grain size of the plagioclase grains , μ_V(D) is ~ 15 μm, the mean core size is ~ 10 μm (Fig. 8 b,c). Comparing the PAROR and SURFOR analyses of the whole grains with that of the albite cores, one finds that the bulk axial ratio of the grains is lower (b/a bulk= 0.49) indicating a more elongated shapes while that of the albite cores is higher (b/a bulk = 0.59) (Fig. 8 b,c). The rose diagrams of the long axes of the grains and the cores indicate a rotation of the cores with respect to the grains of almost 15° in the sense of shear, with the preferred orientation of the cores at 4° while that of the grains is at 171°, in the same direction as the plagioclase grains in the undeformed part.

The albite cores are occasionally truncated by grain boundaries parallel to the foliation trace (Fig. 7b). The nearly constant grain size of undeformed plagioclase and the plagioclase in the mylonite suggests a process of replacement or dissolution and precipitation for the core - rim formation rather than grain growth during the change of shape (Fig. 8 a,b).These feldspar microstructures are indicative of solution transfer during deformation (diffusion creep).

In other words, the fine grained matrix originates from dynamic recrystallization (bt, kfs), static (non-deformational) recrystallization (plg, wm), precipitation (kfs, bt) and myrmekitic feldspar reaction (plg, qtz, wm) during deformation. Most of the quartz in the mylonite occurs in polycrystalline aggregates which have formed by dynamic recrystallization of the magmatic quartz.

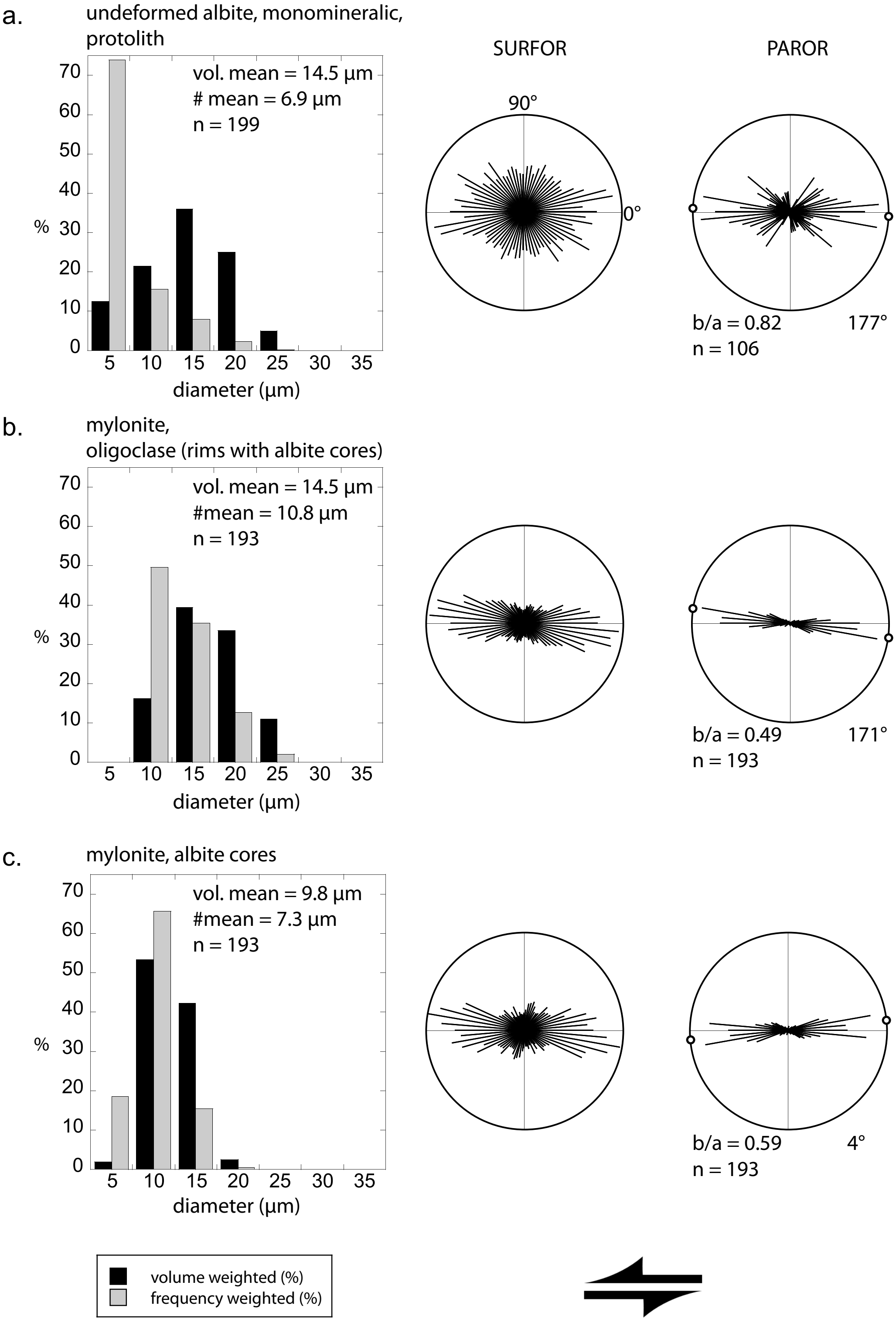

Figure 8: Plagioclase in the protolith and the mylonite. Grain size distributions and SURFOR and PAROR rose diagrams. Bulk axial ratio and bulk preferred orientations indicated for the particle fabric. (a) Albite grains from an monomineralic aggregate in the protolith (assumed to be undeformed by the shear zone). (b) Deformed plagioclase grains of the matrix of the mylonite with synkinematically grown oligoclase rims. (c) Albitic cores of grains from b).

4.2 Ultramylonite

The ultramylonite consists of a phase mixture where the distinction between quartz aggregates and matrix is impossible (Fig. 9 a,b). All of the quartz grains are completely dispersed among the other matrix phases.

4.2.1 Quartz

Quartz grains are generally free of optical subgrains and do not show undulatory extinction. EBSD derived orientation maps show a low density of subgrain boundaries (< 7.5°) which are almost exclusively parallel to the traces of the c-axes, thus probably also related to the dominant basal <a> slip system.

The typical inclined, peripheral c-axis maximum of the mylonite disappears in the ultramylonite (Fig. 10) and the intensity of the CPO, as indicated by the maximum of the pole figure, is much lower than in the mylonite. The M-index decreases from ~ 0.5 in the quartz aggregates of the mylonite to < 0.05 in the dispersed grains of the ultramylonite (compare Fig. 6 and 10).

The grain size of quartz is reduced to a volume weighted mean diameter, μ_v(D) of 62 μm with the very finest fraction in the shear zone center showing a mean of μ_v(D) = 23 μm (Fig. 5b,c). These small grains have an equant shape with bulk axial ratios, b/a of > 0.89. SURFOR rose diagrams show that surfaces are oriented parallel and normal to the foliation (Fig. 5c) implying a square to rectangular shape (Fig. 9b). In the more mica-rich domains, some of the long axes of grains are aligned parallel to the foliation.

From the mylonite to the ultramylonite, the PARIS factor of the quartz grains decreases from an average of ~10% to ~4%. (Fig. 5e). This is consistent with straighter grain boundaries, more rounded corners and less concave grain boundary embayments in the polymineralic ultramylonite. Quartz - quartz grain boundaries are rather smooth corresponding to those observed in the monomineralic quartz aggregates in the mylonite (Fig. 4). Quartz - plagioclase phase boundaries are slightly lobate and show micron-scale bulges (Fig. 9b).

4.2.2 K-feldspar

K-feldspar grains occur in layers of quartz, plagioclase, plagioclase and biotite, or in entirely mixed layers (Fig. 7a, 11). All of the fine grained K-feldspar in the ultramylonite is derived from recrystallization or solution – precipitation (Fig. 11a,c,d). The association of K-feldspar and quartz is most common with K-feldspar filling the space between quartz grains (Fig. 11). The shape of the

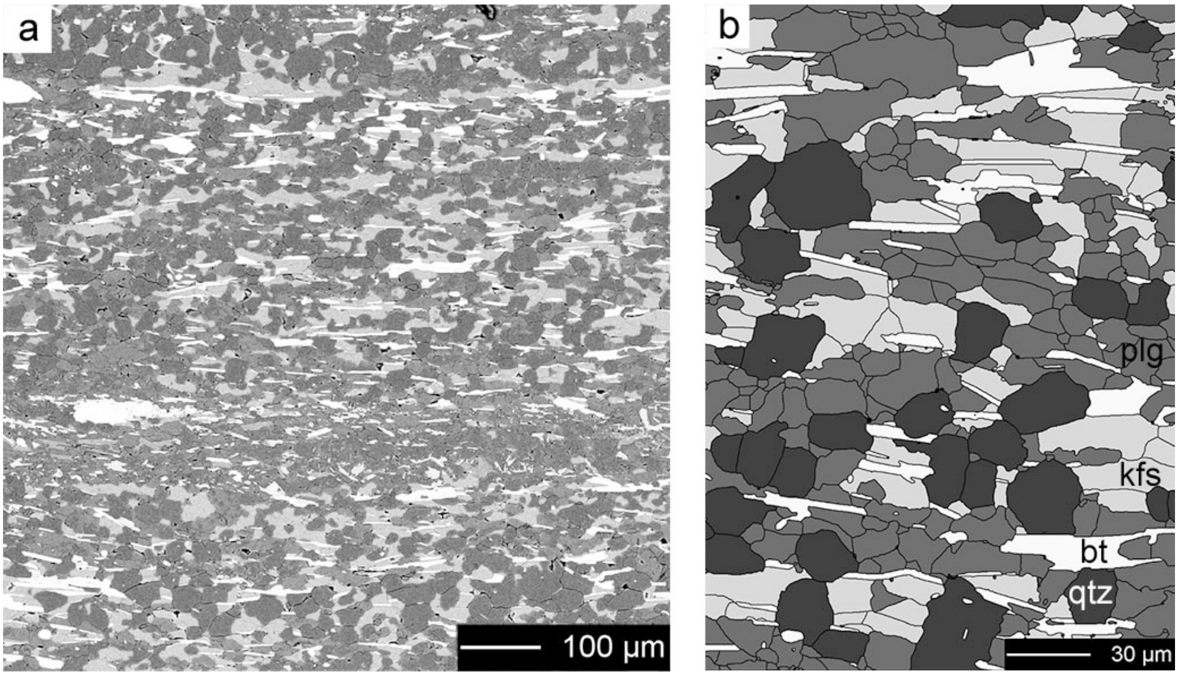

Figure 9: Microstructure of the ultramylonite. (a) SEM/BSE image of the homogenous phase mixture with the 30% quartz formerly contained in the polycrystalline quartz aggregates. (b) Drawing of a microstructure in the ultramylonite, detail of a). Quartz is dark, oligoclase is medium-grey, K-feldspar is light grey and biotite is white. For location see figure 2.

phase boundaries between quartz and K-feldspar indicates the precipitation of K-feldspar in strain shadows (Fig. 11b) and dilatant sites (11a,d) within these layers.

Phase boundaries are often smoothly curved with the K-feldspar forming convex protrusions into the quartz grains. The opposite case does occur but less frequently. Non-recrystallized K-feldspar clasts are only rarely preserved in the ultramylonite; some show myrmekite formation in the close vicinity of K-feldspar precipitation sites (Fig. 11e).

The mean diameter $\mu_V(D)$ of K-feldspar is ~ 15 μm and constant throughout the entire ultramylonite (Fig. 12a). Grains show a preferred particle elongation subparallel to the foliation and yield a bulk axial ratio of ~ 0.52. Particle long axis are aligned at a small angle (~ 175°) with respect to the foliation. SURFOR rose diagrams display an orthorhombic or monoclinic symmetry and show a secondary preferred surface orientation normal to the foliation (Fig. 12a).

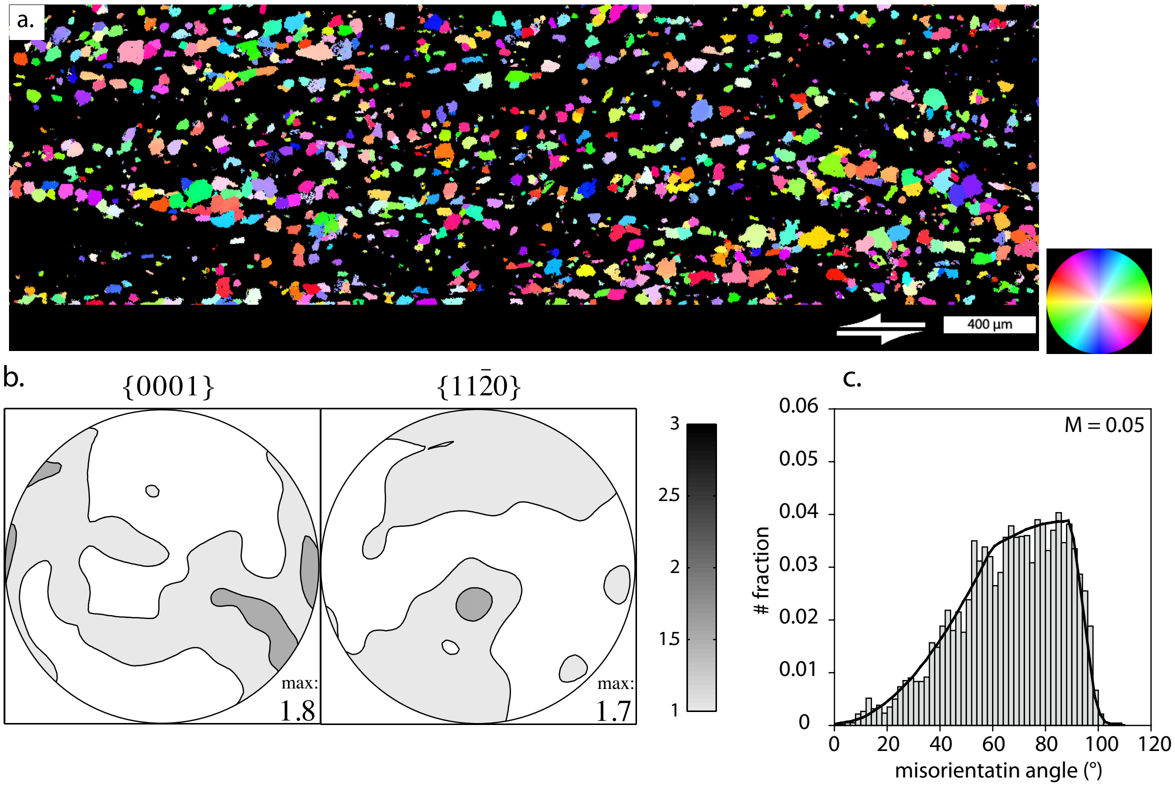

Figure 10: Dispersed quartz grains in the ultramylonite. (a) Dispersed quartz grains in the ultramylonite. C-axis orientation image recalculated from an EBSD derived Euler angle image. (b) Polefigures for [c] and <a> axes, calculated from EBSD data at 10 degree kernel halfwidth. Upper hemisphere, equal area projection. Contours at 0.5 times uniform distribution. (c) Uncorrelated misorientation of quartz in a polycrystalline aggregate. Solid black line marks the calculated random distribution (see text). M-index = 0.05

4.2.3 Plagioclase

Plagioclase grains have a mean diameter $\mu_v(D)$ of 15.0 μm (Fig. 12b). The plagioclase shows a strong grain shape preferred orientation with the particle and surface fabric of the plagioclase being very similar to that of K-feldspar, despite a more accentuated orthorhombic grain shape and a slightly higher bulk axial ratio of ~ 0.54. Particle long axes are inclined very slightly (176°) with respect to the foliation (Fig. 12b).

The average PARIS factors of plagioclase (~ 8%), K-feldspar (~ 10%) and quartz (~ 4%), as well as the smaller bulk axial ratio of the feldspar grains indicate quartz is almost equiaxed and fully convex while the feldspar grains are more elongated and slightly lobate (Fig. 9b).

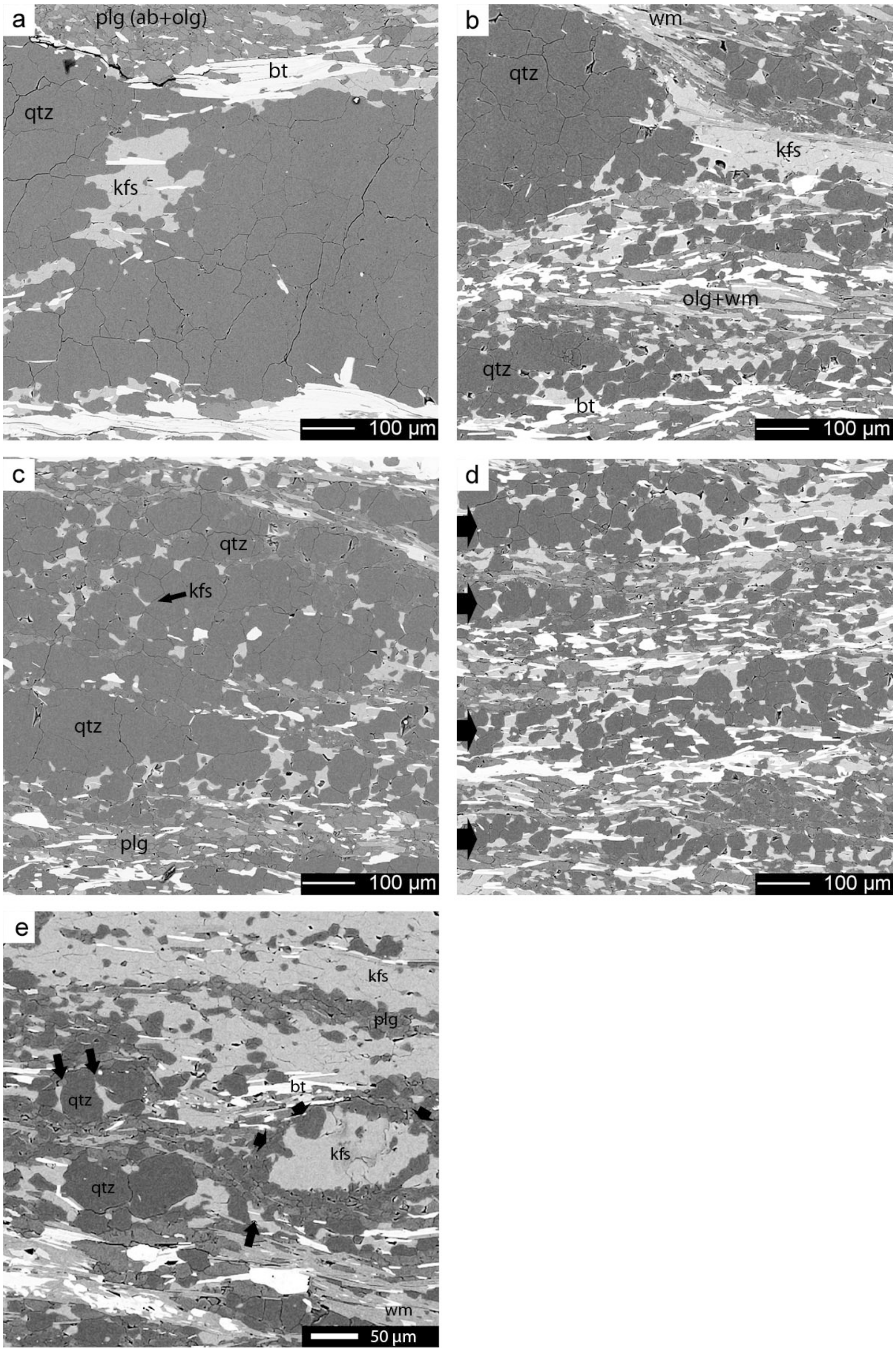

Figure 11: Evolution of microstructures in the transition from mylonite to ultramylonite. (a) Mylonite. Rare localized boudinage of polycrystalline quartz layer with K-feldspar precipitation in the neck. (b) Grain separation at the edge of a relict quartz aggregate by K-feldspar precipitating along grain boundaries. (c) Homogeneous K-feldspar precipitation at triple junctions and grain boundaries inside a quartz aggregate. (d) Layers of dissected quartz aggregates (indicated by arrows) and K-feldspar precipitates. (e) Relict K-feldspar clast, replaced by myrmekite (short arrows) and adjacent K-feldspar precipitation between quartz grains (long arrows). Near top of image a recrystallized K-feldspar layer with plagioclase grains. All SEM/BSE images. Sinistral shear sense. For location see figure 2.

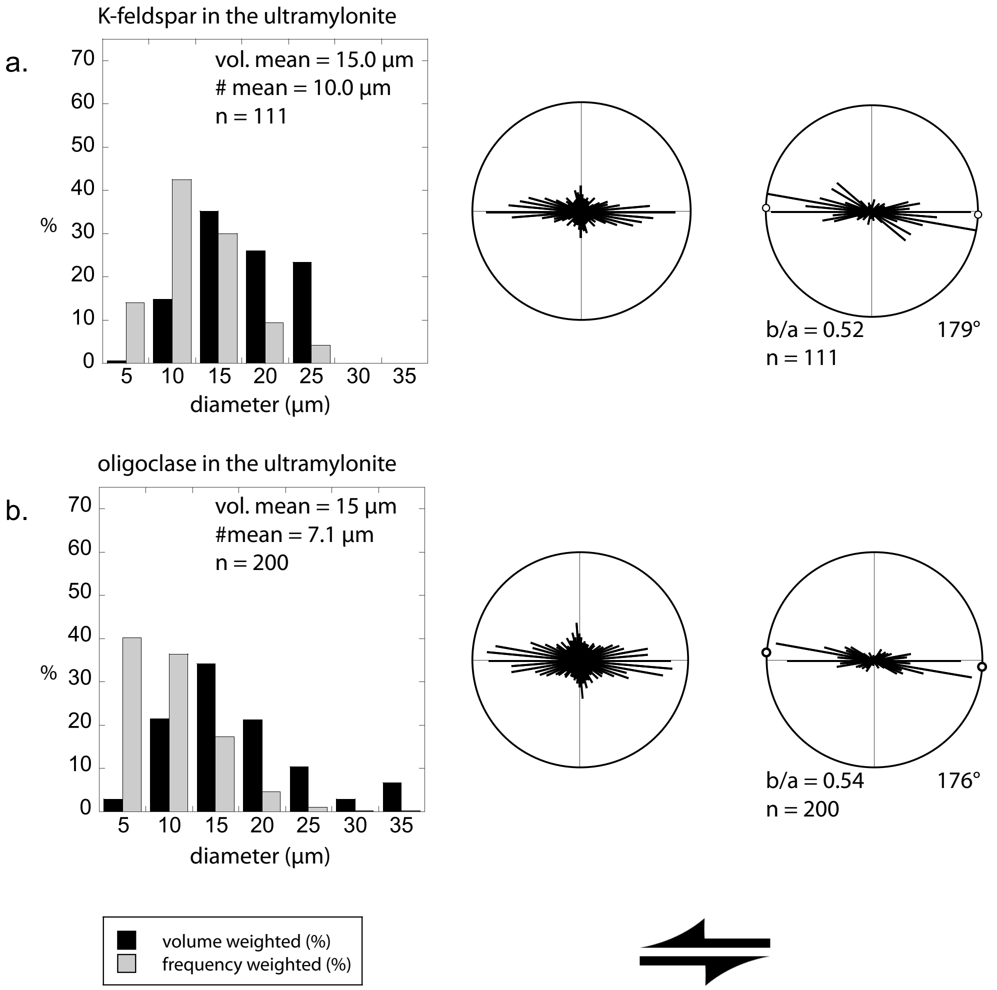

Figure 12: Feldspars in the ultramylonite. Grain size distributions and SURFOR and PAROR rose diagrams. Bulk axial ratio and bulk preferred orientations indicated for the particle fabric. (a) K-feldspar from the ultramylonite preferentially adjacent to quartz grains. (b) oligoclase from the ultramylonite. For the corresponding microstructures see figure 9b.

4.2.4 Biotite

Biotite grains are recrystallized from magmatic grains and occur as single isolated flakes or in layers with an average grain diameter in the same size range as that of the other matrix phases (~20 μm). Biotite layers disappear with increasing strain. In the most highly strained part, single flakes are isolated between quartz, plagioclase and K-feldspar. Kinking and folding of the recrystallized grains is not observed. Together with K-feldspar, some biotite flakes occur as bridges between quartz grains (Fig. 9b).

4.3 Transition zone

The transition zone from the mylonite to the ultramylonite (Fig. 2) is defined as the zone where quartz aggregates disintegrate. Throughout the transition zone changes in texture, microstructure, grain size and spatial distribution of the different phases can be observed.

From the polycrystalline aggregates to single dispersed grains a switch from a monoclinic to an orthorhombic geometry of the SPO together with a decrease of the bulk axial ratios (Fig. 5a,d) is observed. While the quartz grain size is constant in the mylonite ($\mu_v(D)=110\ \mu$m), it decreases to about 20 μm in the ultramylonite and approaches the matrix grain size (e.g $\mu_v(D)=15\ \mu$m Fig. 5b, 12). The grain size decrease begins with the disintegration of the quartz aggregate and continues into the ultramylonite.

At the beginning, near the mylonite, the following observations can be made: quartz aggregates are highly deformed and occur as increasingly thinned layers (Fig. 2,3). At first, isolated K-feldspar can be found in triple junctions, aligned triple (and quadruple) junctions of smaller grains, and along conspicuously aligned grain boundaries of large grains (Fig. 13). Increasing amounts of K-feldspar coincide with straight aligned grain boundaries, which may be continuous over several grains. K-feldspar also forms thin foliation parallel, discontinuous seams inside elongate quartz aggregates (Fig. 13) often grading into continuous K-feldspar seams. From these seams small fin-shaped K-feldspar protrudes in between quartz grains, along (sub)grain boundaries, and, in rare cases, also directly into quartz grains (Fig. 13).

The protrusions are often asymmetric; the asymmetry shows a synthetic orientation with the sense of shear. Occasionally, similar structures also form at the edges of the quartz aggregates. K-feldspar seams inside quartz aggregates may originate from the tails of K-feldspar fish embedded in a quartz layer, but the seams generally occur relatively isolated. Isolated grains of K-feldspar are found at triple or quadruple junctions and grain boundary jogs (Fig. 13). The local crystallographic orientation of the smaller quartz grains adjacent the K-feldspar seams is often rotated with respect to the overall CPO and the quartz grain size is locally decreased in such cases (Fig. 13).

The quartz texture in the transition zone shows a considerably weaker inclined peripheral c-axis maximum compared to that of the mylonite, and the angle between the foliation and the c-axis maximum decreases to a value of 120° to 140° (Fig. 14). The difference corresponds to a synthetical rotation of the c-axis pole figure with respect to the sense of shear. By calculating grain-

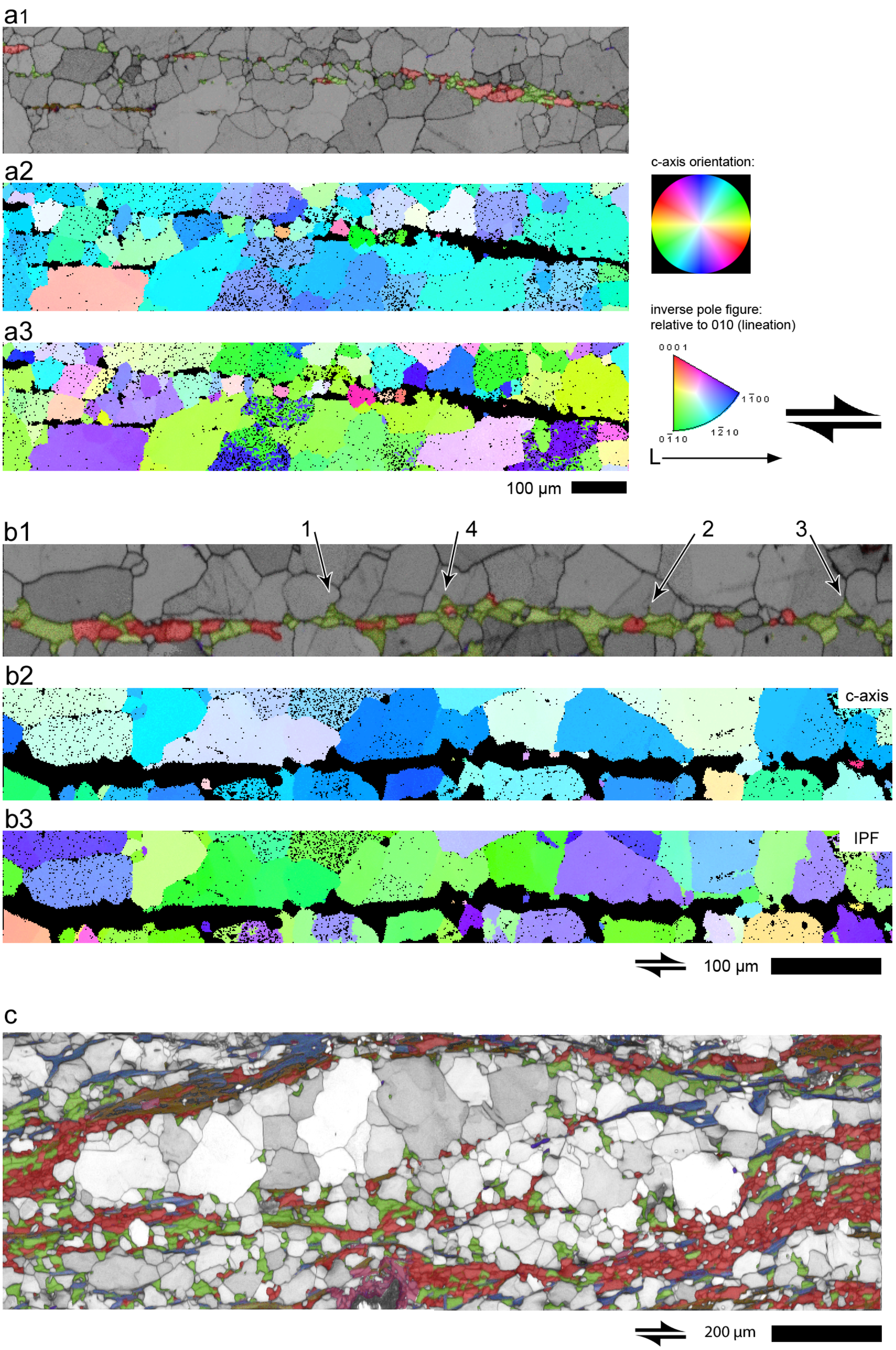
a1
a2
c-axis orientation:
inverse pole figure:
relative to 010 (lineation)
a3
0001
1$\bar{1}$00
0$\bar{1}$10
1$\bar{2}$10
L
100 µm
b1
1
4
2
3
b2
c-axis
b3
IPF
100 µm
c
200 µm

Figure 13(previous page): (a,b) Quartz layers with layer parallel, heterogeneous K-feldspar, biotite and plagioclase seams, found in the highest strained mylonite/ beginning of the transition zone. (a1,b1) EBSD image quality map overlain by EDX-derived combined element map. Red: Al-Na counts (albite, oligoclase), green: K counts (K-feldspar), blue: Fe+Mg counts (biotite), brown: mica. Straight line cutting across grain boundaries are surface scratches of the sample. (a2,b2) Quartz c-axis orientation map. (a3,c3) Quartz inverse pole figure map. Reference direction is the lineation L.
Precipitation occurs at triple junctions and aligned grain boundaries. The quartz grain size is locally decreased due to pinned grain junctions and boundaries. Note small quartz grains surrounded by the K-feldspar precipitates are rotated with respect to their neighboring grains. (b) K-feldspar and plagioclase layer within quartz aggregate developing fin-shaped protrusions between quartz grain boundaries (1), subgrain boundaries (2), dauphine twin (3)boundaries and occasionally into grains (4). Some fins show an asymmetry consistently related to the sense of shear. Maps and color look-up tables are the same as in figure a. (c) Disintegrating quartz aggregate in the transition from mylonite to ultramylonite. EBSD image quality map overlain by EDX derived combined element map. Red: Al-Na counts (albite, oligoclase), Green: K counts (K-feldspar), Blue: Fe+Mg counts (biotite), Brown: white mica. K-feldspar and biotite occupy predominantly the space between quartz grains (grey-white).

size-dependent CPOs it can be seen that the preferred orientation is restricted to the fraction of larger quartz grains (e.g. > 60 μm) (Fig. 14b) both in number-weighted and in area-weighted pole figures.

The grain size of 60 μm was chosen as it is the largest grain size fraction in the ultramylonite. Furthermore, it is the size of grains of the most elongate quartz aggregates, i.e. of the layers that are only one or two grains thick. Grains with $d < 60$ μm reproducibly show a nearly random distribution.
Randomness was tested by comparing the measured maxima, minima and the texture index with the corresponding values of a random orientation distribution function of the same size (number of grains) using the same kernel width (Appendix B). The K-feldspar microstructure depends on whether the grains originate from dynamic recrystallization or from precipitation between quartz grains and subsequent deformation.

Initial K-feldspar precipitates show a preferred particle long axis orientation at an angle to the foliation (22°), inclined against the sense of shear (Fig. 15a,b). With increasing grain separation or by relative rotation of the phase boundaries during progressive shear the K-feldspar long axes become oriented subparallel to the foliation (Fig. 9b, 15e,f).

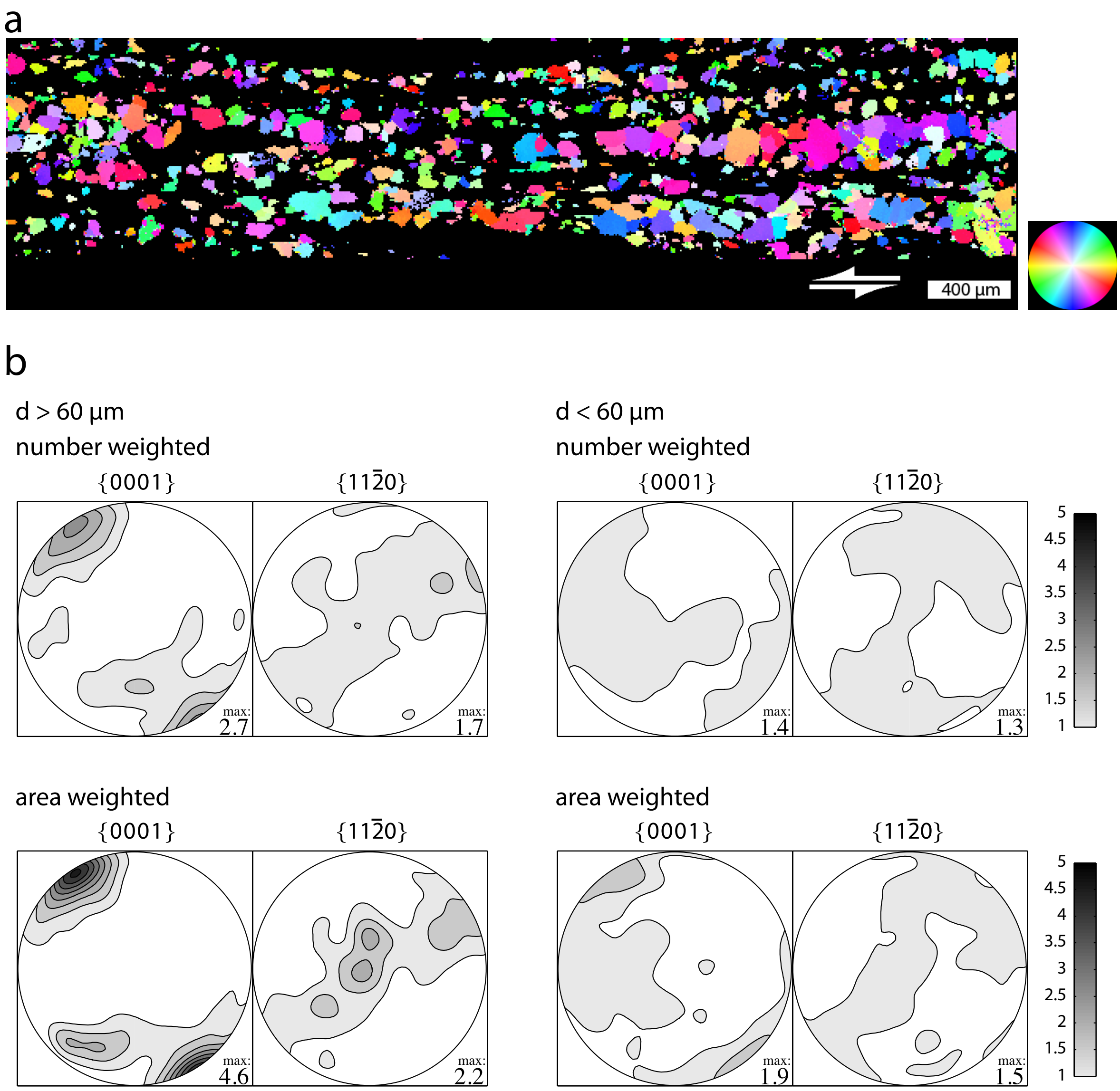

Figure 14: Disintegrating quartz aggregates. (a) C-axis orientation image showing a relict quartz layer in the transition from the mylonite to the ultramylonite. (b) Number and area weighted pole figures for [c] and <a> axis orientation for grains larger (n = 1224) and smaller (n = 7002) 60 μm, 10° kernel halfwidth. Contours from 1 at 0.5 times uniform distribution. The weak c-axis maximum originates from relict layers, exemplarily shown in 16a (purple, see color LUT). The increase of the maxima from number to an area weighted polefigure indicates that the small grains are more randomly oriented than the larger ones. (see Appendix B)

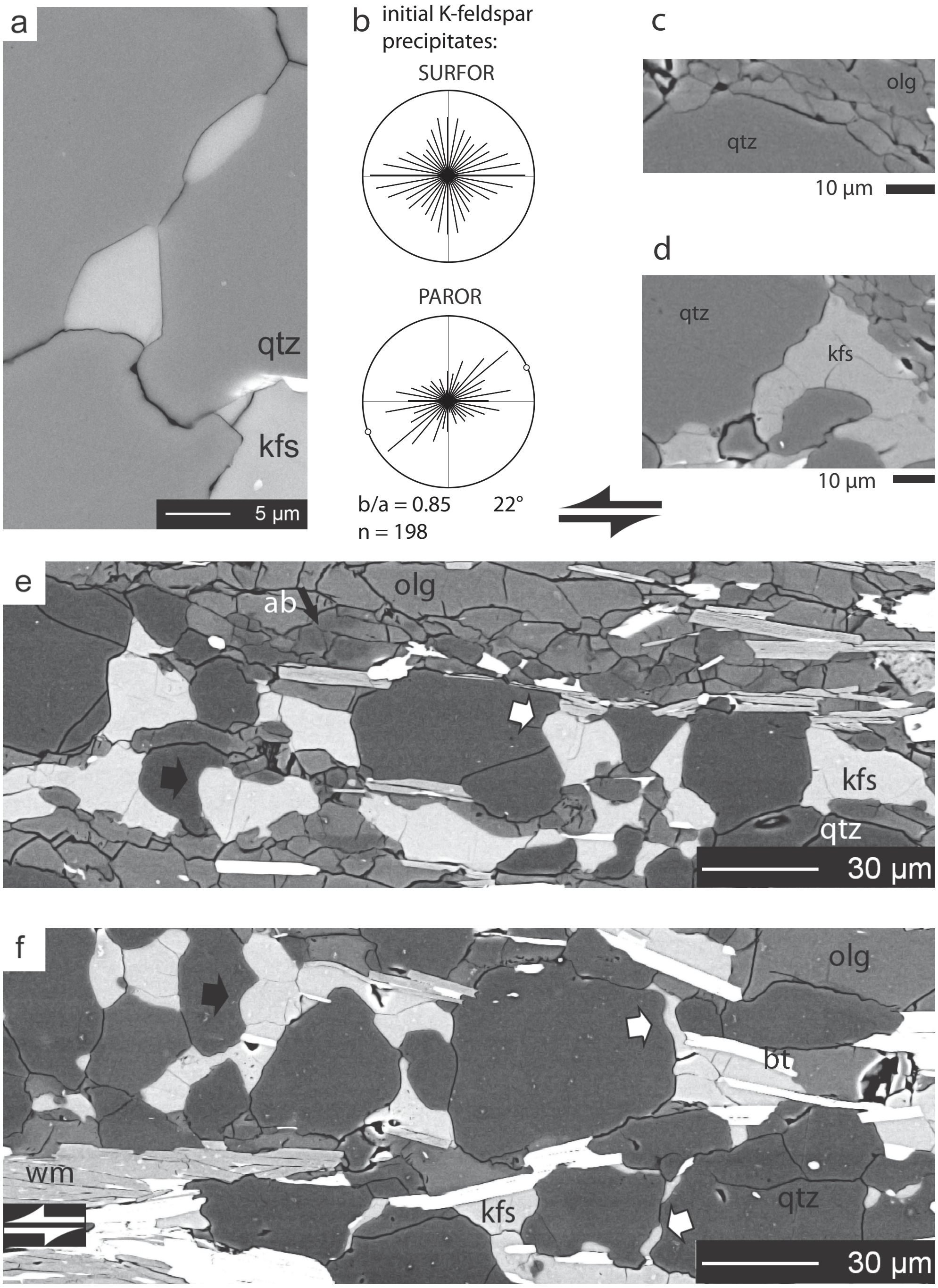

Figure 15: K-feldspar precipitation and phase boundary migration. (a) Initial K-feldspar precipitation between quartz grains in a polycrystalline quartz aggregate in the mylonite. (b) SURFOR and PAROR rose diagrams of K-feldspar precipitates during initial quartz aggregate disintegration, comparable to a) (e.g. Fig. 11c, 13). (c) Oligoclase matrix grains bulging in to a into quartz grain in the mylonite. (d) K-feldspar grows in the quartz aggregate along former quartz grain boundaries. The phase boundary shows an undulatory, lobate structure while quartz grain boundaries commonly are smooth. (e,f) Quartz layers being disintegrated by K-feldspar precipitation. e) layer less stretched; b) layer more stretched. In some cases the shape of former quartz grain grain boundaries is still recognizable (white arrows); K-feldspar bulging into quartz grains (black arrows). All SEM/BSE images.

4.4 Phase distribution

The spatial distribution of phases can be seen on phase maps. These were prepared for quartz, plagioclase, K-feldspar, biotite and white mica (Fig. 13c, 16a). The micas are grouped together as they are rather homogeneously distributed among the other phases and no major differences in microstructural properties are observed. In the transition between mylonite and ultramylonite, quartz, plagioclase and K-feldspar rarely occur in a random distribution of all three phases. Quartz-rich areas are predominantly associated with K-feldspar. Quartz-plagioclase-mixtures are rare. In the layers with the smallest grain size and the highest degree of mixing, quartz grains often align with K-feldspar parallel to the foliation in a festoon-like geometry (Fig. 11d, 16a). As a geometrical consequence of the thinning of the quartz - K-feldspar layer, the foliation-parallel contact-area with plagioclase is increased.

Here, we use a phase distribution analysis that is based on R_{gp} versus grain size plots (Fig. 16b) and we restrict the analysis to the distribution of quartz in quartz-K-feldspar layers. In a number of microstructurally homogeneous areas with a narrow grain size distribution, R_{gp} for disintegrating quartz aggregates were determined. R_{gp} and the mean grain sizes were measured and plotted (Fig. 16b). With decreasing mean grain size, the ratio R_{gp} of grain to phase boundary area decreases indi cating a higher degree of mixing. The minimal grain size possible to analyze depends on the step size of the EBSD maps (1,2,4.5 μm). Nevertheless linear fits are only calculated for areas obtained within the same map. A correction for different step sizes has been applied for Fig. 16c (see below) and the minimal grain size was 12 micron.

4.5 Quartz content

The modal content of quartz does not change from the mylonite to the ultramylonite (Fig. 17). At first the quartz is concentrated in the quartz aggregates. Progressive disintegration of the quartz aggregates leads to a complete mixture of the quartz within the matrix phases.

When measured in the mylonite, using a light microscope, the average content of (visible) quartz is 29 ± 2%. Approximately 5% of the quartz is not visible because it occurs as very small grains in the matrix. Correcting for the ‘invisible’ quartz yields a total quartz content of 30 ± 2 %. In the ultramylonite the quartz contents is found to be 31 ± 1.5% (obtained by thresholding of Si-EDS counts).

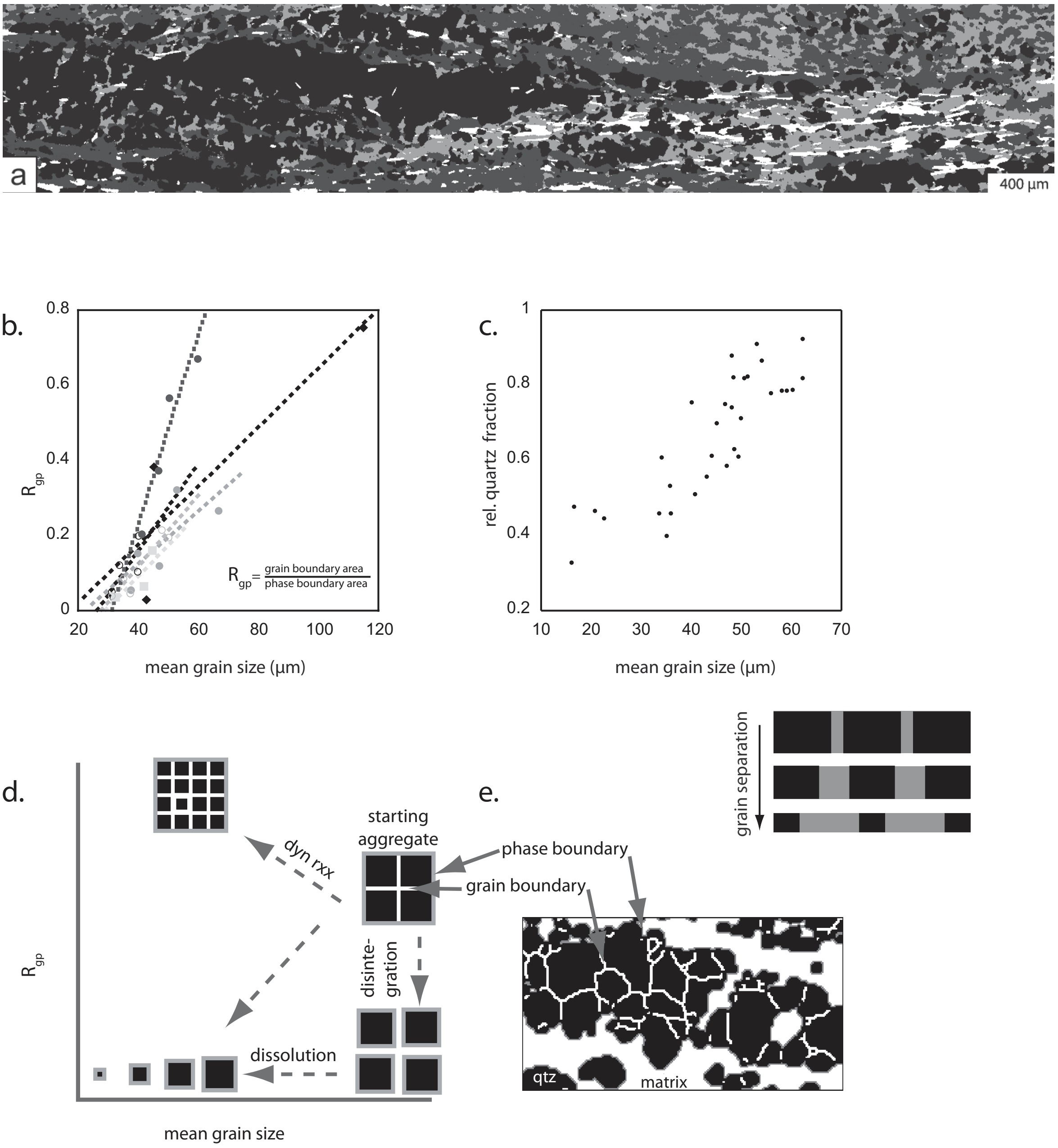

Figure 16: Phase distribution and grain size evolution. (a) Phase map of quartz (black), plagioclase (dark gray), K-feldspar (light grey) and mica (white). The map shows a quartz aggregate in the transition between the mylonite and the ultramylonite with different stages of disintegration. (b) R_{pg} (ratio of grain boundary / phase boundary area) versus the mean grain size in 6 different, laterally disintegrating aggregates (see sample from the transition mylonite - ultramylonite, Fig. 14). Symbols correspond to individual aggregates. (c) Relationship between the mean quartz grain size in a layer and the relative quartz volume fraction. The relative quartz volume fraction in a layer decreases with increasing disintegration, as grains are separated by K-feldspar. In layers with a higher grain separation the mean grain size is smaller. (d) Schematic model of R_{pg} - grain size evolution. Black squares are separated from another by grain boundaries (white) and from the matrix by phase boundaries (dark grey) (e) Example of an analyzed area. The evaluation of R_{pg} and the grain size would correspond to a single point in the diagram b).

These results agree perfectly with those of LeGoff & Ballevre (1990), who calculated 30.43 % qtz for the undeformed Gran Paradiso metagranodiorite and gave a modal quartz content (probably obtained by point counting) of 25 % for the magmatic relics. Menegon et al. (2006) report a bulk content of 27 % quartz in the protomylonite/mylonite estimated by area measurements on thin sections. Thus, the quartz content is the same in the undeformed rock, the mylonite, and the ultramylonite, independent on the scale of observation and the grain- or aggregate size. Chemically there is no significant change in composition through the transition from proto- to mylonite, except a slight decrease in K_2O (LeGoff & Ballevre, 1990) or a decrease in K_2O and an increase in CaO (Menegon et al., 2006) below 1 wt%, respectively.

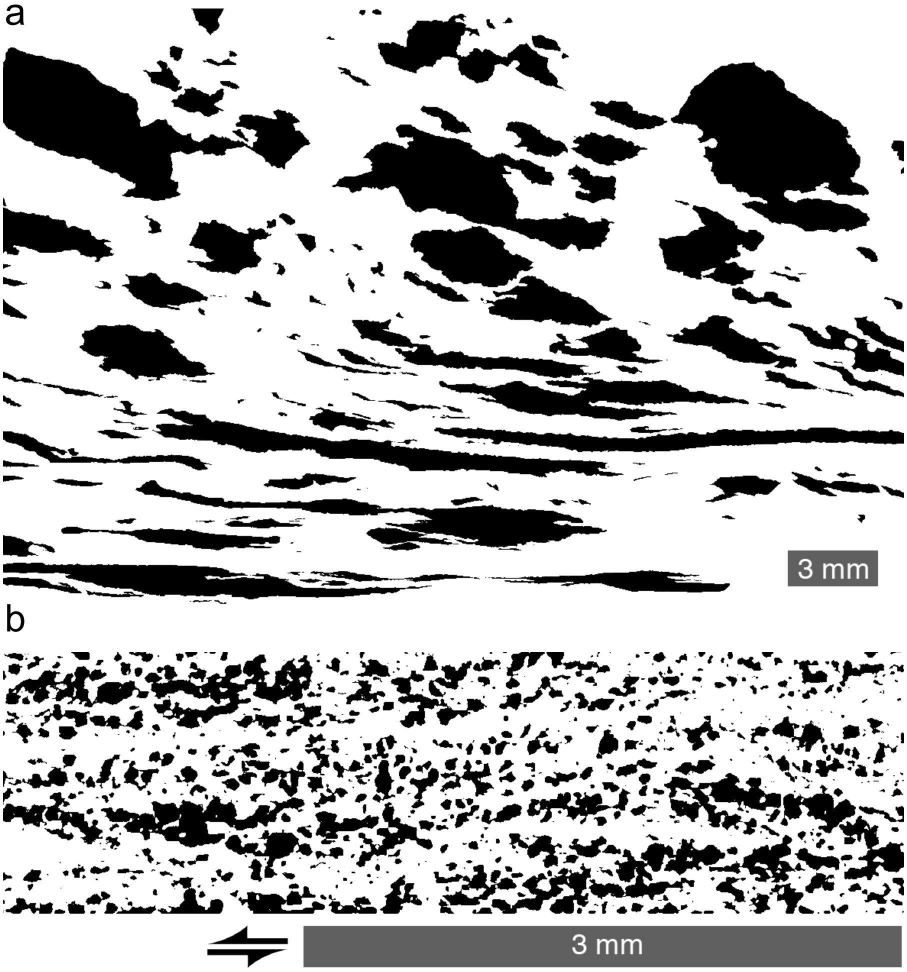

Figure 17: Quartz maps used to determine quartz volume fractions. (a) Black areas in the upper half are partially recrystallized quartz aggregates and magmatic grains, in the lower half completely recrystallized, polycrystalline aggregates in the mylonite. Quartz content 29 ± 2 % (b) Black areas are quartz, mostly single dispersed grains in the ultramylonite. Quartz content 31 ± 1.5 %.

5. Discussion

The following discussion is in part based on an interpretation of the strain gradient in the analyzed shear zone. Generally, a strain gradient in shear zones can result from (1) a gradient in the shear strain rate while the whole shear zone is deforming, or (2) from localization of deformation in the internal parts of the shear zone at later stages of the deformation (type II, Hull 1988, Means 1995), or (3) the shear zone widens with time due to strain hardening so that the outer parts represent later strain increments (type I of Hull 1988, Means 1995). The third possibility can be excluded here because of the lack of flat-topped strain profiles and the fact that strain hardening is very unlikely in the center of the shear zone (see below). The two first possibilities are end member cases and natural shear zones may result from a combination of both. A faster shear strain rate can be caused by a change of rate controlling parameters (e.g. CPO, permeability, bulk diffusivity) or by a switch in the dominant deformation mechanism. As most of these parameters in the Gran Paradiso shear zones are strain-dependent or a consequence of microstructural development (e.g. CPO, SPO, reaction products), we assume that the structures developed along the strain gradient primarily record a progressive strain history (type II shear zones). This implies that microstructures preserved near shear zone center represent later stages, whereas the microstructures near the shear zone margins represent earlier stages of the deformation history obliterated during subsequent strain localization in the shear zone center.

The mylonite is, as an approximation, regarded as a material consisting of two rheologically different phases: (1) polycrystalline, monophase quartz aggregates and (2) polymineralic matrix. The ultramylonite, in contrast, consists only of a mixed polymineralic matrix with a single rheological property.

In the following we will discuss the process of progressive phase mixing, the deformation mechanism in the mylonite and ultramylonite, and the processes involved in the grain size reduction. Finally we will evaluate possible reasons that may cause the phase mixing and rheological implications.

5.1 Phase mixing

The transition from the mylonite to the ultramylonite takes place across a continuous transition zone. Polycrystalline quartz aggregates preferentially disintegrate at grain boundaries which are (sub)perpendicular to the layering by K-feldspar or biotite precipitating in dilatant sites (Fig. 11, 15a,e,f, 16a). One grain thick quartz layers only occasionally persist up to very high strains.

Oligoclase is rarely found between dilatant quartz grain boundaries. The effect of quartz layer disintegration is particularly prominent in high-strain layers, which are only one single grain wide (Fig. 15 e,f). Inside the quartz aggregates, K-feldspar is found either in triple junctions, grain boundary jogs and along grain boundaries oriented at a large angle to the inferred stretching direction (e.g. Fig. 11, 13a,b 15a,e). The latter sites occur preferentially along the aggregate periphery and discrete seams (at lower strains; Fig. 13 a,b), or homogeneously distributed across the entire aggregate (Fig. 11c). The location, shape, and distribution indicate that the K-feldspar and biotite grains must have nucleated in place and do not originate from mixing by neighbor switching during grain boundary sliding (gbs; Figs, 9b, 11a,c, 15). The distribution and shapes of K-feldspar occurrences resemble very much those of the voids observed by Ree (1994) in grain boundary sliding experiments of octachloropropane (e.g. figure 7/8 of Ree 1994) produced during neighbor switching events.

Cavitation is used to describe the process of the formation of dilatant sites (e.g. Pilling & Ridley 1980, Ayensu & Langdon 1996). These sites can be caused by heterogeneous deformation at the grain scale, for example during grain boundary sliding (e.g. Pilling & Ridley 1980, Ree, 1994; Ayensu & Langdon, 1996; Zhang, 1996). Empty pores (cavities) have been observed in rock deformation experiments (Rybacki et al., 2008) and may occur in naturally deformed rocks (Fusseis et al., 2009). However, if the rate of precipitation of intergranular material can occur at a rate that is at least equal to the opening rate, empty voids will not form. Nevertheless, the process of the formation of dilatant sites is very similar to cavitation.

The location of K-feldspar nucleation apart from an adjacent source of potassium and aluminum requires that material transport must have taken place by grain boundary diffusion or, more likely, in a grain boundary fluid film. Only in a few cases, layer parallel seams inside quartz aggregates are formed as tails of small K-feldspar sigma-clasts. Therefore, we infer that the major part of intergranular material inside the quartz aggregates must have formed by syndeformational nucleation and growth. Similar inferences have been made for amphibole growth in plagioclase (Kruse & Stünitz, 1999) or mica in calcite mylonites (Herwegh & Jenni, 2001), and for K-feldspar in polymineralic mylonites (Behrmann & Mainprice 1987).

With increasing strain the amount of K-feldspar and biotite situated between quartz grains increases as documented by increasing distances between grains and an increasing fraction of separated quartz grain boundaries (Fig. 16a,b). In addition, the lobate morphology of some quartz-K-feldspar boundaries indicates that phase boundary migration has taken place (Fig. 15) as previously observed in mylonites by Gower & Simpson (1992) and Stünitz & FitzGerald (1993). This aspect will be considered below in more detail.

5.2 Deformation mechanisms

In the following we will use the term diffusion creep to describe a grain size sensitive deformation mechanism, where grain boundary sliding, diffusion, dissolution-precipitation or other diffusive mass transfer processes contribute to accommodate deformation. Grain boundary sliding can be the result out of a geometrical necessity during grain scale diffusive mass transfer (Lifshitz, 1963) or it can be the main kinematic contribution to viscous deformation (Rachinger, 1952; Mukherjee, 1971; Ashby & Verrall, 1973, Paterson 1990).

5.2.1 Quartz in the mylonite

In the mylonite, polycrystalline, monophase quartz aggregates deform by dislocation creep as indicated by a strong CPO (Fig. 6), an asymmetric, monoclinic SPO (Fig. 5a), and microstructures typical for subgrain rotation recrystallization and grain boundary migration. The CPO suggests that basal <a> is the dominantly active slip system, although CPOs of this type usually are described from instances of deformation temperatures lower than in the Gran Paradiso rocks (e.g. Schmid & Casey, 1986; Stipp et al 2002).

The dynamically recrystallized grain size of monomineralic quartz aggregates is stable across the entire strain gradient of the mylonite. Subgrain boundaries in the recrystallized grains recorded by EBSD and CIP are infrequent. Most subgrain boundaries < 7.5° cut across larger grains and the resulting “cells” are within the lower range of size distribution of recrystallized grains (20-65 μm eq. diameter, Fig. 5d). Subgrain boundaries parallel to the trace of [0001] are interpreted as tilt walls of the basal <a> slip system. Grain boundary morphology and grain shapes indicate that grain boundary migration (e.g. Guillope & Poirier, 1979; Poirier & Guillope, 1980, Jessell, 1987; Drury & Urai, 1990) occurred in addition to subgrain rotation.

In early stages, K-feldspar precipitates occur as isolated grains along quartz grain boundaries, preferentially oriented at a large angle to the inferred stretching direction, in triple and quadruple junctions, and in previously described fin-shaped structures (Fig. 13 a,b). With increasing strain these K-feldspar precipitates connect and coarsen along grain boundaries (Fig. 11, 15, 18). An alignment of grain boundaries parallel to the displacement direction (Fig. 4a,b, 13a) is frequently reported in materials deforming with a contribution of grain boundary sliding (e.g. Drury & Humphreys, 1988; Stünitz & Fitzgerald, 1993; Zelin, 1994; Fliervoet et al., 1997). The occurrence of quadruple junctions (Fig. 13a) can also be taken as an indication of grain boundary sliding (e.g. Ashby & Verrall, 1973; Goldsby & Kohlstedt, 2001) as well as the occurrence of mineral precipitates along certain grain boundary orientations (e.g. Fig. 4b, 15 a,b) in quartz (e.g. Behrmann & Mainprice, 1987, Herwegh & Jenni, 2001). Thus, the quartz-k-feldspar-biotite-microstructures indicate that some grain boundary sliding has taken place during dislocation creep deformation of the quartz aggregates.

Grain boundary sliding commonly occurs during dislocation creep, although to a considerably lesser degree than during diffusion creep, and it is the primary process, which may lead to cavitation (e.g., Crossman & Ashby 1975, Pilling & Ridley 1989, Langdon 1994, 2006, Kassner & Hayes 2003). During grain boundary sliding, cavitation commonly occurs at high angles to the stretching direction (Pilling & Ridley, 1989, Langdon 1994, 2006). Grain boundary diffusion or solution transfer are likely to operate during grain boundary sliding to facilitate relative grain movements past asperities (Ashby & Verall, 1973) though dislocation movement has also been suggested (Crossman & Ashby 1975, Gifkins, 1976; Zhao, et al., 2009). The presence of chemically different phases - K-feldspar and biotite - in dilatant sites, is interpreted that the local shape accommodation of quartz during crystal plastic deformation was not achieved at a sufficiently high rate and cavitation, immediately filled by precipitation of other minerals has taken place. It should be noted that such a cavitation process can only be noted if unlike phases precipitate in dilatant sites – precipitation of the same phases is likely to produce overgrowths on existing grains and will not reveal the dilatancy.

5.2.2 Matrix phases

Plagioclase in the matrix remains at a constant size in the mylonite, in the transition zone, and in the ultramylonite (Fig. 8, 12b). With the onset of deformation in the mylonite albite is synkinematically replaced by oligoclase, and the plagioclase grains change their shape toward more elongated grains. Albite cores are truncated at their long sides by grain boundaries and oligoclase replacement and/or overgrowth occurs at the ends of grains parallel to the stretching direction. These microstructures indicate diffusion creep deformation.

Biotite (and minor white mica) recrystallized grain size remains constant in the mylonite and ultramylonite. Kinking of grains and the formation of interconnected layers (features common in crystal plastic deformation of mica; (Mares and Kronenberg 1993, Kronenberg et al., 1985; Holyoke & Tullis, 2006)) are not observed in the ultramylonite. Instead, with increasing strain, a portion of biotite is found between quartz grains where it must have formed by precipitation. Similar distributions of micas have been reported for rocks undergoing diffusion creep (e.g. Fliervoet et al., 1997; Herwegh & Jenni, 2001). Thus, the observed mica fabrics suggest diffusion creep rather than dislocation creep deformation.

K-feldspar matrix grains initially form recrystallized layers, occasionally intermixed with minor albite/oligoclase. The plagioclase in these layers is in part of myrmekitic origin (Menegon et al., 2006), in part perthitic. Menegon et al. (2008) have concluded that diffusion creep is the dominant deformation mechanism in the fine grained K-feldspar aggregates based on a very weak CPO, which is incompatible with known slip systems. The K-feldspar grain size and SPO is comparable to that of plagioclase (Fig. 7b). In summary, it is concluded that the microstructures of each of the phases K-feldspar, plagioclase and biotite and all phases as a mixture indicate diffusion creep deformation.

5.2.3 Deformation mechanism in the ultramylonite

The transition from a mylonite to utramylonite marks the transition from a 2- phase rheology- to a single- phase-rheology material (ultramylonite). The quartz aggregates are disintegrated (Fig. 9, 11, 15, 18), the quartz grain size has decreased towards the matrix grain size (Fig. 5c, 12, 18), the quartz grain shapes have changed from a monoclinic to a more isometric, orthorhombic geometry, (Fig. 8a,b) and the CPO is almost destroyed (Fig. 10, 14). The very weak residual CPO shows a small angle between the very weak c-axis maximum and the elongation direction. Such quartz fabrics have been observed in rocks deformed by diffusion creep (Hippert 1994, Stallard & Shelley 1995, Takeshita & Hara 1998). A crystallographic control of dissolution-precipitation processes has also been proposed to be capable of producing a CPO (Bons & den Brok, 2000). Note, however, that the strength of the CPO is too weak to be interpreted with any level of confidence.

Apart from the dispersion of about 30 volume percent quartz into the matrix and complete mixing of phases, the microstructural characteristics of the former matrix minerals do not change in the ultramylonite. From all the fabric characteristics (nearly random quartz CPO, complete phase mixing, equant quartz grain shapes), it is concluded that the entire ultramylonite deforms by diffusion creep.

Despite the decreased quartz grain size which approaches the grain size of plagioclase and K-feldspar, dispersed quartz grains still show a SPO different from the other matrix minerals (Fig. 5, 12). The more equant shape of quartz grains can either be interpreted as a relict or alternatively result from grain rotation during diffusion creep of the matrix. Quartz grains in the ultramylonite are traced by tails of K-feldspar precipitates. This may be taken as an indication that quartz still constitutes a mechanically stronger phase inside the ultramylonite.

5.2.4 Matrix SPO and diffusion creep

Rocks deforming by diffusion creep with a dominant contribution of grain boundary sliding often show equant grain shapes (e.g. Boullier & Gueguen,1975; Fliervoet et al, 1997; Kruse & Stünitz, 1999). A weak CPO and SPO in high temperature deformation may be attributed to diffusion creep including relative grain rotation during grain boundary sliding.

In plagioclase experimentally deformed by diffusion creep, a well defined grain shape anisotropy and SPO have been observed (Gomez-Barreiro, 2007). The authors consider grain boundary sliding and alignment of minerals with a shape anisotropy to produce the SPO. In the Gran Paradiso mylonites the plagioclase grain shapes are dynamically modified during deformation and show a strong SPO (Fig. 8). As long as rotation rates are low enough, dissolution-precipitation may lead to anisotropic grain shapes in non-coaxial flow (e.g. Bestmann et al., 2004). Theoretical considerations (Wheeler, 1992, 2009) suggest the formation of a SPO during diffusion creep at low rotation rates and if grain growth rates are low compared to the rate of diffusion. We observe a constant plagioclase grain size and plagioclase shape changes that involve diffusive mass transfer. Thus, the development of a strong SPO in matrix minerals and deformation by diffusion creep and grain boundary sliding are consistent in the case of the Gran Paradiso rocks at low grain rotation rates.

5.3 Grain size reduction

5.3.1 Grain size reduction and phase separation

The grain to phase boundary area ratio R_{gp} and the quartz fraction of a layer both decrease with decreasing grain size (Fig. 16 b,c), indicating that grain size reduction of quartz and mixing of phases occur simultaneously. There are two processes which are considered for grain size reduction or the disintegration of quartz layers, as shown schematically in Fig. 16d: (1) Subgrain rotation (or eventual fracturing) may reduce the grain size but do not cause a phase separation and they do not increase the grain to phase boundary area ratio. (2) If only phase separation (e.g. nucleation of second phases at triple junctions and grain boundaries) occurs, it will require an additional process such as, e.g., dissolution to reduce the grain size subsequently. As both, grain size reduction and phase separation, are found together (Fig. 16 b), these processes must take place simultaneously and must be related.

The dominant grain size-controlling process in quartz is dynamic recrystallization producing a constant grain size in the monomineralic quartz aggregates. Both, subgrain rotation and grain boundary migration recrystallization are inferred to operate together as recrystallization mechanisms. Grain boundary migration is generally inferred to follow the nucleation of new grains by subgrain rotation (e.g. White, 1973, Poirier & Guillope 1979), leading to grain coarsening (e.g. Mercier, 1980; Poirier, 1985; Urai et al., 1986; Knipe & Law, 1987; Ree; 1991; Bons & Urai, 1992; Shimizu, 1998). The constant grain size along the strain gradient in the mylonite indicates that the recrystallization mechanisms are in a dynamic equilibrium with the flow stress (e.g. Goetze & Kohlstedt, 1973; Twiss 1977, Tullis & Yund, 1982, Derby 1990). If the grain size were, in addition to flow stress, controlled by temperature (De Bresser et al. 2001, Shimizu 2008), the effect will not cause a difference in observed grain sizes because it is extremely unlikely that a temperature gradient exists between the mylonite and ultramylonite.

Initial K-feldspar precipitation takes place at triple junctions and along dilatant quartz grain boundaries (Fig. 11c, 13a, 15a) and at these sites, the quartz grain size decreases. Second phases like K-feldspar or biotite are known to impede grain boundary migration and form pinning microstructures (Jessell, 1987, Olgaard & Evans 1988). Consequently, pinning locally arrests the grain size at the approximate size of subgrains by impeding grain boundary migration while subgrain rotation still operates as a grain size reduction process (Fig. 18 a,b). Thus, by nucleation of second phases in dilatant sites and suppressing grain boundary migration, phase separation and grain size reduction are linked processes and directly connected to dynamic recrystallization and cavitation.

5.3.2 Solution transfer and phase boundary migration

Dissolution, diffusion, and precipitation are considered to be sequential processes during diffusion creep of geologic materials under low to high grade conditions (Boullier & Gueguen,1975; Paterson, 1995, Wintsch et al., 2002). Dissolution and precipitation in the Gran Paradiso shear zones are best indicated by several individual microstructures (Fig.15 c-f). The most prominent microstructures are plagioclase grains that protrude into quartz, and the frequent bulging of K-feldspar into quartz (both processes can be termed phase boundary migration). Some geometries of initial quartz grain boundary separations in the fin shaped structures filled by K-feldspar also suggest a replacement of quartz, especially when they form along subgrain boundaries or directly inside intact grains (Fig. 13b). Gower & Simpson (1992) and Stünitz & Fitzgerald (1993) reported phase boundary migration in greenschist facies mylonites between quartz and feldspar without an associated grain size decrease. Similar microstructures showing a high phase boundary mobility have been reported and interpreted to result from material transport during diffusion creep in greenschist and amphibolite facies mylonites (e.g. Behrmann & Mainprice, 1987), in experimentally deformed harzburgite (Sundberg & Cooper, 2008), and in theoretical modeling (Wheeler, 1992). In the absence of better microstructural criteria, phase boundary migration is one indicator to infer dissolution and precipitation in the Gran Paradiso mylonites and ultramylonites.

The individual size of quartz grains in advanced stages of phase mixing is negatively correlated with the distance between grains which are separated by K-feldspar. In a single layer the average grain size decrease correlates with a relative quartz content decrease, as grains are separated and "horizontally" diluted by other phases (Fig. 16c).This is taken as an indicator that the grain size continues to decrease during the extension of the polymineralic aggregate. As dynamic recrystallization does not cause this grain size decrease, dissolution is the most likely explanation for it. The quartz content in the mylonites and ultramylonite are approximately the same (Fig. 17) so that dissolution must be accompanied by precipitation near the sites of dissolution (probably on the micron to mm scale).

There are only few direct indications for quartz precipitation apart from the myrmekite-related quartz. Menegon et al. (2006) suggest that deformation in the host rock towards the mylonitic Gran Paradiso metagranodiorite is greatly enhanced by the formation of synkinematic myrmekite. Stress induced myrmekite formation has also been described by Simpson & Wintsch (1989) showing that dissolution and precipitation may occur simultaneously at high stress, and low stress sites, respectively. Compare figure 11e where K-feldspar precipitates only a few microns away from the myrmekite forming reaction sites at relic K-feldspar clasts. Other direct evidence of quartz precipitation in Gran Paradiso mylonites can be found in rare boudinaged garnet, where quartz grows together with biotite and white mica in the necks.

The volume of dissolved quartz in the ultramylonite (as evidenced from the grains size reduction) is at least 75% (assuming size reduction from 28 μm to 19 μm, see figure 5 b,c). This amount far exceeds the amounts of observed quartz precipitation (see above). Since the quartz content in the ultramylonite is still 30 %, a large fraction of the very fine grained quartz in the ultramylonite must consist of newly formed grains.

Post-kinematic grain growth can be ruled out on the basis of the measured shape preferred orientation and the local preservation of a smaller recrystallized quartz grain size outside the shear zones.

5.4 Origin of the cavitation in quartz aggregates

In quartz aggregates, the K-feldspar and biotite precipitate distribution is heterogeneous at the grain scale but often homogeneous at the aggregate scale (e.g. Fig 11 c,d, 13a). This indicates that the dilatancy/cavitation is generated during rather homogenous flow of the quartz aggregate and not locally by external perturbations.

The presence of precipitates at triple junctions, dilatant grain boundaries and aligned grain boundaries is interpreted to result from cavitation caused by grain boundary sliding (Fig. 18b). The fact that K-feldspar is precipitated implies that filling of dilatant space by diffusional mass transfer/

grain boundary migration or dislocation movement of quartz did not take place at a sufficiently high rate.

The quartz CPO and prism-parallel subgrain boundaries (interpreted as tilt boundaries made up of edge dislocations) suggest that basal <a> is the single dominant sip system.

The von Mises criterion (von Mises, 1928) requires 5 independent slip systems in a polycrystal for homogeneous deformation. Fewer slip systems are required if relaxed constraints or recrystallization is introduced (cross-slip or climb of dislocations) (Groves & Kelly, 1969; Honneff & Mecking, 1978). Therefore, grain boundary precipitates may indicate heterogeneous deformation which can result from the activity of a limited number of slip systems in a deforming phase. Heterogeneous deformation caused by a limited number of slip systems calls for some process to maintain strain compatibility. Possible accommodating processes are for example diffusional mass transfer or grain boundary migration (Khayutin,1974, Means & Jessell, 1986). Grain boundary sliding may arise from heterogeneous deformation and may also cause cavitation instead of accommodating it (Langdon 1994, 2006, Zhang et al.,1996). Zhang et al. (1994b) suggest that a small amount of grain boundary sliding is capable to accommodate heterogeneous grain scale deformation and does not weaken but strengthens the CPO of a polycrystalline aggregate with a single slip system. The contribution to the total strain by grain boundary sliding during dislocation creep remains relatively small, probably <15 % (Kottada & Chokshi, 2007).

5.5 Shear zone localization

Shear zones tend to localize either by an intrinsic instability (Poirier, 1980) like, e.g., strain rate softening, or by an external inhomogeneity (e.g. Segall & Pollard, 1983, Segall & Simpson 1986) such as a precursor structure (Mancktelow & Pennachioni, 2005). In the studied Gran Paradiso shear zones, the existence of a brittle precursor structure was inferred by Menegon & Pennacchioni (2009), based on the macroscopic shear zone distribution and orientation resembling joint orientations in the same rock. From the microstructures this inference can neither be confirmed nor rejected, but additional information is obtained based on microstructural observations: The quartz grain size and thus the flow stress is constant across the mylonite. The switch in deformation mechanism and possible weakening of the rock occurs towards the shear zone center caused by the grain size reduction and phase mixing, especially in thinned quartz layers. The thinning of quartz layers is a progressive strain feature, so that it must have occurred subsequent to initial deformation increments. From these observations, it is clear that the shear zone has narrowed over the deformation history (Hull 1988, Means 1995). Thus, if the shear zones are initiated by brittle precursor structures, the rock volume affected by the "precursor effect" must have comprised the whole width of the shear zone, because a widening of a narrow, crack-like shear zone after its initiation is very unlikely based on the arguments given above. One possibility for an effect of a precursor crack may be microcracking of the rock volume adjacent to the main crack and aqueous fluid infiltration, causing weakening effects by enhancing transport and reaction rates.

6. Conclusions

From microstructural observations along a strain gradient across a 5 cm wide shear zone (from protolith to mylonite to ultramylonite) the following conclusions can be drawn:

In the mylonite, the quartz aggregates (up to 6 mm diameter) deform predominantly by dislocation creep maintaining a dynamically stable grain size of $\mu_v(D) = 110\ \mu m$ while the polymineralic fine grained matrix ($\mu_v(D)d \sim 15\ \mu m$) deforms by diffusion creep.

The ultramylonite in the shear zone center (~ 15 - 25 μm) only one rheological phase (homogeneous mixture of qtz - kfs - plg - bio) is present; deformation is by diffusion creep.

In the mylonite and the ultramylonite, quartz is the phase with the highest viscosity.

The texture and microstructure of the quartz aggregates is characteristic for dislocation creep with subgrain rotation and grain boundary migration recrystallization. With the onset of diffusion creep in the ultramylonite, the surface ODF changes from an monoclinic to an orthorhombic symmetry and the CPO is randomized.

Failure to deform compatibly with the imposed kinematic framework of the matrix (only basal <a> slip system active), leads to a disintegration of the quartz aggregates by nucleation of K-feldspar (and occasional biotite) along dilatant grain boundaries and triple junctions oriented at high angles to the stretching direction (Fig. 18). From the rim to the center of the quartz aggregates, the deformation mechanism changes from dislocation creep to diffusion creep with grain boundary sliding and cavitation with simultaneous precipitation of second phases (Fig. 18).

With the precipitation of K-feldspar and biotite, the grain boundaries in the quartz aggregates (now effectively phase boundaries) are pinned and grain boundary migration is suppressed, causing a local decrease in grain size during dynamic recrystallization from d ~ 110 μm to 60 μm. The decreased grain size is approximately equal to the subgrain size.

Grain size is further reduced during and after the disintegration of the quartz aggregates from d ~ 60 μm to 25 μm such that in the ultramylonite, the grain size of quartz approaches that of the matrix plagioclase and K-feldspar. Dissolution and phase boundary migration contribute to the grain size reduction.

The total volume fraction of quartz (30 ± 1.5%) is constant from the undeformed protolith to the most highly deformed ultramylonite. Dissolution of quartz (leading to the above mentioned grain size comminution) requires that quartz precipitation must take place within the ultramylonite.

During diffusion creep of the polymineralic mixture, the surface fabric of K-feldspar and plagioclase is strengthened which indicates grain boundary alignment, impeded grain growth and K-feldspar precipitation adjacent to quartz grains.

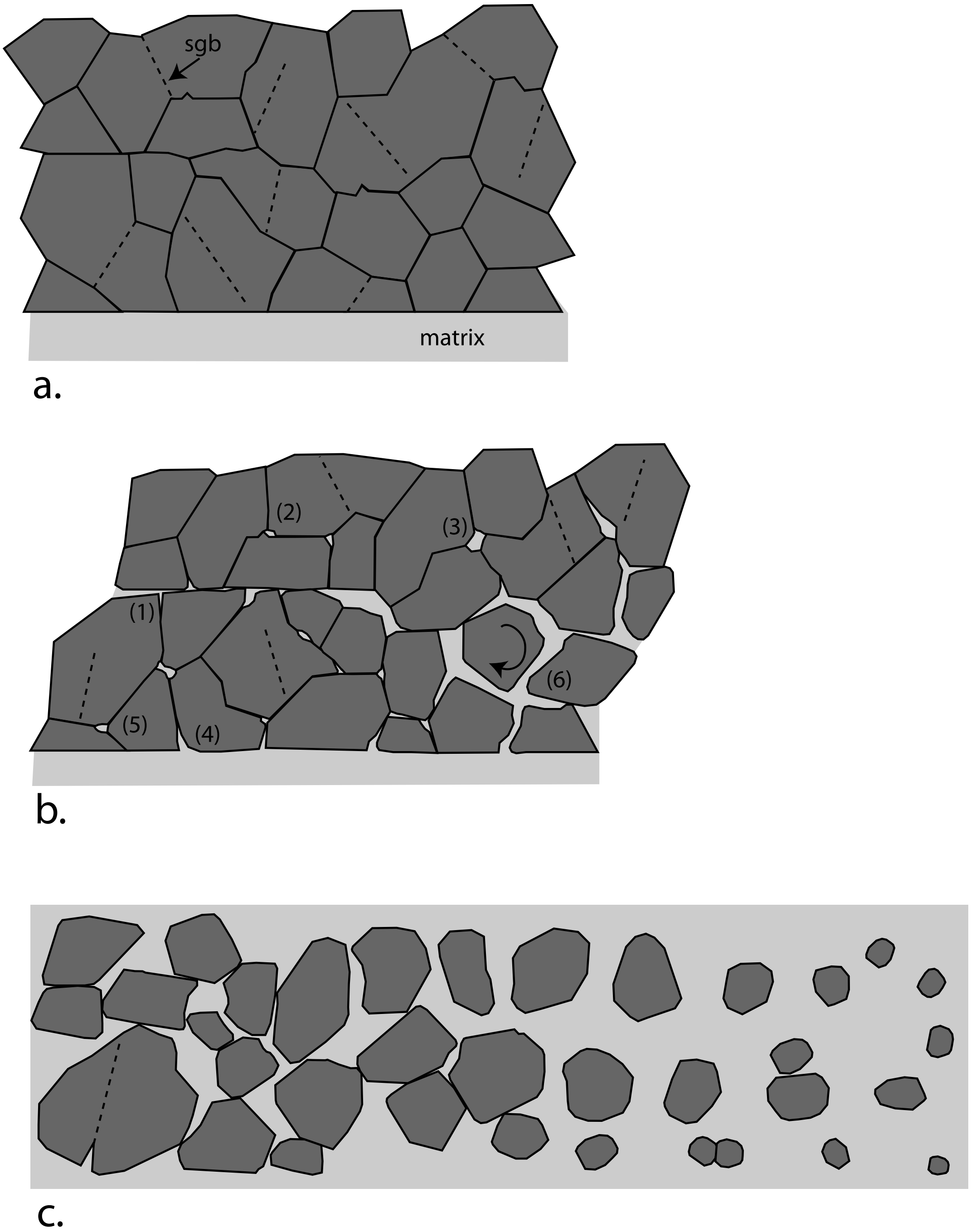

Figure 18: Schematic model of the aggregate disintegration and grain size reduction. (a) Quartz aggregate undergoing dislocation creep with subgrain rotation and grain boundary migration. The subgrain size is smaller than the dynamically recrystallized grain size as grain boundary migration is associated with a grain size increase. As soon as subgrain boundaries (sgb) become grain boundaries they start to migrate. (b) Initial precipitation of K-feldspar in dilatant sites along aligned grain boundaries (1), asperities (2), opening triple/quadruple junctions (3) and matrix- grain boundary junctions leads to pinning of grain boundaries (5). Coalescence of precipitate filled sites is associated with grain rotation and grain boundary sliding and phase boundary migration. (c) The aggregate is disintegrated, no dynamic recrystallization is possible and further grain size reduction occurs by dissolution-precipitation.

Chapter 3

Crystallographic preferred orientations and fabrics in a polyphase rock as shear sense indicators: sheer nonsense?

Abstract

It is presently believed that the fabric and the crystallographic preferred orientations (CPO) of dynamically recrystallized quartz are reliable shear sense indicators. We find that the CPO and the fabric of dynamically recrystallized quartz in a polyphase rock indicates the shear sense not at the global scale of the shear zone but rather at the local scale of the deforming and recrystallizing quartz aggregates.

The object of this study is to understand the development of quartz fabrics and CPOs such that we still may use them as shear sense indicators. We present results of the microstructural analysis of small scale, lower amphibolite facies shear zones in the Gran Paradiso metagranodiorite.

Magmatic quartz grains have recrystallized dynamically forming polycrystalline quartz aggregates that deform as objects with a higher viscosity embedded in a lower viscosity matrix. The grain size of recrystallized quartz is constant across the strain gradient and is the result of combined subgrain rotation and grain boundary migration recrystallization.

We distinguish between a global and a local reference frame, the former with respect to the entire shear zone, the latter with respect to each deforming aggregate. Quartz develops a strong CPO with the [c]-axes forming a peripheral maximum inclined synthetically with the inferred sense of slip on the quartz basal plane. This sense of slip is usually consistent with the local sense of shear.

At low strain the local shear sense of porphyroclasts is systematically opposite to the global shear sense. The crystallographic orientation of the magmatic grain has only a minor influence on the developing CPO.

Flow partitioning between the quartz aggregates and the matrix is proposed to control the kinematics of the aggregates. Spin of the aggregates combined with layer parallel shear along the

aggregates takes place instead of homogeneous simple shear as long as aggregates rotate towards parallelism with the shear zone boundary plane.

The fabric is in most cases related to the CPO such that the maximum of the surface orientation distribution function is always synthetically rotated with respect to the sense of slip on the basal plane of quartz crystals. This situation implies a crystallographic control of the development of the fabric. Orthorhombic surface fabrics are suggested to form at a high grain boundary mobility, monoclinic surface fabrics from at a lower grain boundary mobility.

It is suggested that CPOs and fabrics are only reliable shear sense indicators in polyphase rocks if the most highly strained parts are analyzed and spin of the aggregates with respect to the shear zone boundary has ceased.

1. Introduction

The objective of this study is to understand the development of quartz fabrics and CPO. Dynamic recrystallization and the development of crystallographic preferred orientation (CPO) as a consequence of deformation have been studied intensively and many insights on CPO development in experimentally or naturally deformed rocks were established on monophase material, especially quartzites (e.g. Tullis, 1977; Carreras et al., 1977; Bouchez 1977; Garcia Celma, 1983; Schmid & Casey 1986, Law et al.,1990; Mancktelow 1987; Heilbronner & Tullis, 2006).

Asymmetric CPOs can be used as shear sense indicators (e.g. Berthe et al., 1979; Lister & Hobbs, 1980; Simpson, 1980; Behrmann & Platt, 1982; Simpson & Schmid,1983). In the case of the absence of an internal asymmetry of the [c]-axis polefigures or straight single girdles, the interpretation of the shear sense depends on the external asymmetry and therefore on the chosen kinematic reference frame. Numerical models (Lister et al. 1978; Lister & Hobbs, 1980; Wenk, et al 1989; Jessell & Lister, 1990) reveal that the geometry of the CPOs is related to the applied kinematic framework and strengthens with increasing strain. Such models predict that the CPO rotates as strain increases with respect to the finite strain ellipse. CPOs that show this relation have been reported for natural rocks (e.g. Burg & Laurent, 1978; Van Roermund et al., 1979).

In contrast, some quartz CPOs that have been measured in natural shear zones (e.g. Carreras, 1977; Simpson, 1980; Garcia Celma, 1983), that have been obtained by numerical models (Etchecopar, 1977; Etchecopar & Vasseur, 1987) or from triaxial deformation experiments in a Griggs-type

apparatus (Heilbronner & Tullis, 2006) indicate a major rotation of the CPOs with respect to the shear zone
boundary plane and shear direction; the rotation with respect to the finite strain reference frame is only a minor effect.
Some of the differences of the observations and reference frames can be related to flow partitioning between the observed quartz volumes and the host rock (e.g. Carreras, 1977; Lister & Williams, 1979), but the influence of flow partitioning in pure quartz rocks is not properly understood (e.g. Heilbronner & Tullis, 2006).

We use a microstructure in small scale shear zones and strain gradient across to reconsider the problem. The CPO development can be observed from the initial recrystallization of magmatic quartz grains to fully recrystallized, highly deformed quartz layers. The recrystallized grain size remains constant across the shear zone. This implies that the differential stress remains constant across the shear zone.
The results of the CPO and SPO will be discussed with respect to the influence of the initial orientation of the recrystallizing grains, the choice of the reference frame, and the possibility of flow partitioning between quartz aggregates and the feldspar-mica matrix. The orientation of a CPO for it to be a reliable shear sense indicator and the inferred shear sense must be consistent with other shear sense criteria. For example oblique fabrics (oblique foliations) are easy to recognize and are often found in deformed rocks (e.g. Lister & Snoke, 1984; Knipe & Law, 1987). The intensity and geometry of oblique fabrics has been related to the deformation mechanism (Means, 1981; Schmid et al., 1987) and the influence of grain boundary migration.
As the studied rocks show variable and controversial oblique particle and surface fabrics while the recrystallization mechanism remains constant, the strength and asymmetry of the microstructure will be discussed in relation to the CPO and the shear sense.

2. Geological setting

2.1 Overview

The metagranodiorites of the Gran Paradiso (Fig. 1a) are Permian intrusives and heterogeneously deformed during the Alpine orogeny (Dal Piaz et al., 1972; Bertrand et al.,2005; Le Bayon et al., 2006) preserving meter to kilometer scale low strain domains surrounded by granitic orthogneisses (Callegari et al., 1969; Menegon, 2006). The metagranitoids have been studied structurally and petrologically (e.g. Le Goff & Ballevre, 1990; Brouwer et al., 2002; Menegon, 2006; Menegon et al., 2006/2008, Menegon & Pennacchioni, 2009).

The low strain domains host straight and planar small scale shear zones, in regular, equispaced, subhorizontal (and minor subvertical) groups (Menegon & Pennacchioni, 2009) (Fig. 1b,c). Several orientation groups of shear zones with a regular spacing have been described. Steep shear zones seem to be overprinted by progressive shortening and an associated crenulation with subhorizontal intersection lineations (Menegon & Pennacchioni, 2009). Subhorizontal shear zones are not affected by shortening and no evidence for a later overprint or change in kinematic framework has been observed. The deformation in the hostrock and within the shear zones is assumed to be coeval (Menegon & Pennacchioni, 2009).

The metagranodiorite was metamorphosed during early high pressure conditions at about 500°C - 550°C and 1.0-1.6 GPa (LeGoff & Ballevre,1990) and later under lower amphibolite facies conditions at about 550°C and 0.6-0.7 GPa (Brouwer et al., 2002). The high pressure event has been static and the shear zones have formed after peak pressure conditions.

The samples investigated were taken from subhorizontal small scale shear zones in the Piantonetto valley, Lago Teleccio and the Alpe Drosa area (GP9: 32T372881 / 5038395 GP11/GP12: 32T0371389/5037047) (Fig.1a). Hand specimens display strain gradients from a weakly deformed protolith or host rock to a highly deformed mylonite to ultramylonite. Shear zones are only a few centimeters wide and the associated complete strain gradient can often be observed within one or two thin sections (Fig. 2a,b). Samples GP9 and GP11 are from a medium grained porphyric metagranodiorite with a quartz content of ~30%. GP12 is a micrograniticnic enclave enclosed in the metagranodiorite. The enclave has a biotite-granite composition with a quartz content of ~33% and are devoid of white mica and porphyric K-feldspar. In the field shear zones of samples GP11 and GP12 have similar orientations (S136/21,L132/16;S110/19,L114/18) and are from the same outcrop but have opposite shear senses (Fig. 1b) - GP11 top NW, GP12 top ESE.

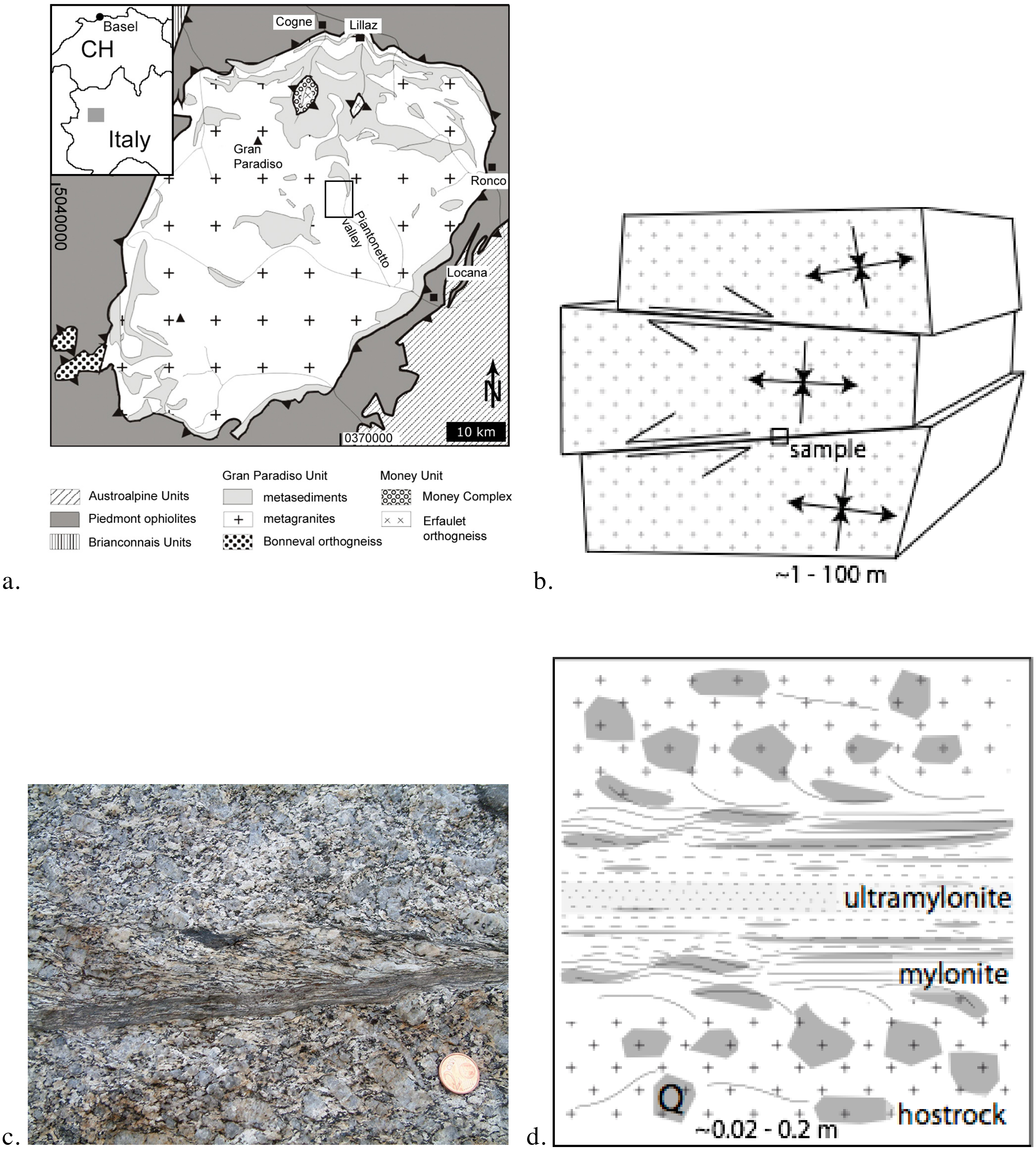

Figure 1: Geological setting: (a) Geological sketch of the Gran Paradiso nappe (after Kassem, 2005; Menegon & Pennacchioni, 2009). Rectangular area indicates the field area in upper Piantonetto valley. (b) Conceptual sketch showing the subhorizontal shear zones in a low strain domain. (c). Field view of shear zones cutting moderately deformed metagranodiorite. Shear sense is top to the west. Diameter of coin is 19 mm. (d) Schematic sketch of a shear zone and the distinction between host rock, mylonite and ultramylonite. Area is representative of rectangular inset in b.

2.2 Internal structure of the shear zones

In the samples we distinguish a protolith or host rock, a mylonite, and an ultramylonite (Fig. 1d). The weak deformation of the protolith is coeval but kinematically different from that of the shear zones. The flow of the protolith is predominantly coaxial (Menegon & Pennacchioni, 2009) while flow in the shear zones is dominated by non-coaxial flow. The mylonite contains a strain gradient, which is defined by the orientation of the sigmoidal foliation. The ultramylonite forms in the most highly strained parts, the foliation is parallel to the shear zone boundary.

The least deformed parts of the mylonite show a weak foliation defined by the preferred elongation and orientation of polycrystalline plagioclase and biotite aggregates and occasionally of up to 15 mm long K-feldspar porphyroclasts. Quartz grains of magmatic origin are up to 10 mm in size in GP11 and ~1 mm in GP12. At intensely deformed sites, e.g. adjacent to relatively rigid K-feldspar porphyroclasts, magmatic quartz grains begin to dynamically recrystallize.

In the more highly strained part of the mylonite, K-feldspar clasts, biotite, and quartz are completely recrystallized. Relict K-feldspar grains are present as porphyroclast. Recrystallized K-feldspar, plagioclase aggregates and biotite form interconnected layers with a variable degree of mixing of the mineralogical phases. Magmatic quartz grains have recrystallized to polycrystalline aggregates.

The sigmoidal deflection of the foliation clearly indicates the shear sense in both samples (Fig. 2). In the most highly strained parts of the mylonite quartz aggregates and all other phases from parallel layers. In the transition to the ultramylonite, the quartz aggregates disintegrate and mix with K-feldspar, plagioclase, biotite ± white mica to form a polymineralic fine grained ultramylonite (Kilian et al., 2011a, Chapter 2).

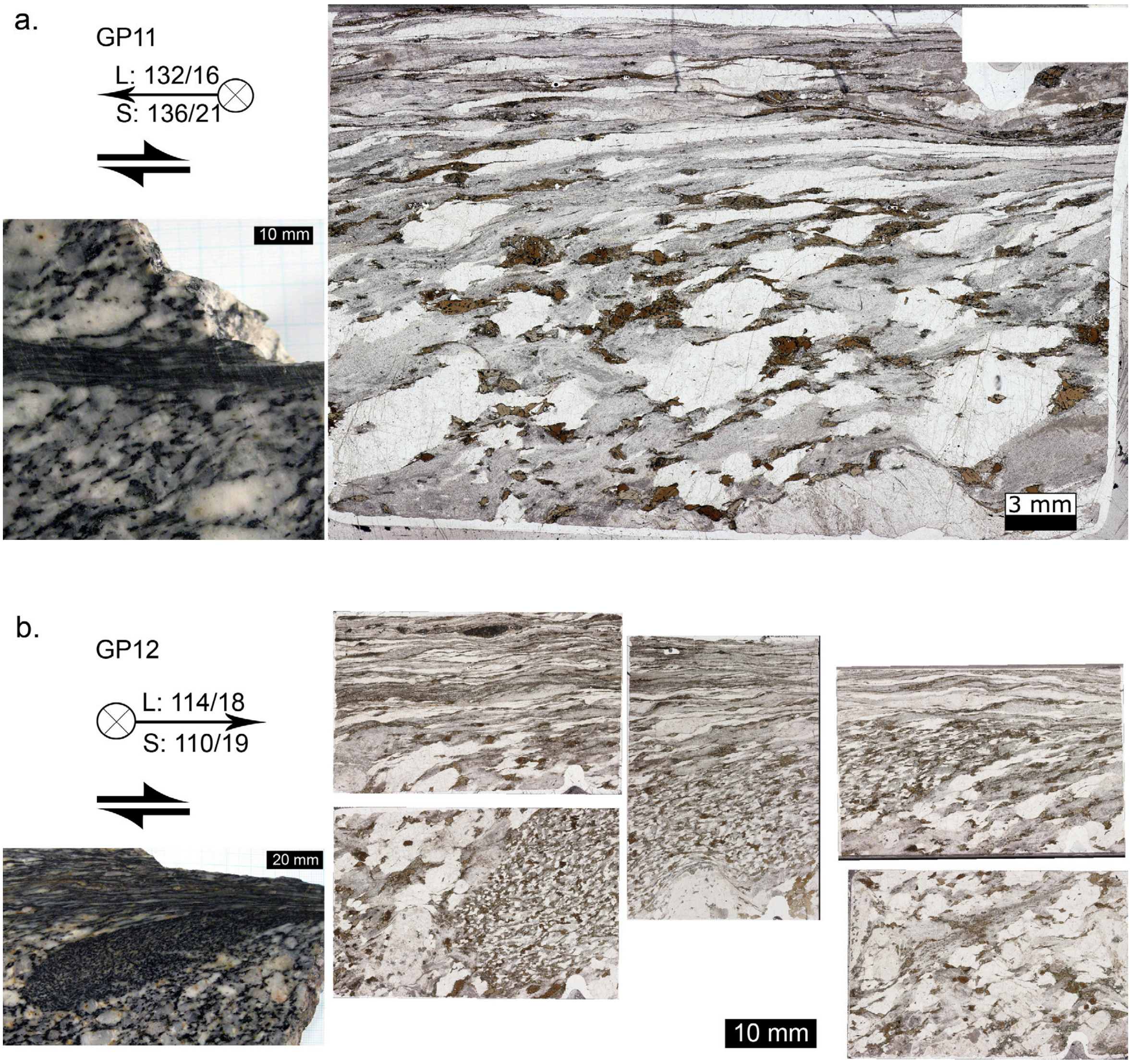

Figure 2: Samples: Polished rock surface and thin section views of sample GP11 and GP12. GP11 is a medium grained metagranodiorite. GP12 contains a microgranitic enclave with a smaller size of mineral aggregates. Thin sections are scanned with plane light, quartz is white, biotite is brown, fine grained plagioclase aggregates are grey, K-feldspar is light grey.

2.3 The matrix

In the following, the term matrix is used to describe the partial or complete mixture of all phases but quartz, i.e. of fine grained K-feldspar, biotite, plagioclase, white mica and accessory garnet, epidote, ± clinozoisite, the latter only present in the weakly deformed rocks (Fig.3a). The quartz aggregates are embedded in this matrix considered as more rigid particles.

The matrix minerals will be briefly reviewed.

The plagioclase is of either albitic or oligoclase composition. In the weakly strained part albite is more frequent while in the highly strained part oligoclase predominates due to the lower pressure metamorphic conditions during shearing. Plagioclase occurs in the undeformed part in polycrystalline, fine grained aggregates, partially intergrown with variable amounts of white mica or clinozoisite (Fig. 3a). Undeformed plagioclase aggregates are pseudomorphs after undeformed magmatic plagioclase and reach sizes up to 1-10 mm (Fig. 3d). Mica grains at the size of albite grains are intergrown following one, two, or three different preferred orientations, which resemble former plagioclase cleavage planes (mostly [010] and [101]) (Fig. 2d). Aggregates deform easily between K-feldspar, quartz or biotite clasts which results in the parallel alignment of the intergrown white mica. Plagioclase grain sizes remain constant throughout the strain gradient with a volumetric mean of 15 μm.

SEM backscatter images show zonations of albite cores rimmed by oligoclase (Fig. 3b). The width of oligoclase rims is larger in the direction parallel than normal to the foliation.

A smaller portion of plagioclase originates from perthitic albite exolution or myrmekitic reaction in K-felspar clasts (see also Menegon et al., 2006, 2008). K-feldspar occurs in the host rock and in the weakly deformed part as perthitic porphyroclasts. Some large clasts fracture and it is suggested that they initially recrystallize by dissolution-precipitation creep (Menegon et al., 2006). With increasing strain, K-feldspar occurs in monomineralic polycrystalline layers with a relatively constant grain size of about 10 to 20 μm, occasionally mixed with some plagioclase grains.

Magmatic brown biotite is kinked and recrystallized marginally to fine grained biotite. Biotite aggregates may contain small garnet grains along the grain boundaries. In the moderately strained mylonite, recrystallized biotite grains form layers. With increasing strain recrystallized biotite grains occur intermixed in the polymineralic layers and pure biotite layers disappear.

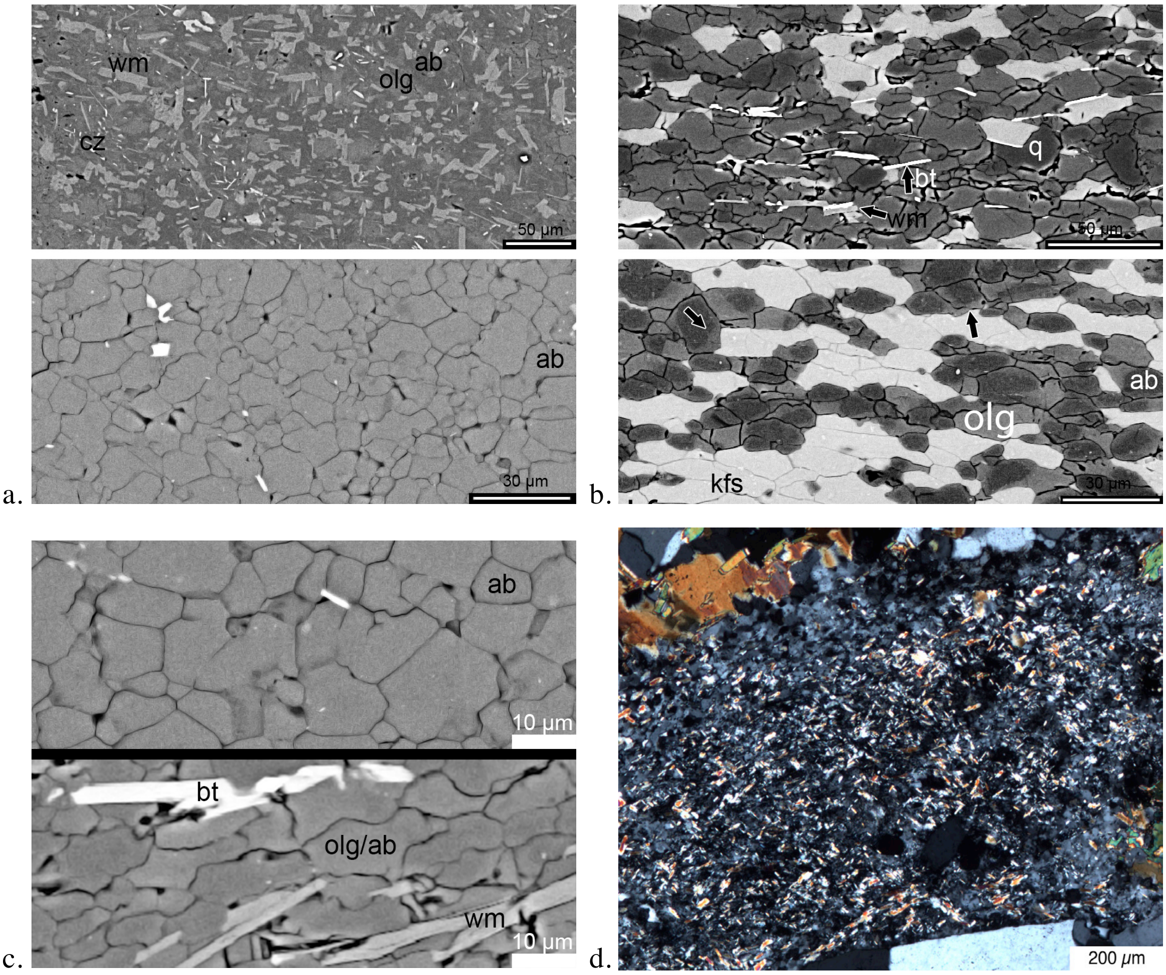

Figure 3: Matrix: (a) SEM / BSE micrograph of the undeformed plagioclase matrix with white mica (wm) and clinozoisite (cz) intergrown with albite (ab) and oligoclase (olg). Relatively pure albite aggregates are also common. (b) SEM / BSE micrograph of the deformed matrix forming a polyphase mixture with albite, oligoclase, K-feldspar (kfs), biotite (bt) and quartz (q). Note oligoclase rims growing around albite cores. (c) Comparison of undeformed and deformed matrix plagioclase. The grain size remains approximately constant, grains have higher aspect ratios, more lobate shapes, and are more anorthite-rich in the deformed aggregates. (d) Micrograph (crossed polarizers) of white mica intergrown with a polycrystalline plagioclase aggregate (pseudomorph). Note two oblique directions, interpreted to resemble former plagioclase cleavage planes. All images are of sample GP11 except (b) lower picture and (c) lower picture which are from sample GP4 (see Kilian et al, 2011a, Chapter 2).

In the centers of the shear zones a gradual homogenization, dispersion and grain size reduction of quartz grains into the polymineralic matrix is observed forming an ultramylonite. This change in microstructure takes place by intergranular dilatancy and K-feldspar and biotite precipitation between quartz grains (Kilian et al., 2011a, Chapter 2).

3. Analytical methods

3.1 Reference frames and definitions

We use XYZ as a global reference frame where X is the lineation and transport direction in the shear plane (= parallel to the shear zone boundary plane), Z is the pole of the shear zone boundary and Y is the transverse direction (Fig. 4). The local reference frame X_aYZ_a is defined by the trace of the aggregate long axis X_a (in XZ), the pole to X_a (= Z_a) and the transverse direction Y is shared with the global reference frame (Fig. 4). Angles are counted positive and against the global shear sense from X or X_a. As a consequence. angles will be couter-clockwise = positive for a dextral shear zone; Fig. 4).

φ is the angle between an aggregate and X, θ is the angle of a [c]-axis pole figure maximum with X in the XZ-plane, and β is the angle between a [c]-axis pole figure maximum and X_a, measured against the global shear sense,

In the most highly strained parts it is impossible to distinguish between the orientation of the shear zone boundary and the aggregate long axis orientation ($X \approx X_a$). In some cases quartz aggregates are curved and it is difficult to determine a unique aggregate orientation. In these cases the orientation of the aggregate median line has been used.

The corresponding matrix foliation Φ is the mica or plagioclase grain shape defined foliation, measured at the same distance to the shear zone boundary as the quartz aggregate (Fig. 4). Directly adjacent to a quartz aggregate the matrix foliation is deflected, so it has been avoided to measure in this situation.

The terms synthetic and antithetic refer to the same or opposite local shear induced sense of rotation with respect to the global shear induced sense of rotation respectively.

3.2 Determination of the crystallographic preferred orientation

The quartz crystallographic preferred orientation (CPO) was analyzed using computer integrated polarization microscopy (CIP) (Panozzo Heilbronner and Pauli, 1993; Heilbronner, 2000) and EBSD (Venables & Harland, 1973; Adams et al, 1993). CIP allows the calculation of c-axis orientation images and c-axis pole figures. EBSD allows the calculation of complete textures. CIP was usually employed for the evaluation of large areas (< 35 mm^2) because CIP is much less time consuming than EBSD.

For the CIP analysis, extra thin sections (thickness ~ 20 μm) were used. The input images (1300 by 1030 pixel) were acquired with a monchromatic IR sensitive camera (Axiocam MRm) on a ZEISS Axioplan microscope. Apart from c-axis orientation images, three principal misorientation images were calculated - the CIP software can be downloaded from http://pages.unibas.ch/earth/micro. CIP misorientation images show the angular deviation of the c-axis (at each pixel) from a fixed (external)reference direction. The principal misorientation images are calculated with respect to X,Y,Z. They serve as the basis for supervised image segmentation and grain size determination.

Using a ZEISS Evo50 SEM, equipped with a Digiview II EBSD camera and OIM software (TSL-Ametek), the Euler angles were determined and represented as orientation maps at step sizes of 1 to 5 μm. Polefigures were calculated from the raw EBSD data using MTEX (Hielscher & Schaeben, 2008). For further details see Kilian et al. (2011a, Chapter 2). EBSD was also used to improve the CIP derived segmentations in aggregates where the overall [c]-axis misorientations are relatively low.

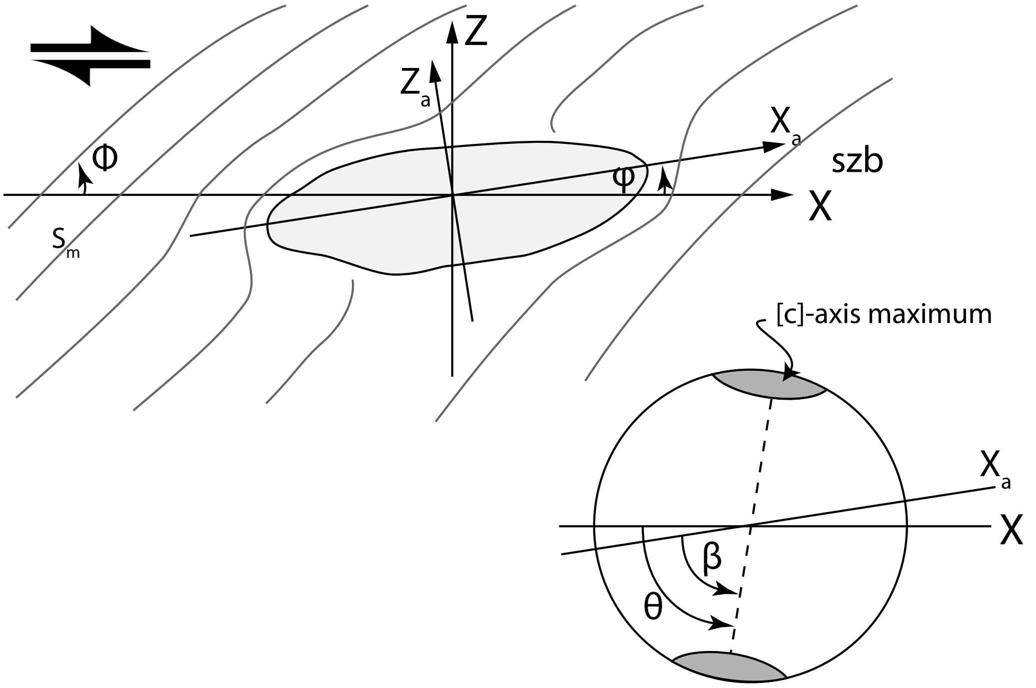

Figure 4: Reference frames and definitions of global and local reference frames: The global reference frame is parallel to the shear zone boundary (szb). The local reference frame is parallel to the quartz aggregate. φ is the angle of the quartz aggregate long axis with respecxt to X, θ is the angle of the peripheral quartz [c]-axis maximum with respect to the global reference direction X, β is the angle of the peripheral quartz [c]-axis maximum with respect to the local reference direction X$_a$ (θ-φ = β). Φ is the angle between X and the main foliation (S) in the matrix. See text for explanation.

3.3 Grain size analysis

Grain sizes were derived from grain maps that were obtained by supervised segmentation of CIP derived misorientation images using the freeware Image SXM (http://www.ImageSXM.org.uk) and the Lazy grain boundaries macro (http://pages.unibas.ch/earth/micro). The orientation difference of [c]-axes across grain boundaries of segmented grains is > 7.5°.

The 2D grain size distributions are obtained by calculating the area equivalent diameters, $d_{equ} = 2 \cdot \sqrt{(\text{area}/\pi)}$ of the sectional areas and calculating the corresponding distribution of 3-dimensional spheres using the STRIPSTAR program (Heilbronner & Bruhn, 1998; http://pages.unibas.ch/earth/micro/index.html). 3D grain size distributions are presented as volume weighted (v(D)) or number weighted (h(D)) histograms. The mean diameter is the arithmetic mean of v(D) or h(D): $\mu_v = \sum (v_i(D_i) \cdot D_i)$ and $\mu_h = \sum (h_i(D_i) \cdot D_i)$.

3.4 Analysis of microstructure

The microstructure is described in terms of particle and surface orientations using the PAROR (Panozzo, 1983) and SURFOR (Panozzo, 1984) method. Typical results yield length weighted rose diagrams of long axes of grains (PAROR) and rose diagrams of grain boundary surfaces (SURFOR). The projection functions $B(\alpha)$ and $A(\alpha)$ yield the bulk fabric anisotropy. The rose diagrams obtained by SURFOR were used to calculate the characteristic shape of the fabric by linking up all surface elements in the order of increasing slope (see Schmid et al.,1987).

Axial ratios b/a_{bulk} of the aggregate were calculated from the ratio of the minimum and the maximum of $B(\alpha)$ and the preferred orientation of grain long axes and grain boundary surfaces are derived from the angle α_{min} of $B(\alpha)$ and $A(\alpha)$ respectively. b/a_{bulk} is different from the arithmetic mean of axial ratios of individual particles because b/a_{bulk} also depends on the orientation distribution function of the particlelong axes.

Particle and surface orientations of dynamically recrystallized rocks have been used previously to describe the effect of strain and recrystallization on grain shapes (Lister & Snoke, 1984; Schmid et al., 87; Stipp et al.,2002). The asymmetry of the particle and surface orientation distribution function can be used to infer the shear sense.

For entire quartz aggregates the aspect ratio, long axis orientations, and areas have been determined on manually produced bitmaps of the aggregates. In the case of the coarse grained granodiorite, the best fit ellipses calculated with ImageSXM. In the case where the ellipse fit was poor, angles and axes of the aggregates were measured by hand.

In the micrograniitic sample GP12 quartz aggregates are small and homogeneously distributed, but display a large spread in shape. Here, tessellation of autocorrelation functions (ACF) (Heilbronner; 2002) were on the bitmaps. To ensure that the resulting ellipses are not an effect of the single aggregates but to obtain as much tiles as possible several sizes of ACF tiles have been selected covering the entire aggregate, 3 tiles with > 100 aggregates/tile, 15 tiles with ~50 aggregates/tile, 26 tiles with 10-20 aggregates/tile. An ACF tile is the area covered by the autocorrelation function. The ACFs have been thresholded at the level corresponding to the average aggregate area and the aspect ratio and long axis orientation of the resulting ACF have been measured from the best fit ellipse.

4. Results

4.1 Shape preferred orientation of sheared quartz aggregates

With increasing strain quartz aggregates progressively elongate and change their long axis orientation towards a smaller angle φ (between X and X_a) concomitant with the rotation of the corresponding matrix foliation (Fig. 5a).

Figure 5b shows the quartz aggregate orientation and aspect ratio measured in GP11 and GP12. Sample GP11 has a larger aggregate size and is more heterogeneous. The measured values do not correspond to the line indicating the expected aspect ratio and ellipse orientation for a passive marker in simple shear and plane strain (strain ellipse) given by $a/b = [(2/\tan 2\Theta)+2\sqrt{(1+1/\tan^2\Theta)}]^2$ (e.g. Ramsay & Huber, 1983) for the aspect ratio a/b and the orientation Θ of a. Instead, the quartz aggregates tend to show lower aspect ratios for given angles of the aggregate with respect to the shear plane (Fig. 5b). Sample GP12 is more homogeneous, aggregates are smaller, and the ACF derived data shows the same trend as sample GP11. For a given angle φ (between X and X_a), the corresponding aspect ratio is smaller than it would be expected for a passive marker deformed by simple shear plane strain.

If the angle φ of quartz aggregates is compared with a corresponding matrix foliation orientation Φ, it is often smaller than Φ in the mylonite (Fig. 5,c). This relationship is found to be more consistent in sample GP12 than in GP11.

In the most highly strained mylonite, aggregates are aligned parallel to the shear plane and reach aspect ratios > 25, separated by matrix layers. The quartz layer thickness is highly variable and can

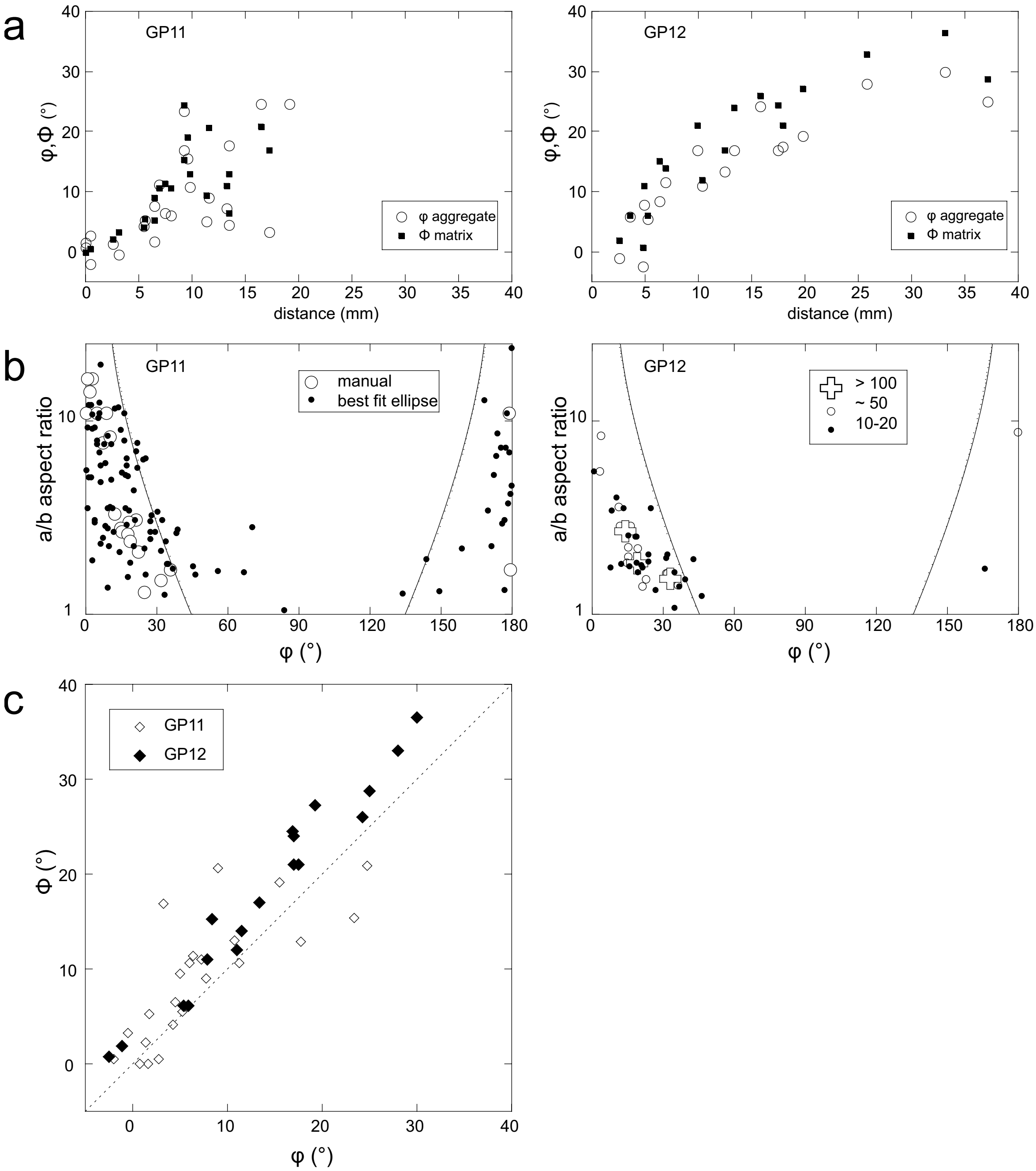

Figure 5: Shape preferred orientation of quartz aggregates and matrix: (a) Variation of orientation of quartz aggregates and of corresponding matrix foliation orientation with distance from the shear zone center (= 0). (b) orientation φ and aspect ratio of deformed quartz aggregates. The black lines indicate the rotation angle and aspect ratio of a passive marker during plane strain simple shear. Data for GP11 is obtained directly from best fit ellipses (black circle) and manually measured large aggregates (open circle). Data for GP 12 is obtained from ACF analysis. Numbers denote approximate number of aggregates included in each ACF tile. For discussion see text. (c) Relationship between aggregate orientation φ and corresponding matrix foliation orientation Φ. The dotted line indicates φ = Φ.

decrease down to the diameter of a single grain (towards the center of the shear zone). Boudinage and pinch-and-swell structures are rare and occur in more heterogeneous parts of the samples, associated with the development of shear bands.

Measurements show that there is no trend towards a decrease of the cross sectional area of aggregates with increasing aspect ratio or decreasing aggregate orientation φ (Fig. 6) as the strain of the aggregate increases. Difficulties in the interpretation arise as high aspect ratios aggregates extend across the entire thin section rendering it difficult to measure them, and small aggregates show a large spread in orientation and aspect ratios.

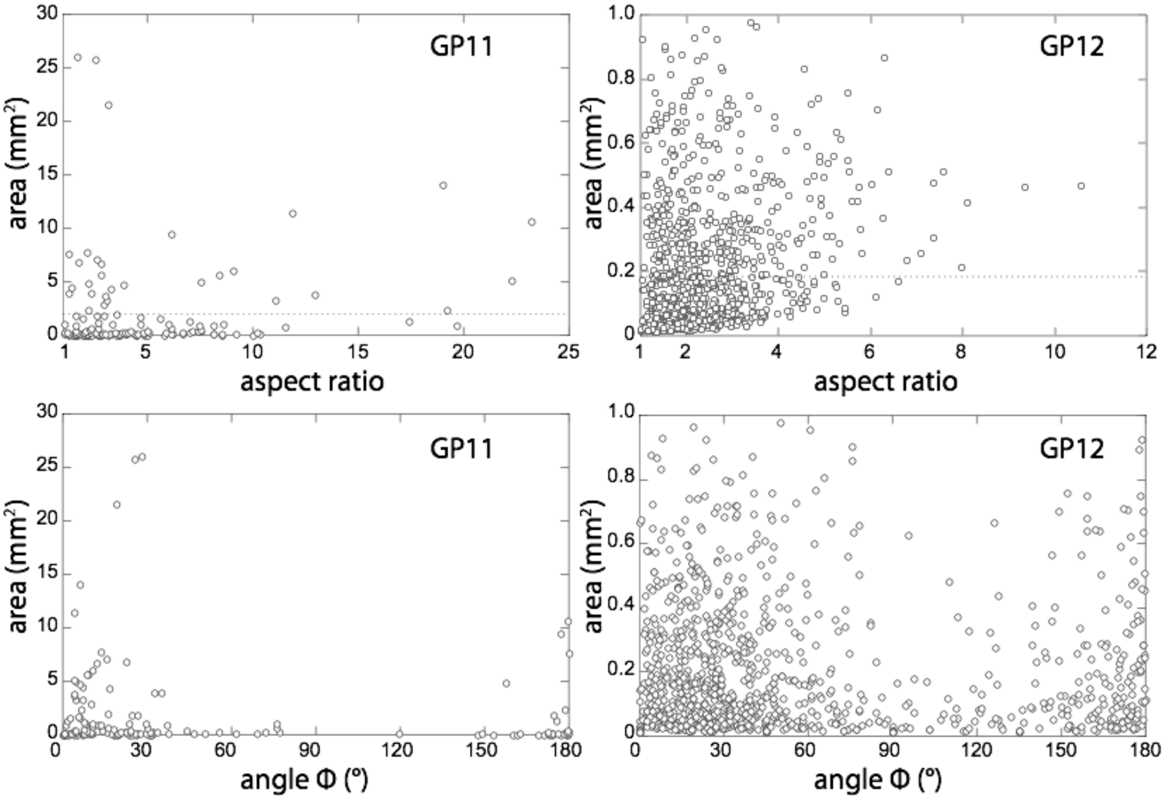

Figure 6: Cross sectional areas of quartz aggregates from sample GP11 and GP12 and the corresponding aspect ratio and orientation φ (derived from best fit ellipses).

4.2 Quartz microstructures

In the weakly deformed mylonite the quartz aggregates are composed of magmatic grains rimmed by recrystallized grains. Recrystallization preferentially starts at the edges of magmatic grains forming core and mantle structures (White, 1976) (Fig.7a). Relict magmatic quartz grains show a sweeping extinction and are commonly segmented by optical subgrain boundaries which occasionally form chessboard patterns (Baeta & Ashbee, 1969, Kruhl, 1996). With increasing strain the fraction of recrystallized grains progressively increases until all magmatic grains are entirely consumed (Fig. 7b,c, 8). The magmatic grain from which recrystallized grains originate will be termed parent grain (Halfpenny et al., 2006).

Sample GP12 (Fig. 9) contains smaller quartz aggregates which are completely recrystallized at lower strain than in the coarse grained metagranodiorite. The recrystallized grain size in GP12 is approximately the same as in the metagranodiorite GP11 as will be shown in detail.

Recrystallized grains generally show a microstructure ranging from interlobate - interlocking to polygonal and square to diamond shaped grains (Fig. 7d,e,f). Grain boundary segments are straight to curved and frequently meet at angles <120°, although at the small scale triple junctions the angle can be close to 120°. Occasionally quadruple junctions are present (Fig. 7e).

4.3 Quartz crystallographic preferred orientation (CPO)

Fully recrystallized aggregates develop a strong CPO. The dominant CPO type is a strong peripheral [c]-axis maximum with an external asymmetry with respect to both reference frames, XZ and xz (Fig. 8,9). The peripheral maximum occasionally grades into a weak straight girdle.
With increasing strain the peripheral [c]-axis maximum strengthens (Fig. 8,9) and the spread in the [c]-axis pole figure decreases.

Bulk CPOs for groups of aggregates have been calculated to be able to compare our results with those of previous studies which were done on quartzites, quartz veins, or polycrystalline material in general (Simpson, 1980; Garcia Celma, 1983; Schmid & Casey, 1986, Dell'Angelo & Tullis, 1989; Law et al.,1990 Stipp et al., 2002; Heilbronner & Tullis, 2006). Aggregates are grouped in a weakly, an intermediately, and a highly deformed part (Fig. 10). Parent grains are not included in the CPO calculation.

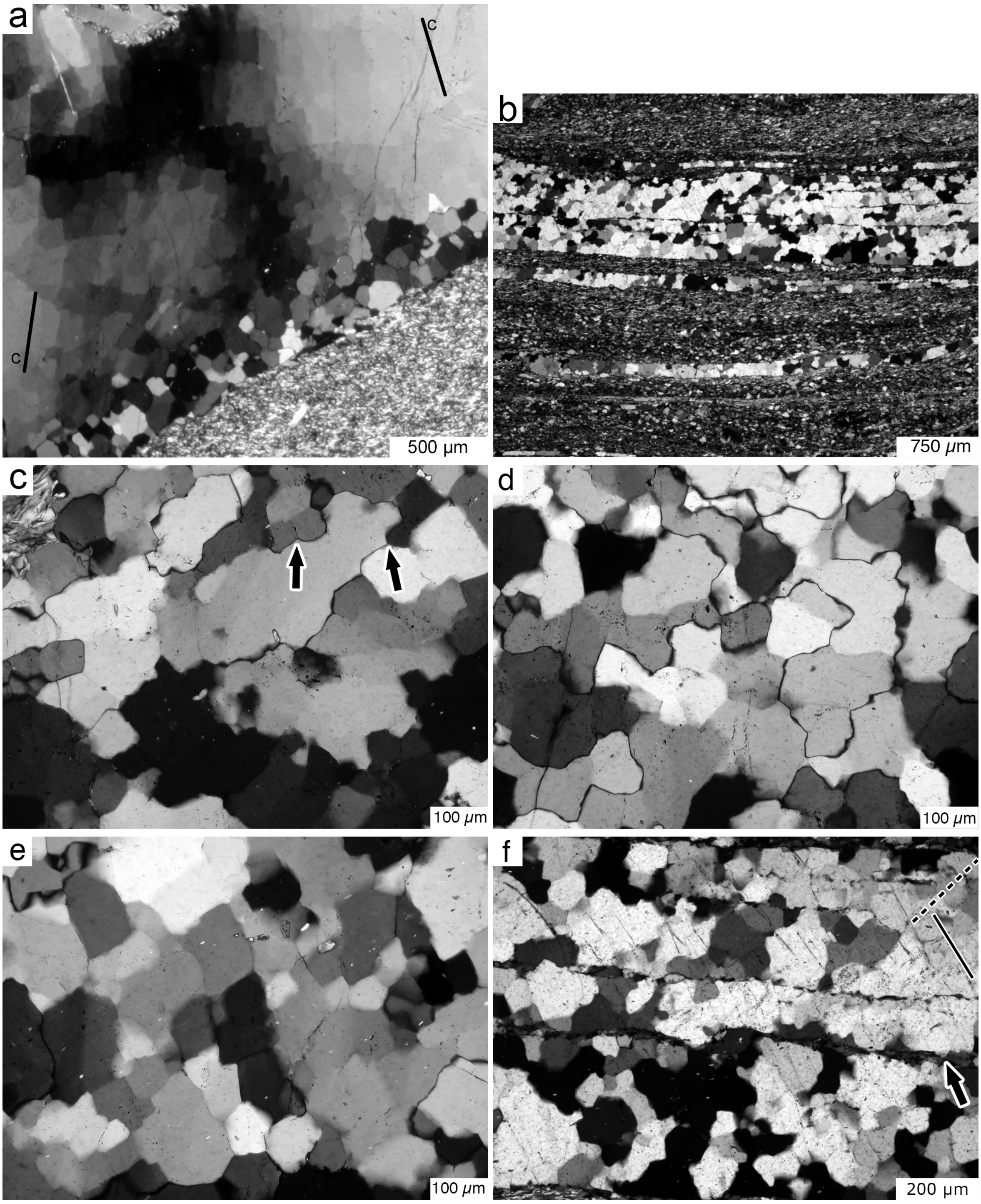

Figure 7: Quartz microstructures: (a) Parent magmatic grain showing chessboard pattern subgrains and recrystallized grains at the margin. Incipient quartz deformation in the mylonite (GP11). (b) Fully recrystallized quartz aggregate in the highly strained part of the mylonite, forming parallel layers with the matrix (GP9). (c) Grains in a partly recrystallized aggregate in the mylonite. Note grains being replaced by grain boundary migration (arrows). Subgrain rotation (GP11) is also common. (d) Slightly lobate microstructure in fully recrystallized aggregate in the mylonite. Note straight grain boundary segments at smaller scale (GP11). (e) Diamond shaped grain boundary

(Figure 7 continued) alignment in fully recrystallized aggregate in mylonite. Grain boundary segments can align across several grains (GP9). (f) Detail of (b) showing a weak oblique preferred orientation of grain boundaries (stippled line) in inclusion rich quartz aggregate. Thin straight inclusion trails with the orientation of the solid line trace late cracks, which crosscut grain boundaries without offset. Some inclusions align along (former) grain boundaries, parallel to the preferred orientation of the grain boundaries and are partly included inside grains (solid line) (GP9).

Intermediately deformed aggregates are in most parts completely recrystallized and oriented at an angle (GP11: ~14 - 25°/ GP12: ~ 22 - 30°) to the shear zone boundary plane. The high strain aggregates are entirely recrystallized and make an angle < 14° (GP11) and < 22° (GP12) to X (Fig. 10).

The bulk CPOs of the weakly deformed aggregates show a broad spread of peripheral maxima about a rotation axis parallel to Y. Single maxima are sub-perpendicular (GP 11), and double maxima are at a small angle (GP 12) to the corresponding foliation (Fig. 10).

The bulk CPOs of the medium strained aggregates show a weak single girdle with a broad peripheral maximum (Fig. 10). The CPO of GP12 can also be regarded as the peripheral part of a cross girdle, composed of separate, differently oriented aggregates. The maximum in GP 11 is slightly inclined against the global sense of shear (Fig. 10).

The bulk CPOs in the most highly strained aggregates are close to identical to the CPOs obtained from single, highly strained aggregates and show a strong externally asymmetric peripheral single maximum inclined with the sense of shear (~70-75°) (Fig. 8, 9, 10). The internal asymmetry is very weak and may resemble a weakly kinked single girdle (Schmid & Casey, 1986, Mancktelow 1987).

The bulk CPO of the entire shear zones is similar to the CPOs measured in the most highly strained aggregates (Fig. 10) in the case of GP11 but shows an asymmetric spread of [c]-axis orientations along the periphery. The bulk CPO of GP12 also shows a spread along the periphery but a main maximum is less pronounced.

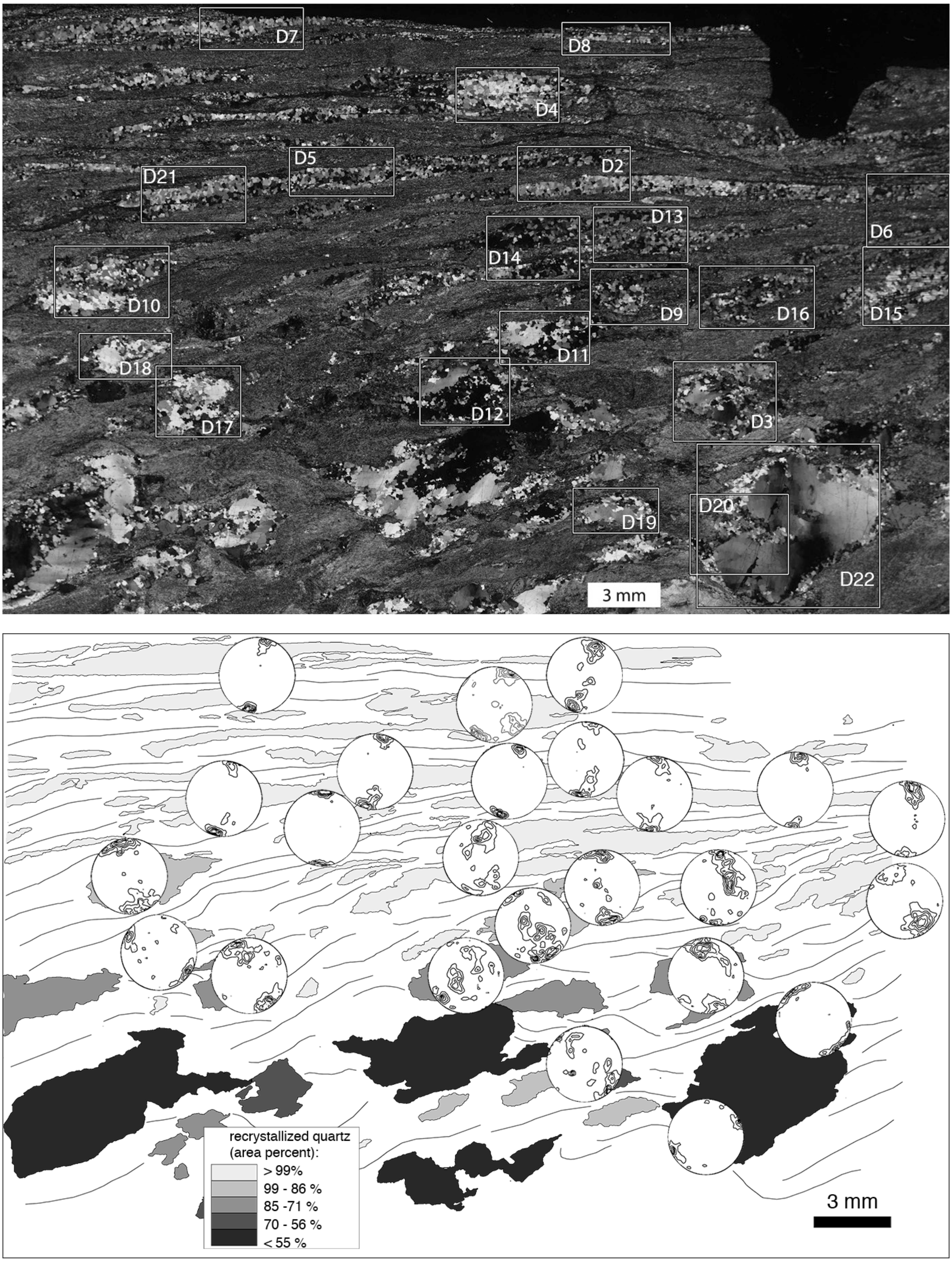

Figure 8: Overview of sample GP11: (a) Thin section of GP11 (crossed polarizers) with CIP sampling sites indicated. (b) Drawing of quartz aggregates and traces of the matrix foliation. Grey values of the quartz aggregates indicate percentage of recrystallized grains. [c]-axis pole figures of recrystallized grains. Contours at 1,2…8 times uniform.

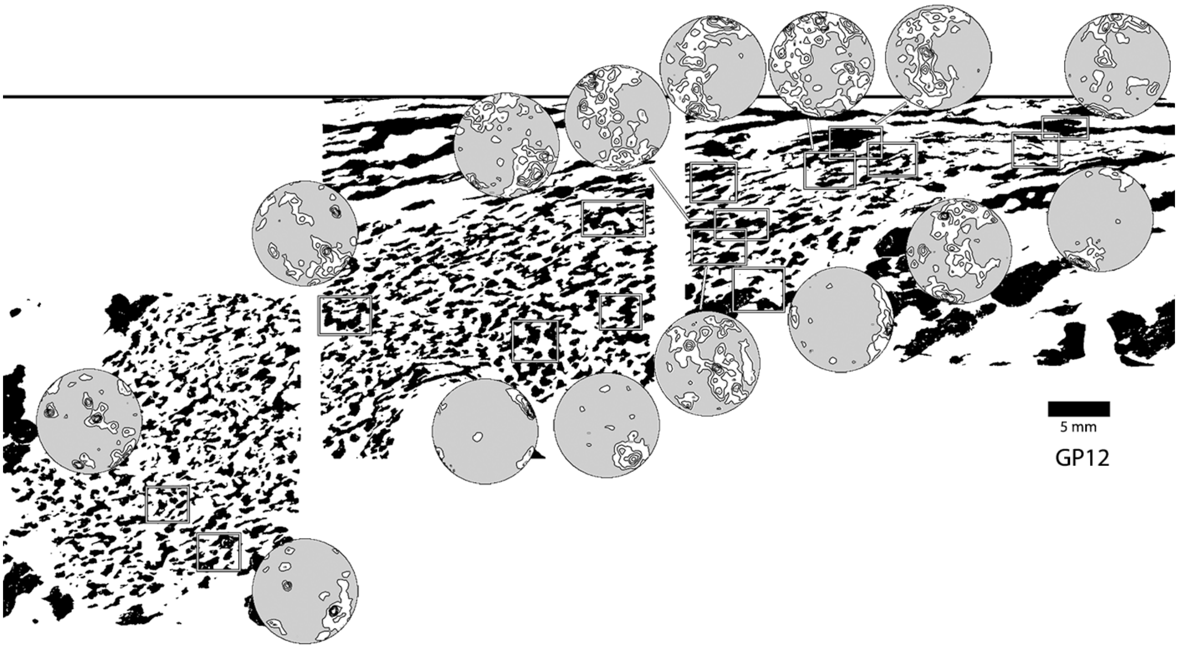

Figure 9: Overview of sample GP12. Quartz aggregates are black. Percentage of recrystallized grains in the small aggregates in the enclave is ~ 94% in the left section, and > 99 % in the right section. [c]-axis polefigures of recrystallized grains. Contours at 1,2…8 times uniform.

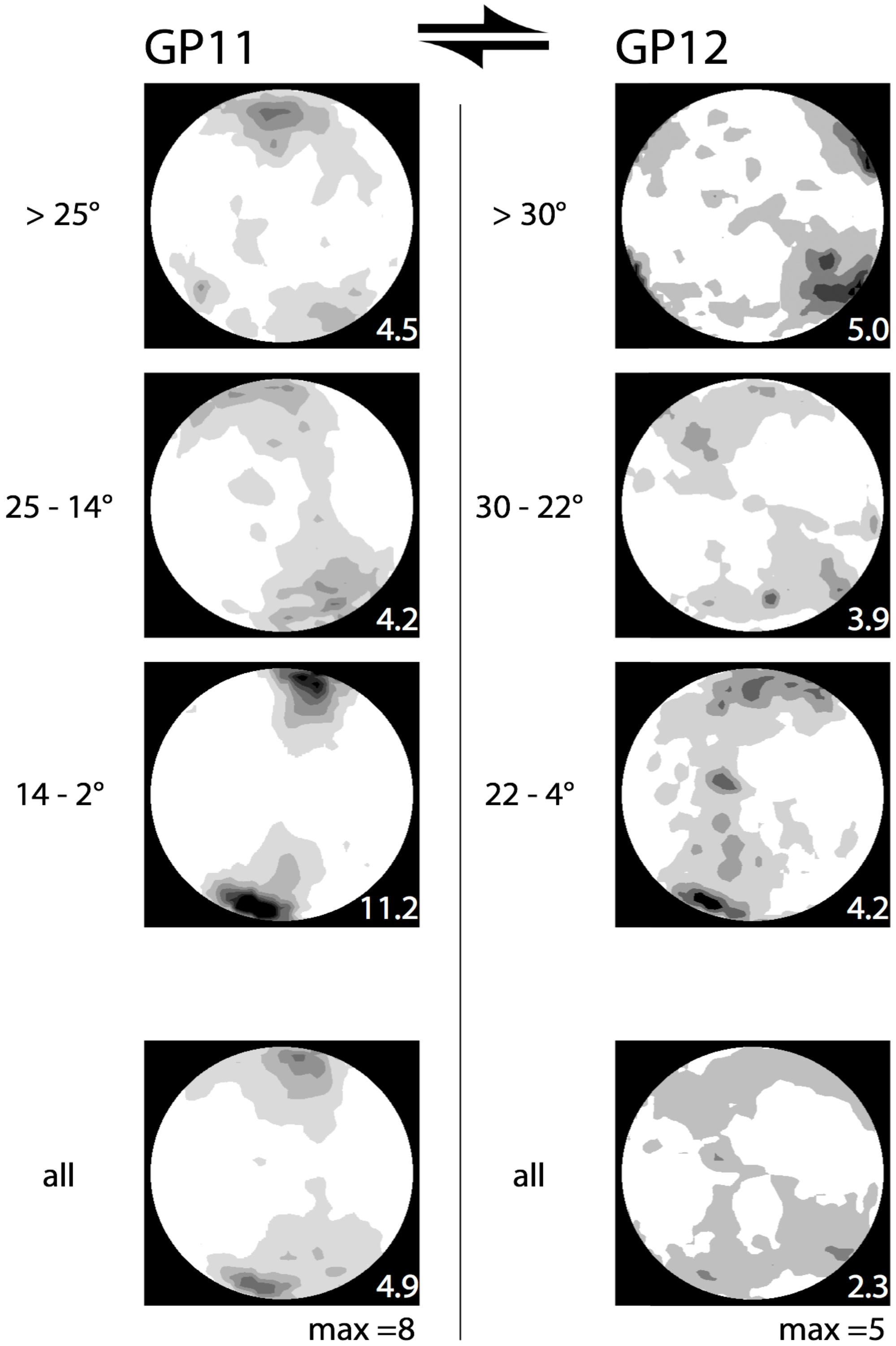

Figure 10: bulk pole figures of GP11 and GP12. Numbers to the left indicate the angle φ between X and X_a. The CPO is calculated from 3 groups of aggregates with φ in the indicated range. All aggregates are oriented with respect to the global reference frame XYZ. The pole figure at the bottom is calculated from all aggregates across the shear zone.

4.4 Quartz grain size

Recrystallized grains have a μ_v(D) of 120 μm and μ_h(D) of 65 μm (Fig. 11a) which remains constant throughout the strain gradient (Fig. 11b). In most cases the grain size has a broad unimodal distribution ranging from approximately 20 - 300 μm with very few grains > 200 μm (Fig. 11a). The number weighted distribution is skewed towards smaller grain sizes.

The grain size in the single-grain-thick-layers (25 - 150 μm), which form at high strain, is approximately the same as in the other quartz aggregates.

The parent grains and the recrystallized grains contain subgrains. Three categories of subgrain sizes were measured in the chessboard-type subgrains. In the non-recrystallized grains equivalent diameters were determined from areas enclosed by subgrain boundaries with μ_h(d) ~ 70 μm and μ_v(d) ~ 100 μm (Fig. 11c). A conversion to 3D was not performed as the measured subgrain boundaries are sub-perpendicular to another and could only be measured in grains with the c-axis subparallel to the plane of observation, and therefore do not represent random samples. Additionally, separate measurements were made on the distances between optical subgrain boundaries which are dominantly parallel and perpendicular to the trace of the c-axis (Fig. 11d). The average distance between boundaries parallel to the basal plane is ~ 70 μm and parallel to the prism plane is ~ 60 μm. An area equivalent diameter of 73 μm can be calculated, if subgrains are assumed to be rectangular with side lengths defined by the average boundary spacing. All of these subgrain determinations yield similar sizes of μ_h(d) around 60 to 70 µm (Fig. 11c,d).

Some of these boundaries are decorated with inclusions which show structures indicative of pinning pinning. The sizes of optical subgrains is difficult to interpret as some may represent large angle grain boundaries and as some are parallel to the basal plane. Subgrain boundaries parallel to the basal plane are usually interpreted as tilt walls formed by edge dislocation of the prism-[c] slip system (e.g. Trepied &Dunkhan, 1980; Kruhl, 1996).

4.5 Particle and surface fabrics

Fabrics are displayed in the XYZ reference frame. The intensity of the fabric can vary laterally within a single quartz aggregate without any change in CPO geometry, grain size, or visible aggregate stretch.

A particle fabric (PAROR) is not pronounced in any of the quartz aggregate whereas a surface fabric (SURFOR) is more common (Fig.12).

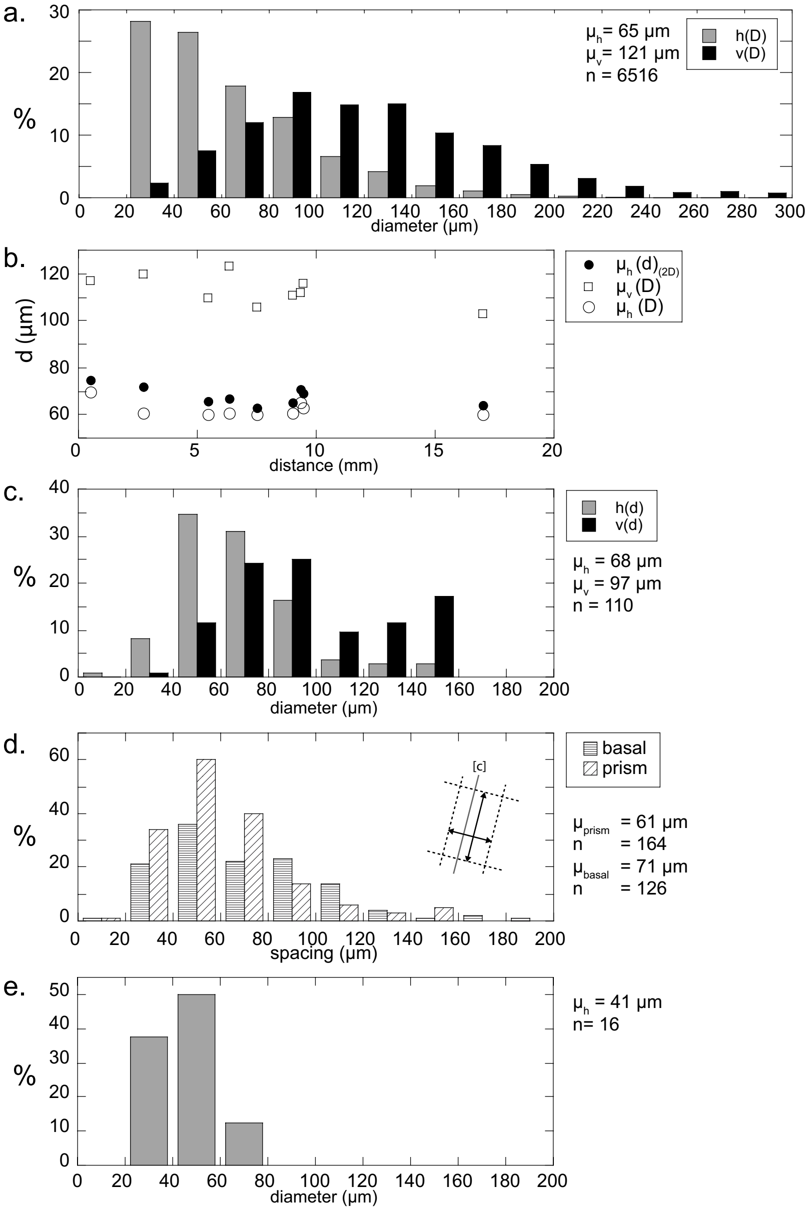

Figure 11: Grain and subgrain sizes: (a) Size of dynamically recrystallized quartz grains v(D) is volume weighted, h(D) is number weighted. Histogram of all grains of all aggregates analyzed in GP11. (b) Average grain sizes of recrystallized quartz as μ_v (volume weighted), μ_h (number weighted) and $\mu_{h(2D)}$ (number weighted 2D) in GP11 obtained from histograms of single aggregates. Distance is in mm from the shear zone center (= 0), same as in Fig. 5 a. (c) Equivalent diameter of areas enclosed by optical subgrain boundaries in parent grains. h(d) is the number weighted, v(d) is the volume weighted distribution of equivalent diameters of circles. (d) Distances between optical subgrain boundaries in parent grains, parallel to the trace of the basal and the prism plane. (e) Subgrain sizes in recrystallized grains, determined from EBSD maps.

Inside recrystallized grains the density of optical subgrain boundaries is low. There are usually at most 1 to 2 present in the largest grains. The subgrains were derived from EBSD maps and their diameters vary between 20 and 65 μm (Fig. 11e). In that case only subgrains were selected which are bound by at least two subgrain boundaries with a misorientation angle smaller 7.5°. Although they are relatively infrequent, they are assumed to represent the size of subgrains forming during dynamic recrystallization.

The anisotropy of the particle fabric is low and the bulk axial ratios b/a_{bulk} obtained from the particle projection function are generally larger than 0.80 with an average of b/a_{bulk} of 0.89, which is close to isotropic (= 1). Rose diagrams of grain long axes show a stronger preferred orientation (Fig. 12). Rose diagrams of the surface fabric of recrystallized grains typically grades from monoclinic to orthorhombic and always shows an external asymmetry (Fig. 12). One maximum aligns preferentially at an angle (< 40°) relative to X_a. A second maximum usually develops at a high angle ~ 70 - 90° to the main maximum (Fig. 12). The most consistent description is found with respect to the local reference frame X_aYZ_a.

The orthorhombic to symmetric geometries of surface fabric rose diagrams often show two constrictions between the maxima while the monoclinic type has one constriction which is close to normal to the [c]-axis maximum (Fig. 12). The orientation of the minor or major constriction coincides with the orientation of the [c]-axis maximum. The maximum in the rose diagram is rotated in the same sense the [c]-axis maximum is rotated with respect to Z_a (e.g. GP11-1D2/15, Fig 12, 13).

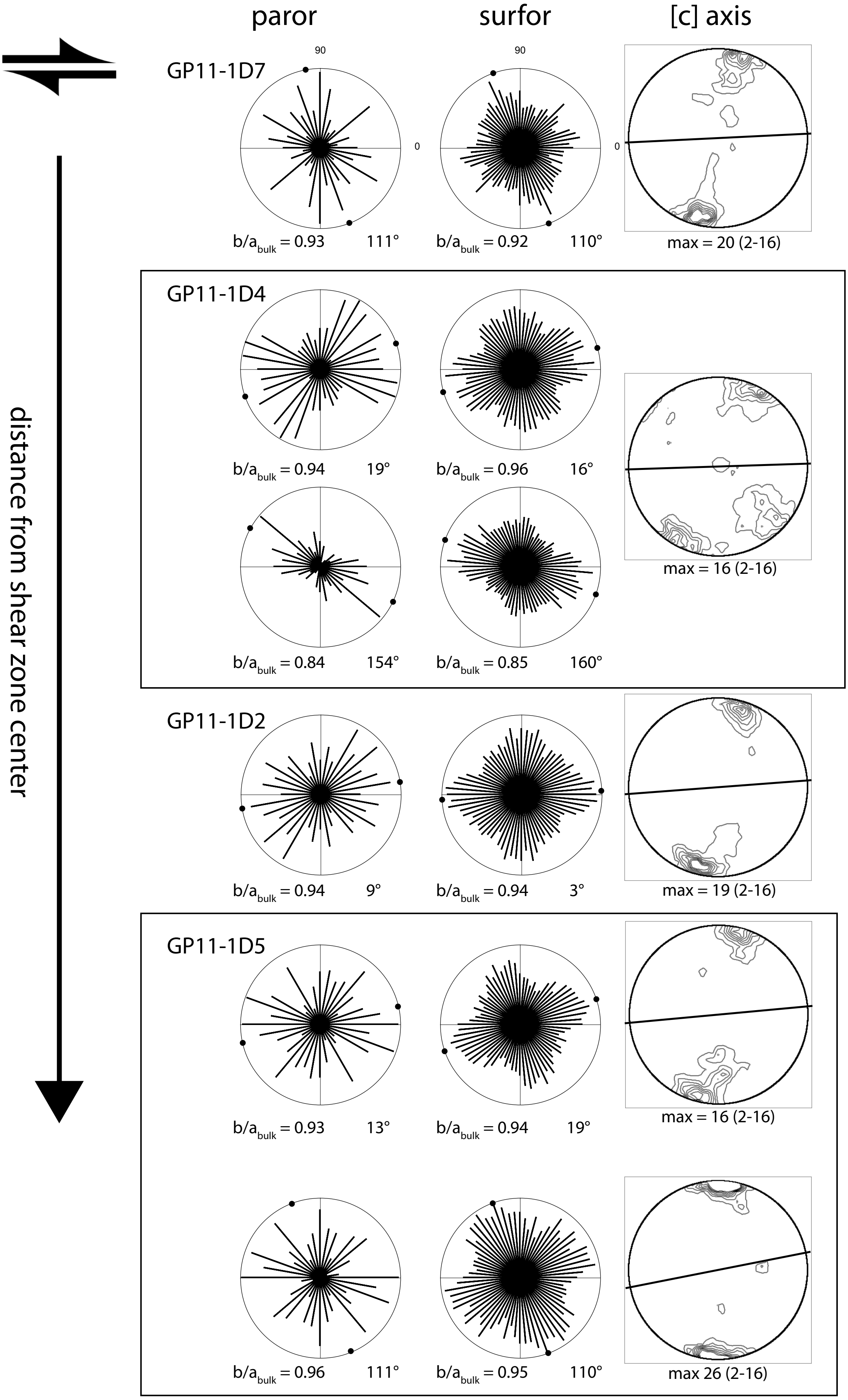
paror
surfor
[c] axis
GP11-1D7
90
0
90
0
b/a_bulk = 0.93 111°
b/a_bulk = 0.92 110°
max = 20 (2-16)
GP11-1D4
b/a_bulk = 0.94 19°
b/a_bulk = 0.96 16°
max = 16 (2-16)
b/a_bulk = 0.84 154°
b/a_bulk = 0.85 160°
GP11-1D2
b/a_bulk = 0.94 9°
b/a_bulk = 0.94 3°
max = 19 (2-16)
GP11-1D5
b/a_bulk = 0.93 13°
b/a_bulk = 0.94 19°
max = 16 (2-16)
b/a_bulk = 0.96 111°
b/a_bulk = 0.95 110°
max 26 (2-16)
distance from shear zone center

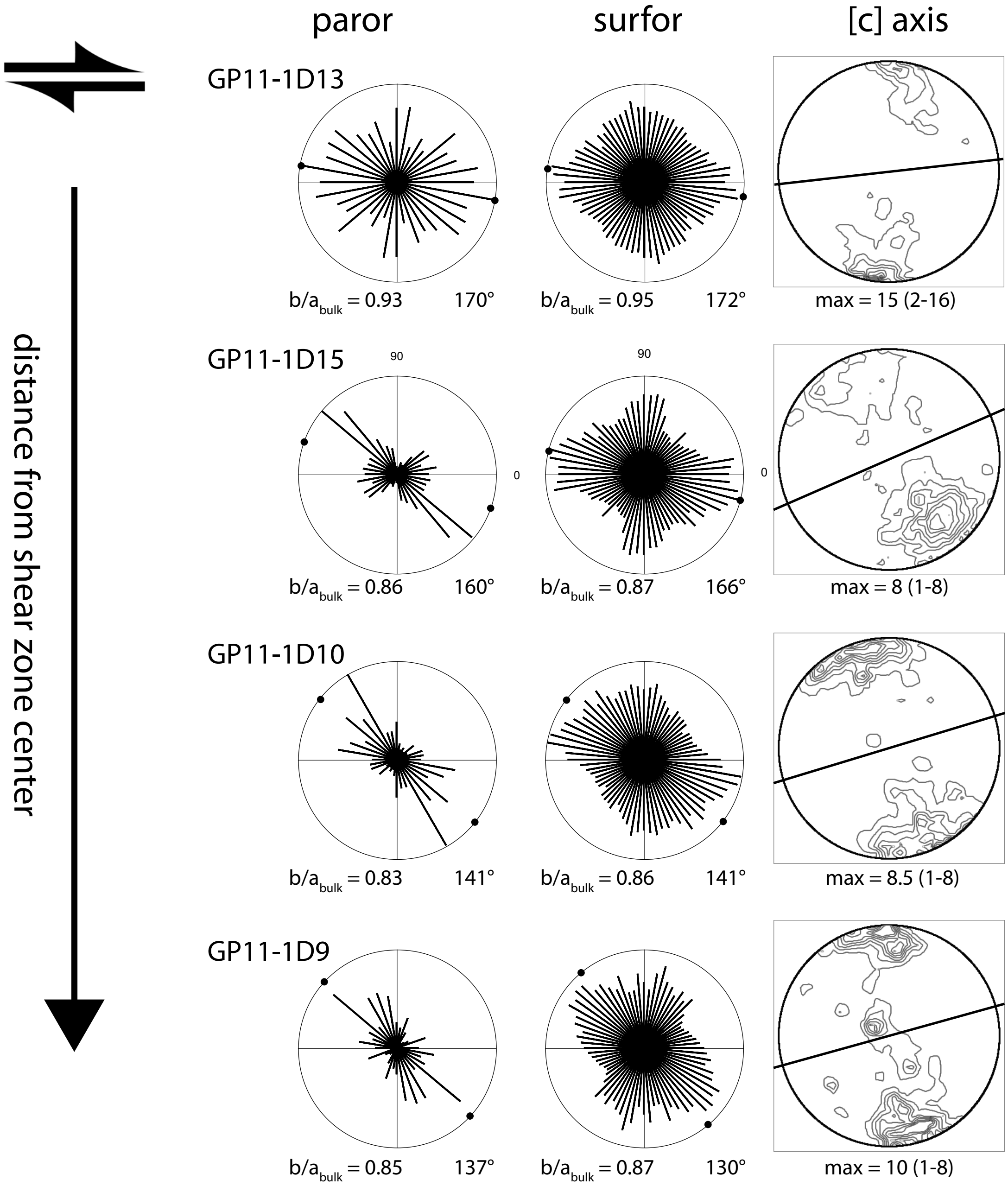

Figure 12: Overview of part of the data of GP11: Sampling sites are indicated in Fig. 8. Samples are ordered with increasing distance from the shear zone center. Rose diagrams of particle (PAROR) and surface (SURFOR) farbic, b/a$_{bulk}$ and orientation, [c]-axis pole figure. Site GP11-1D4 has two different fabric diagrams each for one of the orientation domains. Site GP11-1D5 contains two aggregates, and therefore two sets of fabric diagrams and pole figures are shown. Maxima are indicated, contours are 2,4,…16 and 1,2…8 times uniform distribution. Black line in the pole figure is the aggregate long axis orientation φ. (see Appendix C for a more complete list of analyzed sites)

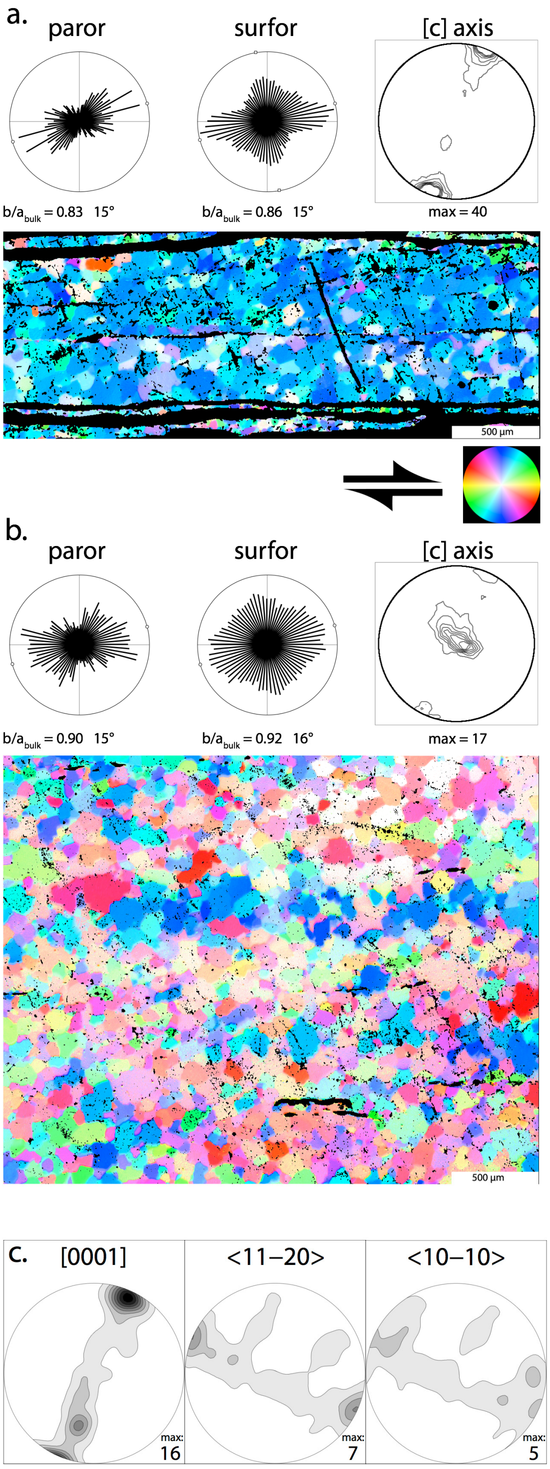

Figure 13: CPO and fabrics in a highly deformed mylonite, (GP9): Rose diagrams of particle and surface fabrics, [c]-axis pole figure and [c]-axis orientation images of fully recrystallized quartz aggregates. Axial ratio b/a_{bulk} and the angle of the bulk orientation obtained from the projection function. Pole figures contoured at 2,4…16 times uniform distribution. (a) Typical quartz aggregate with a peripheral [c]-axis maximum and an asymmetric particle and surface fabric. (b) Aggregate with [c]-axes preferentially oriented in the Y-direction and a weaker shape fabric. (c) EBSD pole figures of a recrystallized quartz layer similar to (a) (GP9-4). Kernel half width 7.5 degree. Contours at 1,3,5… times uniform distribution.

5. Detailed observations

In the following section the geometric relations of the polefigures, the fabrics and the quartz aggregates is analyzed in more detail.

5.1 Rotation of the polefigures

The most common CPO is represented by a polefigure with a single peripheral [c]-axis maximum (Fig. 13a), and <a> axes forming a girdle perpendicular to the [c]-axis maximum with a weak maximum at the periphery (Fig. 13c). Occasionally <m> axes occupy the peripheral position. The area measured in the EBSD to obtain the CPO is smaller than the area usually used for CIP and the kernel width used for calculating the ODF is 7.5° for the EBSD data and 5° for the CIP. Therefore the value of the maxima of polefigures cannot be compared.

In the mylonite the position of the polefigure maximum changes relative to the reference frames (XYZ, X_aYZ_a) with increasing strain. In the highly strained mylonite, where the global and the local reference frame are essentially parallel, the orientation of the polefigure remains constant. The polefigure maximum is consistently inclined with the sense of shear with respect to the shear zone boundary as well as with respect to the aggregate long axis (Fig. 14a,b, 10, 12,) in the highly strained part.

At aggregate orientations of $\varphi > 15°$, the CPO maximum is preferentially oriented at $\beta \geq 90°$ with respect to the aggregate orientation (Fig. 12, 14a,b). Towards a smaller angle φ, β decreases below 90° (Fig. 12, 14a,b) when quartz aggregates become subparallel to the shear zone boundary (X).

In GP12, φ decreases towards the shear zone center and β and θ decrease accordingly but a) two distinct groups are distinguishable (separated at d ~10 mm or $\varphi \sim 15°$) and b) a smaller relative rotation occurs inside these groups for the angle β (c-axis with respect to aggregate) (Fig. 14b). This behavior is less obvious in GP11 which shows a greater range in the distribution of β and θ (Fig. 14a).

In both samples (GP11, GP12) the total change of θ is larger than that of β, i.e. the [c]-axis maximum rotates less with respect to the aggregate than with respect to the shear zone boundary, though both rotate with increasing strain synthetically with the local sense of shear (Fig. 15, 14a,b,).

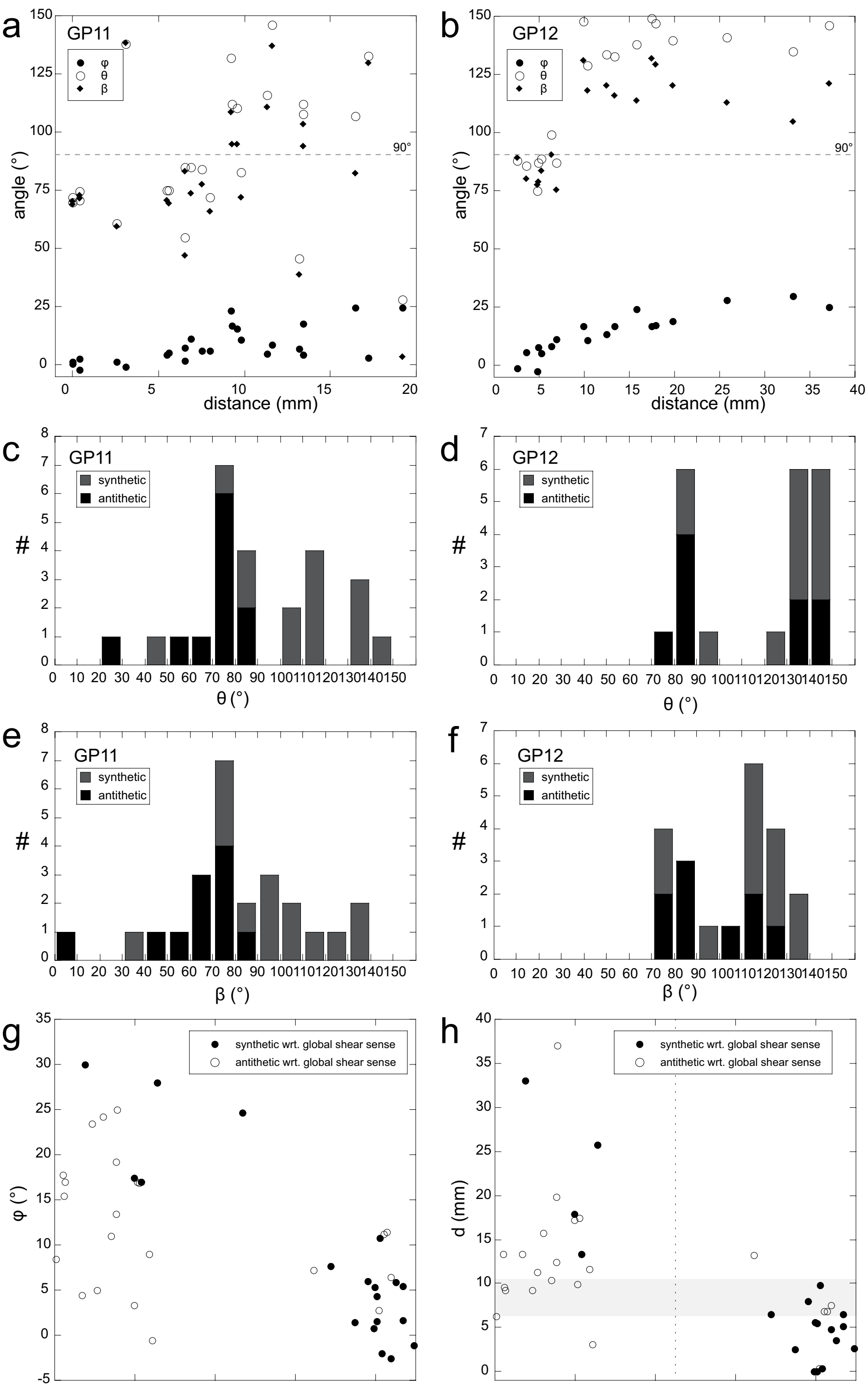

Figure 14: (a),(b) Variation of the angles β,θ and φ for GP11 and GP12 with distance from the shear zone center (= 0). (c,d) Histograms of CPO maxima orientations with respect to the global reference frame (θ). Antithetic and synthetic shear senses are indicated and determined from the fabric asymmetry and other available shear sense criteria. (e,f) same as c,d but with the CPO maxima with respect to the local reference frame (β). (g) Orientation of β - 90 (trace of the basal plane, see text) with respect to φ. (h) Orientation of β - 90 (normal to the c-axis maximum) relative to the distance from the shear zone center. For g,h the different symbols indicate a synthetic or antithetic shear sense in the aggregate. Data from both, GP11 and GP12.

At high strain, the polefigure maxima show identical angles. (Fig. 12, 13, 14a,b). $\beta = \theta \sim 70°$ remains stable and do not change with increasing strain, i.e. it is considered to be a stable end orientation of the polefigure for these mylonites, because it occurs only in the highest strain regions before the quartz layer start to disintegrate (see also Appendix D).

The [c]-axis polefigures of parallel layers, one and multiple grains thick, do not show a difference in geometry (Fig. 16) and β is 65° and 70° respectively. The values of the polefigure maxima are 16 and 19, indicating a slightly higher strength of CPO in in the multiple grains thick layer.

In the case of perturbations of the flow plane in the fully recrystallized layered parts of the shear zone (e.g. flow around garnet or other more or less rigid inclusions) the polefigure rotates with the layer orientation (Fig. 17). The angle β remains ~70° while θ varies up to 30° with the local layer orientation.

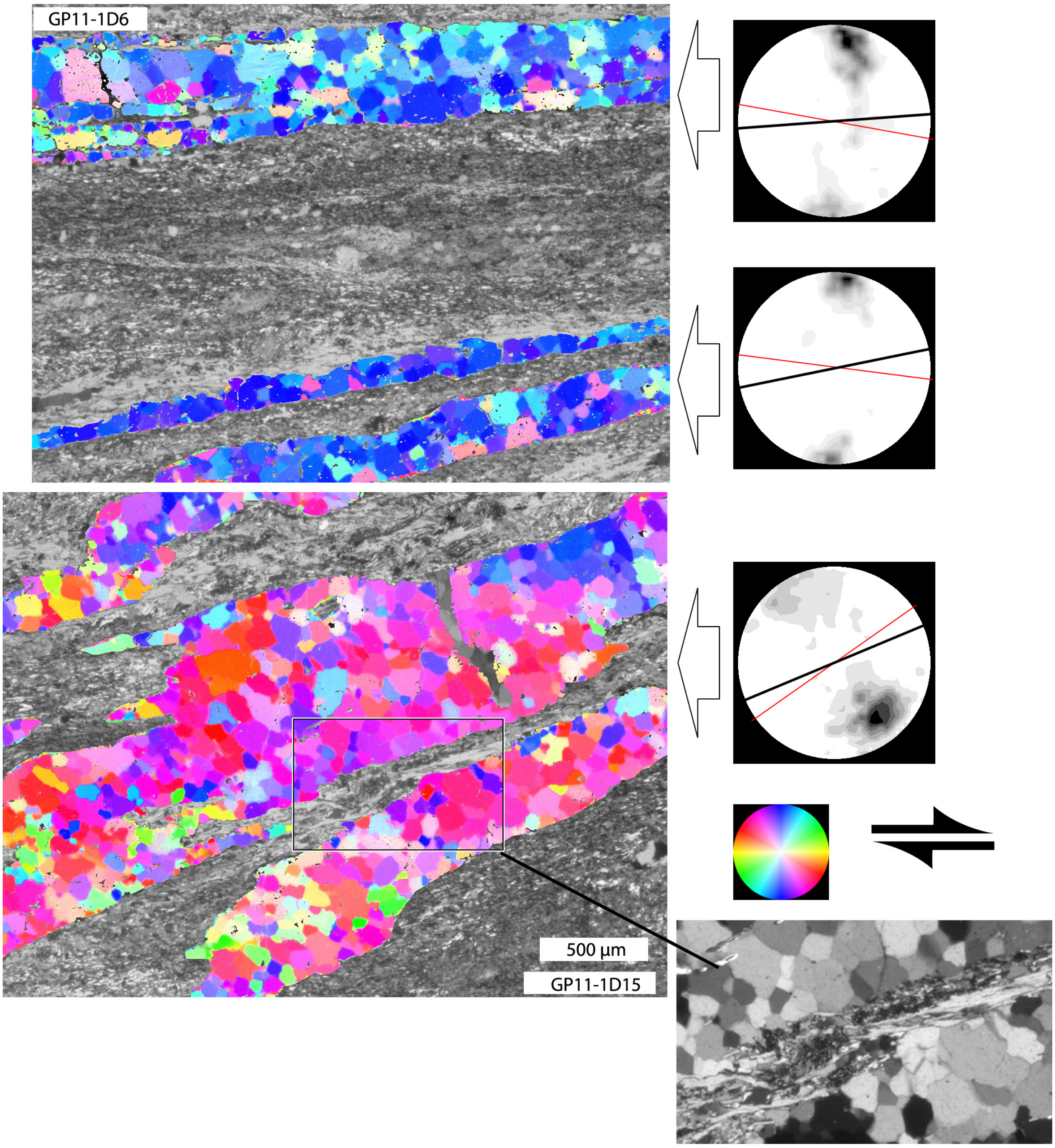

Figure 15: Reorientation of the CPO across a strain gradient: [c]-axis orientation images of quartz aggregates progressively rotated into parallelism with the shear zone plane. The red line in the pole figures indicates aggregate long axis, and the black line indicates the normal to the CPO maximum. The indicated shear sense is the global shear sense.

The fabric developed in the lower domains is caused by the local inverse shear sense. Note the mica seams between the lower two quartz aggregates indicating a sinistral sense of shear between the layers. See Fig. 12 for details of the CPO and the fabric of GP11-1D15.

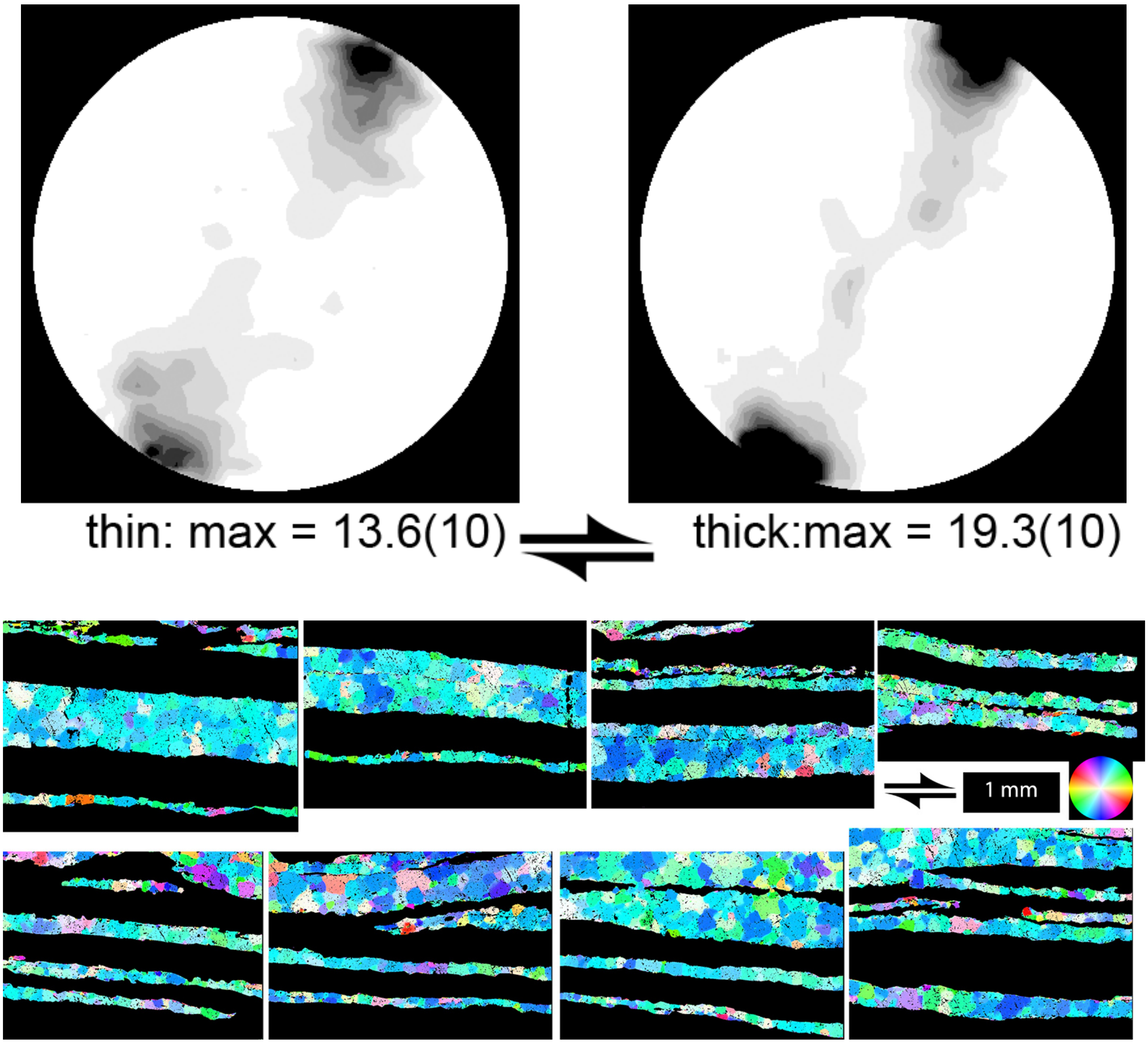

Figure 16: Comparison of polefigures obtained from a thin layer (left) and a thick layer (right) in GP9. The thin layer is ~100 μm (~ 1 grain) thick and directly adjacent and parallel to the thick layer which is several grains thick (~300-600 μm). Total length of measured layers is about 22 mm. The maximum of the polefigure is indicated, the displayed maximum is 10 and gray values correspond to 1,2..10 times uniform distribution. [c]-axis orientation images of the adjacent thin and thick layers. Layers are laterally continuous but not overlapping due to small sampling gaps. (see Appendix D)

5.2 Special polefigures

A less abundant polefigure type is a [c]-axis maximum which spreads from the center of the pole figure (Y-maximum), towards 135° and has two independent peripheral minor maxima at ~65°.Such Y-maxima only occur in certain domains. Parent grains that have a [c]-axis orientation close to the Y-direction and that are suitably oriented for prism <a> glide show Y-orientations in the recrystallized rims (Fig. 8, GP11-1D12/D14).

5.3 Relationship between parent and recrystallized grains

The relationship between recrystallized grains, parent grains, and matrix will be described in more detail using the site GP11-1D20/22 of the low strain part of GP11 (Fig. 18).

The porphyroclast (parent grain) shows a chessboard pattern (Fig. 7a). The CIP color look-up table in figure 17 is in that case not suitable to highlight the orientation difference that defines the chessboard pattern.The [c]-axis orientation within the parent grain is rotated about 30°around Y and two main domains (pg1 and pg2) can be defined (Fig. 18). The matrix foliation wraps around the porphyroclast (Fig. 8, 18). In the lower left part the foliation is deflected by a local micro-shear-zone oriented at 145° to X with a synthetic sense of shear with respect to the global shear sense (developed between a K-feldspar porphyroclast and the quartz aggregate), and in the upper left part, an antithetic micro-shear zone is present.

Around the parent grain a thin mantle of recrystallized grains is formed, the width ranging from 1 to a few grains (Fig. 18). The [c]-axis orientation in the mantle can be subdivided into three sectors with different angular relationships to the parent grain. Recrystallized grains in the mantle in the upper left and upper right parts (facing the more highly deformed matrix) have a peripheral c-axis maximum rotated with respect to the parent grain orientation against the global shear sense (Fig. 18, domain 3, 4). In the lower left of the mantle, which is bounded by a local micro-shear-zone, a peripheral maximum is rotated with respect to the parent grain orientation synthetically with the local shear sense but at a larger angle than normal (Fig. 18, domain 1). The [c]-axis orientation in the lower right part shows a dispersion towards steeper inclinations and a smaller rotation against the global sense of shear (Fig. 18, domain 5). In all cases the peripheral maximum of the recrystallized grains is oriented at an angle of 70 to 90°with respect to the matrix around the quartz aggregate and is strictly related to the local kinematics of the matrix.

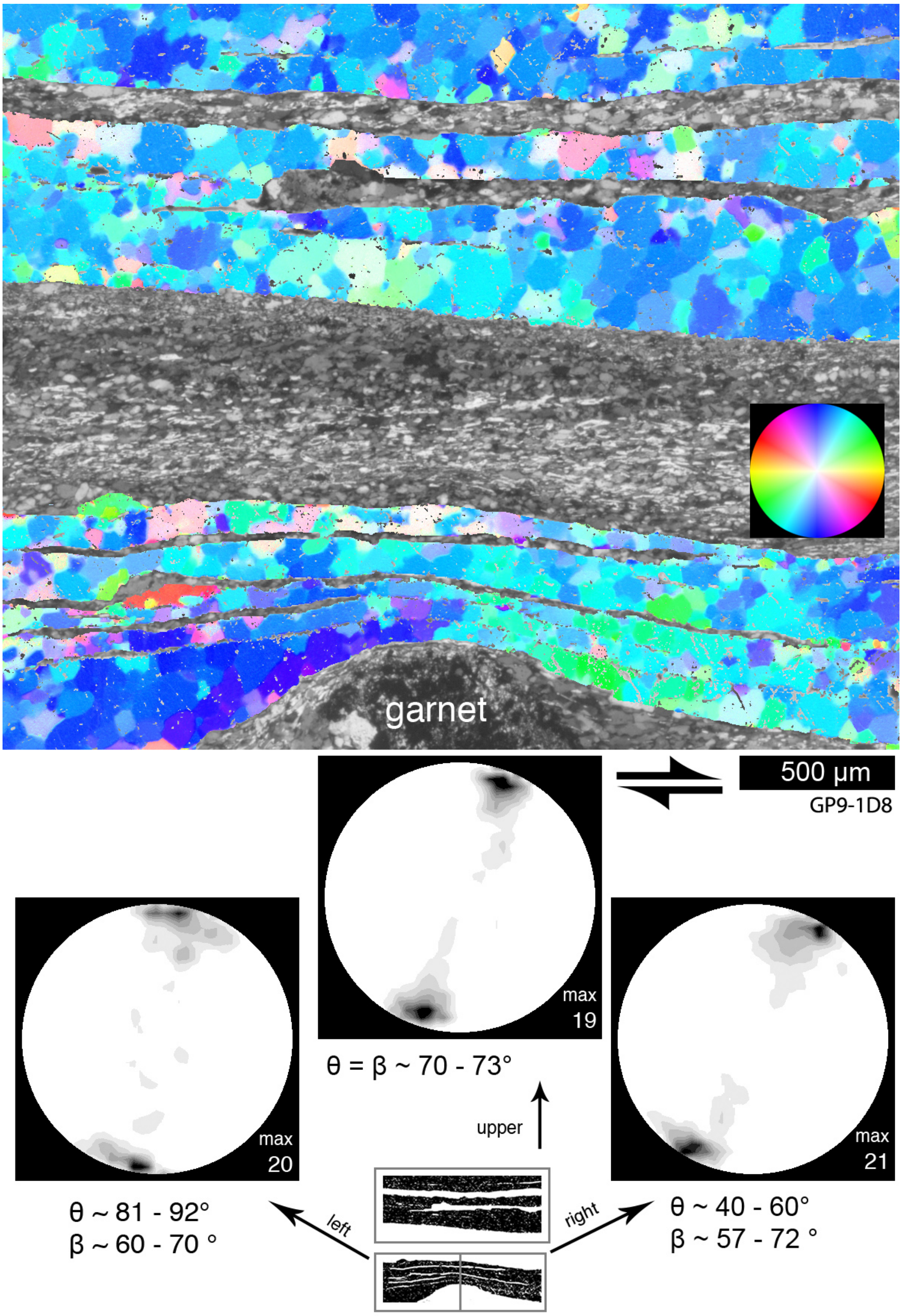

Figure 17: Local rotation of the CPO: [c]-axis orientation image of recrystallized quartz aggregates in a highly strained part of GP9. The layers are parallel to the matrix and change their orientation around a garnet porphyroclast. Note the local orientation deviation of quartz [c]-axes. Pole figures of upper layers and left and right part of the lower layer. The angle θ changes with the orientation in the lower layer, β remains approximately constant at 70°.

As the matrix wraps around quartz aggregates there are domains where the distribution of the c-axes of recrystallized grains shows a misorientation gradient with respect to the parent grain and the CPO of recrystallized grains can be considered as a dispersion of the parent grain orientation (Fig. 18, domain 2,4). This situation would normally be interpreted as host-controlled recrystallization (by progressive subgrain rotation). However, for the same clast, other domains show a considerable misorientation of recrystallized grains with respect to the parent grain and no gradient in misorientation of recrystallized grains (domains 1, 3, 5, Fig. 18). Thus, the host controlled recrystallization only occurs where the parent grain is suitably oriented for a dispersion of its orientation in the local kinematic framework.

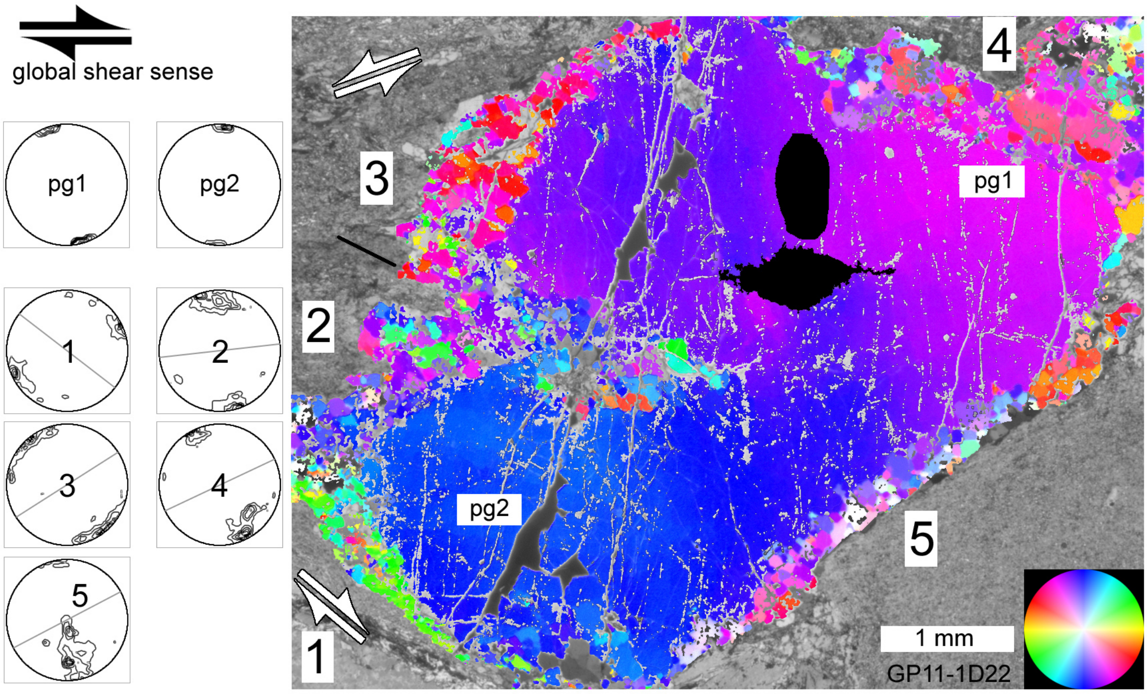

Figure 18: (GP11-1D22) [c]-axis orientation image: Incipient recrystallization of a magmatic porphyroclast showing lattice rotation of ~30° in the parent grain orientation. Two orientations pg1 and pg2 are separated. Orientation of recrystallized grains at the margins are determined by the local shear sense in the matrix and are shown in pole figures of the corresponding sectors. Global shear senses are indicated by black arrows, local shear senses by white arrows (For locality and trace of the local foliation see Fig. 8). Stippled lines in pole figures indicate the local foliation plane

5.4 Local and global shear sense

The global shear sense was determined by the deflection of the foliation of the shear zone, whenever available SC'-shear bands, and, where possible, marker offsets (GP11). The local shear senses have been established based on independent shear sense indicators (sigma clasts of mica or plagioclase, drag of mica seams e.g. Simpson & Schmid, 1983; Passchier & Trow, 1996) which are then compared with the shear senses indicated by the CPO and the fabric (e.g. Behrmann & Platt, 1982; Law et al., 1986; Schmid &Casey, 1986; Mancktelow, 1987). The interpretation of the latter depends on the chosen reference frame (e.g. Lister & Williams, 1979) and may be ambiguous in the case of weak CPOs (Passchier, 1983).

The CPOs of the Gran Paradiso mylonites have a peripheral [c]-axis maximum rotated synthetically with the local shear sense so that the angle β is < 90°. The [c]-axis maximum rotates less with respect to the local reference frame as long as X and X_a are not parallel. In other words, while β decreases from 5 to 15 mm by an angle of ~40-50°, θ decreases by an angle of 50-70°.

The CPO and fabric are in most cases consistent with the local sense of shear.
Three cases can be distinguished: 1) In the most highly deformed parts, both, the local CPO and SPO show the global shear sense of the shear zone. 2) In the intermediate parts (φ >15°), most aggregates show a shear sense contrary to the global shear sense, consistent with the CPO and fabric. 3) Few aggregates with φ ~5-15° show a local CPO consistent with the global shear sense while a weak fabric indicates the opposite shear sense (e.g. GP11-1D13) (Fig. 12).

Figures 14c-f show histograms of β and θ. Two peaks are present at ~70-80° and 110-130°. The gap between the peaks is smaller in the β histogram. Most aggregates with an antithetic shear sense (with respect to the global shear sense) are found at angles $\beta > 90°$ or $\theta > 100°$.

The relation of the synthetic and antithetic shear senses with respect to the distance or φ are expressed as a function of β - 90 in Figure 14g,h. As the polefigures form peripheral [c]-axes maxima, β - 90 gives the orientation of the trace of the basal plane. Below a distance d ~ 5-10 mm which corresponds to an angle φ ~ 10-15° aggregates show a synthetic sense of shear and above which most aggregates show an antithetic sense of shear (Fig. 14 g,h).
If β is > 90° the fabric preferentially shows an asymmetry corresponding with a shear sense opposite to the global shear sense (Fig. 12, 15).

5.5 Relation of polefigure geometry and the fabrics

Surface and particle fabric seem not to be independent of the polefigure geometry. Aggregate GP11-1D4 is found in the highly strained part of the shear zone, elongated parallel to the shear plane X and X_a (Fig. 8, 19). The aggregate consists of two separate domains with contrasting fabrics and polefigures. The bulk CPO shows two peripheral maxima oriented at about 60° and 140°. The stronger one at 60° is consistent with the global shear sense despite being more inclined than the usual polefigures (70°) measured in the high strain part. Each of the two maxima originates from a separate domain. The fabric of each domain shows an asymmetry corresponding with the domain polefigure in the relation described earlier. The orientation of the maxima of the bulk fabrics of each domain make an angle to the polefigure maximum (rotating the fabric maximum onto the polefigure maximum counter-clockwise is positive and against the sense of shear) of 40° (SURFOR) and 45° (PAROR) in the domain with $\beta < 90°$ and -20° (SURFOR) and -10° (PAROR) in the domain with $\beta > 90°$ (Fig. 12, 19). These domains correspond to those aggregates which show a synthetic or antithetic shear sense, respectively.

In summary the relation between the polefigure, the fabric and the sense of shear for two different typical aggregates is summarized in Figure 20a,b.

In an aggregate where φ is small, the polefigure maximum is inclined with the sense of shear ($\theta = \beta < 90°$). The shear sense is the same as the global shear sense. The characteristic shape has an asymmetry consistent with the shear sense and with the polefigure.

In an aggregate with $\varphi > 15°$ the polefigure maximum is inclined against the global shear sense ($\theta > 90°$) but with the local shear sense ($\beta < 90°$). The local shear sense is opposite to the global shear sense. The characteristic shape is again consistent with the local shear sense and the polefigure.

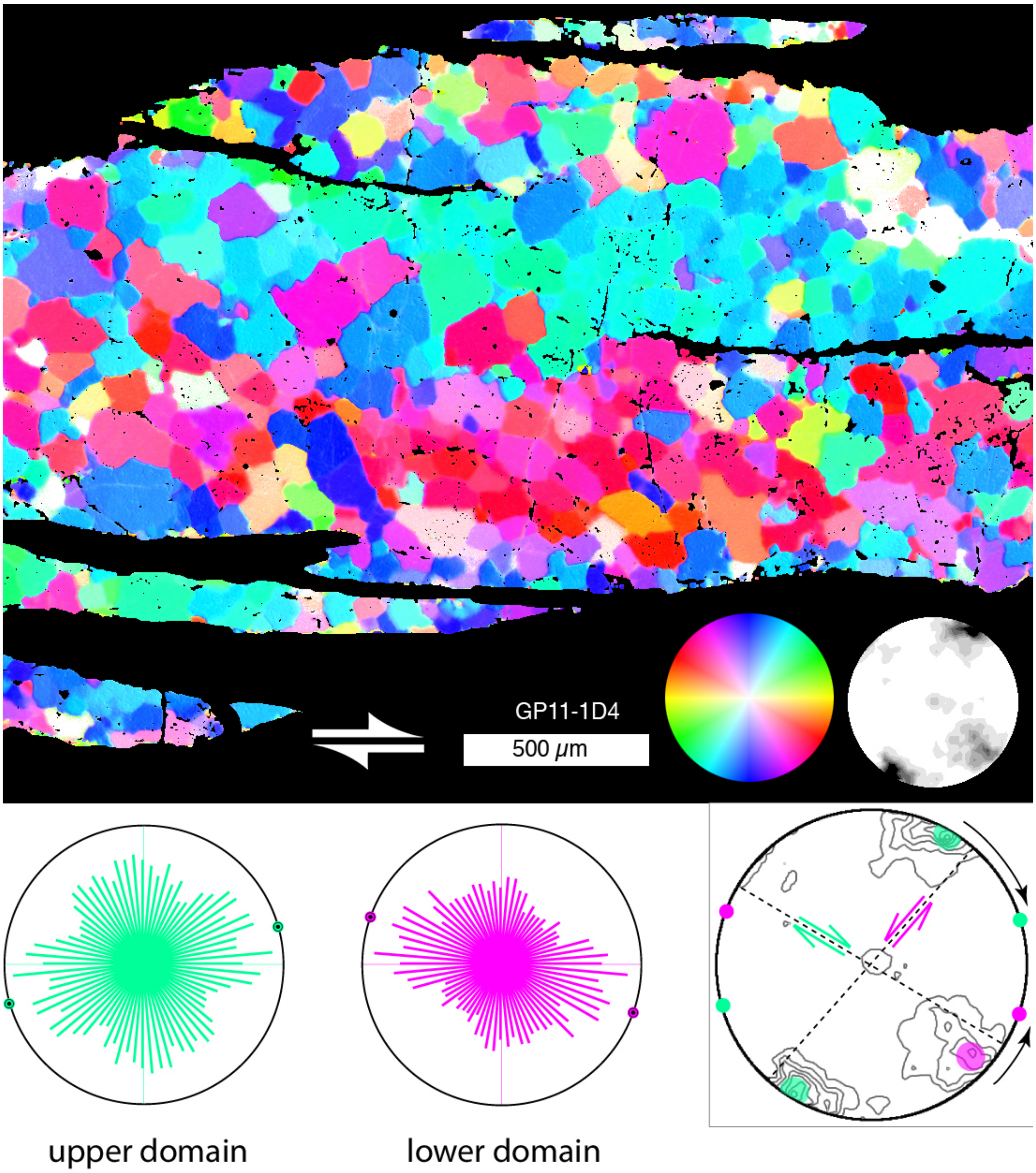

Figure 19: [c]-axis orientation image of recrystallized quartz aggregate from the highly strained mylonite (GP11-1D4). The global shear sense is dextral, corresponding with [c]-axis orientations showing blue-greenish colors (stronger peripheral maximum of the pole figure). Note the oblique fabric in the red domain, inclined against the global and main local sense of shear. SURFOR rose diagrams of the upper and lower domain. The polefigure shows the maxima of each domain, the plane perpendicular to the maxima (= basal slip plane, stippled line), the maxima of the projection function of the surface elements (solid dots). The rotation of the "surface" maxima relative to the polefigure maxima is in both domains synthetic with respect to the inferred sense of slip on the basal slip plane. The sense of slip is synthetic with the global shear sense in the upper domain and antithetic in the lower domain.

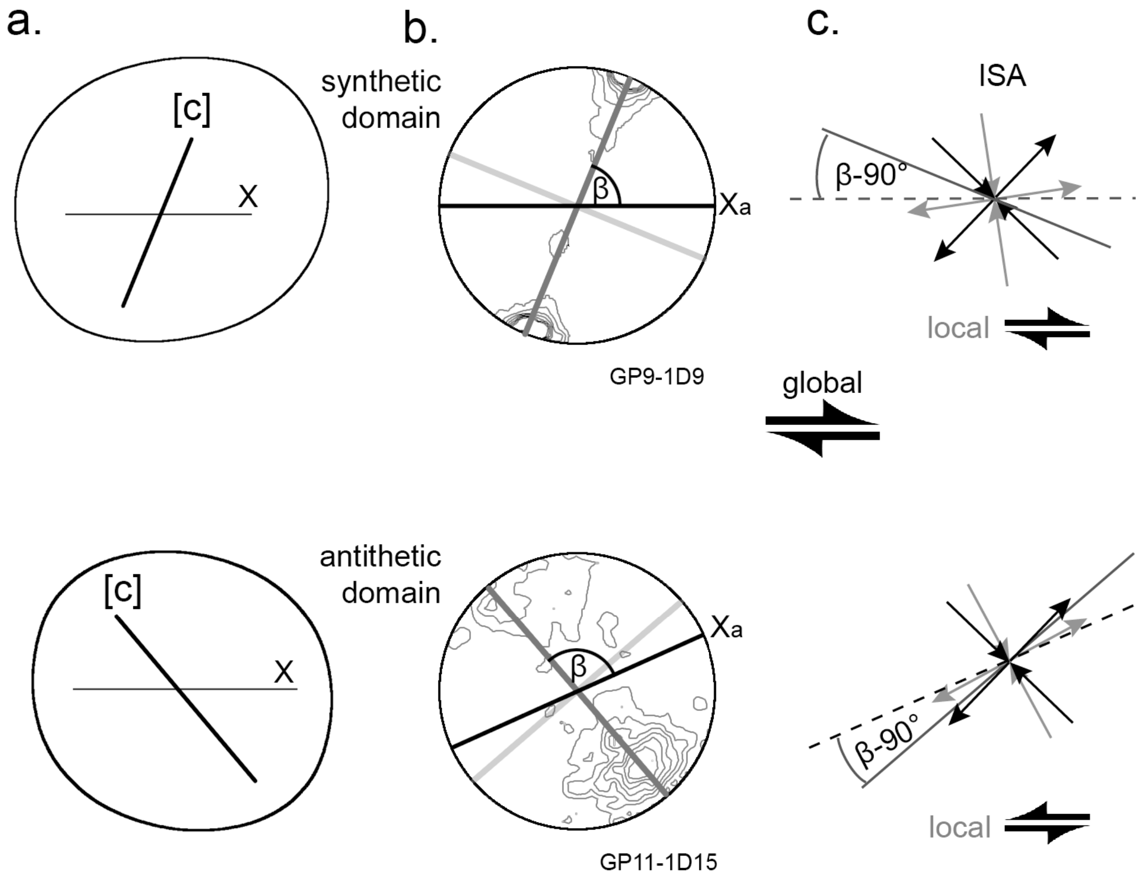

Figure 20: Summary of the SPO and CPO analysis showing (a) the characteristic grain shape (derived from the SURFOR rose diagram) with a trace of the [c]-axis pole figure maximum of recrystallized grains, (b) the pole figure and (c) Two hypothetical instantaneous stretching axes (ISA). The grey line indicates the trace normal to the [c]-axis maximum (trace of most basal planes of quartz crystals), the black line the aggregate orientation φ. (see Fig.12 and 13a for details of the fabric)

The top row is obtained from an aggregate with a typical CPO and SPO, parallel to the shear plane. The bottom row is obtained from an aggregate inclined to the shear plane, showing an antithetically rotated CPO and SPO maximum.

The trace of the basal plane (β-90) is antithetically rotated (with respect to global sense of shear) with respect to the aggregate orientation (grey line) of GP11-1D15.

Two inferred ISA are shown, one stable to the global reference frame (black) which is always at 45° with respect to the shear zone boundary and one rotated with the sense of shear about an angle smaller than the aggregate rotation (grey). See text for discussion.

6. Discussion

The discussion will focus on the most important points of the observations, namely

(1) that the quartz aggregates are mechanically slightly stronger than the matrix which is demonstrated by their bulk shapes, their faster rotation and their slower stretch than the matrix during progressive simple shear deformation.

(2) that the recrystallization of porphyroclasts in moderate strain parts is only partly host-controlled and mostly controlled by the local kinematics.

(3) that the CPO show local shear senses which may deviate from the global shear sense at moderate strains

(4) that the fabric depends on the CPO.

6.1 Deformation of matrix and quartz aggregates

The quartz aggregates are embedded in a polycrystalline matrix. The coexistence of albite core and oligoclase rim and the disperse distribution of biotite in the polycrystalline matrix are microstructures which indicate diffusive mass transfer. Initial recrystallization of K-feldspar has been reported to be accompanied by dissolution-precipitation processes (Menegon et al., 2008). Based on the microstructures and the increasing mixture of phases, it is inferred that diffusion creep is the dominant deformation mechanism in the matrix (Kilian et al., 2011a, Chapter 2). This conclusion is supported by the constant and small grain size of ~10 μm in the matrix.

In contrast, quartz aggregates deform by dislocation creep, as shown by their progressive asymmetric CPO and fabric development. The quartz aggregates have convex shapes and the matrix warps around porphyroclasts and partly recrystallized quartz aggregates. These observations indicate that quartz aggregates are mechanically stronger than the matrix. This is also consistent with the fact that quartz deforms by dislocation creep whereas the matrix deforms by diffusion creep as long as differential stresses are low enough. However, quartz aggregates neither coalesce to form continuous layers nor do they not boudinage. Both observations are consistent with extrapolations of experimentally derived flow laws (see Chapter 5) and indicate that the effective viscosity of quartz is higher than that of the matrix.

Strain theory predicts that the angle of an aggregate orientation with respect to the flow plane decreases with increasing aspect ratio. This applies to rigid (e.g. Passchier, 1987; Marques et al., 2005; Mulchrone, 2007) or deformable particles (e.g. Schmid & Podladchikov. 2003; Mulchrone &

Walsh, 2006). In the case of a particle viscosity being higher than the embedding matrix, it is expected that the particles rotate faster and change their aspect ratio more slowly than the matrix (e.g. Freeman, 1987; Schmid & Podladchikov, 2003; Mulchrone & Walsh, 2006).

The angle φ of the quartz aggregate is slightly smaller than the angle Φ of the corresponding foliation trace in the matrix, i.e. the rotation of the quartz aggregates is faster than that of the matrix foliation. If we assume a bulk simple shear progressive deformation in the shear zone, this can be interpreted as if the quartz aggregates show a higher apparent shear strain deduced from the aggregate orientation with respect to the corresponding foliation in the matrix. In contrast the shear strain deduced from the aspect ratio R of the aggregates using $\gamma = (R - 1)/\sqrt{R}$ is lower than that of the corresponding matrix. Fig. 5b shows the relation of the aspect ratio R and the angle φ of the quartz aggregates. The values fall within the field where particles rotate more and stretch less than expected for a passive marker in progressive simple shear.

An alternative interpretation is to assume that the quartz aggregates behave as passive markers and to explain particle behavior by a more complex flow type than for simple shear (Fossen & Tikoff, 1993). A deviation from plane strain or a volume change would result in a change of the cross sectional areas of quartz aggregates with increasing strain. However, the cross sectional areas of aggregates in the XZ plane do not show a significant size decrease with R or φ. (Fig. 6). We conclude that no significant deviation from plane strain or volume loss has occurred in the quartz aggregates. Instead, the rotation angles and aspect ratios of the quartz aggregates are consistent with a higher viscosity of the quartz aggregates than matrix, and the quartz aggregates do not behave as passive markers.

6.2 Recrystallization of parent grains

Relict magmatic quartz grains (porphyroclasts) become progressively replaced by recrystallized grains towards the shear zone center. The initial recrystallization takes place by progressive subgrain rotation with an increasing misorientation of the recrystallized grains with respect to the parent grain. Most traces of subgrain boundaries found in dynamically recrystallized grains are parallel to traces of the prism planes. These are consistent with misorientation produced by basal edge dislocations with an <a> Burgers vector, associated with the activity of the basal <a> slip system (Baeta & Ashbee, 1969; Trepied et al., 1980). When the subgrains become grain boundaries, they become mobile, and grain boundary migration occurs, consuming (sub)grains towards the inner part of the recrystallizing rim. This process takes place until the relict old grain is entirely consumed (White, 1976; Drury & Urai, 1990; Halfpenny et al., 2006) rim of recrystallized grains forms which is primarily related to the kinematic framework of the matrix around the parent grain (Fig. 18). The orientation of the parent grain has little influence on the recrystallized grains.

This progress of subgrain rotation recrystallization from rim to core is expected to produce a misorientation gradient towards the outer margin of the parent grain, as it is observed in region 4 of pg1 (Fig. 18). However the fact that in most other regions the CPO develops according to the local kinematic framework without a misorientation gradient (especially regions 1 and 3 in Fig. 18) suggests that a critical large angle misorientation is achieved after small strains, and grain boundary migration effectively dominates the recrystallization. It is obvious that not only the shear sense but also the orientation of the shear plane is important for the orientation of the CPO (Fig. 17, 18). Host control clearly is less important than local kinematics. In the following, it will be addressed, how the local kinematics can vary.

6.3 CPO development and the relation to the kinematic framework

C-axis polefigures are often either monoclinic or orthorhombic, the former referred to as internally asymmetric. The orthorhombic axes can be inclined with respect to an external reference frame, which is referred to as externally asymmetric. It has been suggested that the asymmetry of a pole figure can be used to infer the shear sense (Etchecopar, 1977; Berthe et al., 1979; Lister & Hobbs, 1980; Simpson, 1980; Behrmann & Platt, 1982; Simpson & Schmid,1983). According to theoretical CPO models (Lister & Hobbs, 1980) and CPOs measured in well constrained shear zones (e.g. Behrmann & Platt, 1982; Law et al., 1986; Schmid &Casey, 1986; Mancktelow, 1987) a monoclinic polefigure geometry serves as a reliable shear sense indicator. We measured CPOs with a peripheral [c]-axis maximum to a weak straight single girdle or partial straight single girdle which are internally symmetric (orthorhombic). Single girdle CPOs without an internal asymmetry are frequently measured in natural shear zones (e.g. Burg & Laurent, 1978; Simpson, 1980; Garcia Celma, 1983; Law et al.,1990) as well as obtained from numerical modeling (Etchecopar & Vasseur, 1987; Wenk et al., 1989). The applicability of an orthorhombic single girdle as a shear sense indicator depends in that case on the reference frame and the chosen CPO model (e.g. Lister & Williams, 1979, Schmid & Casey, 1986).

There are controversial observations whether the single girdle orientation rotates with respect to the finite strain axes or the global kinematic framework (45° to the infinitesimal strain axes for homogeneous progressive simple shear) of the shear zone boundary plane or with respect to both.

Girdle orientations that remain stable with respect to the kinematic framework (shear zone boundary plane) are predicted in numerical models (Lister & Hobbs, 1980; Wenk et al, 1989; Jessell & Lister, 1990) and in some experiments (Bouchez & Duval, 1982; Dell'Angelo & Tullis, 1989) and real shear zones (Burg & Laurent, 1978; Hudleston, 1980; Van Roermund et al., 1979). The polefigures in these cases basically rotate with respect to the orientation of the finite strain axes. In some of these studies a main maximum remains constant with respect to the shear zone boundary plane while a minor orientation population rotates with the inferred finite strain axes towards the main maximum (Bouchez & Duval, 1982; Hudleston, 1980; Dell'Angelo & Tullis, 1989; Jessell & Lister, 1990)

Other studies indicate that the external asymmetry of the polefigure undergoes only minor rotation with respect to the orientation of the inferred finite strain axes (Carreras, 1977; Simpson, 1980; Garcia Celma, 1983; Schmidt & Casey, 1986; Etchecopar & Vasseur, 1987; Heilbronner & Tullis, 2006) and major rotation occurs with respect to the shear zone boundary plane with increasing strain. At high strain single girdle or peripheral maxima tend to rotate synthetically with the sense of shear resulting in an orientation that cannot be related to finite strain anymore (e.g Schmid & Casey, 1986).

The quartz polefigures measured in the Gran Paradiso mylonites show major rotations with respect to X and minor ones with respect to X_a (Fig. 15, 17, 18). We observe that the [c]-axis maximum is inclined with the local sense of shear and that the CPO reaches a stable position (~ 70°) as soon as aggregate rotation ceases at high strains. The relative inclination is also attained with respect to the local reference frame if strain is large enough (Fig. 14). In the most highly deformed mylonite the stable orientation of CPO maxima does not change with increasing strain as long as layers remain parallel to the shear zone boundary (Fig. 17).

From these observations we conclude that the CPO develops related to the local kinematic framework but not related to the finite strain ellipsoid and not related to the global kinematic framework.

The rotation of the local kinematic framework with respect to the global reference frame causes the apparent discrepancy with predictions of numerical models (Lister & Hobbs, 1980; Etchecopar & Vasseur, 1987; Wenk, 1989; Jessell & Lister, 1990) and experimental or natural shear zones (Burg & Laurent, 1978; Van Roermund et al., 1979; Bouchez & Duval, 1982). We explain the discrepancy - at least in part - by pointing out that in these studies where the developing polefigures rotate with respect to the shear zone boundary (e.g. Carreras, 1977; Simpson, 1980; Garcia Celma, 1983; Heilbronner & Tullis, 2006) the kinematic frame work also rotates, the kinematic vorticity number increases with progressing deformation or that steady state has not been reached. Schmid & Casey (1986) suggest that a rotation of a single girdle may result from an increasing non-coaxiality (increasing kinematic vorticity number) or from accumulation strain by of progressive simple shear. Heilbronner & Tullis (2006) observe a major rotation of the polefigure with respect to the shear zone boundary with increasing strain in shear experiments.

In the weakly deformed mylonite the polefigure orientation is variable with respect to the aggregate orientation and the shear zone boundary plane. The local kinematic framework controls the CPO of the recrystallized grains (Fig. 15, 18). The local kinematic framework results from the flow behavior of the matrix around the quartz aggregates and from the aggregate dynamics. This is for example indicated by contrasting texture asymmetries derived from the same parent grain at opposite sides. External CPO asymmetries of opposite directions found around quartz aggregates have been interpreted as opposite shear senses caused by strain partitioning around porphyroclasts (Simpson 1983, Jerabek et al., 2007).

Aggregates do not undergo coalescence and the CPO is derived form the deformation and recrystallization of a single crystal (or bicrystal in some cases) which - by its nature - has a single crystal orientation. The bulk CPOs of the recrystallized aggregates thus originate from several different initial parent grain orientations. Bulk CPOs with respect to X and X_a are compatible with the CPOs of single aggregates. This indicates that the influence of the parent grain orientation on the CPO development is of very minor importance.

It is now obvious that why the interpretation of the bulk CPOs is not straightforward. For sample GP11 the polefigure incorporating all aggregates across the strain gradient shows a peripheral, synthetically inclined main maximum and an antithetic dispersion of [c]-axes (Fig. 10). Polefigures with similar geometries have been measured in naturally deformed quartzites (Heilbronner, 2009) which show domainal CPO components and in clasts of an experimentally deformed quartzite which was deformed under general shear (Dell'Angelo & Tullis, 1989). The bulk polefigure for GP12 also shows two more densely populated areas, one from synthetically sheared, one from the antithetically sheared domains (Fig. 10). Nevertheless it is more difficult to interpret as the densities of the synthetic part of the polefigure are lower. This is related to the fact that less highly strained domains were measured in that sample.

The similarity of polefigures obtained in polycrystalline material with the bulk polefigures which are integrated across the strain gradient poses the questions if individual aggregates bound by a weak matrix can be compared with individual grains in a quartzite.

The polefigures of the recrystallized rims of parent grains seem to attain an orientation in response to the matrix kinematics already at relatively low strains. A fast rotation of the polefigure with respect to the local shear sense can yield an explanation for the distributions of angles β and θ. The distribution of the angles β yields a tight gap around 90° which is consistent with an instability of a [c]-axis orientation at $\beta = 90°$ (Fig. 14 e-f). The presence of a systematically opposite shear sense associated with angles of $\beta > 90°$ in aggregates with angles $\varphi > 15$ is responsible for the second maximum in the β-distribution (Fig. 14 g-h).

It is concluded that the CPO orientation depends mainly on the kinematic framework of the aggregates. The CPO orientation adjusts with increasing strain in the aggregate towards a stable position (with respect to the local kinematic framework). The local kinematic framework changes inside the shear zone as aggregates rotate. The change of the orientation of local kinematic framework competes with the strain depend rotation of the CPO towards the stable orientation.

6.4 CPO - fabric relation

We observe that the polefigures inclination coincide with the asymmetry of the particle and surface fabric. The particle fabrics are usually weak, but in the case of a preferred orientation, the polefigures shows a steeper inclination than the particle and surface orientation distribution functions with respect to Xa (Fig. 12).

The surface fabrics are orthorhombic but have an external asymmetry or are monoclinic (Fig. 12). SURFOR rose diagrams show a constriction which coincides with the orientation of the [c]-axis maximum (Fig. 12, 19). This contrasts with observations in dynamically recrystallized quartzites, where the minor maximum of the SURFOR rose diagram is interpreted to coincide with the polefigure maximum (Stünitz, 1991).

We will use the term ”slip sense” related on the basal <a> slip system which is perpendicular to the [c]-axis maximum of the recrystallized aggregates. Clearly the term “sense of slip” for an entire aggregate is not useful in the case of aggregates with a non-domainal CPO and where several slip systems are active.

In the aggregates studied here, we find that wherever the sense of slip in the aggregate coincides with the local shear sense the fabric asymmetry reflects the shear sense (Fig. 15, 19, 20).

GP11-1D4 is situated in the highly strained part of the mylonite and shows two [c]-axis orientation domains, one that points against the shear sense (Fig. 19). The particle and surface fabric of each domain is consistent with the polefigure asymmetry. However there is no reason to assume an opposite shear sense associated with that domain. Observations of similar coincidences in domainal microstructures have been interpreted as being due to the effect of the sense of slip on the slip system in combination with grain boundary sliding and migration (Pauli et al., 1996). Here we assume that the [c]-axis orientation and the fabric in the antithetic domain is the effect of an antithetic slip (Fig. 19).

The initial formation of the domainal microstructures described by Pauli et al. (1996) is interpreted to originate form former orientations of parent grains. In the case of the quartz aggregates in the Gran Paradiso shear zones we observed that the CPOs readily adapt the local kinematic framework and ignore the parent grain orientation. However, there are alternatives, e.g. folding around a lineation parallel axis, that can account for the antithetic domain in the highly strained mylonite.

Linking fabric and crystallographic preferred orientation:

We observe structures associated with two processes that link the development of grain boundaries to the crystal lattice: 1) Subgrain rotation recrystallization which produces boundary orientations depending on the slip system and the dislocation type (Baeta & Ashbee, 1969; Trepied et al., 1980; Llloyd et al., 1997), 2) grain boundary migration which is influenced by anisotropic grain boundary energies (Bons & Brok , 2000; Kuntcheva et al., 2006; Becker et al., 2008).

Possibility 1: Subgrain rotation recrystallization:

Subgrain boundaries are preferentially parallel to the prism plane and interpreted as tilt boundaries of basal edge dislocations with burgers vector <a> (e.g. Trepied et al., 1980). To explain the angular relation with respect to the [c]-axis, grain boundaries are required to rotate relative to the [c]-axis. A rotation of the grain boundary in the sense of a rotation of a material plane with respect to the grain would require that the grain deforms internally. As most grains have orientations which are apparently suitable for slip the grain deformation should not be a limiting factor. Nevertheless grains have relatively equant shapes.

The single maximum polefigure is not consistent with large lattice rotations unless there is substantial compensation by the spin of grains in the opposite direction. A combination of grain rotation (spin) and an internal opposite [c]-axis rotation (e.g. Hobbs et al., 1976, Pauli et al., 1996) would serve as an explanation - implying grain scale strain partitioning. The presence of only one dominant slip system producing a strong CPO has been invoked to require a compensating "conjugate" slip system, or sliding surface (Macktelow, 1987; Schmid, 1994, Pauli, 1996).

In fact, we observe grain boundary arrangements similar to the orthorhombic fabrics of diamond shaped grains (Fig. 7e) that have been previously reported and interpreted as related to grain boundary sliding (Lister & Dornsiepen; 1982; Luan & Paterson, 1992; Hanmer, 2000).

To summarize, subgrain rotation recrystallization would have to be accompanied by grain boundary sliding to explain the CPO-fabric relation but can account for monoclinic fabrics.

Possibility 2: Grain boundary migration

Another possibility for the relation of the surface fabric with the CPO would be the preferred development of grain boundaries with a certain relation to the quartz lattice. The preferential development of rhombohedral planes has been suggested for lower amphibolite facies conditions and higher (Kruhl & Peternell, 2002). Kuntcheva et al. (2006) also report a preponderance of rhombohedral planes despite a large variation of possible planes forming grain boundaries. They conclude that planes subparallel to the [c]-axis have higher surface energies than boundaries around 25-50° to the [c]-axis. This could explain the constriction in the rose diagrams of surface fabrics which is situated around the orientation of the [c]-axis and for the formation of the more symmetric surface fabrics with the diamond shaped grains (e.g. GP11-1D5). Nevertheless, it does not account for monoclinic fabrics related to the sense of slip.

The strength of the surface fabric measured by a/b_{bulk} is variable but the surface orientation distribution functions (rose diagrams) indicate that the intermediately strained aggregates have relatively strong fabrics (Fig. 12). In the highly strained mylonite the type and the strength of the fabric varies considerably (e.g. Fig. 7d,e,f). The lateral variation of the quartz fabrics can be related either to changes in the grain boundary mobility, e.g. by the distribution and concentration of second phase particles (e.g Olgaard & Evans, 1986) or by a cyclic recrystallization process where the observed microstructures constitute a step in a continuous process (Knipe & Law, 1987). The distribution of inclusions aligned along some grain boundaries and continuous inclusion trails trending grain boundaries and that cut through grains (Fig. 7f) is indicative for pinning and mimetic growth during grain boundary migration (Lister & Snoke, 1984). Therefore, the variability in the quartz microstructure (Fig. 7e,f) can be explained with a variation of the gain boundary mobility.

Comparison of both possibilities: subgrain rotation - grain boundary migration

A lower grain boundary mobility is in favor of the first possibility: grain boundaries can rotate as material planes during subgrain rotation and deformation of the grain. A higher grain boundary mobility would result in a higher impact of the second possibility: anisotropic grain boundary energies. Both comply well with the observations of strong monoclinic surface fabrics in inclusion rich parts and more internally symmetric fabrics in inclusion poor parts of quartz aggregates. The difference between the slightly stronger surface fabrics in the intermediately strained aggregates compared to the most highly strained aggregates can be related to differences in the contribution of both processes - subgrain rotation (with grain boundary sliding) and grain boundary migration recrystallization.

Therefore we consider that the marked constriction in the surface orientation distribution functions is related to a favored development of boundaries that are not parallel to the trace c-axis. When grain boundary migration is fast enough the symmetric fabrics develop. Locked or slower migrating grain boundaries additionally receive a mechanical component because grains continuously deform internally.

Both cases are possible; whether the internally symmetric or asymmetric surface fabrics develop is thought to depend on the grain boundary mobility - the amount of pinning particles. The difference in grain and subgrain size indicates that grain growth during dynamic recrystallization takes place to maintain the stable grains size (Fig. 11, Chapter 2).

6.5 Flow partitioning

As outlined earlier the R, φ data of the quartz aggregates supports the interpretation that quartz deforms as the higher viscous object in a lower viscous matrix. The apparent flattening (Menegon & Pennacchioni, 2009) of the quartz aggregates can be attributed to a higher rate of rotation (spin) and a lower strain rate in the quartz aggregates compared to the matrix. As we do not see a clear trend towards smaller cross sectional areas of aggregates with increasing strain, the interpretation of volume loss respectively a deviation from plane strain (Fossen & Tikoff, 1993) cannot be confirmed. Nevertheless a plane strain stretching nature of the shear zones cannot be ruled out.

In the case of a more highly viscous particle deforming in a less viscous matrix or if a low viscosity interface is present between the aggregates and the matrix, the shear induced vorticity would be translated into components of shear induced spin of the aggregate and an addition of a coaxial component of flow inside the aggregate (Lister & Williams, 1983). Therefore the aggregate would rotate with respect to the matrix and deform with an additional pure shear component. The extent of this partitioning is dependent on the degree of decoupling of the particle-matrix interface and the viscosity ratio (e.g. Iishi, 1992; Schmid & Podladchikov, 2003). The transition to a flow type with a lower kinematic vorticity number in an aggregate as a result of deformation partitioning implies that the instantaneous stretching axes (ISA) rotate with respect to the global reference frame (Lister & Williams, 1983). Numerical modeling of the kinematics in multilayers as a function of layer orientation and viscosity contrast (Ishii, 1992; Jiang, 1994) that deform by bulk simple shear, predict a spin of the ISA within the higher viscous layer with the sense of vorticity. Additionally the higher viscous layers experience a lower shear induced vorticity and a higher spin.

Translated to our samples this implies that the ISA inside the quartz aggregates is less inclined than in the matrix and that the flow type deviates from simple shear to sub-simple shear (Means, 1981). The fact that quartz aggregates deform by a power law while the matrix deforms by linear viscous creep is not so important because we can assume Reuss bound conditions (Hutchinson, 1976) and that the stresses remain below the equiviscous point (see Chapter 5). A constant differential stress across the mylonite is based on the constant dynamically recrystallized grain size (Fig. 11b).

The possibility of a rotation of the ISA in good agreement with the orientation of the active slip systems inside the recrystallized grains (either in the composite aggregates GP11-1D4 and or the "reverse" GP11-D15) (Fig. 19, 15) and the actual shear sense recorded in the aggregates. We observe that the basal planes in the recrystallized aggregates (respectively the CPO maximum) are inclined with respect to X_a. A displacement in the observed sense along the basal plane can only be realized if the ISA deviates from the fixed 45° orientation (Fig. 20c,19).

The reversal of the shear sense experienced by some aggregates during intermediate strain ($\varphi > 15°$) can be explained by the partitioning of flow between the aggregates and the matrix. As the ISA is expected to rotate - at least to some degree - with the aggregate, the shear induced spin has to be compensated by flow parallel to the layer (- matrix interface) with the opposite sense of vorticity as the global flow. In other words, the global non-coaxial flow is discontinuous inside the quartz aggregates, therefore aggregates spin, and therefore layer (aggregate) parallel shear must take place (Fig 15, GP11-1D15). Similar observations have been reported on dikes which are dragged into a shear zone (Lister & Snoke, 1984).

As an alternative to ISA rotation by flow partitioning inside the shear zone one can argue that the bulk flow in the shear zone itself is sub-simple shear. Menegon and Pennacchioni (2009) show that the shortening direction in the southern Gran Paradiso is at a high angle to the horizontal shear zones. Their reasoning is based on the shear zone orientation distribution, shapes of mafic enclaves in the rock volumes between the shear zones and shapes of quartz aggregates inside mylonitic shear zones. We believe that quartz aggregates in the shear zones do not behave as passive markers. One argument against the assumption that the flow type inside the shear zones and in the hostrock is identical, is again the fact that the shear zones must have a lower effective viscosity, and hence flow partitioning has to be expected (e.g. Jiang, 1994). The shear zones are lower viscous layers which implies that flow in the shear zones should have a higher shear induced vorticity than the hostrock.

6.6 Implications for the interpretation of shear senses and microstructures

The microstructures and the CPO development discussed above are typical for the shear zones of the Gran Paradiso. They consists of higher viscous quartz aggregates deforming by dislocation creep in a lower viscous matrix deforming by diffusion creep at lower amphibolite facies conditions. In similar situations and in general situations that yield a potential for flow partitioning, shear sense interpretations based on fabrics and CPOs have to be done carefully.

We observe that the CPO develops with respect to the aggregate kinematic reference frame and not the global reference frame. This situation can lead to an erroneous interpretation of orthorhombic c-axis polefigures if the kinematic reference frame is assumed to be fixed to the shear zone boundary. Therefore care has to be taken in the interpretation of CPOs that do not have monoclinic [c]-axis polefigures.

We also observe opposite shear senses in aggregates oriented at small angles to the main shear zone. Without the knowledge of the global reference frame, for example if the shear zone boundary or the direction towards increasing strain is not known the interpretation of shear senses can yield the wrong shear zone kinematics. This can be overcome if the highest strained parts of the shear zones are analyzed and aggregates reached a stable position with respect to the shear zone (parallel layering, high aspect ratio). Additionally multiple measurements in different aggregates are recommended.

The particle and surface fabrics in quartz aggregates are principally dependent on the CPO orientation. The active slip system is basal <a> which is fairly common at low to higher metamorphic conditions (Schmid & Casey, 1986; Takeshita, 1996; Stipp et al., 2002). If grain boundary mobility is low, a monoclinic particle and surface fabric can be related on the sense of the resolved slip on the basal plane. The sense of the resolved slip on the basal plane does not necessarily coincide with the global shear sense. An anisotropic distribution of the basal planes allows that slip can also be antithetic with respect to the shear sense.

An orthorhombic surface fabric is indicative of a higher grain boundary mobility and therefore only as reliable as the shear sense information obtained form the CPO.

7. Conclusions

The development of the crystallographic preferred orientation of quartz in small scale shear zones has been studied in the Gran Paradiso metagranodiorite which formed at lower amphibolite facies conditions. Quartz deforms by dislocation creep and the feldspar-rich matrix by diffusion creep. We pay special attention to the separation of a global reference frame, which corresponds with the shear zone and a local reference frame related to the individual quartz aggregates.

Quartz aggregates deform as more highly viscous particles in a weaker matrix which results in flow partitioning and a deviation of the local kinematic framework of the quartz aggregates from the global kinematic framework of the shear zone.

The crystallographic orientation of the non-recrystallized magmatic quartz grains has a minor influence on the developing CPO. Already at low strain, the initial CPO is usually related to the local kinematic framework.

The orientation of an orthorhombic [c]-axis polefigure depends on the local kinematic framework and not on the global kinematic framework.

The orientation of the polefigure reflects the combination of the local kinematic framework, the strain dependent rotation of the CPO towards the stable position inside the aggregate, and the rotation of the aggregates within the global reference frame.

The CPO maximum is usually synthetically inclined with the local shear sense and stable at ~70°.

Flow partitioning can explain the systematically opposite shear sense at aggregate inclinations > 15° with respect to the shear zone boundary.

Quartz grains initially recrystallize by subgrain rotation recrystallization and subsequent grain boundary migration as soon as boundaries become mobile. Grain boundary migration erases most of the progressive misorientation in the old grains and cause a high misorientation with respect to the old grain.

Dynamic recrystallization reaches a steady state in terms of grain size and CPO at relatively low strain and grain boundary migration controls the microstructure.

Particle and surface fabrics are related to the c-axis orientation and monoclinic fabrics are consistent with the sense of slip along the basal <a> slip system, not necessarily with the shear sense.

Whether monoclinic or orthorhombic fabrics develop depends on the grain boundary mobility. Pinned grain boundaries are assumed to develop deformation controlled fabrics while mobile grain boundaries tend to develop fabrics controlled by crystallography, e.g. anisotropic surface energies.

We recommend that CPO and fabric measurements in rocks that are suspicious of flow partitioning should only be performed in the most highly strained part with a ceased aggregate rotation, in multiple aggregates. A knowledge of the shear zone boundary orientation is indispensable.

Chapter 4

Shear zone rheology, deformation mechanisms, and quartz water content in the Truzzo granite

Abstract

Small scale shear zones develop in low strain domains of the Truzzo granite, Tambo nappe in the Central Alps. The Truzzo shear zones nucleate at high temperature by coalescence of recrystallizing feldspar phenocrysts and fine grained plagioclase aggregates. Subsequent formation of a phase mixture results in flow by diffusion creep. Advanced shear zone propagation is related to fracturing at the shear zone tip.
Coarse grained, monomineralic quartz aggregates embedded in a polymineralic matrix deform by dislocation creep. Quartz aggregates disintegrate in the polymineralic matrix along grain boundaries. Subsequent deformation at higher differential stresses leads to a relative hardening of the fined grained phase mixture in the shear zones with respect to the coarse grained granitic host rock.

FTIR spectra indicate that quartz is essentially free of structural water. Primary fluid inclusions in magmatic grains are drained during high temperature recrystallization by grain boundary migration. Primary submicron-sized, intragranular white mica is expelled from the recrystallized grains by the migrating grain boundaries. Subgrain rotation recrystallization becomes active during the later high stress (or higher strain rate).

Molecular water in fluid inclusions in unrecrystallized K-feldspar, stable biotite and synkinematic myrmekite indicate that water was present during deformation. Deformation does not affect the water content of quartz grains. This indicates that either the recrystallization mechanism plays a crucial role for the incorporation of water in quartz or that water reported in previous studies in fine grained quartz aggregates is mainly contained in the grain boundary region.

The deformation of “dry” quartz at low differential stresses and geologically reasonable strain rates suggests that weakening of quartz at fluid present conditions may be related to processes at grain boundaries.

1. Introduction

Pre-orogenic granitoids usually preserve undeformed domains. High strain deformation in these domains may be evident only in small scale shear zones (e.g. Tauern: Mancktelow & Pennacchioni, 2005; Gran Paradiso: Menegon & Pennacchioni, 2009; Tambo nappe: this study). Low strain domains are usually enclosed by an homogeneously deformed rock, e.g an orthogneiss. Regarding the deformation in the shear zones and in the orthogneiss, several interpretations of the deformation sequence are possible.

The shear zones can be a relict of the initial stages of deformation in the whole rock mass and deformation did not proceed in the low strain domains during later stages. In that case the low strain domain - shear zone association locally predates the orthogneiss and presents an initial stage of deformation in the rock mass. Alternatively, deformation in the orthogneiss and in the shear zones are related by a coeval but heterogeneous response to the displacement field imposed on the rock. In that case the shear zones do not present an early stage of deformation but rather represent different strain rates within the rock mass. A third possibility is that after orthogneisses and low strain domains formed, both are locally overprinted by the small scale shear zones. Which of these situations had occurred cannot always be decided unequivocally.

All situations have in common that deformation localizes in narrow zones and that frequently an association with fractures is reported. Several authors suggest that a pre-existing brittle precursor can be responsible for the localization of shear zones (Segall & Pollard, 1983; Segall & Simpson, 1986; Guermani & Pennacchioni, 1998; Mancktelow & Pennacchioni, 2005; Pennacchioni 2005). Fractures and microfractures may provide pathways for fluids which lead to H_2O- weakening and the enhancement of synkinematic reactions (e.g. Kronenberg et al., 1990; FitzGerald & Stünitz 1993; Mancktelow & Pennacchioni, 2005). The association of fractures and viscous shear zones can also be related to stress concentrations at propagating shear zone tips which may lead to fracturing immediately proceeding the shear zone propagation (e.g. Fusseis & Handy, 2008).

Discrete, well defined shear zones in the Truzzo granite in the basal part of the Tambo nappe in the central Alps are preserved inside non-deformed to low strain domains enclosed by granitic orthogneiss. The shear zones terminate either in a joint-like structure or broaden and delocalize inside the low strain domain. Displacement across the shear zone increases with the width of a mylonitic to ultramylonitic core of the shear zone.

Potential mechanisms contributing to the localization of the shear zones in the low strain domains in the Truzzo granite and their rheologic history will be discussed based on the results of the detailed analysis of microstructures and crystallographic preferred orientations (CPO) of quartz. The presence of fracture-like shear zone tips will be discussed within the scope of deformation mechanisms and shear zone evolution as well as the significance of quartz water weakening (e.g. Kronenberg et al., 1990; Nakashima et al., 2008).

Among other factors, the localization of deformation and its propagation in shear zones depend on the rheology as a function of the microstructure. Strain dependent changes in the microstructure as well as changes in the rheology related to the boundary conditions will be discussed for the shear zones in the Truzzo granite.

A second part of this chapter will deal with the potential effect of water in quartz on the mechanical behavior during deformation in the amphibolite facies shear zones.
Several studies suggest an importance of water incorporation into quartz during deformation. Hydrolytic weakening refers to the decrease of strength associated with molecular water during crystal plastic deformation observed during experimental rock deformation of single or polycrystals (Griggs & Blacic, 1964: Kekulawala et al., 1978,1981; Kronenberg & Tullis, 1984, Paterson 1989). FTIR measurements in quartz or quartz aggregates reveal molecular water in the form of H2O contained in fluid inclusions or grain boundaries. The effect on strength is related to water in freezable and non-freezable fluid inclusions while structural hydroxyl or proton defects do not influence the mechanical behavior (Kekulawala et al., 1981; Kronenberg et al., 1986).

In naturally deformed quartz rich rocks Fourier transform infrared spectroscopy (FTIR) observations (Kronenberg et al., 1990; Nakashima et al., 1995; Gleason & DeSisto, 2008) suggest a correlation of the water content in quartz aggregates and shear strain. Fracturing, fluid infiltration, and the formation of a water enriched zone is interpreted to lead to strain localization and subsequent deformation to assist water distribution inside the quartz (Kronenberg et al., 1990).

Quartz recrystallization associated with shear zones developed in the Truzzo granite in the Tambo nappe, central Alps, takes place at lower rates compared to feldspar recrystallization. Quartz constitutes a more viscous phase than feldspar during the initial deformation.

To explore the reason for the unusual apparent strength of quartz the water content was measured by FTIR spectroscopy. The large grain size in the sheared Truzzo granite makes it possible to determine intragranular water content in non-recrystallized and individual recrystallized quartz grains. Contrary to most studies on experimentally or naturally deformed quartz the recrystallization of quartz grains in the Truzzo granite is governed by grain boundary migration with only subordinate subgrain rotation during the main deformation phase. The effect of the recrystallization mechanism on the intragranular water content will be discussed. Further, it will be explored if the relative weakening of quartz with respect to feldspar can be related to water in quartz or is due to other reasons.

2. Geology

2.1 Overview

The Permian Truzzo granite in the Penninic Tambo nappe in the Central Alps (Fig. 1a) is subjected to heterogeneous alpine deformation (Marquer, 1991; Marquer et al., 1994). The Truzzo granite intruded late into polyphase deformed Variscan basement and its deformation is interpreted to be only of Alpine age (e.g. Marquer, 1994).

Heterogeneous deformation of the Truzzo granite gave rise to the preservation of undeformed and low strain domains in the size of up to 100s of meters embedded in mylonitic Truzzo granite (Fig. 2a,b). Undeformed domains still show magmatic structures (Fig. 2a). Locally, a magmatic fabric is preserved in the form of aligned K-feldspar phenocrysts.

There is a gradual transition from mesoscopically undeformed granite to mylonitic Truzzo granite within several decimeters to meters (Fig. 2b) forming a mylonitic orthogneiss. Well defined, regularly spaced, straight and small scale shear zones are developed inside the low strain domains (Fig. 3) as well locally extend into the the orthogneiss. Deformation in the orthogneiss, outside the low strain strain and partially undeformed domains is also heterogeneous but generally high and penetrative.

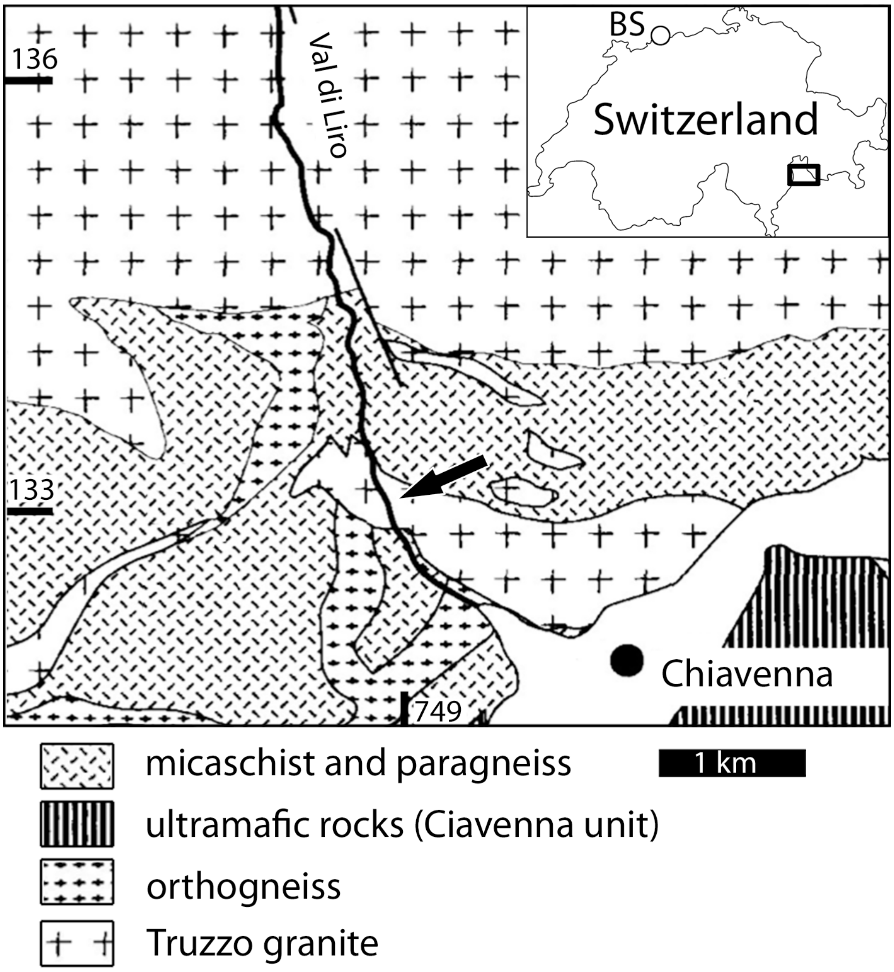

Figure 1: Overview: Simplified geological map of the southernmost part of the Tambo nappe (modified after Marquer et al., 1998). The black arrow indicates the area with outcrops of low strain domains. Outcrop area of a low strain domain in the Truzzo granite in the lower Liro valley, (748944,132923 to 748888,133092)

In the following, undeformed domains and low strain domains will be referred together as *low strain domains*. The penetratively deformed Truzzo granite around the low strain domains will be termed *orthogneiss*. The rock in which the shear zone develops is the *host rock*.

Different crosscutting relationships of the shear zones with the foliation in the orthogneiss are observed: Some shear zones cut the foliation of the mylonitic orthogneiss, whereas some shear zones are merge into the foliation of the mylonitic orthogneiss. In some cases shear zone terminations can be observed within the low strain domain. Microstructural overprinting relationships will be presented in the results section.

D1 deformation is associated with a first foliation and anastomosing shear zones on the nappe scale developed during top-to-the-NW shearing (Marquer, 1991). Alpine D1 is early and subduction-related (Schmid et al., 1990) and is estimated to initiate at pressures of up to 1.3 GPa and temperatures above 550° C based on phengite substitution in white micas (Massonne & Schreyer, 1987; Baudin & Marquer, 1993). The D2 deformation is reported to be associated with rapid decompression at temperatures still above 550° C forming shear zones at all scales related to an E-W stretching at the nappe scale (Marquer, 1991; Marquer et al., 1994). Later D3 deformation occurred during cooling and is associated with a heterogeneous refolding of D1 and D2 structures, more penetrative in the southern part of the nappe (Baudin et al., 1993); D4 is brittle normal faulting (Marquer, 1991).

The very southernmost part of the Tambo nappe experienced the highest pressures and temperatures during D1 and D2 (Engi et al., 2004). Huber and Marquer (1998) propose temperatures of ~ 550°C for the D1 deformation at ~1.2 GPa and ~650° C for the D2 deformation at 0.8-0.9 GPa in the southern Tambo nappe. D3 deformation should commence with 550°C at 0.4 GPa.

Marquer (1991) describes shear zones that are related to the D2 deformation event based on their orientation and kinematics. Nevertheless, in the studied area no intersection relations have been reported. Baudin et al. (1993) report that some shear zones in the Tambo nappe are initiated during D1 and were reactivated during D2, probably referring also to the shear zones in the southern part of the nappe. However it is not clear which scale of shear zones these authors consider in their studies.

2.2 Sample area

The shear zones of this study have been sampled from a low strain domain, which is at least several tens of meters wide. It is located in the southernmost part of the Truzzo granite from an outcrop in the lower Liro valley (748944,132923 to 748888,133092).

Shear zones trend NW-SE to N-S and dip ~ 30-60° to the E and NE. Lineations plunge E. The foliation in the orthogneiss trends roughly N-S in the E and W of the low strain domain, and E-W in the S (Fig. 4).

Shear zones are planar over the exposed area (> 10 m). Single shear zones are from several mm to ~0.1 m wide. The strain gradient at the margin of the shear zone is in most cases steep (Fig. 5a), but a foliated zone several 10s of mm wide can locally be developed (Fig. 5b). The shear zones usually grade into a fine grained ultramylonite within a few mms. Occasionally this strain gradient gradient cannot be observed and the foliated granite seems to be truncated by the ultramylonite. Some of the broadest shear zones exhibit less deformed parts in their core and the highest strain at their margins (Fig. 5a). Locally, the shear zones can be thinned into narrow shear bands connecting the highly deformed parts of two shear zone margins (Fig. 5c,d).

Two types of shear zone ‘terminations’ are observed. In the first type of terminations shear zones delocalize into more homogeneously deformed areas with transitions of SC and SC’ foliations (Fig. 6a). In these areas K-feldspar grains and plagioclase aggregates form tails which define the C and C’ foliation (Fig. 6 c,d). Shear zones originating from C and C’ planes extend into areas of less deformed host rock.

The second type of shear zone ‘termination’ is presented by shear zones which become continuously thinner (Fig. 7). The width of the core decreases together with offset and deformation intensity of the host rock. The shear zone forms anastomosing fracture-like branches which cut through K-feldspar clasts. At the outermost tip only a fracture-like structure with no measurable offset is preserved. The transition from a 0.1 m wide ultramylonite to a fracture-like tip takes place within less than 10 meters, (the displacement direction is inclined ~20-30° to the outcrop).

2.3 Samples

The host rock of the shear zones is a porphyric granite with up to 0.1 m long K-feldspar phenocrysts. Sample Tr3 contains shear zones (3 -20 mm) out of an anastomosing network (Fig. 8). K-feldspar deforms marginally and recrystallized tails are dragged into the shear plane. Biotite layers which are parallel to elongate quartz and K-feldspar aggregates show an internal foliation which is parallel to the shear zone (Fig. 8). Tr3-3 contains a discrete shear zone (approximately a C plane) with a strain gradient defined by the orientation of the foliation, which consists of a compositional layering of the recrystallizing minerals (Fig. 8a). Tr3-1 is a part of more homogeneously deformed host rock between the shear zones (Fig. 8b). Sample Tr1-4 contains a discrete thin shear zone (1-4 mm) which forms as a C-plane in a general SC-geometry (Fig. 8c).

Samples focusing on the behavior of the mature shear zones are from a broad (~0,1m) ultramylonitic zone (Tr6/Tr12: 748912, 133011) (Fig. 9a). Sample Tr7 (748950, 132924) contains a very thin fracture-like shear zone cutting a macroscopically undeformed mafic enclave and a granite in a marginal part of the low strain domain (Fig. 9b).

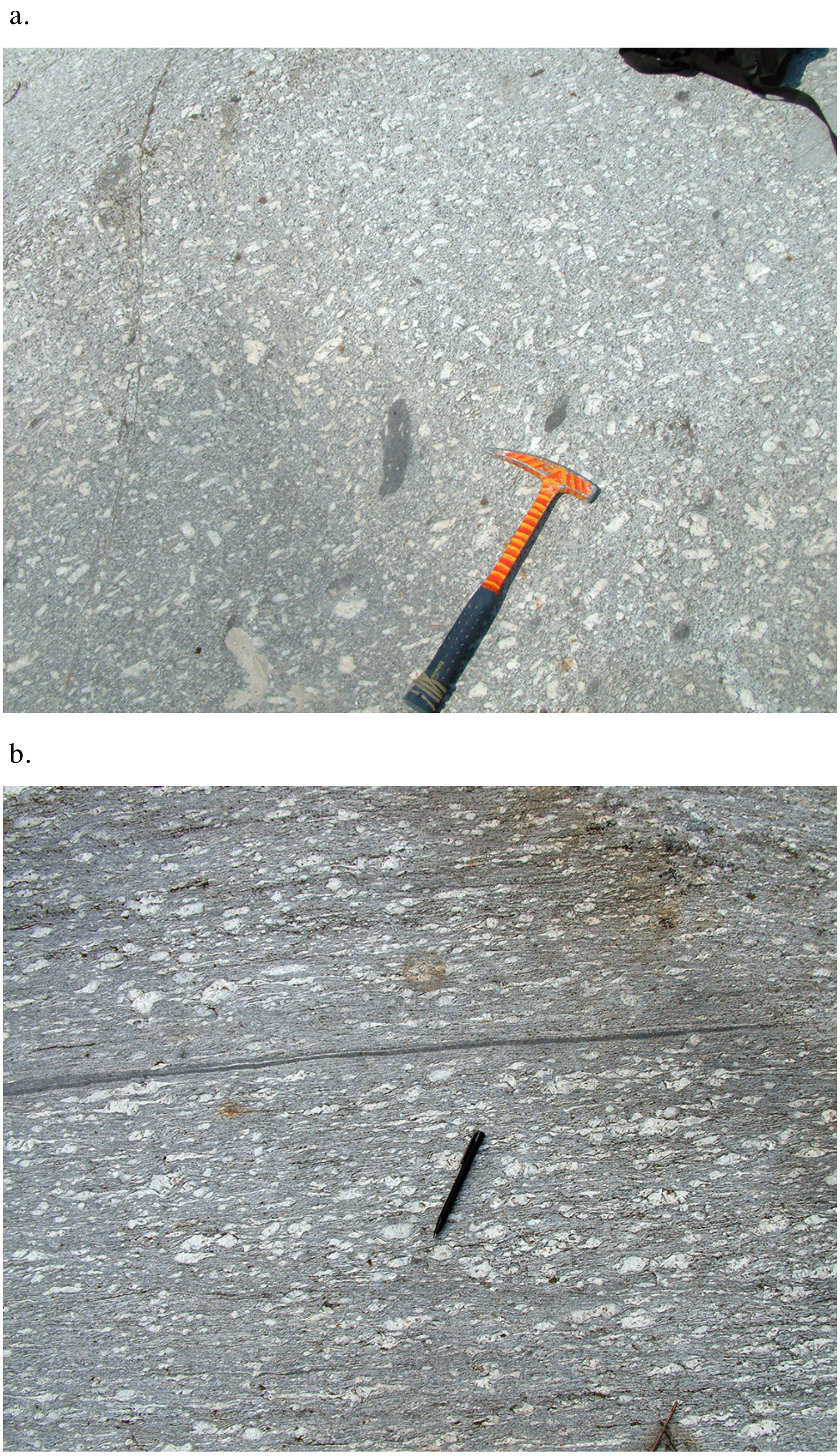

Figure 2: Truzzo granite and mylonitic orthogneiss: (a) Relatively undeformed Truzzo granite of a low strain domain. Enclaves are almost undeformed and K-felspar phenocrysts do not show a preferred orientation. (b) Highly strained orthogneiss derived from the Truzzo granite, surrounding the low strain domains. The dark elongate lenses are stretched magmatic enclaves. Former K-feldspar phenocrysts from porphyroclasts.

Figure 3: Shear zone: Small scale, straight shear zone cutting through the granite in the low strain domain.The lineation is not parallel to the outcrop. Looking west. Detail of this shear zones are in figure 5 a,b and .c

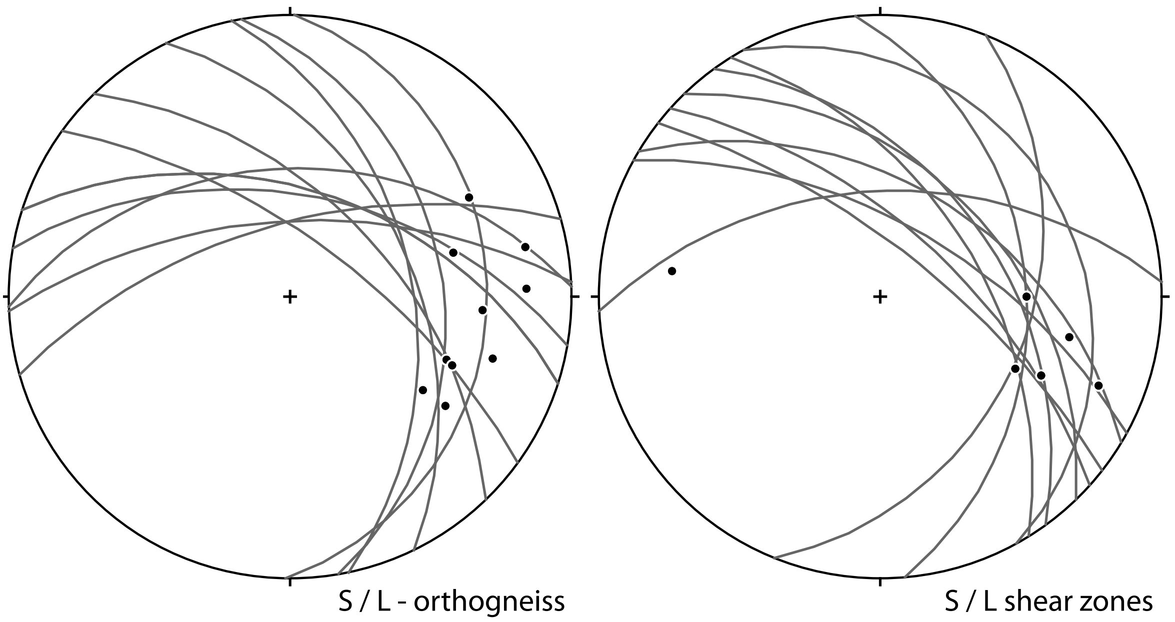

Figure 4: Orientations: Foliation (S) and lineation (L) in the orthogneiss and in the shear zones inside the low strain domain. Lower hemisphere.

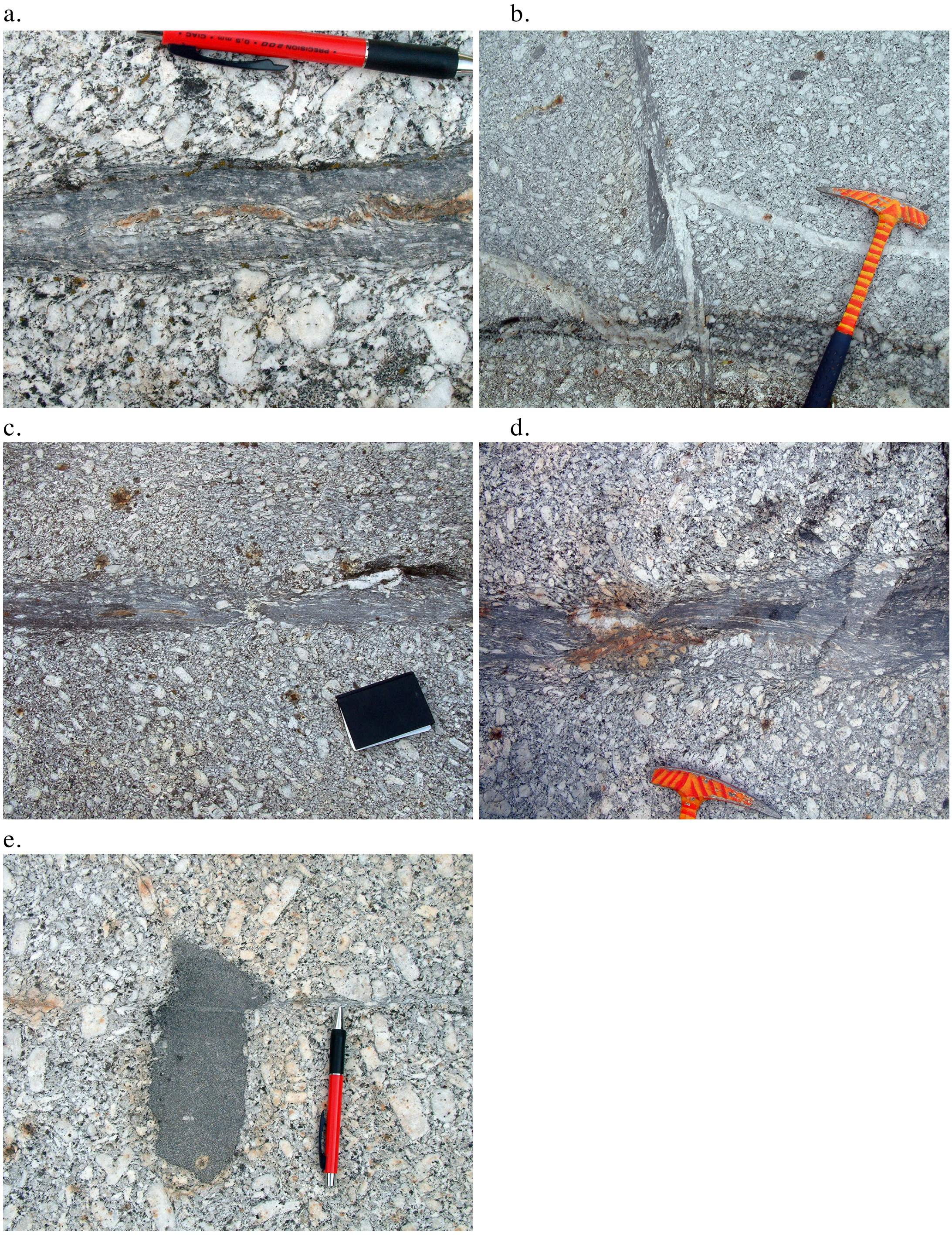

Figure 5: Macroscopic aspects of shear zones: (a) Broad shear zone showing a discontinuous strain gradient and a less deformed central part of the shear zone. The lineation plunges about 20° to the right. The shear sense is sinistral. The shear sense indicated by marginal folding of the hostrock is only apparent. (b) The same shear zone as in (a) deforming a small aplite dike. The shear zone develops on a one side a continuous strain gradient in which a mafic enclave is deformed. Sinistral shear sense. (c) shear zones which developed symmetric necking. The neck volume contains quartz and K-feldspar. Dextral shear sense. (d) shear zone showing asymmetric necking. Sinistral shear sense. (e) Small discrete shear zone with only little deformation of the hostrock. The offset in the enclave is only apparent as the lineation plunges about 25 ° to the right. Figure (a) and (b) are details of figure 3

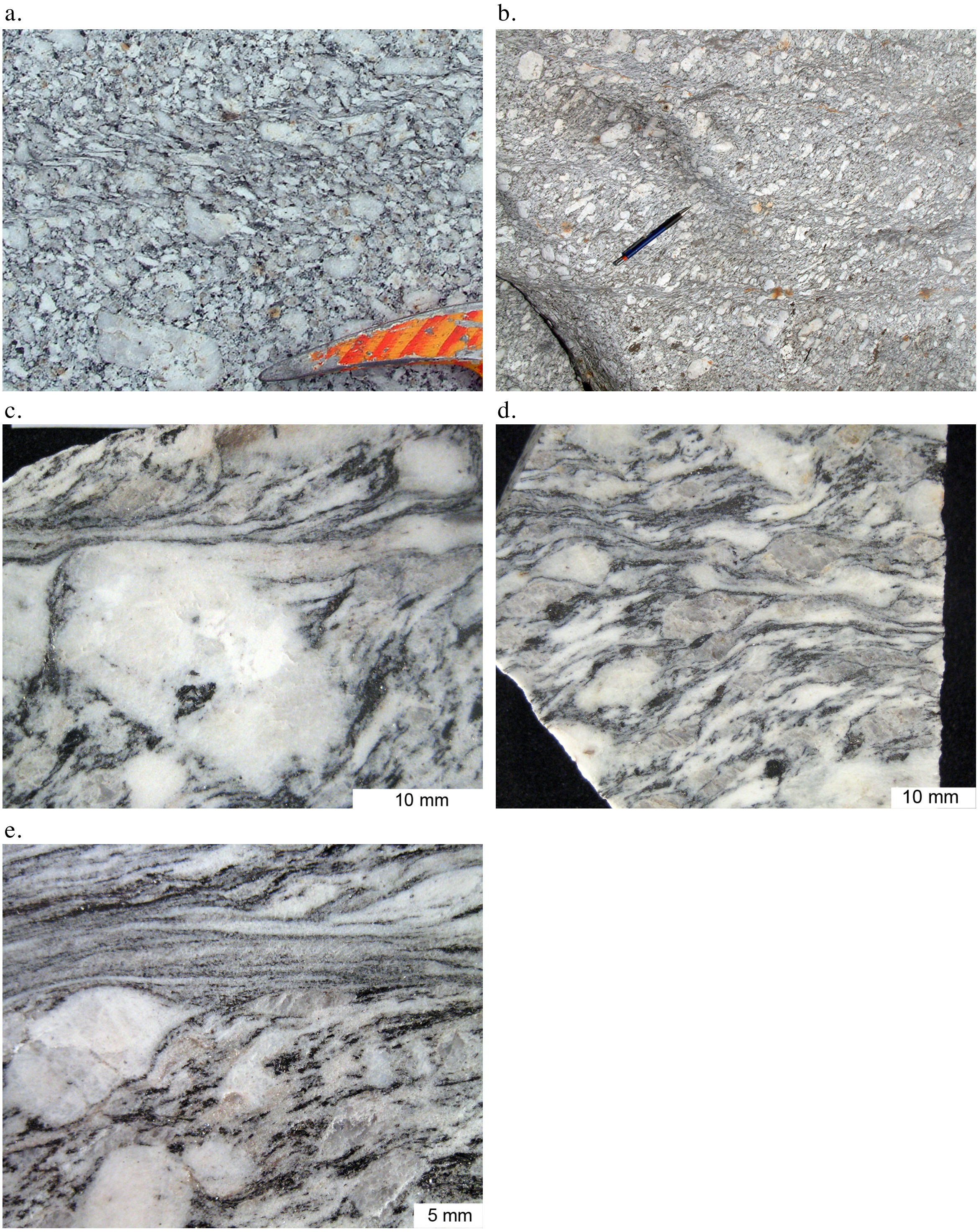

Figure 6: Shear zone - SC(SC’ relation: Examples of weakly (a) to moderately (b) deformed granite with shear zones initiating out of C or C’ shear bands. The shear band foliation is principally defined recrystallized K-feldspar, plagioclase and biotite aggregates. Quartz forms porphyroclasts together with unrecrystallized K-feldspar (c) Sample Tr1-4,(d) sample Tr1-1. (e) Shear zone localizing out of a more homogeneously deformed area, sample Tr3-4.

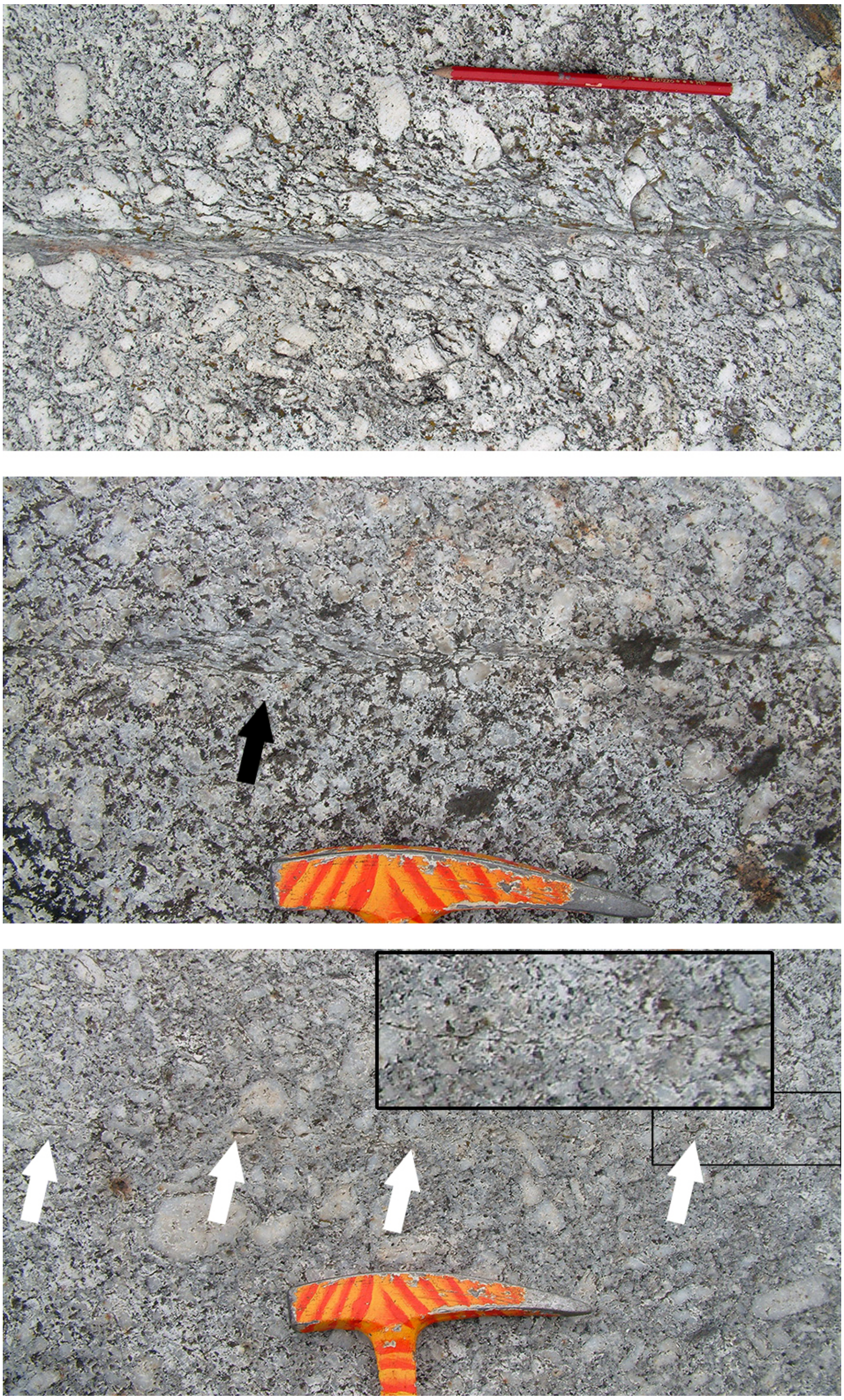

Figure 7: Shear zone - fracture transition: Transition of a shear zone to a crack-like tip. Between each photo are approximately 1-2 m. The lineation plunges about 20° to the left. Note, the crack-like structure in the lower image (white arrows) cuts through K-feldspar grains. In the middle image very thin crack-like shear zones form anastomosing branches in a compressional bridge (black arrow). Shear sense is sinistral.

a. Tr3-3

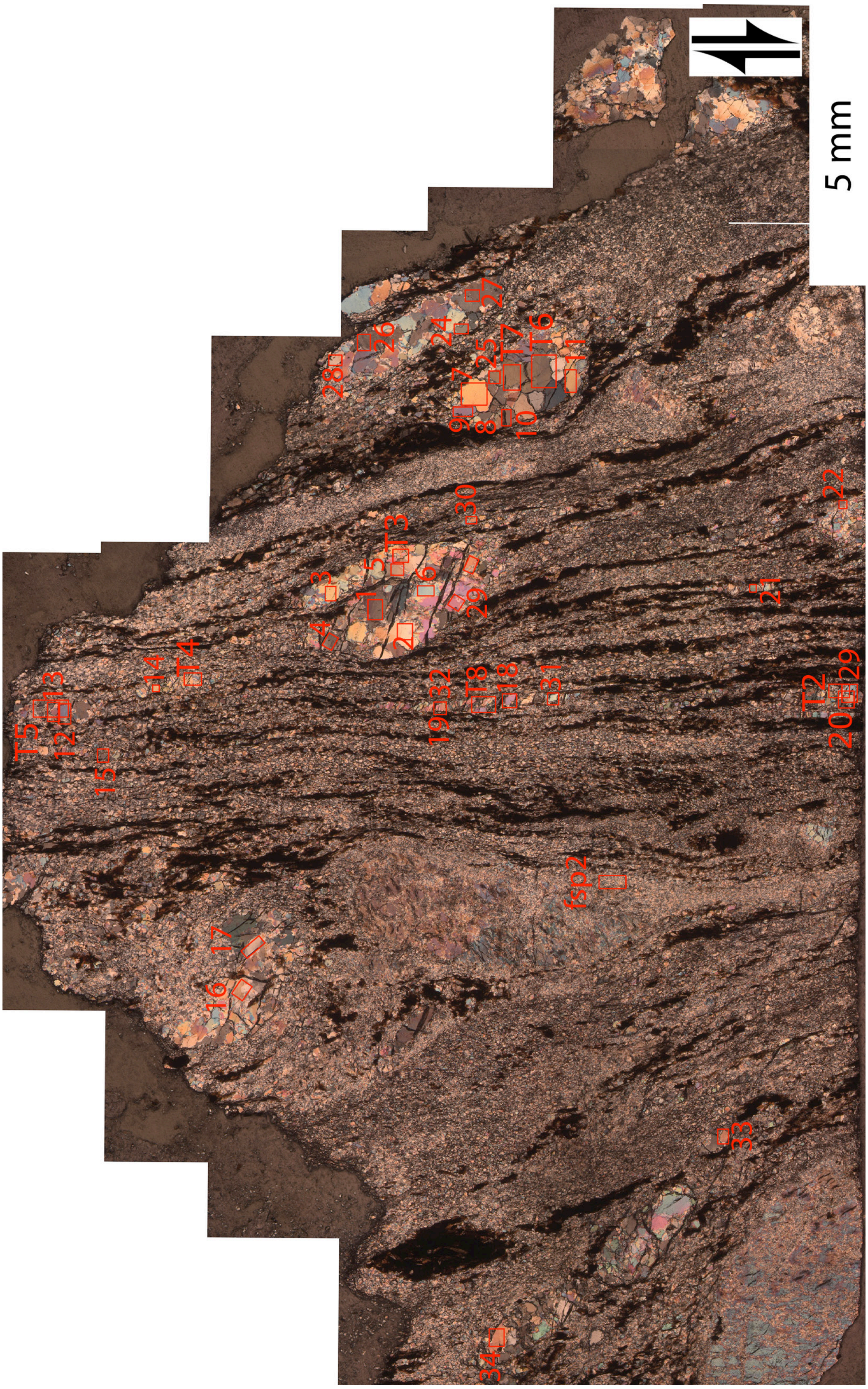
5 mm
28
26
24
27
25
T7
T6
11
7
9
8
10
30
T3
5
3
1
6
29
4
2
22
21
14
T4
13
T5
12
15
19
32
T8
18
31
T2
20
29
fsp2
17
16
33
34

b. Tr3-1

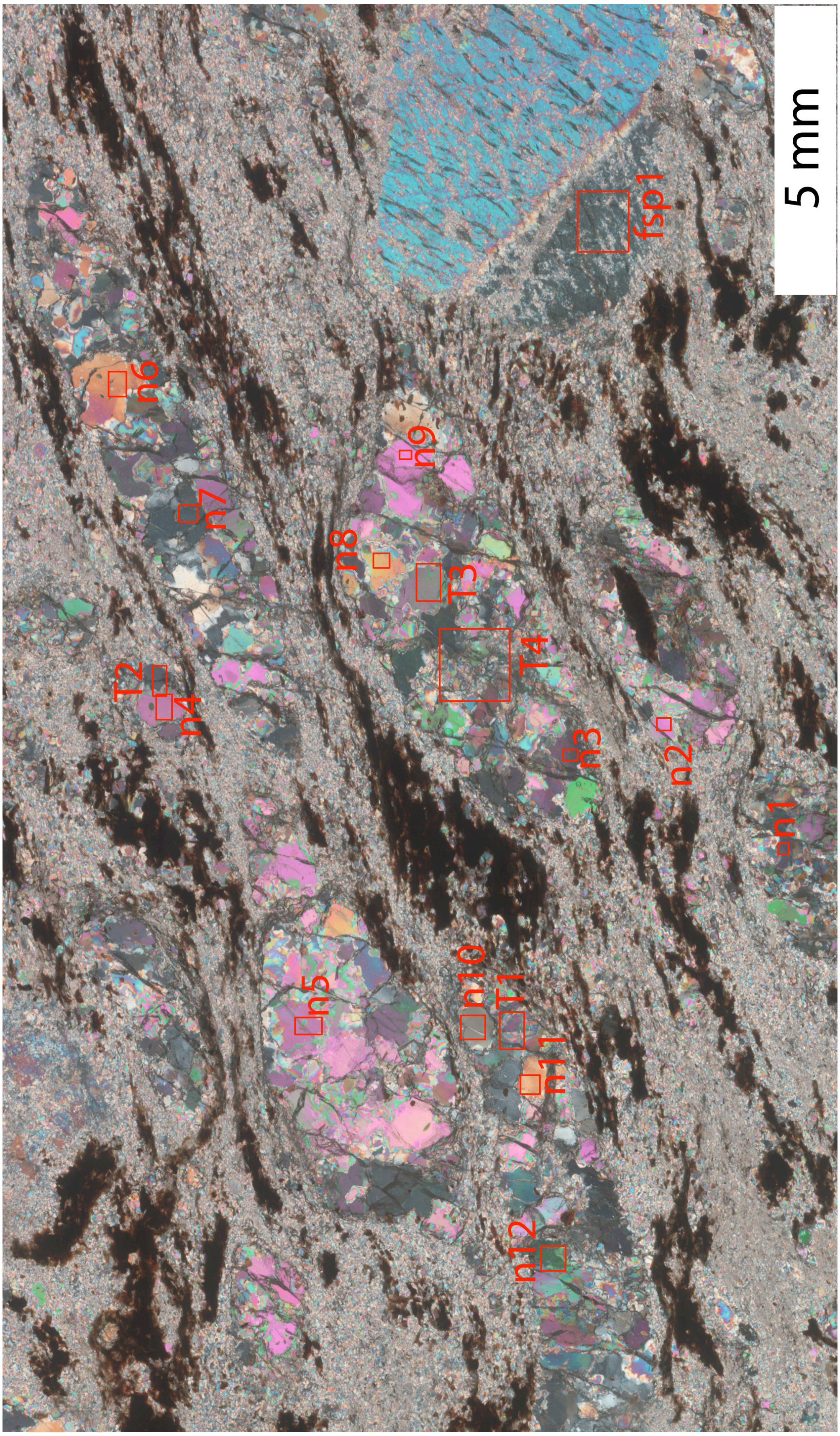

c. Tr1-4

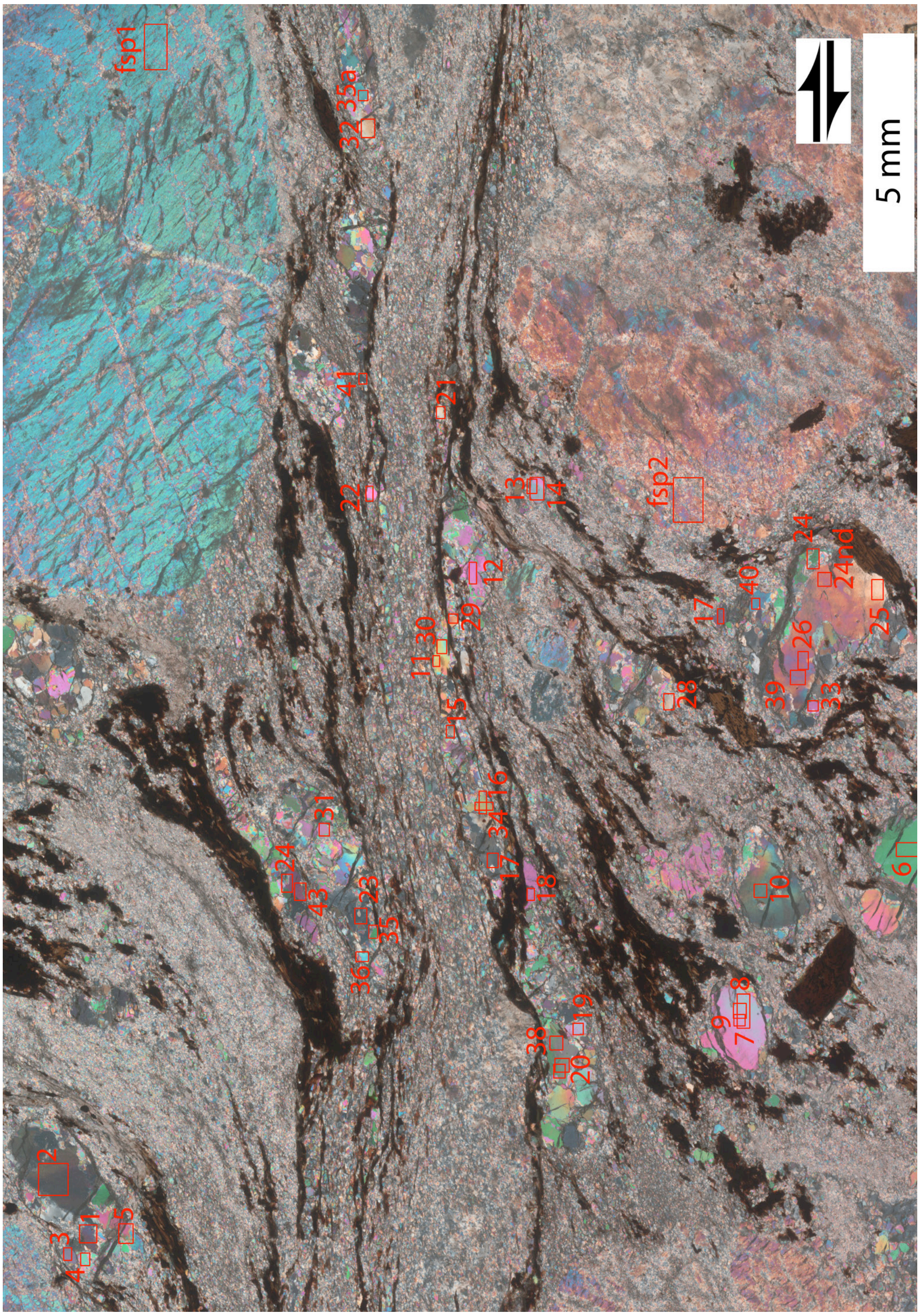

Figure 8: Samples: (a) Micrograph of a thick-section of sample Tr3-3. (b) scan of thick-section of sample Tr3-1 and (c) of sample Tr1-4. Crossed polarizers. The high interference colors are caused by the section thickness between 120 and 200 μm. Quartz shows clear third to forth order interference colors. K-feldspar has also high order interference colors but a dusty appearance. Fine grained grey masses are plagioclase and polymineralic phase mixtures. Number and frames indicate sites of FTIR measurements. See Appendix I for the corresponding spectra.

a.

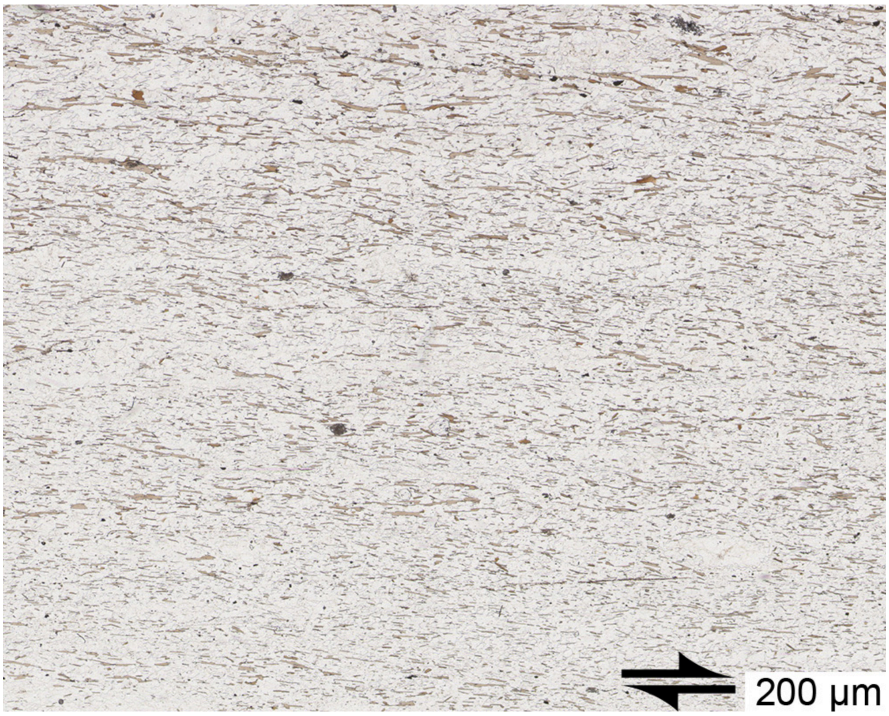

b.

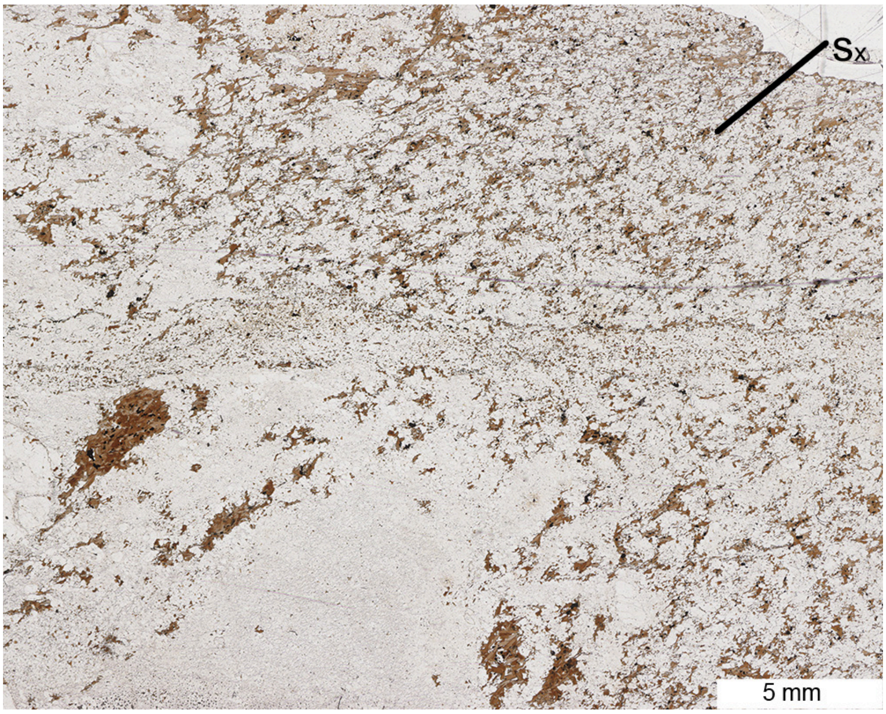

Figure 9: Samples:(a) Scan of a thin section of sample Tr6, am ultramylonitic core of a broad shear zone. Strain is assumed to increase from top to bottom. Shear sense is dextral. (b) Scan of a thin section of sample Tr7 showing an offset micrgranitic enclave. Compare figure 5e. The shear sense indicated by the offset is dextral. The biotite foliation (Sx) overprints the fabric developed in the thin shear zone and not unassociated to the shear zone movement.

3. Methods

3.1 Fourier transform infra-red analysis (FTIR)

FTIR spectra of single quartz grains have been acquired using a Nicolet Magna560 FTIR spectrometer on a NicPlan microscope at Texas A&M University, Center of Tectonophysics. Spectra have been recorded for wavenumbers from 650 to 4000 cm-1 at a resolution of 4 cm-1 with non-polarized light at room temperature with a collection time of 320 seconds per spectrum and 512 scans. A background has been recorded for every single spectrum. Variable aperture widths between 30*30 μm to 200*200 μm have been used to omit fractures and inclusions inside single grains.

The integral absorbances from 3000 - 3800 cm-1 have been calculated after the spectra have been corrected for a horizontal baseline using pbg provided by Asimov et al., 2006 and Omnic8.0© (Thermo Sci.). If necessary a mica peak at ~3624 cm-1 was subtracted from a common baseline prior to the determination of the integral absorbance related to water absorbance. Various calibrations exist for the determination of the water content in quartz measured from FTIR spectra (e.g. Katz, 1962; Paterson 1982; Libowitzky & Rossman,1997; Stipp et al., 2006).

From some samples FTIR-spectra of K-feldspars were also acquired. The calibration of Johnson & Rossman (2003) was used which differs by a factor of about 1.65 from the calibration by Hofmeister & Rossman (1985) as used in Kronenberg & Wolf (1990). No polarization was used and spectra were only acquired from one direction per feldspar grain, so that results only yield a qualitative estimate of the water content in K-feldspar.

Determination of white mica content inside quartz grains from FTIR spectra:
A peak at ~3624 cm-1 in the FTIR spectrum is caused by white mica (Serratosa & Bardley, 1958). The peak is found in quartz grains which contain inclusions of up to 10 μm long mica platelets. More commonly, optically clear quartz grains contain inclusions below 1 μm size.

FTIR spectra of muscovite from Methuen Township, Ontario, Canada (Mares & Kronenberg, 1993) were recorded parallel to [001]. Sheets of variable thickness between 105 - 15 μm (105 to 63 μm show a peak saturation) are obtained by manual cleaving. Sheet thicknesses were determined with a micrometer screw (see Appendix F).

Wt % muscovite ($100*m_{mus}/m_{qtz}+m_{mus}$) is calculated by deriving an integrated molar absorption coefficient k (L cm-2 mol-1) from the integral absorbance of the pure muscovite sheets using wt $\%_{ms}=(100*M_{mus}*A_{mus})/(d*\varrho_{qtz}*k)$ (Stolper, 1982). m is the mass, M is the molar mass, A is the integral molar absorption coefficient, d the sample thickness and ϱ_{qtz} the density of quartz. The composition for the muscovite used for calibration is given by Mares & Kronenberg (1993) and is similar to phengites analyzed in the Truzzo granite (Marquer et al., 1994) (see Appendix G).

The peak used for the calibration is at 3629 cm-1, and not 3624 cm-1, due to the differences in composition. The calculated values must be regarded as a lower limit as dioctahedral micas have OH-bound axes (sub)perpendicular to (001) (Serratosa & Bradley, 1958) and experience the largest IR absorbance with the beam parallel to [001]. Mica inclusions are found to be oriented randomly.

Double polished thin sections of 120 to 200 μm have been prepared using Deiberit 502 dental wax as a glue. The wax shows a strong IR peak for the CH bonds at 2850, 2920 and 2955 cm-1 which can be present in spectra if the wax was not fully removed. Such spectra can always be used because as the wax does not contain any significant absorption in the range or 3000-3800 cm-1 (see Appendix H).

Sample Tr3-3 and Tr3-1 have been additionally heated for 24h at 120°C. This reduces a broad absorption band caused by water bound on surfaces of cracks and open grain boundaries while a broad band due to fluid inclusions is not affected by the heating procedure.

3.2 Microstructures and CPO

Microstructures in the ultramylonitic samples were examined using scanning electron microscope backscatter electron (SEM/BSE) images. EBSD orientation maps and EDX (energy dispersive x-ray spectroscopy) element maps were prepared from selected samples. C-axis polefigures and orientation maps were obtained by CIP (ref) in polycrystalline, monomineralic quartz aggregates and by EBSD in the polymineralic ultramylonite and in the samples previously used for FTIR analysis.

Particle and surface fabrics for quartz were quantified using PAROR and SURFOR (Panozzo, 1983,1984) on segmented EBSD orientation maps. Angles are always counted against the sense of shear with 0° parallel to X.

3.3 Crystallographic preferred orientation (CPO) dependent fabrics

Orientation maps have been calculated using ”flat” inclination and azimuth images and orientation look-up tables that produce binary images which only display certain orientations using CIP2 (Heilbronner & Pauli, 1993). “Flat” refers to grains which are assigned a single mean orientation. Grains are defined by a grain boundary map. The input azimuth and inclination images are obtained from EBSD Euler angle images. For details see Chapter 2.

Particle and surface fabrics were calculated the binary images which only contain grains of a certain orientation specified in the look-up table.

3.4 Fabric dependent CPO

The masking of grains which contribute to a certain fabric element is not straightforward and therefore the EBSD grain segmentation of OIM® was used which provides one orientation per grain, the long and short axis of a best fit ellipse and the orientation of the grain ellipse long axis. CPOs were calculated from the mean grain orientation using the Mtex toolbox (Hielscher & Schaeben, 2008) for certain values of the grain long axis orientation and aspect ratio.

The long axis orientation of grains segmented by OIM® does not cover orientations of -5 to +5° and 85 to 95°, both of which orientations must be considered as a fault in the OIM® software. Manual segmentation does not show a gap in particle orientations parallel to the coordinate axes. Angles are always counted against the sense of shear with 0° parallel to X.

3.5 Chemical composition

The chemical composition minerals was determined on a Jeol JXA8600 microprobe equipped with an Thermo UltraDry energy dispersive spectrometer. Feldspar compositions are calculated with 8 oxygen per formula unit, mica compositions with 11 oxygen ignoring H_2O.

3.6 Grain size analysis

Grains sizes are always given as the diameter. $\mu_h(D)$, $\mu_v(D)$ are the number and the volume weighted mean diameter of spheres calculated from the distribution of the equivalent diameter obtained from the crossectional areas of grains. $\mu_h(d)$ is the number weighted mean equivalent diameter obtained from the crossectional areas of grains. For details on the grain size analysis see Methods in Chapter 2.

4. Results

4.1 Petrography and microstructures in the Truzzo granite and shear zones

4.1.1 Petrography and microstructures: overview

Primary magmatic minerals are quartz, microperthitic K-feldspar, plagioclase$_1$, brown biotite$_1$, white mica$_1$ and opaques. Magmatic single quartz grains are ~5-10 mm in diameter. Some magmatic grains show no indication for intracrystalline deformation while others show recovery related structures such as subgrains parallel to the prism-planes and chessboard pattern (the latter associated with high temperature, the former with lower temperature recovery).

Recrystallized quartz grains form around the margins and inside magmatic grains (Fig. 10a). The size is highly variable (60-600 μm) and in cases it is difficult to distinguish recrystallized grains from relict magmatic grains in the light microscope (Fig. 10b). In highly stretched layers the mean grain size $\mu_{v(D)}$ is 260 μm and $\mu_{h(d)}$ is 110 μm. Grains show a weak shape preferred orientation (Fig. 11).

Recrystallized quartz grains in aggregates have lobate grain boundaries, show island structures and left-over grains. Some recrystallized grains contain optical subgrain boundaries. This is most obvious in highly stretched layers as all grains can be expected to be recrystallized.

In some samples, especially in those from a weakly deformed part of the low strain domain as well as in broad shear zones (Tr6), recrystallized grains show subgrain boundaries, small optical subgrains and a higher grain boundary lobateness (Fig. 12a,b). Optical subgrain cells are approximately ~ 20-60 μm diameter. Parallel optical subgrain boundaries usually trace the quartz prism planes.

Magmatic K-feldspar grains form large idiomorphic crystals. K-feldspars clasts are internally dissected by mixtures of fine grained oligoclase (An$_{20}$) and quartz (Fig. 13). Oligoclase - quartz mixtures occupy either fractures, indicated by the offset of twin boundaries in the K-feldspar or replace former coarse perthite domains (An$_{0-2}$). The remaining K-feldspar show cross-hatched fine perthite lamella and locally (late) flame perthites (An$_{0-10}$). K-feldspar recrystallizes along the rims and forms fine grained (10-30 μm) tails (e.g. Fig. 8c).

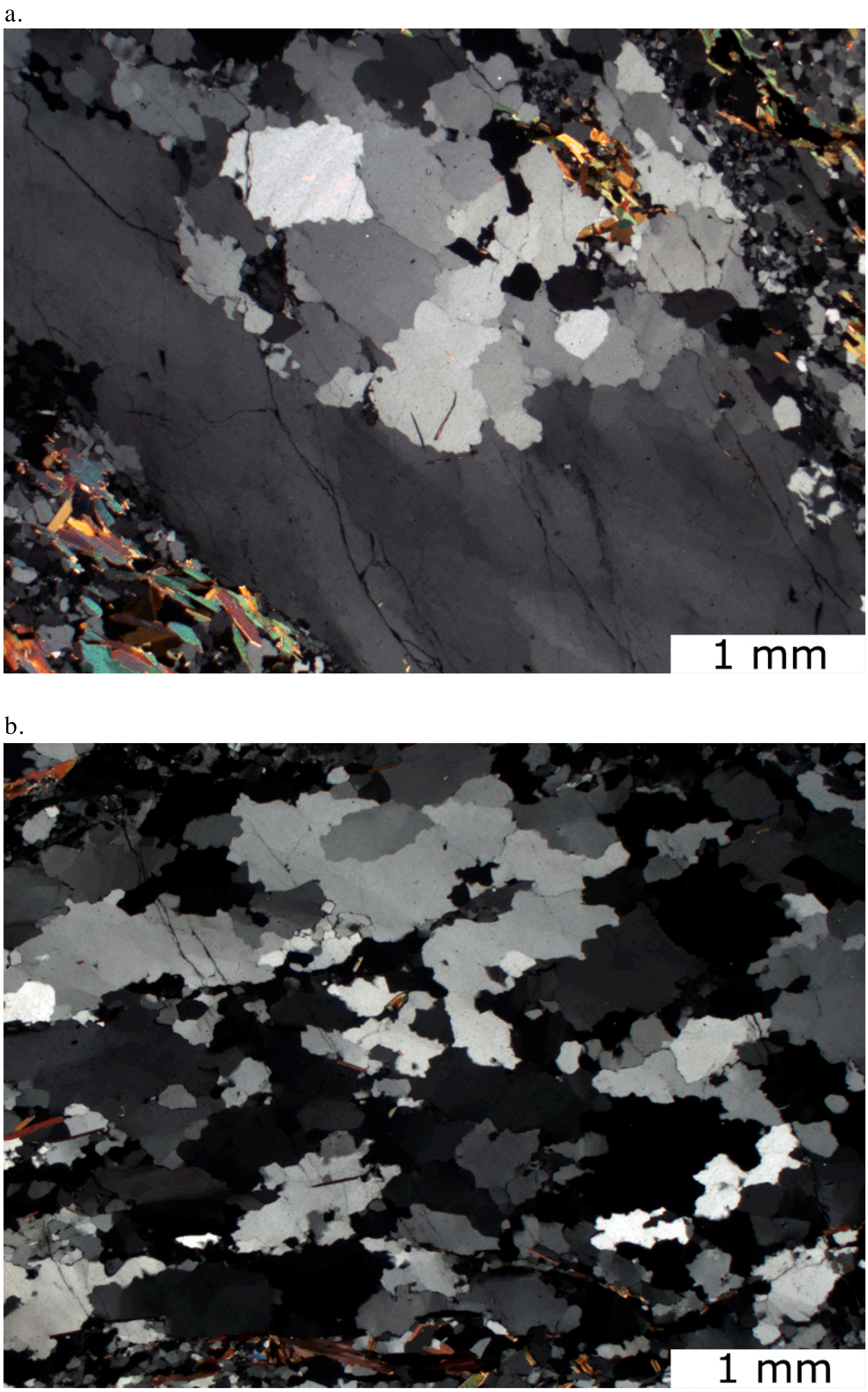

Fig 10: Quartz microstructure (1): (a) Magmatic quartz grain partially replaced by recrystallized grains. Sample Tr-1, outside of a shear zone. (b) Recrystallized grains. The microstructure is inferred to have formed by grain boundary migration recrystallization. It is difficult distinguish recrystallized grains from relicts of magmatic grains. Sample Tr1-2b.

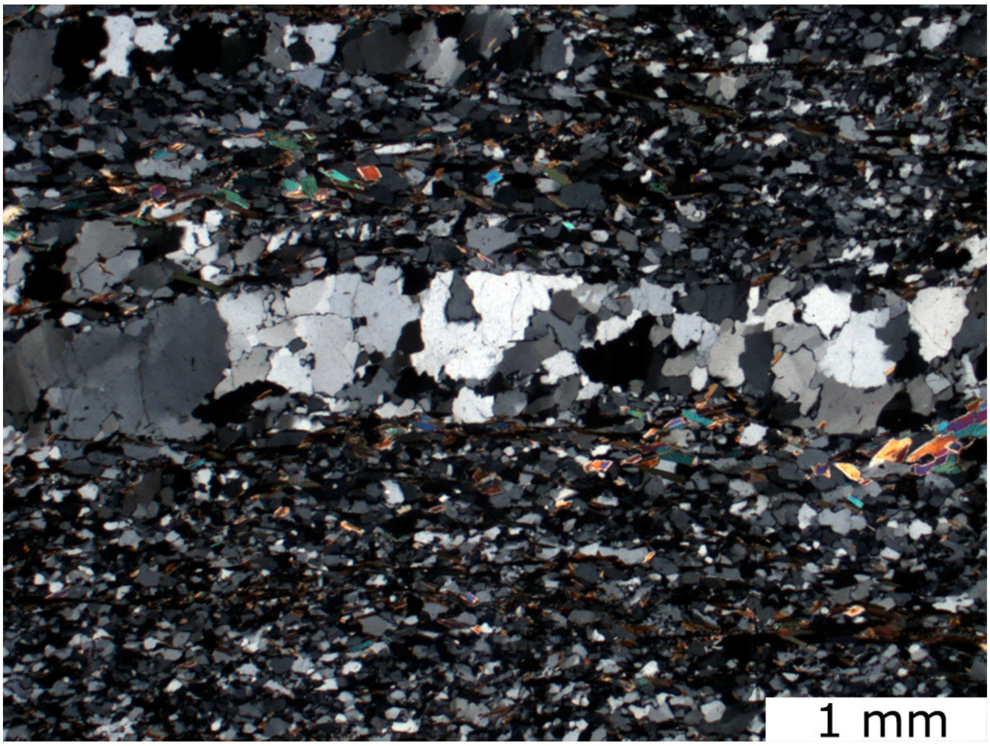

Figure 11: Layer of recrystallized quartz: Micrograph, crossed polarizers of a foliation parallel layer of recrystallized quartz. Sample Tr12. The microstructure is dominated by grain boundary migration recrystallization though some grains show optical subgrain boundaries. Shear sense is dextral.

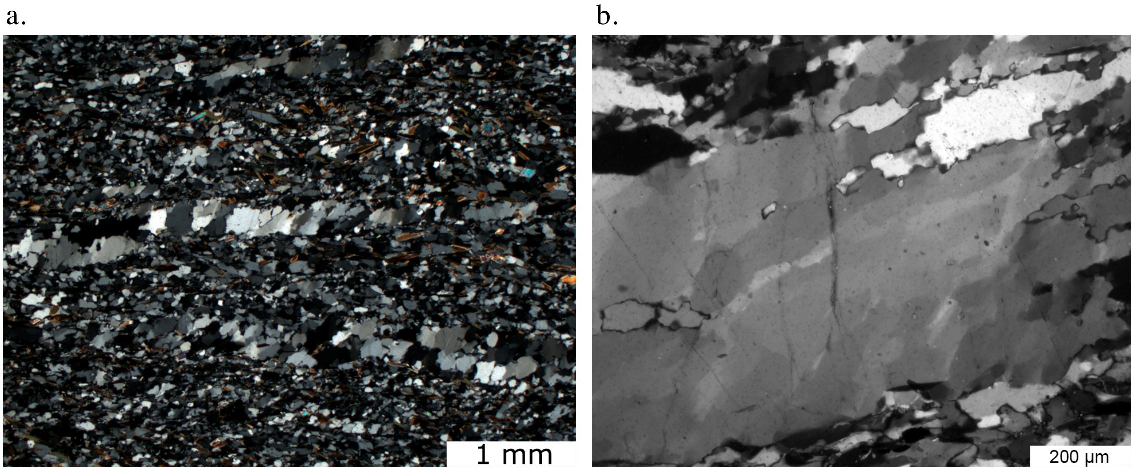

Figure 12: Overprint on quartz microstructure (1) and (2): (a) Micrograph, crossed polarizers of a fully recrystallized quartz layer showing an oblique particle fabric, locally optical subgrain boundaries and small recrystallized grains along the grain boundaries of the large grains. (b) Micrograph, crossed polarizers of a large recrystallized quartz grain which shows intense dissection by optical subgrain boundaries and lobate grain boundaries as well as newly recrystallized grains in the upper right. Sample Tr12.

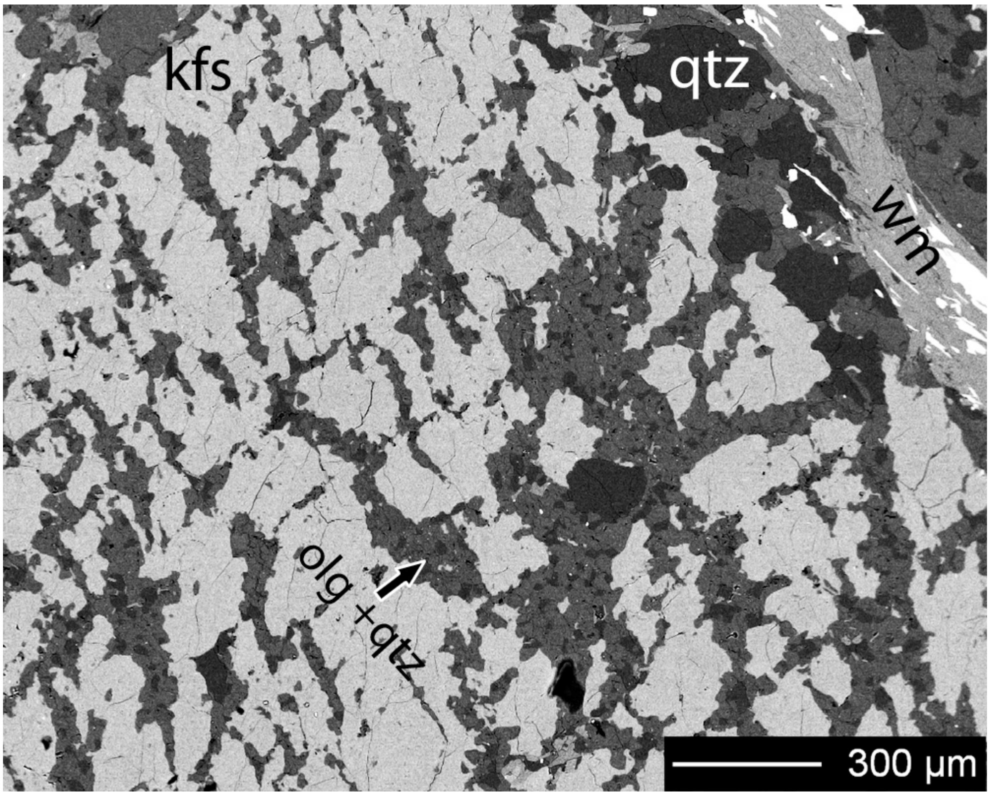

Figure 13: Replaced perthites in K-feldspar: SEM/BSE image of a K-feldspar grain which is dissected by lamellae of fine grained oligoclase - quartz mixtures. Sample Tr1.

Unrecrystallized K-feldspar crystals contain inclusions of biotite and polycrystalline granoblastic plagioclase$_2$ (An_{20} grains with An_{26} cores) and white mica$_2$ pseudomorphs after idiomorphic plagioclase$_1$ (Fig. 14, Appendix K). Occasionally, relics of the magmatic plagioclase$_1$ are preserved in these inclusions inside K-feldspar. The inference of a magmatic origin is based on the microstructure but the composition of plagioclase inclusions is to the same as the fine grained plagioclase$_2$ in the pseudomorphs, the plagioclase$_2$ in the replaced perthites, myrmekites, and inside the matrix (An_{20}). Occasionally fine grained plagioclase inside the pseudomorphs contains cores of An_{26} composition, and locally patches of albitic composition (An_{0-5}) occur.

Pseudomorphs have thin quartz rims between plagioclase$_2$ and K-feldspar (Fig. 14). The transformation of magmatic plagioclase did not happen as a result of dynamic recrystallization but by neocrystallization to a more Ca-rich composition, probably after high pressure and during high temperature conditions. Outside of K-feldspar magmatic plagioclase$_1$ has never been observed. Fine grained plagioclase$_2$ + white mica$_2$ aggregates are common everywhere. The grain size of plagioclase$_2$ is ~10-40 μm.

Magmatic biotite$_1$ has a brown color and contains abundant inclusions of opaques. Recrystallized biotite$_2$ forms around magmatic biotite as well as dispersed between the other components. Recrystallized grains are inclusion free and show the same brown color as the magmatic grains. At low strain biotite$_2$ forms layers and polycrystalline aggregates whereas at high strain it occurs as single, non-connected grains in polymineralic mixtures.

Magmatic white mica$_1$ is occasionally intergrown with biotite$_1$. In some aggregates white mica$_2$ is seen to be replaced by biotite$_2$, occasionally associated with epidote and clinozoisite. White mica$_2$ most often forms in plagioclase grains of all types. The white mica$_2$ composition inside pseudomorphs is equal to the composition of white mica$_2$ in the matrix (see Appendix K).

Idiomorphic garnet (d ~200 μm) grows within folia of recrystallized biotite$_2$ or inside plagioclase$_2$ aggregates rimmed by biotite. Clinozoisite or epidote are rarely associated within the feldspar mixtures but occasionally found in mica domains. Other accessory minerals are idiomorphic apatite forming porphyroclasts and zircon.

Myrmekites nucleate at the plagioclase inclusions and bulge into the K-feldspar and are also observed to form along fractures and marginally to K-feldspar clasts as well as inside the recrystallized K-feldspar tails (Fig. 14). Some oligoclase - quartz mixtures originate from coarsened myrmekites.

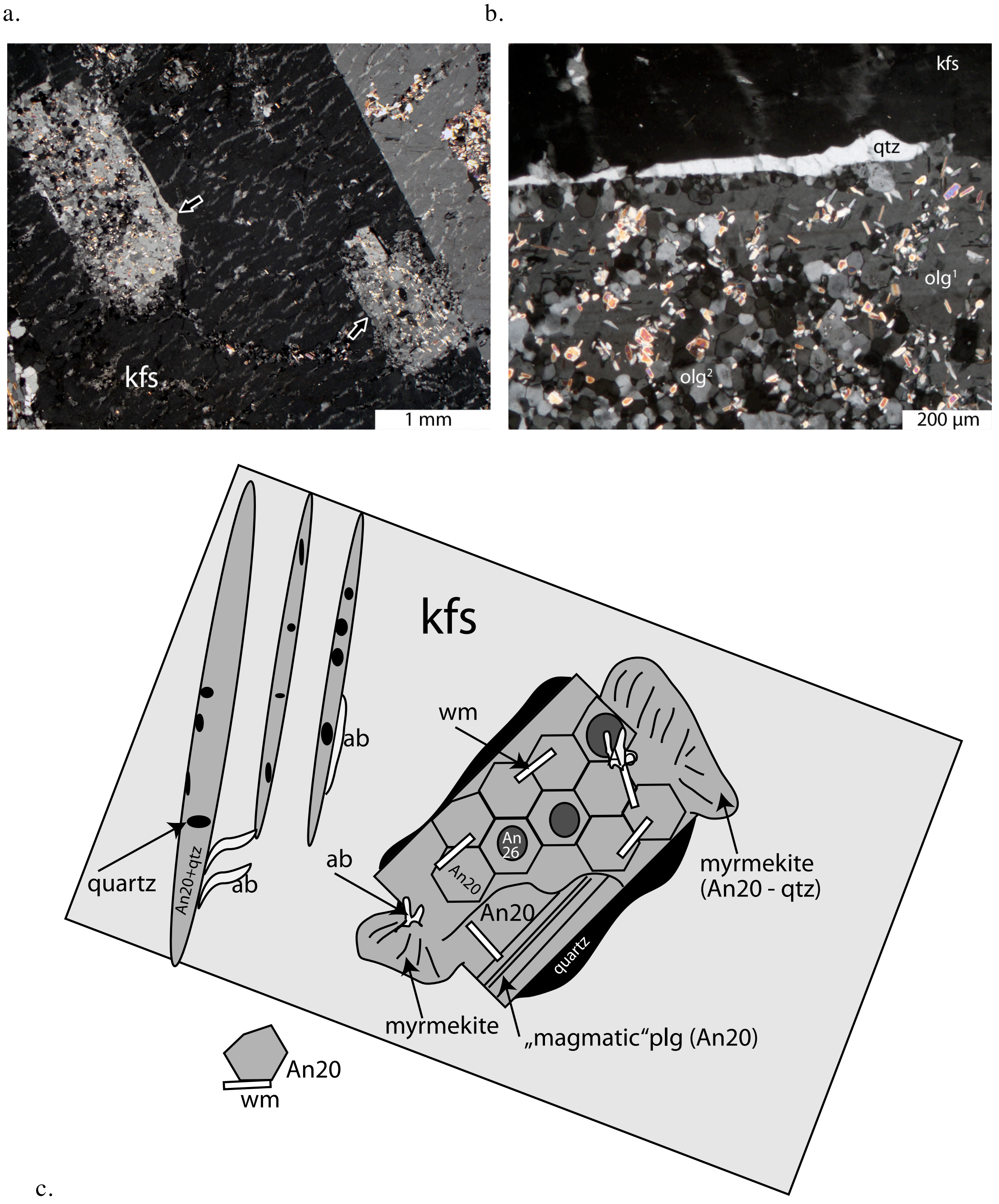

Figure 14: (a),(b) Plagioclase inclusions in K-feldspar: Micrograph, crossed polarizers of a large magmatic K-feldspar phenocrysts showing in inclusions relicts of magmatic plagioclase.The magmatic plagioclase is partially replaced by fine grained plagioclase. White mica is intergrown with both, recrystallized and the plagioclase inclusion. Sample Tr1. See text for discussion. (c) Conceptual sketch showing the composition and relation of phases of inclusions in K-feldspar. kfs: K-feldspar, ab: albite, AnX:plagioclase with X% anorthite component, wm: white mica. The white mica composition inside the inclusion and in the matrix are identical (see Appendix K).

4.1.2 Overprinting relations

In some samples, e.g. Tr7 elongate aggregates of recrystallized biotite$_{2,3}$ may show an internal foliation defined by the orientation of biotite$_{2,3}$ flakes which is oblique to the aggregate long axis (Fig. 9b). This orientation of the internal foliation is parallel to the preferred biotite orientation in fine grained mafic enclaves where biotite$_{1,2}$ forms clusters of few grains. This overprint is observed in samples close to the margin of the low strain domain. More highly deformed parts of the mylonitic Truzzo granite also show an overprint of an earlier high temperature asymmetric fabric by a biotite$_{2,3}$ foliation.

Another type of overprint is observed in thin layers in the broad shear zones. Quartz shows a strong substructure, subgrains and a very small recrystallized grain size (~< 20 μm) and fine grained layers of recrystallized biotite, white mica$_3$ together with epidote, clinozoisite and rarely chlorite (Fig.15). White mica$_3$ replaces biotite$_2$ in these layers. These layers are close to the above mentioned quartz aggregates which show prismatic subgrains (Fig. 12).

Chloritized biotite is infrequent and only found in few samples. Magmatic biotite as well as recrystallized biotite$_{1,2}$ can be chloritized, and also undeformed inclusions of biotite inside K-feldspar are affected. Therefore chloritization is assumed to be static and late.

4.1.3 Fluid and solid inclusions

Magmatic quartz grains usually contain fluid and solid inclusions (Fig. 16a,b). Fluid inclusions occur either in dispersed clouds or in discrete fluid inclusion trails (healed cracks). Healed cracks cut across grain boundaries and may occur in recrystallized grains (Fig. 16a).

Recrystallized grains are generally free of dispersed fluid inclusions (Fig. 16). Recrystallized grains inside the shear zone are optically clear and only have inclusions of larger biotite flakes and infrequently discrete fluid inclusion trails (Fig. 16c,d).

Fluid inclusions have variable shapes ranging from negative crystal shapes to irregular, stretched or decrepitated shapes (Fig. 16). In the larger inclusions, a liquid and a CO_2- rich gas phase can be identified. Occasionally two bubbles are observed which do not homogenize at temperatures up to 45°C.

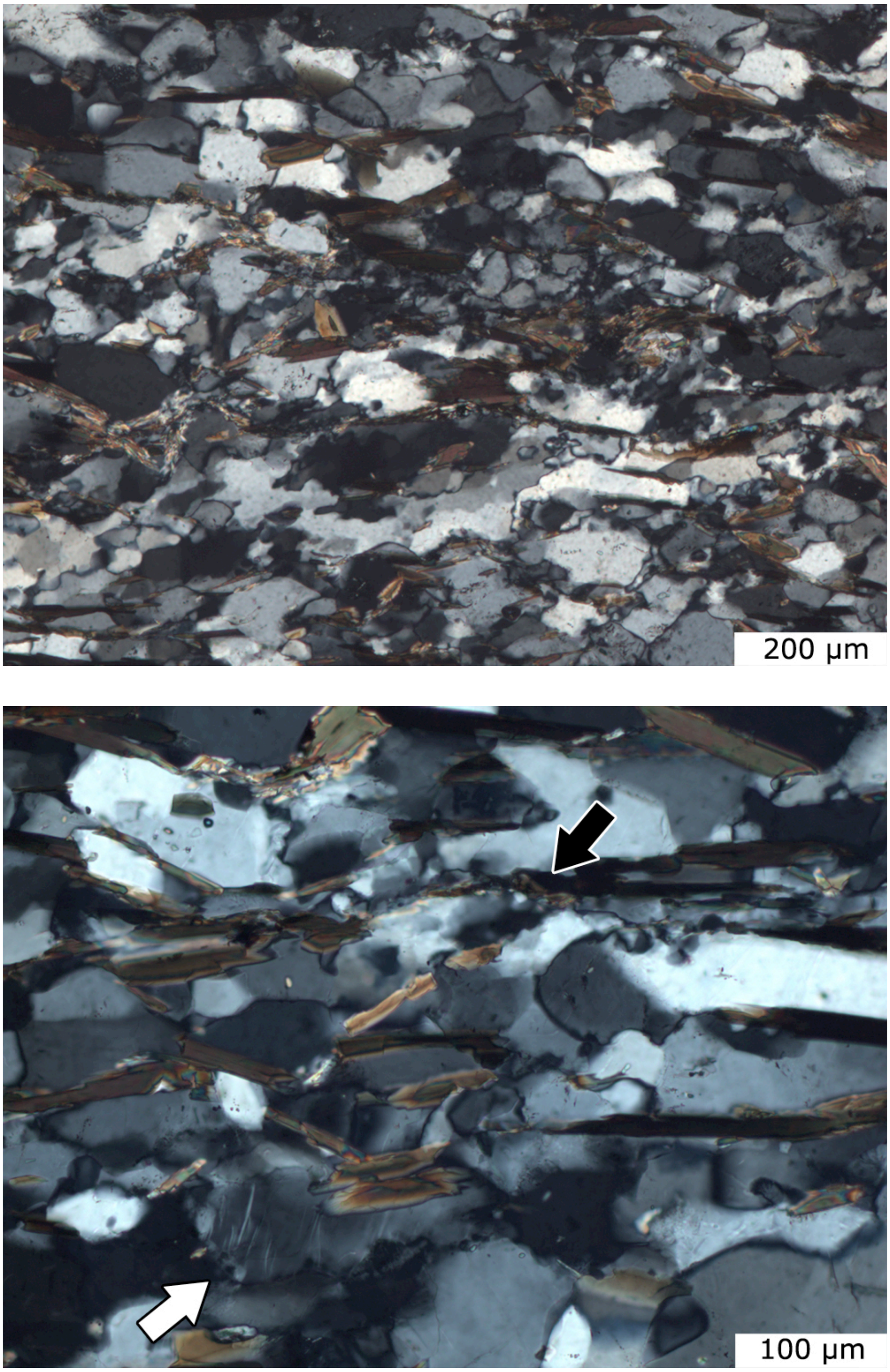

Figure 15: Late overprint in the ultramylonite: Micrographs, crossed polarizers, showing the latest overprint observed in the ultramylonitic cores of shear zones. Biotite breaks down and dispersed quartz grains recrystallize by subgrain rotation and bulging to a much smaller grains size in continuous layers (black arrows). K-feldspar shows albitic flame perthites (white arrow) (Sample Tr12).

Most solid inclusions are mica sheets and needles of variable size. Magmatic quartz grains show the finest inclusion size, often less than 5 μm in length. Very rarely, large idiomorphic white mica occurs inside magmatic quartz grains.

In recrystallized grains directly adjacent to very inclusion rich magmatic quartz grains the size of solid inclusions is increased > 10 μm. The coarsened inclusions in the recrystallized grains often are brown biotite (Fig. 16c). Most recrystallized quartz grains in the highly strained regions are free of small mica inclusions. Nevertheless some recrystallized quartz grains show large (~50 μm) subhedral brown biotite inclusions which are frequently associated with small satellite biotite grains (Fig. 16d).

4.1.4 Quartz aggregates

Quartz aggregates deform heterogeneously inside the feldspar matrix. The elongation of quartz aggregates is variable, both inside the shear zones and in the low strain domains (Fig. 8). In the central part of the shear zone in sample Tr3-3 the aspect ratios of directly adjacent quartz aggregates varies between 1.5 and > 15. Some shear zones are only slightly wider than the large quartz aggregates and therefore homogenous deformation is not to be expected.

In the broad ultramylonitic shear zones (Tr6) quartz aggregates may form layers (with aspect ratios > 40) which are a few grains thick (Fig. 11). In some parts of the ultramylonite short quartz aggregates form sigma clasts.

4.1.5 Ultramylonite and phase mixtures

The widest shear zones accommodate the highest displacement and develop ultramylonitic layers. The transition from the undeformed or low strain rock to the ultramylonitic layers occurs over a very small distance (Fig. 5). The high degree of phase mixing and, the highest strains are found at the margins of such shear zones (Fig. 5a,c,d). The ultramylonite consists (sample e.g. Tr6) of a phase mixture with only relict K-feldspar and quartz aggregates as porphyroclasts. Individual quartz grains have a grain size of about $\mu_{h(d)}$ 45 μm and $\mu_{v(D)}$ 70 μm which is also the range of oligoclase and K-feldspar grains (Fig. 17a). Biotite is dispersed as single grains between the feldspar and quartz (Fig. 17a, 9a).

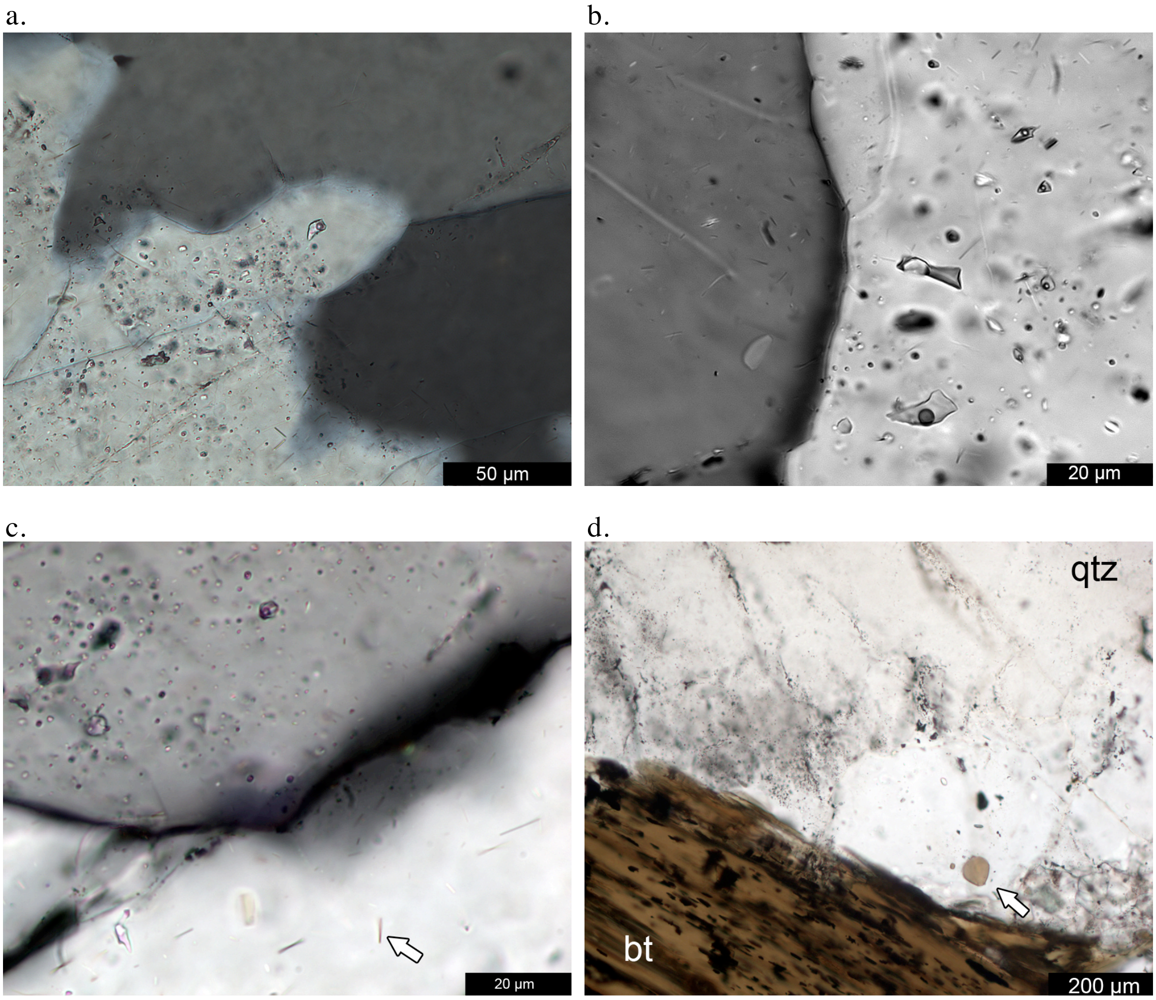

Figure 16: Fluid and solid inclusions in quartz: (a) Micrograph, crossed polarizers of a fluid inclusion rich magmatic quartz grain (left) and two recrystallized grains which only contain few fluid inclusions. A fluid inclusion trail cuts acoss the grain boundary between the magmatic and the recrystallized grain. (b) Micrograph, crossed polarizers of a magmatic grain with variably shaped fluid inclusions (right) and a recrystallized grain (left) free of fluid inclusion but with few biotite needles. (c) Micrograph, crossed polarizers of a magmatic grain with fluid inclusions (top) and a recrystallized grain (bottom-right) free of fluid inclusion but with larger biotite needles. (d) Micrograph, plane polarized light of magmatic biotite (bt) and a magmatic quartz grain with irregular clouds of fluid and solid inclusions. An inclusion-free quartz grain migrates into the magmatic grain and contains a larger inclusion of biotite with small satellite inclusions (white arrow) (Sample Tr1).

K-feldspar - quartz layers form by the disintegration of polycrystalline quartz aggregates and the preferential precipitation of K-feldspar and biotite between quartz grains (Fig. 17b,c). Quartz aggregates preferentially separate along dilatant grain boundaries subnormal to the foliation (Fig. 17). Two types of quartz grains can be distinguished. Elongate and obliquely oriented quartz grains in quartz - K-feldspar layers originate from disintegrated former pure quartz layers (Fig. 17b). Some quartz grains formed by coarsening of myrmekites and replaced perthites. The latter grains are more round and smaller (Fig. 13). At higher strain the degree of phase mixing increases and the distinction between quartz grains of different origin is not possible.

Quartz , plagioclase (oligoclase/andesine), K-feldspar, and biotite show grain-scale phase boundary bulges (Fig. 17d). In the complete phase mixtures phase boundary migration is common between plagioclase. Quartz and boundary bulges are found pointing towards both migration directions. Plagioclase preferentially bulges into K-feldspar and K-feldspar preferentially into quartz.

4.1.6 Quartz crystallographic preferred orientation and microstructures

Quartz crystallographic preferred orientations of recrystallized grains have been determined using CIP and EBSD. In general four different microstructural situations can be distinguished: (1) fully recrystallized but weakly deformed quartz aggregates, often situated in the deformed wall rock at shear zone margins, (2) fully recrystallized quartz aggregates which form shear-zone-parallel layers, (3) partially disintegrated quartz layers, and (4) fully dispersed quartz grains in a homogeneous phase mixture.

These 4 microstructure types each have a characteristic grain size, fabric, texture, and phase distribution:

(1) Coarse grained, completely recrystallized quartz aggregates are developed in homogeneously deformed areas where initial shear zones develop with SC/SC' foliations (Fig. 10b). Aggregates are deformed and slightly elongate. These aggregates do not no show a crystallographically preferred [c]-axis orientation that can be distinguished from random (Fig. 18). The microstructure in these aggregates indicates recrystallization by grain boundary migration. Most grains are elongated subparallel to the aggregate elongation. The grain size ranges between 300 and 1000 μm diameter with a mean of $\mu_{h(d)}$ 650 μm. Some grains show prism parallel optical subgrain boundaries.

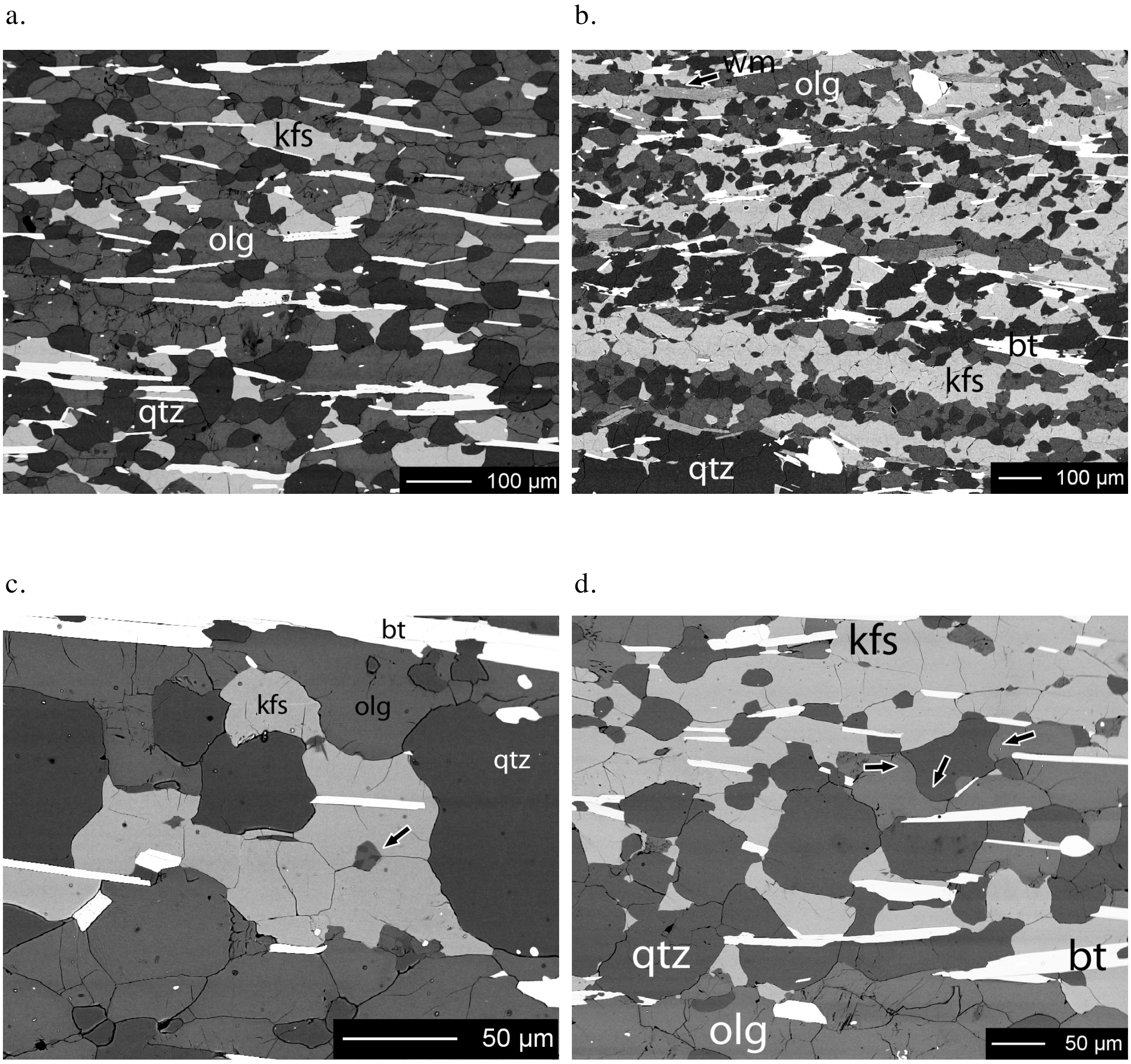

Figure 17: Microstructures in the phase mixture: SEM/BSE images of (a) a phase mixture of quartz, oligoclase, K-feldspar and biotite in the ultramylonitic part of the shear zone. (b) Disintegration of quartz layer by K-feldspar precipitation between quartz grains. Note the angular shape and the oblique orientation. (c) K-feldspar and biotite precipitate between quartz grains. Note the formation of a small volume of myrmekite in the K-feldspar. K-feldspar bulges preferentially into quartz while oligoclase bulges into K-feldspar (d) Quartz- K-feldspar- oligoclase biotite mixture. Phase boundaries are curved and migration directions are bipolar (arrows). qtz:quartz, olg: oligoclase, kfs: K-feldspar, bt: biotite, wm: white mica.

(2) Entirely recrystallized aggregates form layers, which are a few grains wide, within the shear zones (Fig. 19a). The microstructure in the layers are indicative for grain boundary migration recrystallization. Layers show CPOs composed of combinations of four CPO elements: an inclined peripheral [c]-axis maximum subnormal to the layer, single maxima subparallel to the lineation

(see Appendix J), a girdle subnormal to the layer, and a Y-maximum. Maxima are rotated with the shear sense into slightly inclined orientation (Fig. 19b).

Quartz grains show a particle fabric with a b/a_{bulk} of 0.83 at 5°. The rose diagram of the surface orientation distribution function (ODF) has a monoclinic geometry and a major maximum close to the lineation and a minor maximum at ~50° This asymmetry is consistent with the shear sense inferred from sigma clasts and the interpretation of an oblique mica foliation as a C' foliation (Fig. 19c). The mean grain size in e.g. Tr6-2 of $\mu_{h(d)}$ of 70μm and $\mu_{v(D)}$ of 260 μm (n ~150) is smaller than quartz aggregates in the shear zone margin (Fig. 19d).

(3) Thin quartz layers laterally disintegrate by dilatancy between quartz grains typically filled by K-feldspar precipitation (Tr6-2-27c, Tr6c) (Fig. 20a). In this way, quartz and K-feldspar form bimineralic layers. The quartz CPO is weak but distinct from random (Fig. 20b). Area weighted pole figures show a major maximum of [c]-axes at the periphery at ~130° with respect to the lineation and a minor maximum at the periphery at ~10° (Fig. 20b). The distribution of <a>-axes is less systematic and forms a weak girdle perpendicular the [a]-axis maximum (Fig. 20b). The grain size has a mean $\mu_{h(D)}$ of 35 μm and $\mu_{v(D)}$ of ~ 80 μm (n = 1093) (Fig. 20c).

Disintegrated layers consist of small, separated quartz grains and clusters of few larger quartz grains. Large grains show subgrain boundaries parallel to the trace of the prism plane. The particle fabric has a b/a_{bulk} of 0.72 at ~15°. The rose diagrams of the surface orientation distribution function are orthorhombic with a single maximum at ~15° in the rose diagram (see section 4.2, Fig. 28).

(4) Dispersed quartz grains occur in polymineralic layers which consist of a homogeneous distribution of plagioclase, K-feldspar, biotite and ± white mica (e.g Tr6-2-7-20) (Fig. 21a). Relict clusters of quartz grains are present but only a few grain boundaries are preserved. The [c]-axis CPO is very weak but distinct from random. [c]-axes form a peripheral maximum to a weak single girdle at ~40° and <a>-axes form a weak maximum at the periphery, perpendicular to the [c]-axis girdle (Fig. 21b).

The uncorrelated misorientation is close to random and the correlated misorientation distribution shows a peak between 5-10° (Fig. 21c). This peak indicates the presence of subgrain boundaries and probably low angle orientation relations between adjacent grains in relict clusters, despite the globally weak CPO.

The grain size has a mean $\mu_{h(D)}$ of 35 μm and $\mu_{v(D)}$ of ~ 55 μm (n =2728) (Fig. 21d). Larger grains occasionally show prismatic subgrain boundaries. Quartz displays a weak particle fabric with a b/a_{bulk} of 0.8 at ~10° and a slightly stronger, orthorhombic surface fabric with a maximum at 10-15° in the rose diagram (see section 4.2, Fig. 29).

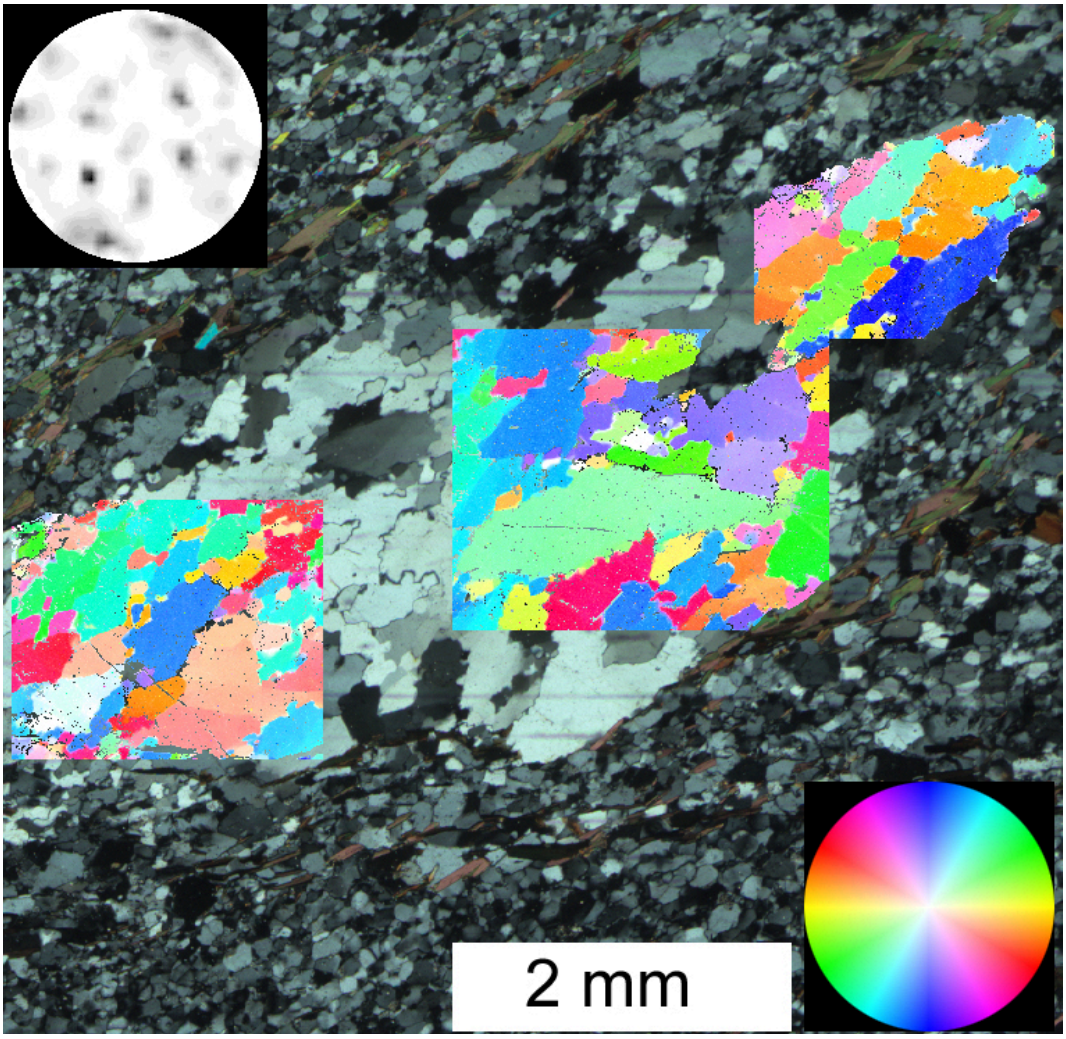

Figure 18: Quartz microstructure (1): CIP-derived quartz c-axis orientation image underlain with the thin section scan, crossed polarizers. The maximum of the joined polefigure is around 10 which is the result of the single grain effect. The polefigure cannot be distinguished from a random polefigure.

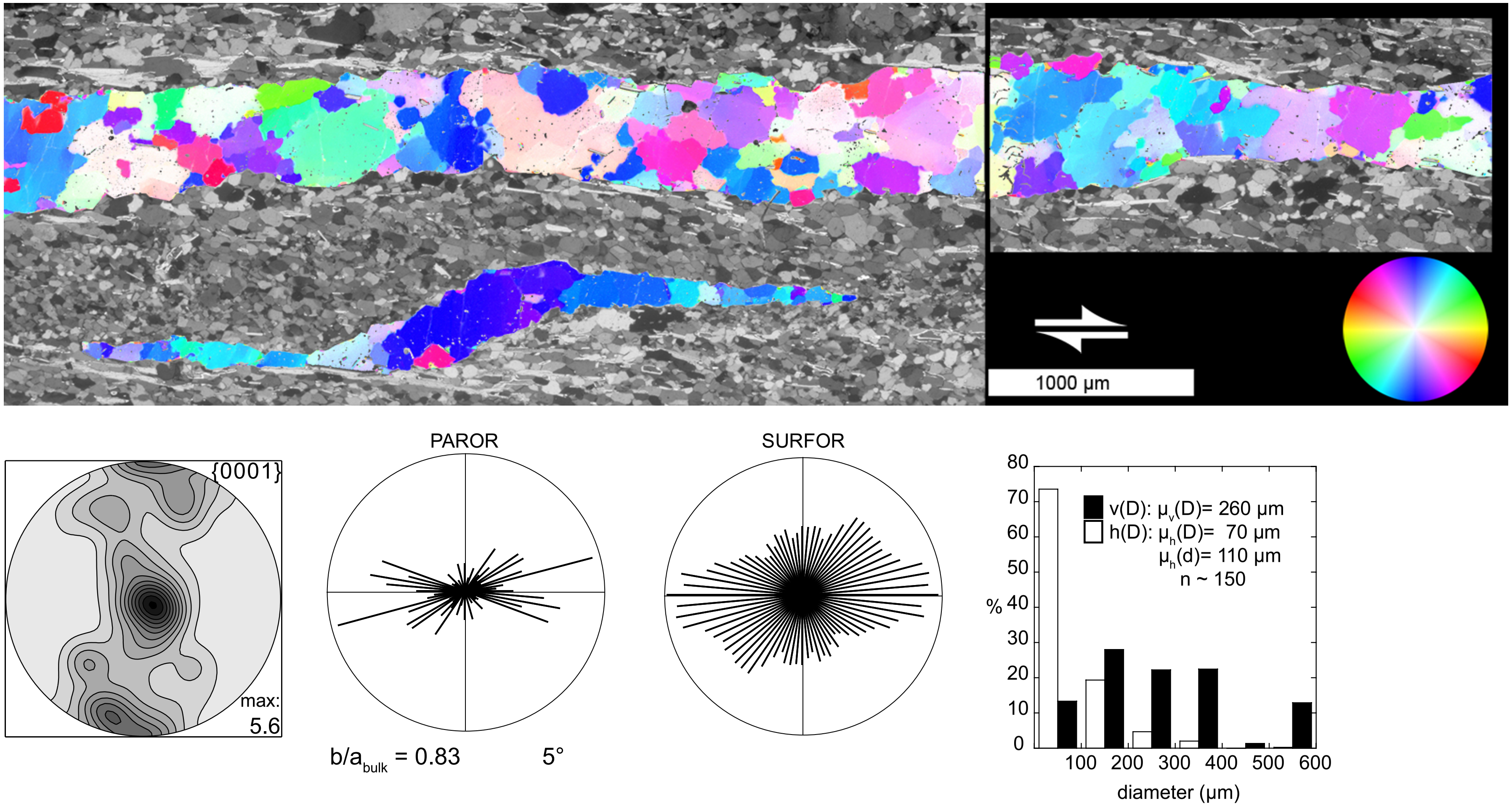

Figure 19: Quartz microstructure (2): (a) CIP derived quartz c-axis orientation image underlain by a circular polarization micrograph. (b) c-axis polefigure, calculated with 10° kernel halfwidth, area weighted, contours each 0.5 times uniform distribution. The corresponding maximum for 5° kernel halfwidth (CIP-standard) is 10.1. (c) PAROR and SURFOR rose diagrams. (d) Grain size distribution.

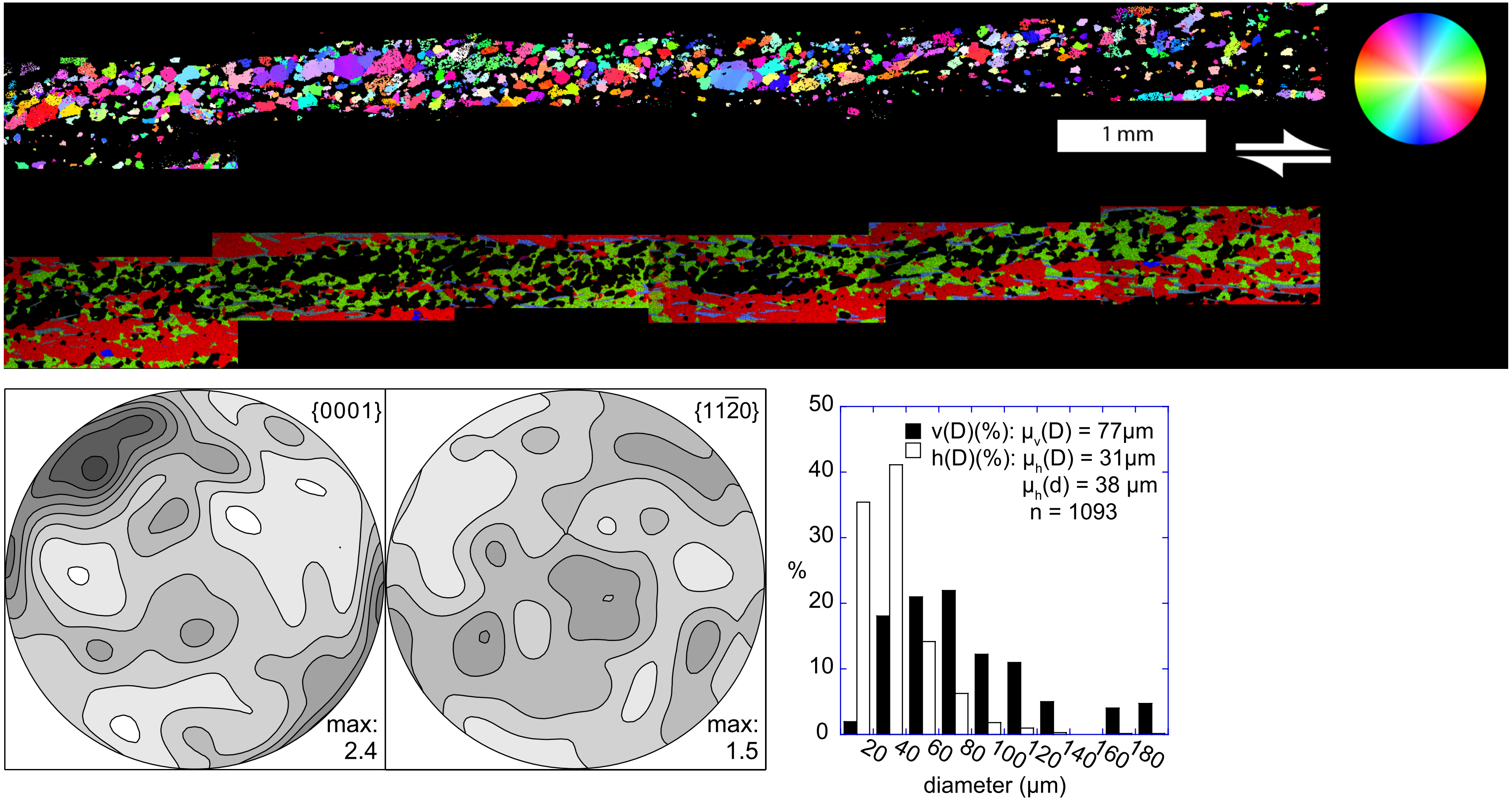

Figure 20: Quartz microstructure (3): (a) EBSD derived c-axis orientation image and EDS derived composition maps. Step size 5μm. Dextral shear sense. Black= quartz, Red= plagioclase, Green= K-feldspar, Blue= mica,others. (b) Polefigure for c and a-axes, 10° kernel halfwidth,area weighted,contours each 0.3 times uniform distribution. (c) Grain size distribution. Sample Tr6c.

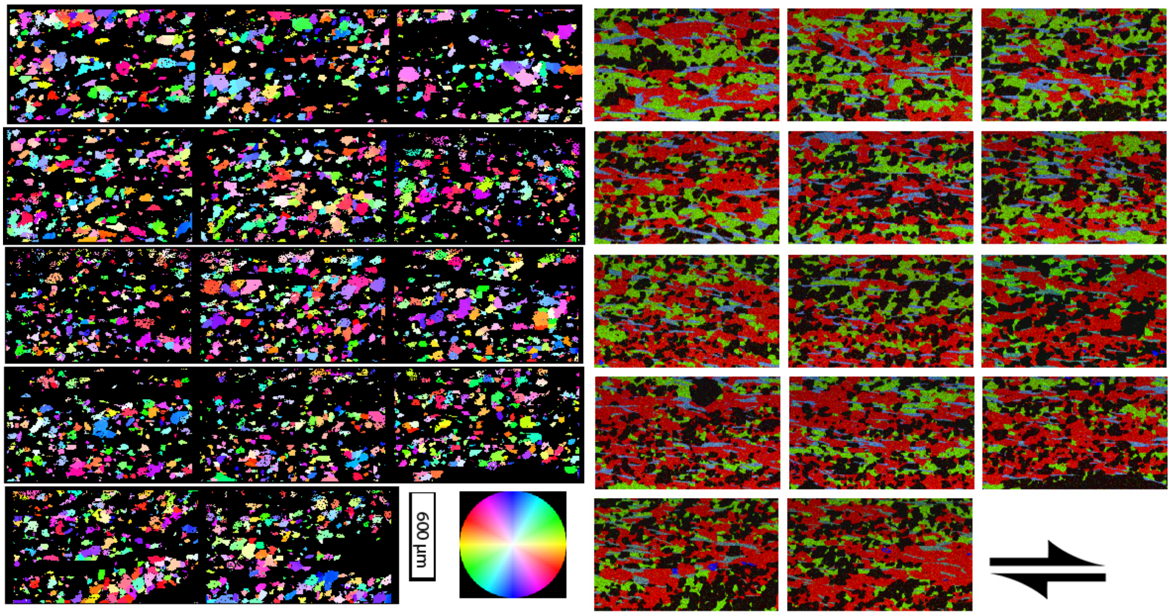

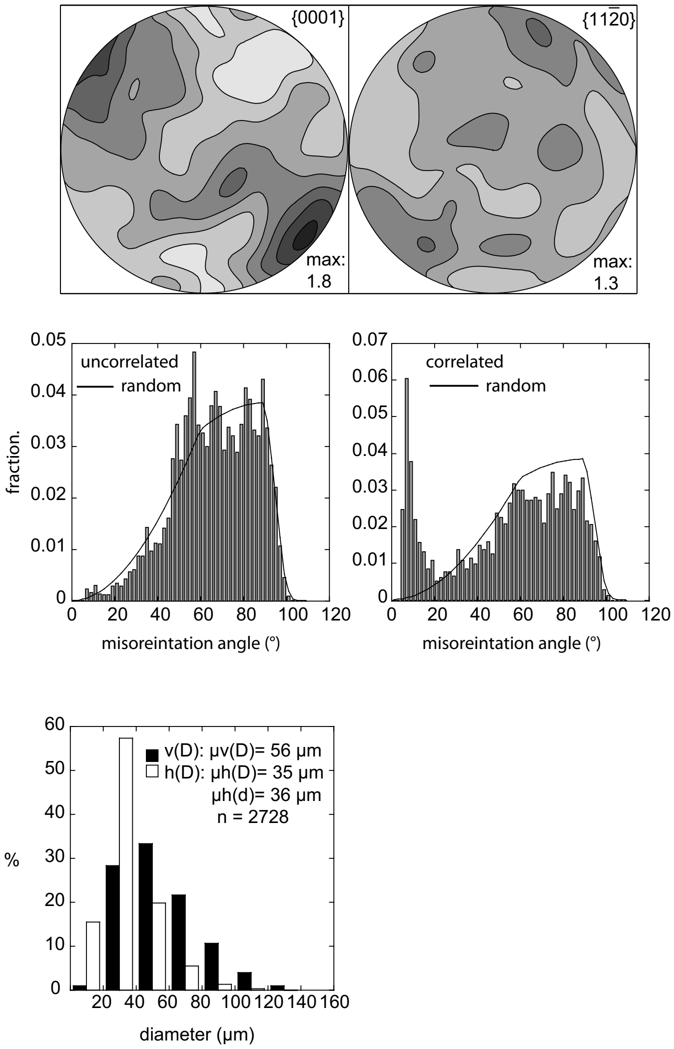

Figure 21: Quartz Microstructure (4): EBSD derived c-axis orientation image and EDS derived composition maps.Step size 6 μm. Black= quartz, Red= plagioclase, Green= K-feldspar, Blue= mica,others. Maps are acquired in a lateral continuous layer but have gaps of few microns between each map. Dextral shear sense. (b) Area weighted c- and a-axis polefigure. 10° kernel halfwidth, contours at 0.3 times uniform distribution. (c) Uncorrelated and correlated misorientation histograms. Black line indicates random distribution function for the rhombohedral system. (d) Grain size distribution.
Sample Tr6-2-7-20

4.2 Detailed relation of CPO, fabric, and grain size

Quartz in microstructures of type 3 and 4 with dispersed grains, a particle preferred orientation, and weak CPOs have been analyzed in more detail.

CPO for different grain sizes, grain elongations and long axis orientations orientations are compared. Additionally the particle and surface fabrics of grains owing to a certain component of the [c]-axis pole figure have been calculated. In all cases the strength of the CPO are very weak, but most [c]-axis pattern can be distinguished from random.

In microstructure (3) (Tr6c_1-6) the smallest grains show a peripheral [c]-axis maximum at ~110-120° (Fig. 22a). The position of the peripheral maximum shifts with increasing grain size and all Y-position distributions disappear (Fig. 22). The largest grain size fraction shows a [c]-axis maximum at ~170°, and a second weaker one at ~130° to the lineation. There is only little difference between area and number weighted pole figures, suggesting that single grain or grain size effects inside the grain size intervals do not contribute in different ways to the pole figure geometry.

Grains larger than a 100 points (56 μm) have a mean axial ratio of ~0.45 (Fig. 23). Pole figures calculated for grains with such a small axial ratio (<0.5) show the peripheral [c]-axis maximum close to the lineation and a second maximum at ~140° (Fig. 23). Grains with axial ratios >0.5 show some Y-position distribution and a peripheral maximum at 120° to the lineation (Fig. 23). There is little difference between number and area weighted pole figures but the mean grain size of the former interval is 81μm and the latter is 73 μm.

The additional incorporation of grains larger 50 points (40 μm) does not change the CPOs significantly.

Grains smaller than 50 points show a relatively even distribution of the orientation of their long axes - despite the incapability of OIM® to give grain long axis orientations values parallel to the coordinate axes (e.g. Fig. 22). Towards larger grain sizes the mean orientation of grain long axes shifts towards a narrower distribution and smaller angles with the lineation (Fig. 22).

Grains (> 50 points) with long axis orientations lying in the main, most densely populated interval of 0 - 60 ° show [c]-axis pole figures with a peripheral maximum close to the lineation and a minor maximum around 130°. The latter maximum is less pronounced in the number weighted polefigures (Fig. 24). Grains with long axis in oriented in all other directions (60 - 180°) produce a CPO with a peripheral [c]-axis maximum at ~130°.

Therefore in microstructure (3) two groups can be separated. Larger grains, which are more elongated and oriented at a small (+) angle to the lineation (~20-30°) show a preferred [c]-axis orientation at a small (-) angle to the lineation (~175°). Smaller, less elongated grains and also grains oriented in any orientation but not consistent with the sense of shear (60-180°) show a preferred [c]-axis orientation at 120-130°.

In microstructure (4) (Tr6-2-7-20) [c]-axis pole figures do not show different strengths for different grain size intervals (Fig. 25) but consistently exhibit a peripheral maximum at ~120 - 140° to the lineation. <a>-axes do not form characteristic pattern but the highest concentrations are located at the periphery of the pole figures.

The mean axial ratio is ~0.45 and no significant changes in the pole figure geometry can be observed for grains of lower or higher axial ratios (Fig. 26). Most grain long axes are oriented at 20-30° to the lineation. The pole figures derived for the intervals of 0 - 70 ° and 70 - 180° do not show large differences despite the latter one having slightly stronger maxima, but peripheral maxima pointing towards 120- 140° (Fig. 27). Number and area weighted pole figures do no differ significantly.

Thus, in microstructure (4) the CPO does not change with grain size, the elongation, or the orientation of the long axes of grains. The preferred [c]-axis orientation remains at ~120 - 140° to the lineation.

CPO dependent fabrics

For microstructure (3) SURFOR and PAROR fabric analyses were carried out for grains that have mean [c]-axis orientations either inside or outside a 90° wide cone centered at the [c]-axis maximum of the bulk, area weighted pole figure (Fig. 28).

There is no significant difference between the value and the direction of b/a_{bulk} and surface ODF rose diagrams for both orientation groups. The rose diagram of surface ODF of grains outside the 90°cone shows a weakly monoclinic geometry while the surface ODF rose diagram of grains inside the 90° cone shows an orthorhombic geometry.

Particle fabrics show a similar behavior with both , b/a_{bulk} of ~0.7 at ~20° and particle ODF rose diagrams that do not differ significantly.

Mean crystallographic orientations of grains of microstructure (4) have been subdivided into orientations inside and outside a 90° cone around the orientation of the bulk maximum of the area weighted [c]-axis pole figure (Fig. 29). SURFOR and PAROR bulk fabric do not show a significant

difference with an a/b_{bulk} of 0.8 at 10-20° for both orientation groups. Surface ODF rose diagrams obtained from grains oriented outside the 90° cone show a weakly monoclinic geometry.
Additionally two groups or orientations were defined inside and outside a 40° wide girdle oriented perpendicular to the peripheral <a>-axis maximum. The b/a_{bulk} is slightly smaller for grains with mean orientations outside the girdle (0.75 to 0.85). Surface and particle orientation rose diagrams show an internal orthorhombic geometry and no difference to one another.

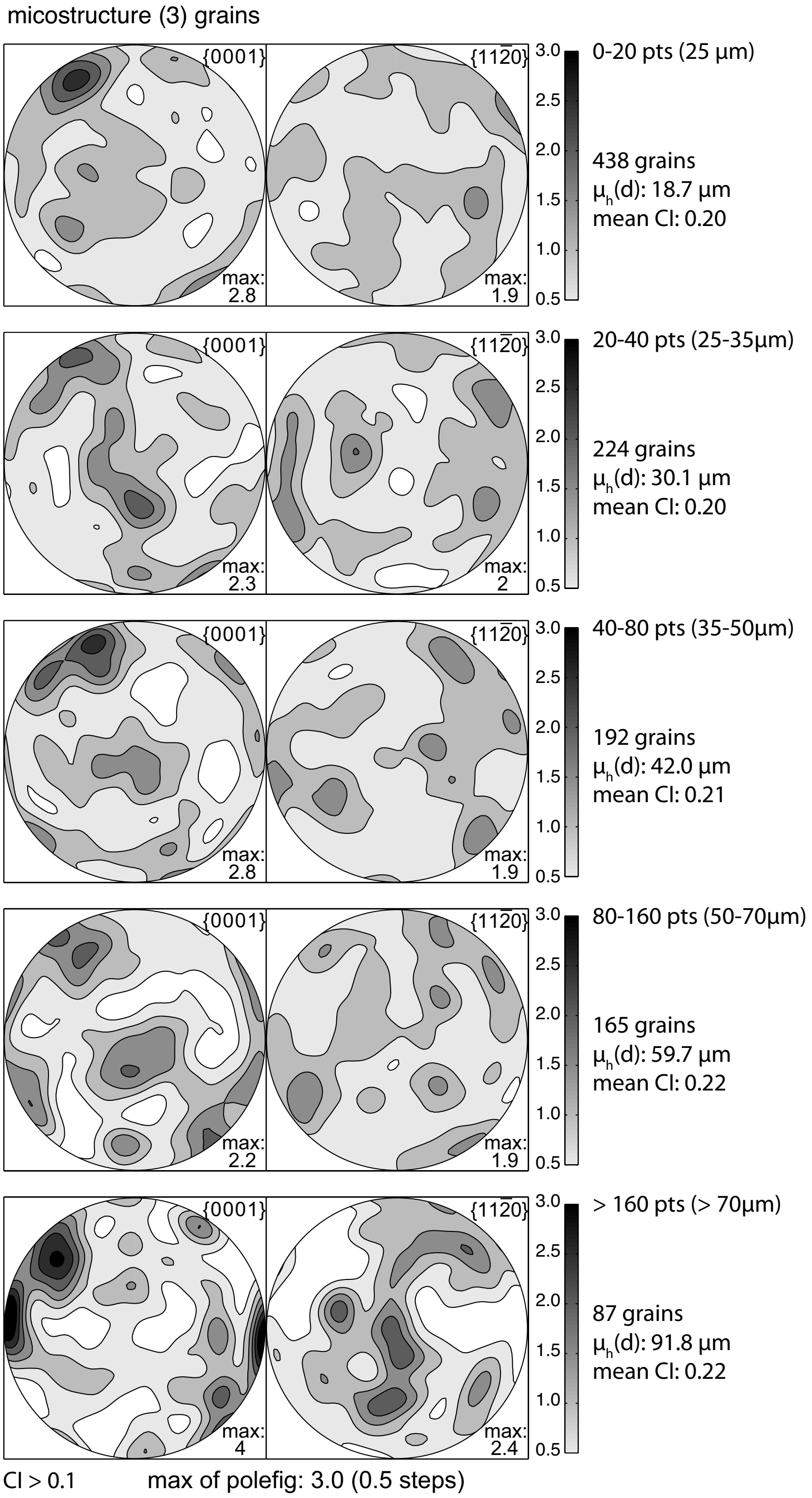

Figure 22: Dependence of the CPO on the grain size in quartz microstructure (3): C- and a-axis polefigures derived from the mean orientation of grains. Grain size intervals of 0-20, 20-40,40-80, 80-160 and > 160 points (step size 5 μm). Individual orientations are weighted by the area the grain. 10° kernel halfwidth. Mean grain size, mean confidence index (CI) and number of grains indicated. Dextral shear sense (see figure 20). Tr6c.

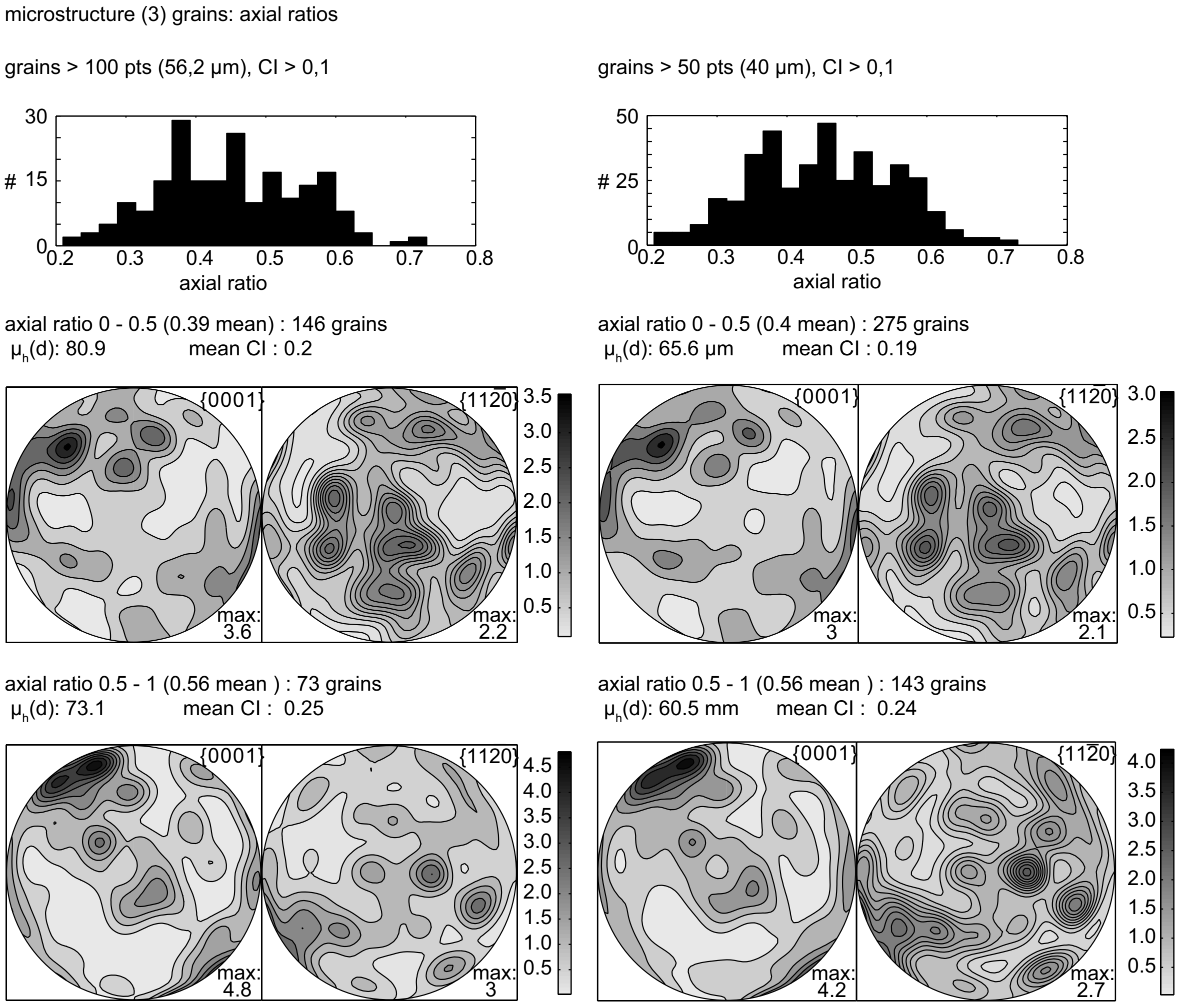

Figure 23: Dependence of the CPO on the grain axial ratio in quartz microstructure (3): Histograms of axial ratios of grains, larger 100 and larger 50 points (step size 5 μm). C- and a-axis polefigures derived from the mean orientation of grains. Individual orientations are weighted by the area the grain. 10° kernel halfwidth. Upper row of polefigures for grains with axial ratios < 0.5, lower row for grains with axial ratios > 0.5. Mean axial ratio, grain size and confidence index is indicated. Dextral shear sense (see figure 20). Tr6c.

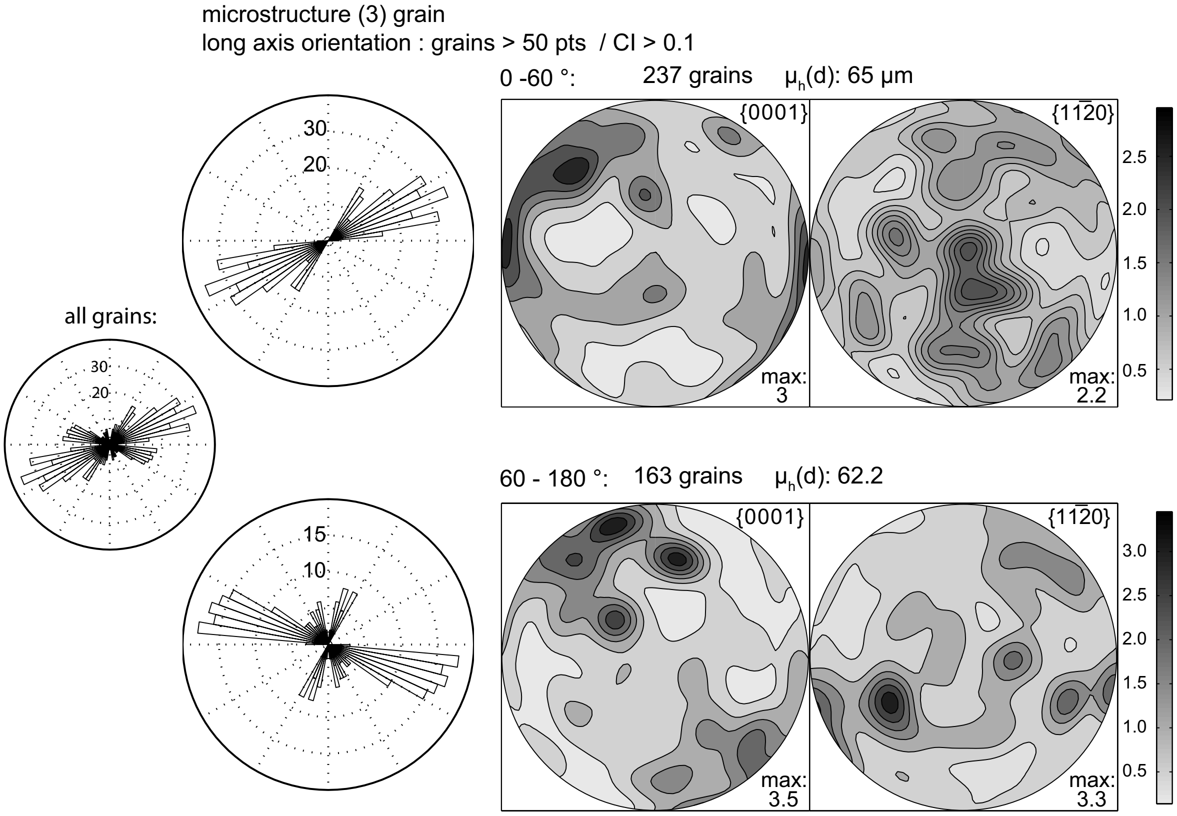

Figure 24: Dependence of the CPO on the grain long axis orientation in quartz microstructure (3): Rose diagrams of long axis orientation for grains larger 50 points (step size 5 μm). C- and a-axis polefigures derived from the mean orientation of grains. Individual orientations are weighted by the area the grain. 10° kernel halfwidth. Upper row of polefigures for grains long axis orientations of 0-60°, lower row accordingly for 60-180°. The shear Mean axial ratio, grain size and confidence index is indicated. Dextral shear sense (see figure 20).Tr6c.

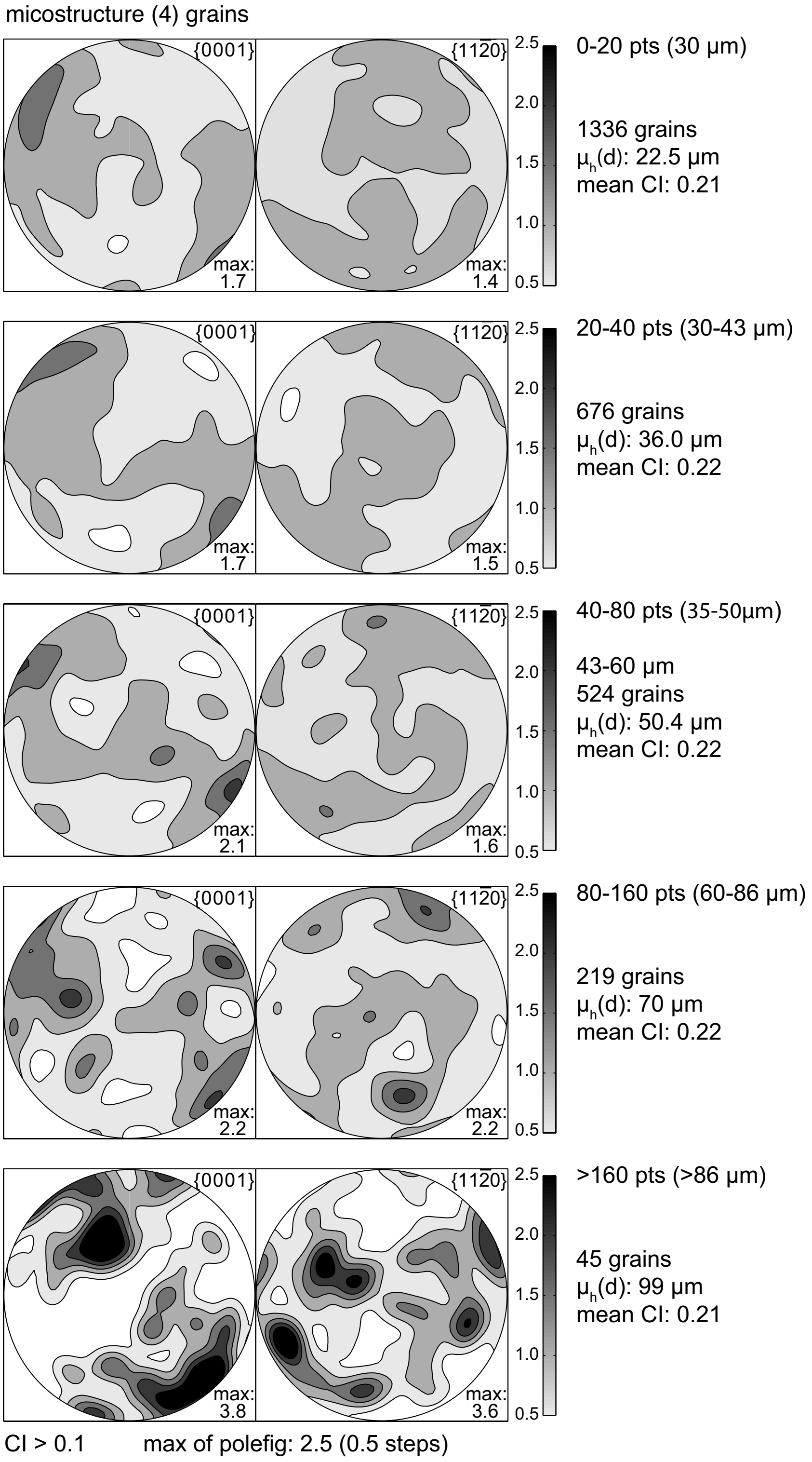

Figure 25: Dependence of the CPO on the grain size in quartz microstructure (4): C- and a-axis polefigures derived from the mean orientation of grains. Grain size intervals of 0-20, 20-40,40-80, 80-160 and > 160 points (step size 6 μm). Individual orientations are weighted by the area the grain. 10° kernel halfwidth. Mean grain size, mean confidence index (CI) and number of grains indicated. Dextral shear sense (see figure 21).Tr6-2-7-20.

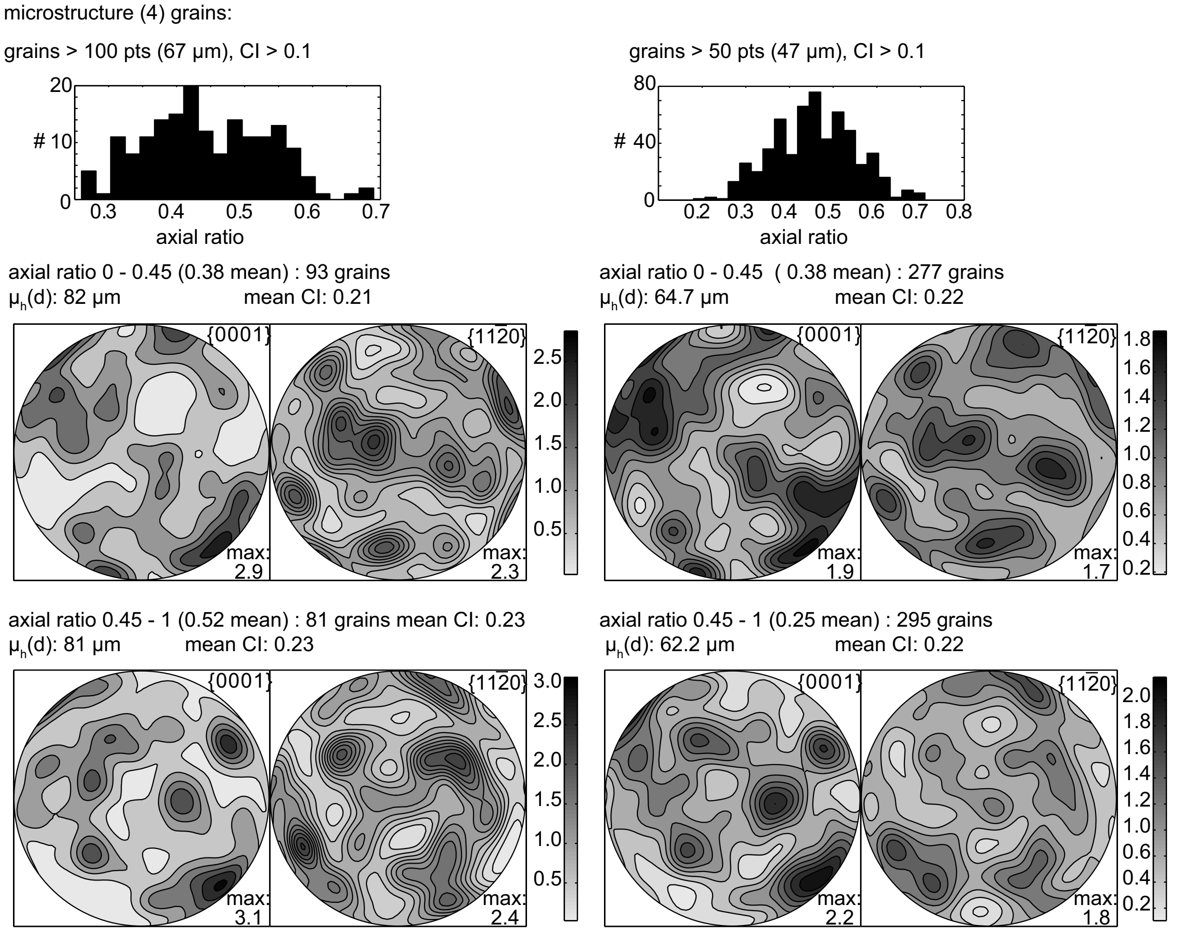

Figure 26: Dependence of the CPO on the grain axial ratio in quartz microstructure (4): Histograms of axial ratios of grains, larger 100 and larger 50 points (step size 6 μm). C- and a-axis polefigures derived from the mean orientation of grains. Individual orientations are weighted by the area the grain. 10° kernel halfwidth. Upper row of polefigures for grains with axial ratios < 0.45, lower row for grains with axial ratios > 0.45. Mean axial ratio, grain size and confidence index is indicated. Dextral shear sense (see figure 21). Tr6-2-7-20.

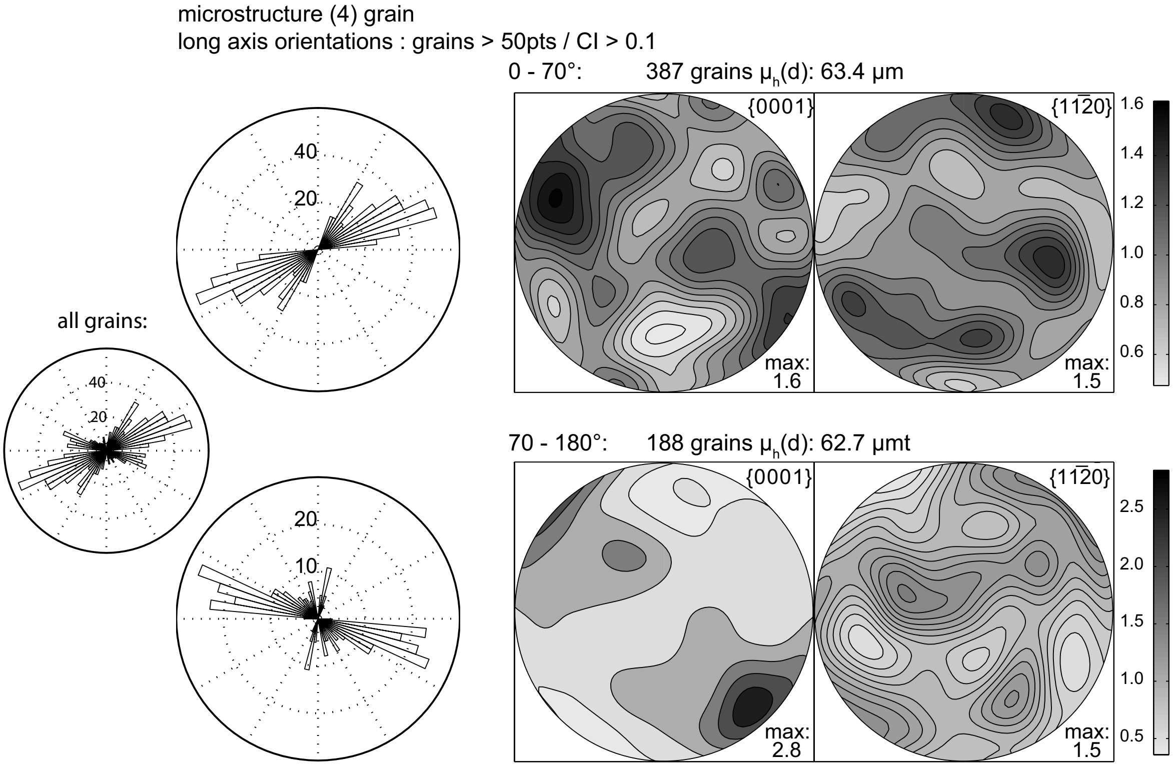

Figure 27: Dependence of the CPO on the grain long axis orientation in quartz microstructure (4): Rose diagrams of long axis orientation for grains larger 50 points (step size 6 μm). C- and a-axis polefigures derived from the mean orientation of grains. Individual orientations are weighted by the area the grain. 10° kernel halfwidth. Upper row of polefigures for grains long axis orientations of 0-70°, lower row accordingly for 70-180°. The shear Mean axial ratio, grain size and confidence index is indicated. Dextral shear sense (see figure 21). Tr6-2-7-20.

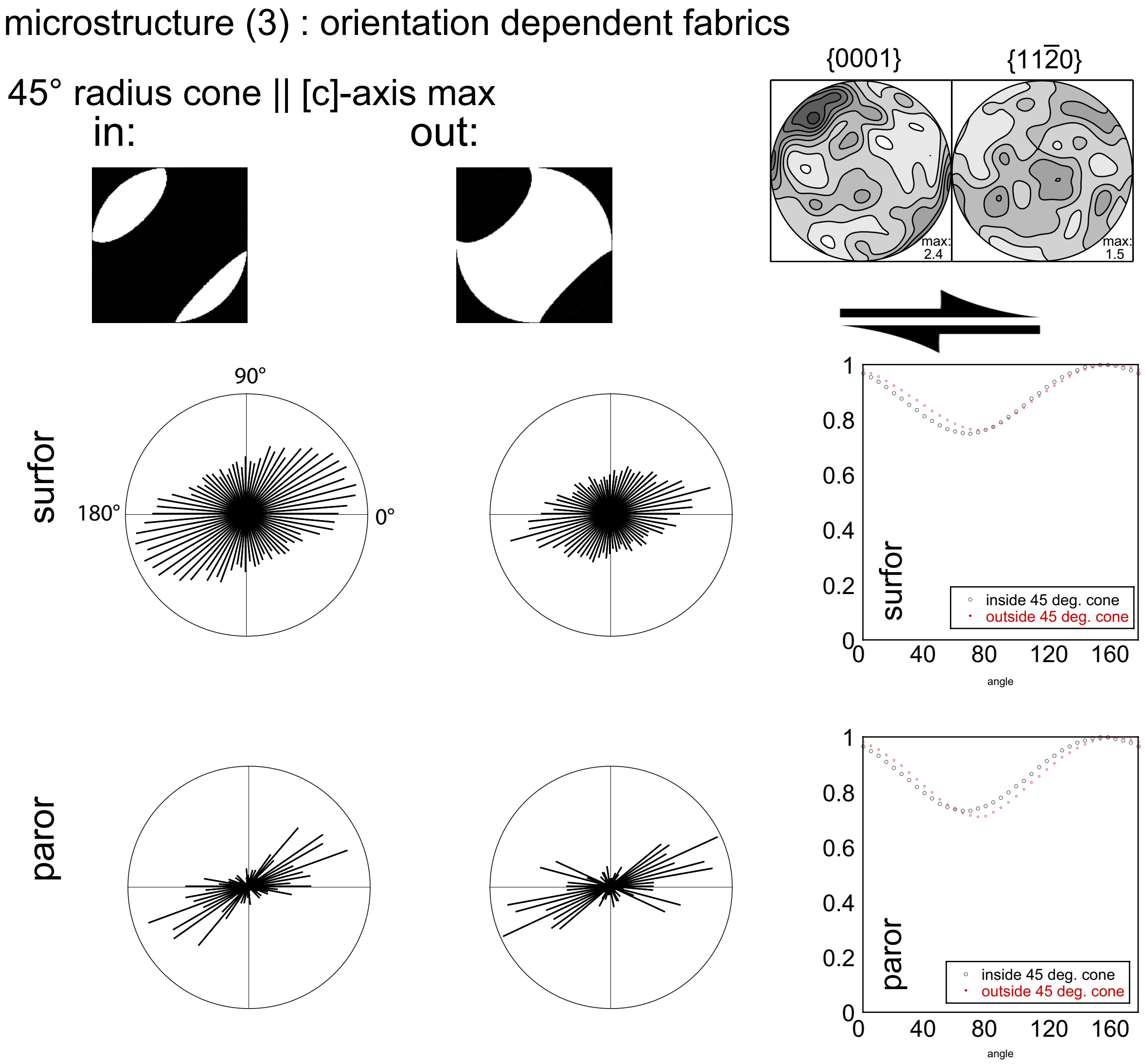

Figure 28: Fabric dependence on the CPO for quartz microstructure (4): SURFOR and PAROR rose diagrams and projection functions of grains inside and outside a 90° cone around the c-axis maximum. Tr6c. See text for explanation.

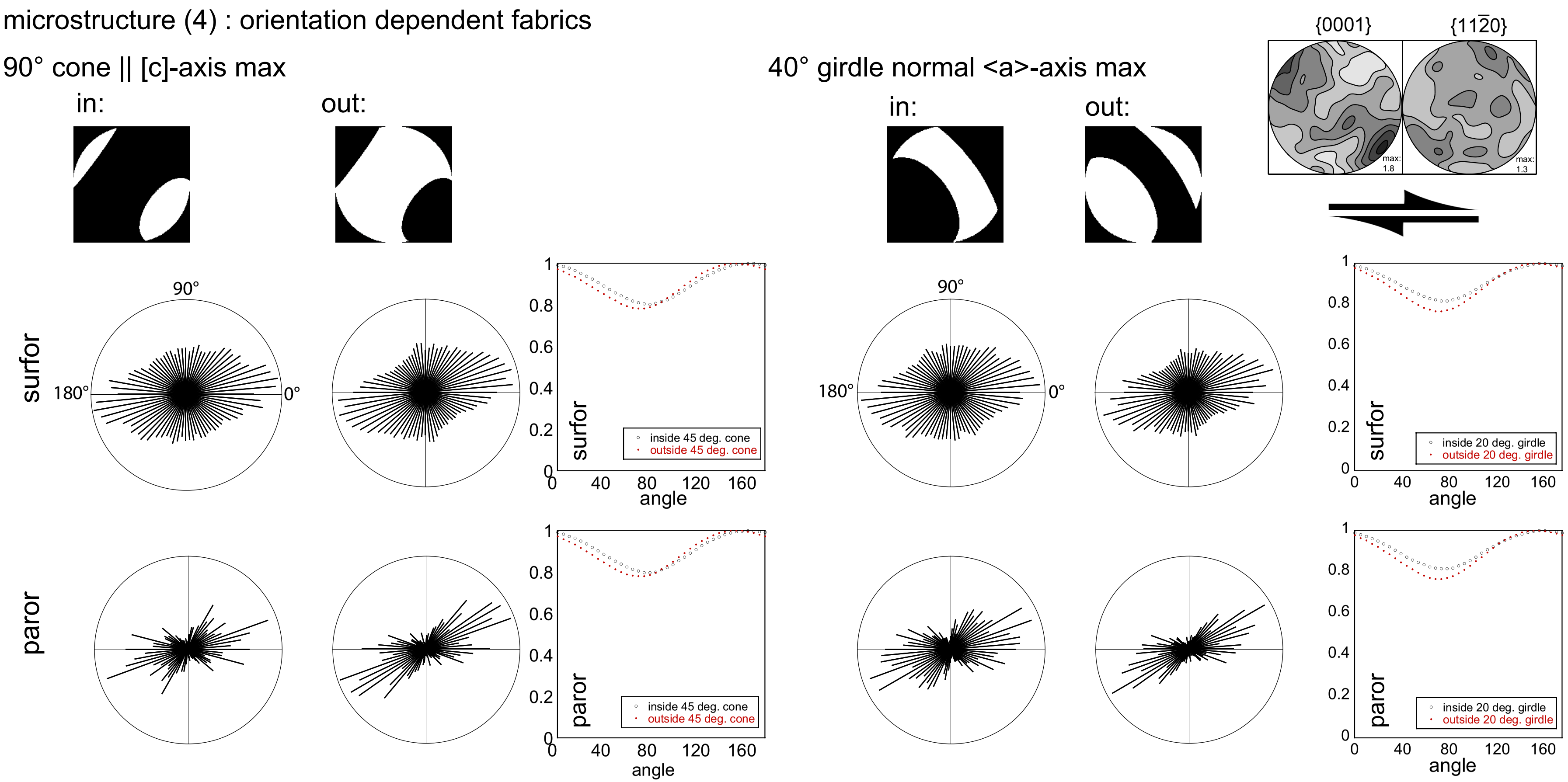

Figure 29: Fabric dependence on the CPO for quartz microstructure (4): SURFOR and PAROR rose diagrams and projection functions of grains inside and outside a 90° cone around the c-axis maximum and inside and outside a 40° broad girdle perpendicular to the a-xis maximum. Tr6-2-7-20. See text for explanation.

4.3 Fourier transform spectroscopy (FTIR)

Samples used for the FTIR analysis are from thin shear zones (Tr1: 748888, 133092) and thin shear zones in more homogeneously deformed areas (Tr3: 748894,133050) in the low strain domain (Fig. 6c,d,e).

FTIR spectra are acquired on magmatic quartz grains and grains from microstructure (1) and (2) (Fig. 8). Single grains of microstructure (3) or (4) are too small to attain a sufficiently large signal to noise ratio and in most cases grains are thinner than the thick-section rendering single grain measurements impossible. Different types of spectra are distinguished. Completely flat spectra (e.g site Tr3-3_6, Fig. 30), spectra with discrete peaks (e.g site Tr1-4a_21_3rd, Fig. 31), and spectra with a broad absorption peak between 3000 and 3800 cm-1 (e.g site Tr1-4a_26, Fig. 32) (see Appendix I). A discrete peak at ~ 3624 cm-1 is caused by white mica and may occur in all three previous types of spectra.

Flat spectra do not show absorbance peaks between 2800 and 3800 cm-1 of an identifiable height above noise and interferences, except the C-H pair peaks which are related to wax contamination after preparation (Fig. 30, 31, 32; Appendix H). Wax related peaks do not occur in the 3000-3800 cm-1 region (Fig. 33a, Appendix).

The most common discrete peaks are observed at 3195, 3205, 3305, 3375-3380, 3483 and 3596 cm-1. The most prominent of the peaks is the 3375-3380 cm-1 peak. Nevertheless peaks are low with the highest normalized absorbances of 0.1 cm-1 which is about the range reported for brasil quartz (Katz, 1962; Aines & Rossman, 1984; Kronenberg & Wolf, 1990). Most normalized absorbances of discrete peaks are lower and there is a transition between flat spectra and spectra with discrete peaks. Flat spectra and spectra with discrete peaks are characteristic for clear regions inside quartz grains. Spectra of heat treated samples (Tr3-3, Tr3-1) which were acquired across cracks, grain boundaries, and fluid inclusions are either flat or show discrete peaks (Fig. 33b).

Spectra acquired across areas which contain fluid inclusions show a broad absorption band between 3000 and 3800 cm-1 (e.g site Tr3-1_T3;Tr3-1n_8, Fig. 33a). In most cases the fluid inclusions are primary and occur in dispersed clouds in magmatic grains. No systematic spectral difference with late fluid inclusion trails has been observed. Spectra obtained in fluid inclusion rich areas are not affected by the heat treatment.

Spectra with a small signal to noise ratios cannot be used for quantification (e.g site Tr3-3_30, Fig 30; site Tr1_4a_40, Tr1-4a_24_2nd; Fig. 32). Nevertheless these spectra can be classified as a flat spectrum, a mica spectrum or a broad band absorbance spectrum based on their shape.

The water content is given by H/Si*1e6 and is calculated with the calibration of Katz (1962). See the Appendix E for the values of the integral molar absorption coefficient of the calibrations of Stipp et al. (2006) and Paterson (1982). The calibration of Katz (1962) was done on discrete peaks in clear quartz single crystals while the Paterson (1982) calibration was obtained from glasses and hydrous minerals and the calibration by Stipp et al. (2006) on polycrystalline, fine grained aggregates with broad absorption bands. The Katz (1962) calibration seems the most appropriate and will overestimate the water content obtained from spectra with a broad band absorption. Nevertheless, the integral molar absorption coefficients provided by Stipp et al. (2006) and Paterson (1982) (for 3000 - 3780 cm-1) is about 2.3 and 0.7 times the integral molar absorption coefficient of Katz (1962), respectively.

Clear areas (n=60) show a range of 2-260 H/Si*1e6. “Dirty” areas (n=35) which include cracks, fluid inclusions and grain boundaries show a range of 3 - 2580 H/Si*1e6 (Fig. 34a). The spread of the values obtained from the “dirty” areas is related to the different amount a fluid inclusions, grain boundary areas or cracks incorporated in the measurement area. No systematic reason for the variation of the integral absorbance in the clear area was found. The highest values are, judged from the shape of spectra, associated with very small inclusion that have not been detected prior to the spectrum acquisition. One potential reason for the spread is the large error related to the determination of a integral molar absorbance from flat spectra which is highly dependent on the baseline correction and the noise.

The content of white mica inside clear quartz grains can be up to 0.2 wt% and most white mica bearing grains show contents of ~ 0.15 wt% (Fig. 34b).
Biotite peaks are most likely not found in the FTIR spectra of recrystallized or magmatic grains. Magmatic grains contain white mica inclusions which may be very difficult to detect optically. Recrystallized grains contain coarsened biotite which is larger and can be detected more easily and therefore can be avoided during FTIR measurements.

Recrystallized grains have been distinguished from non-recrystallized, magmatic grains. Recrystallized grains replace magmatic grains by grain boundary migration or develop high angle boundaries by progressive misorientation through rotation recrystallization (Fig. 30, 32). The latter situation is rarely observed. Recrystallized grains are preferentially free of white mica (Fig. 32, 34c, d). In some cases of recrystallized grains which show a minor white mica content, small white mica flakes could be identified. In other cases the white mica content in recrystallized grains occurs when grains are recrystallized by rotation recrystallization. Most spectra of non-recrystallized grains show a higher mica content together with a variable water content. Grains which could not be classified as recrystallized often show a white mica peak. These grains occur frequently in deformed polycrystalline quartz aggregates (e.g. site Tr3-3_T6/7, Fig. 8a).

Spectra of recrystallized grains are preferentially free of the mica signal whereas non-recrystallized grains usually show the white mica peak (Fig 30, 32, 34d).
There is no significant difference in the water content of recrystallized or non-recrystallized clear grains (Fig. 34d). Recrystallized or non-categorized grains have higher populations of grains with a very low water content (< 30 H/Si*1e6).

FTIR spectra of K-feldspar grains show broad a broad absorption band between 3000 and 3800 cm-1 (Fig. 35). The areas in which the spectra are acquired are not clear and contain perthite exolution lamellae and clouds of fluid inclusions. The estimated water content yielded by the calibration of Johnson & Rossman (2003) is about several 100s to 1000s H/Si*1e6.

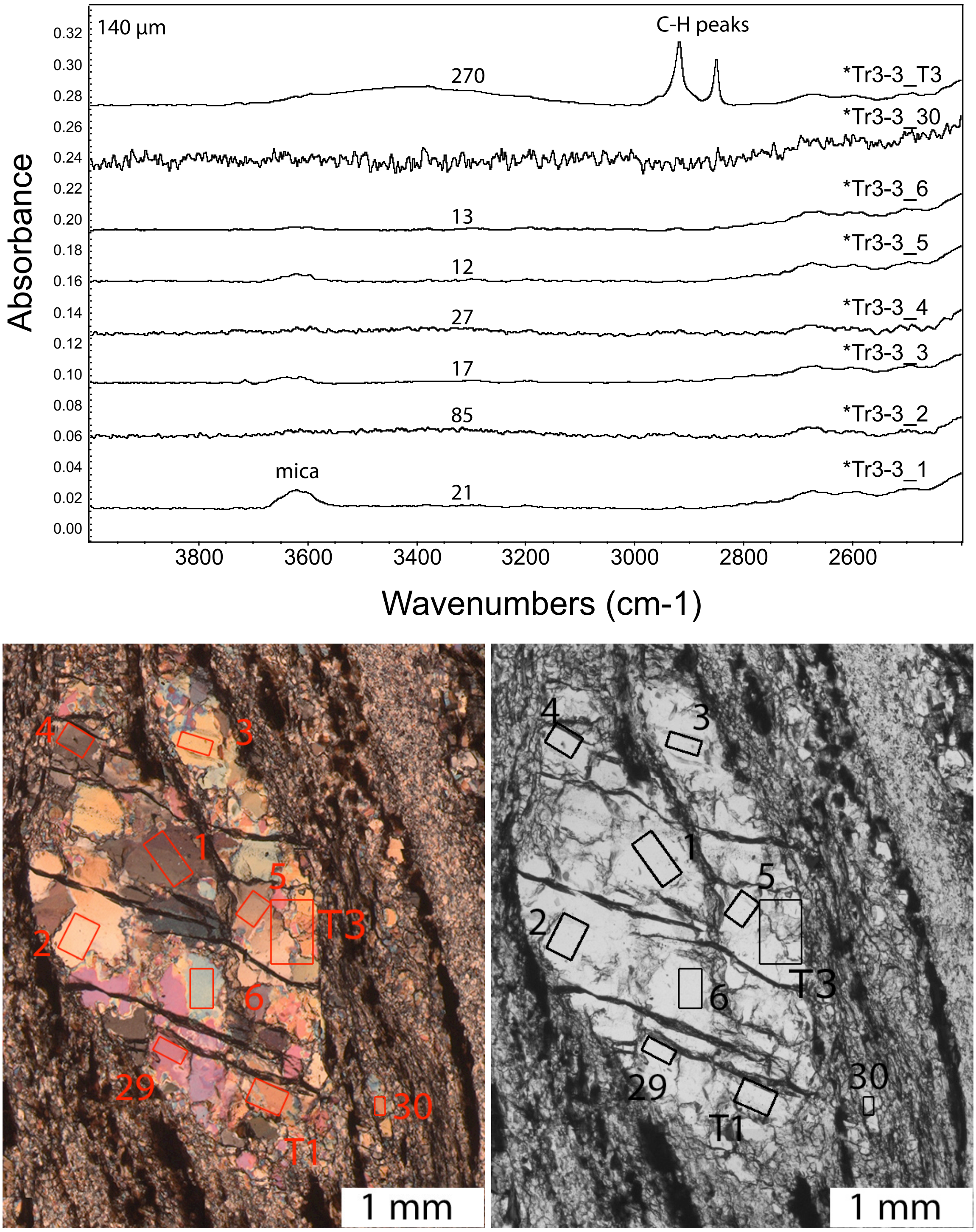

Figure 30: FTIR spectra from a deformed quartz aggregate in Tr3-3: (a) Various FTIR spectra acquired inside grains and one across grain boundaries (Tr3-3 _T3). (b) Micrographs with crossed polarizers and plane polarized light showing the sites where FTIR spectra were acquired. Detail of figure 8a. Some grains (e.g Tr3-3_1) show a weak white mica related peak at 3624 cm-1. Number along spectra give the calculated H/Si1e6 content. See text for discussion.

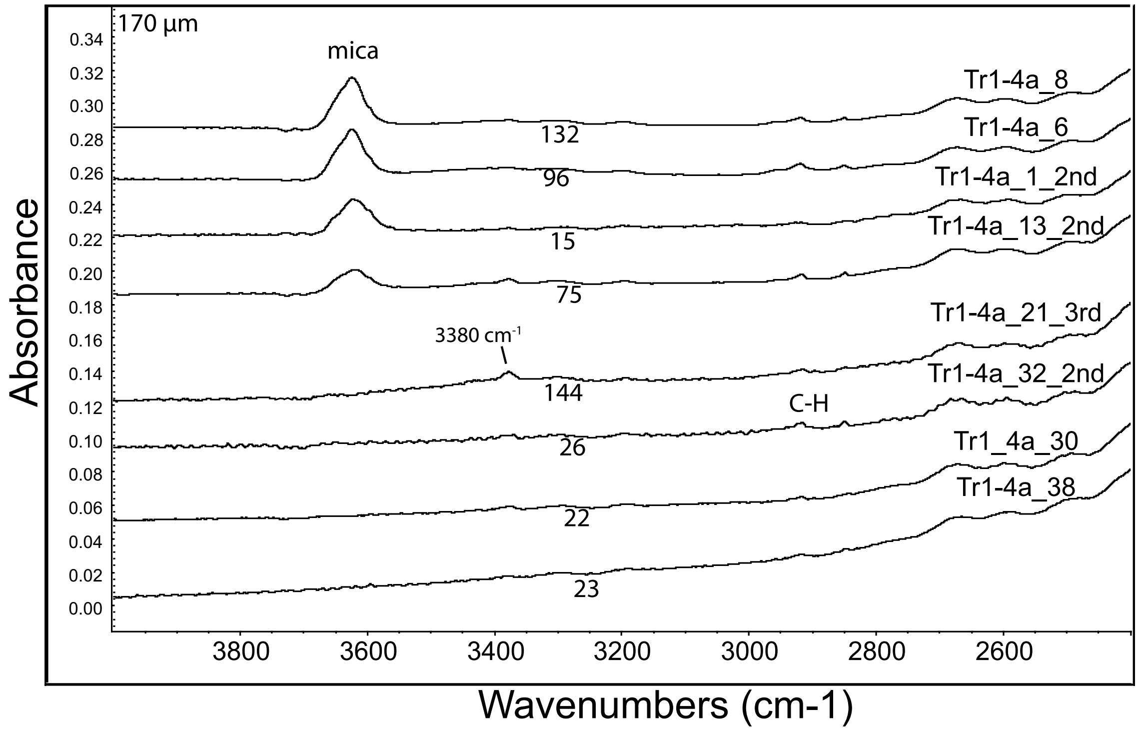

Figure 31: Effect of white mica peaks: FTIR spectra with and without white mica peaks at 3624 cm-1. For comparability spectra are normalized for 170 μm section thickness. Flat spectra (e.g. Tr1-4a_30 and Tr1-4a_1_2nd) and spectra with discrete peaks (e.g Tr1-4a_21_3rd and Tr1-4a_13_2nd) may show an absorbance peak at 3624 cm-1. Spectra of unrecrystallized grains contain the white mica peak, while the grains lacking the 3624 cm-1 peak are recrystallized. See figure 8c for location.

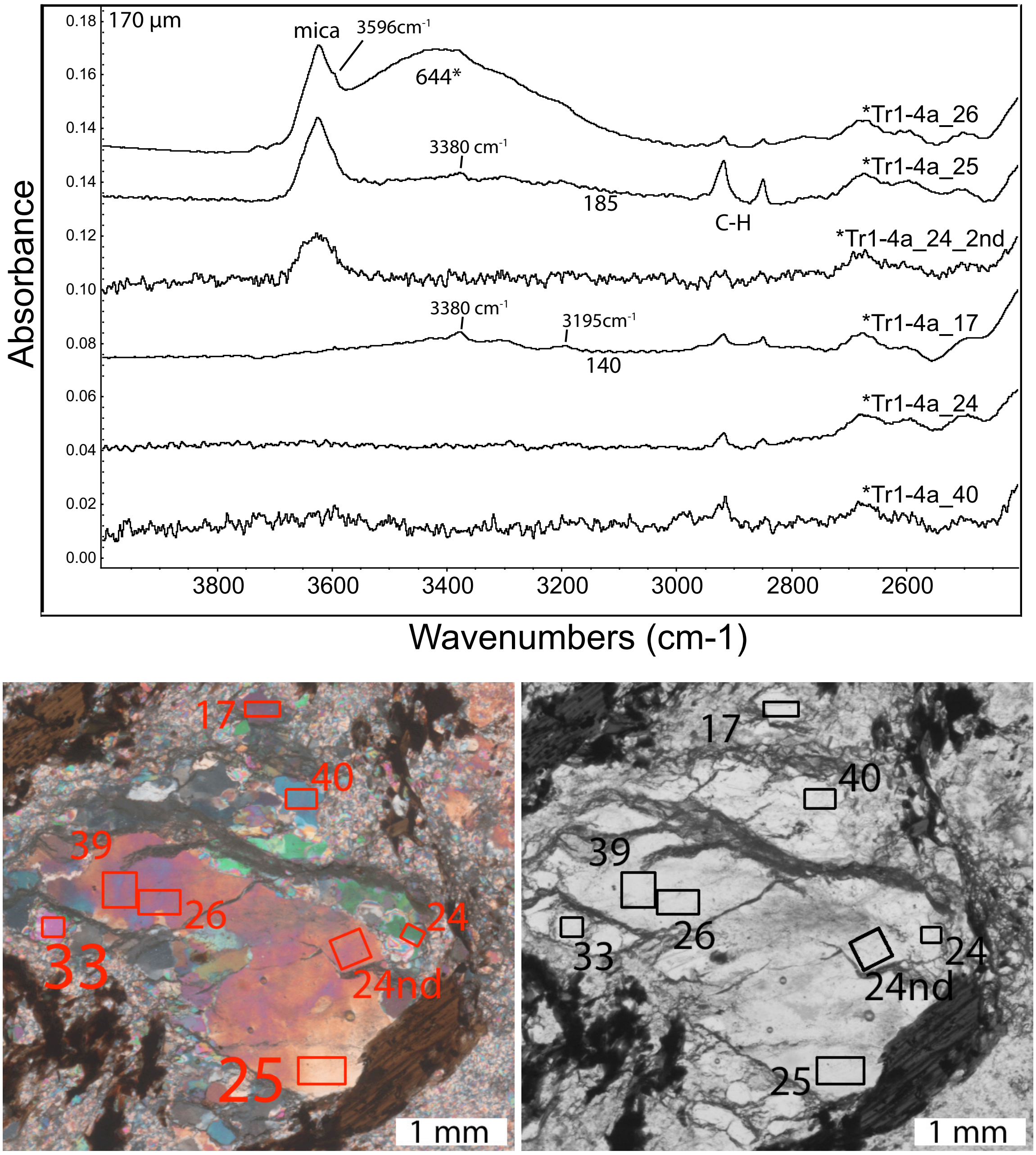

Figure 32: FTIR spectra from a recrystallizing quartz grain Tr1-4a: (a) Various FTIR spectra acquired inside grains. (b) Micrographs with crossed polarizers and plane polarized light showing the sites where FTIR spectra were acquired. Detail of figure 8c. Some grains (e.g Tr1-4a_25 and 26) show a white mica related peak at 3624 cm-1. Spectra of grains which are recrystallized (e.g. Tr1-4a_24) lack the white mica signal present in the magmatic grain (e.g. Tr1-4a_24nd). Number along spectra give the calculated H/Si1e6 content. See text for discussion. Spectra which are not shown but have a frame and a number, can be found in the Appendix I and were not suitable for evaluation.

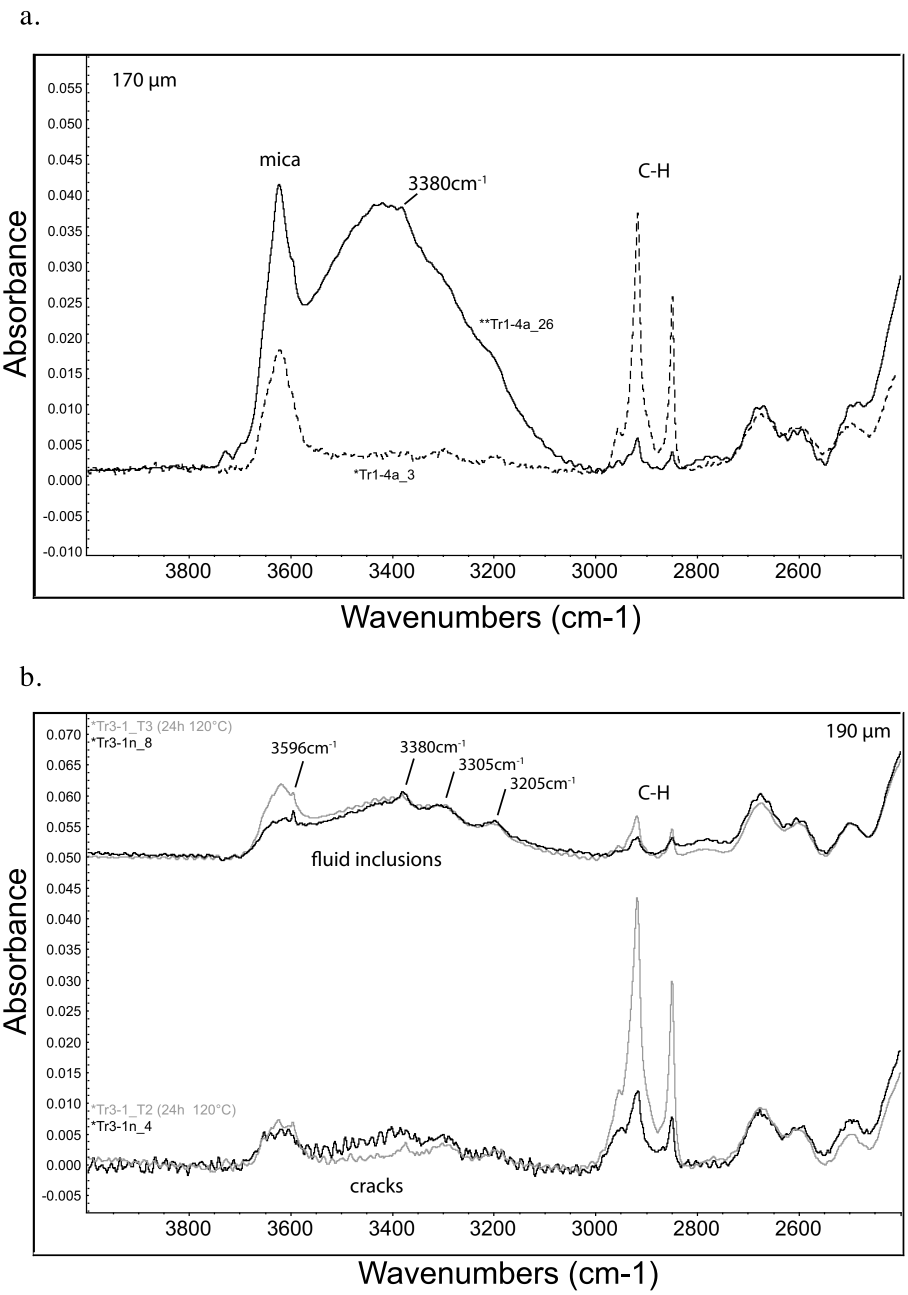

Figure 33: Effects on the water related peaks: (a) FTIR spectra with a white mica related peak and wax contamination. The spectrum with the broad absorbance band is acquired in a fluid inclusion rich area, the flat spectrum in a clear grain. The C-H elated peak has no influence on the broad band absorbance between 300-3800 cm-1. (b) Effect of heat treatment: Spectra were acquired before and after heat treatment for 24 hours at 120 °C. The heat treatment has no effect on fluid inclusion rich areas while water contained in cracks (or grain boundaries) can be removed. The Tr3-2_T2 was acquired at a slightly lager area, thus showing a higher signal to noise ratio.

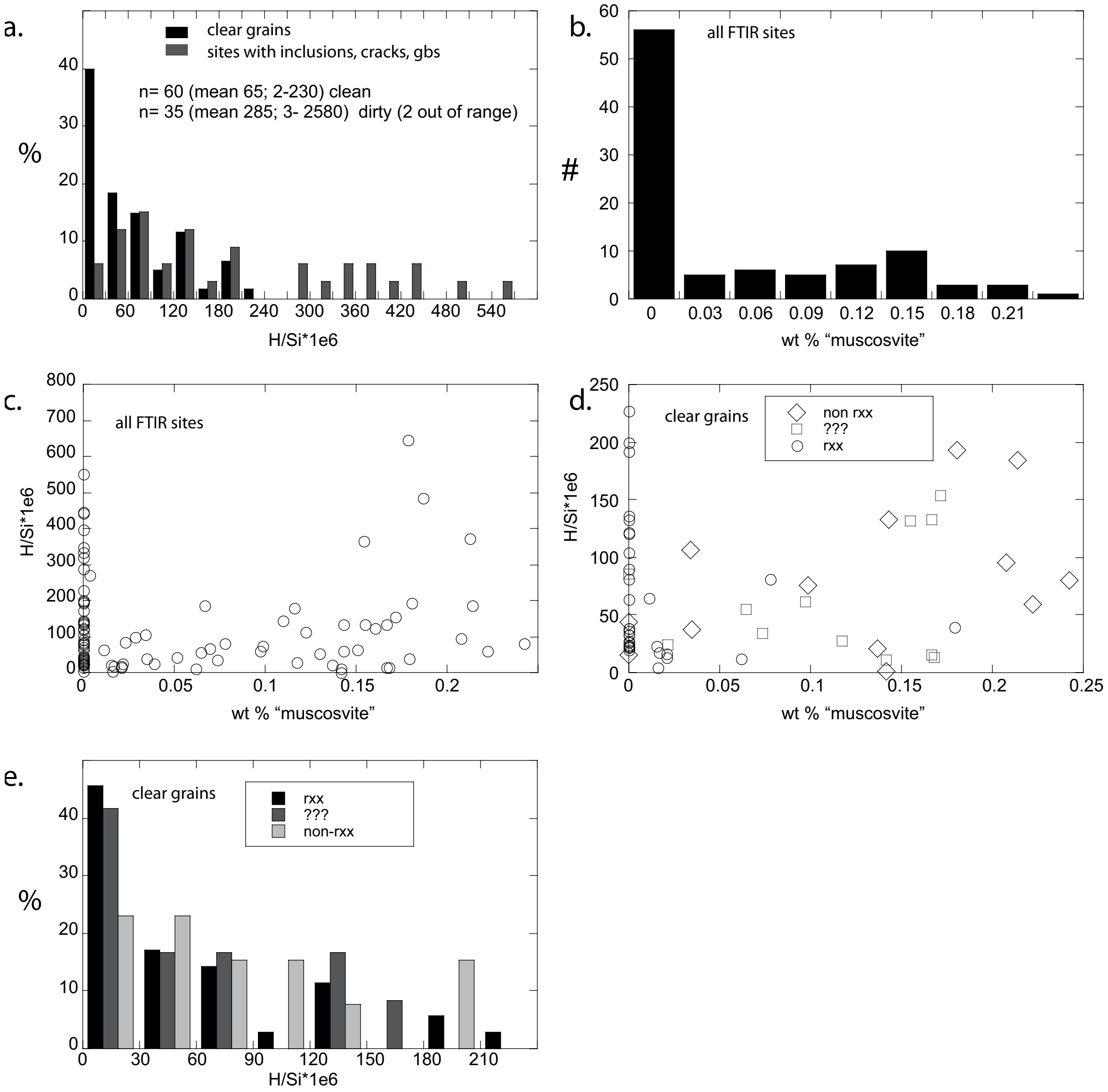

Figure 34: Water and white mica content of FTIR spectra: (a) Histogram of the water content in H/Si*1e6. Measurements of clear grain areas are separated from those containing cracks, inclusions and grain boundaries. (b) Histogram of the calculated white mica content determined from all recoded FTIR spectra. (c) Comparison of the white mica content and the water content, including all FTIR spectra. (d) Comparison of the white mica content and the the water content separately for recrystallized, magmatic and unidentified grains. (e) Histogram of the water content of recrystallized, magmatic and unidentified quartz grains.

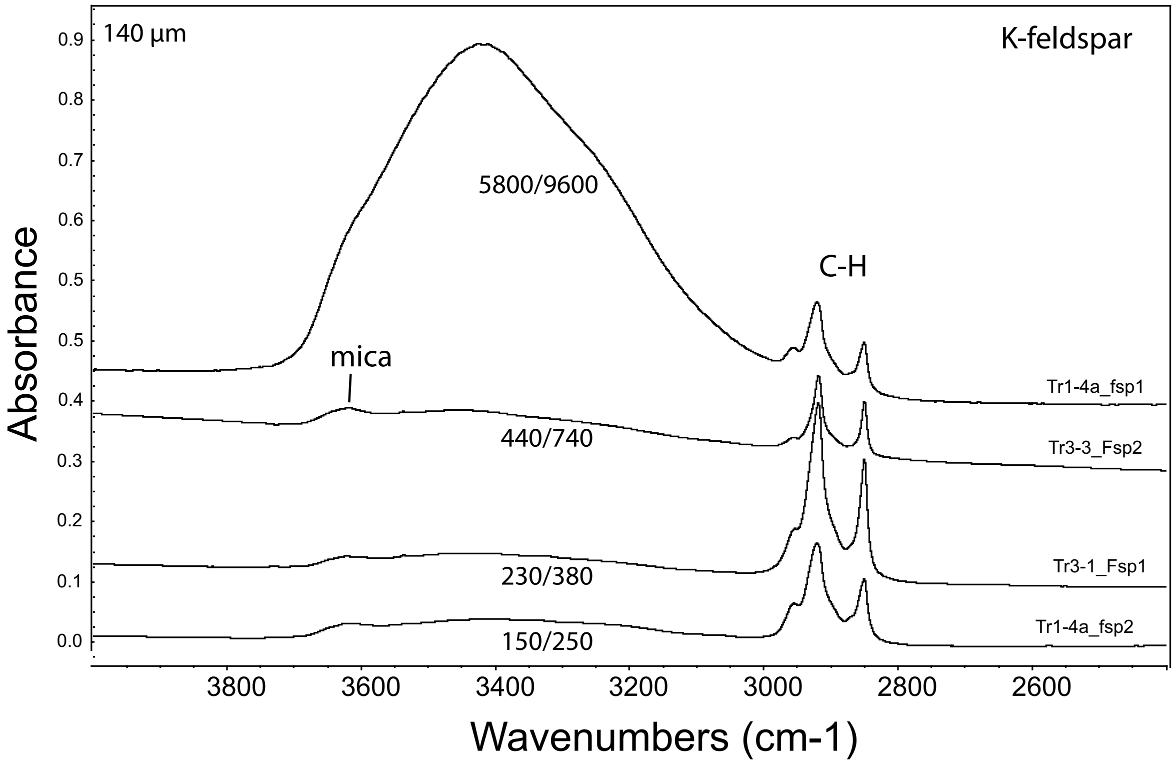

Figure 35: FTIR spectra of K-feldspar: FTIR spectra acquired in relatively clear areas of K-feldspar. For position see Figure 8a,b (fsp-sites). The first number gives a molar ppm H based on Johnson & Rossman (2003), the second based on Solomon & Rossman (1982).

5. Discussion

5.1 Quartz microstructures and deformation mechanism

Quartz microstructures originate from the recrystallization of magmatic grains. The quartz microstructure (1) is typical for low strain deformation. The dominant recrystallization mechanism is grain boundary migration recrystallization (e.g. Poirier & Guillope 1979; Jessell, 1987; Drury & Urai 1990; Stipp, 2002) which produces a large grain size (~650 μm) (Fig. 10, 18).

The CPO is difficult to evaluate as aggregates are composed of too few grains (Fig. 18). Some grains can be interpreted to be preferentially oriented for the activation of the prism [c] and the basal <a> slip systems. Nevertheless it is not possible to distinguish the weak CPO from a random CPO based on the intensity of the maxima as single grains produce the pole figure maxima.

Quartz microstructure (1) is not strictly connected to deformation in the shear zones but is also found in weakly deformed parts of the host rock. The recrystallization mechanism as well as the large grain size indicates deformation at high temperature - low stress or low strain rate.

Microstructure (2) develops a smaller recrystallized grain size (70/110 μm), a fabric and a CPO (Fig. 19). This microstructure is only found inside the shear zones and records later stages of the shear zone formation. The CPOs which are developed in these aggregates are consistent with a combination of basal <a> and prism <a> slip systems (Fig. 19). Few aggregates also show grains which are in an orientation suitable for the activity of the prism [c] slip system (Appendix). While the latter slip system is usually interpreted to be related to high temperatures (e.g. Mainprice et al., 1986) the former two should be active at lower temperatures (e.g. Stipp et al., 2002). The recrystallized grain size is smaller than in microstructure (1) and therefore it may be suggested that deformation of the quartz aggregates inside the shear zones took place at a higher differential stress or lower temperature compared to microstructure (1) (Hirth & Tullis, 1992; Stipp et al., 2002).

In some grains of microstructure (1) and (2) subgrains and small volumes of new grains developed which are smaller than the typical recrystallized grain size (Fig. 12). Grain boundary lobes of such grains are also much smaller than in microstructures (1) and (2). Such microstructures occur inside and outside the shear zones and are interpreted as a later overprint. As an even later part of this later overprint thin layers of finely recrystallized quartz (~20-30 μm), white mica and chlorite formed from brown biotite and are found parallel to the foliation inside the ultramylonite in the shear zone (Fig. 15). These quartz microstructures are comparable with recrystallization by bulging and subgrain rotation recrystallization (BLGII-SGR of Stipp et al., 2002b) and overprint microstructures (2) to (4).

The smaller recrystallized grain size and another recrystallization regime are interpreted to form at either a lower temperature or a higher differential stress than microstructure (1) to (4). The breakdown of biotite clearly indicates that the deformation temperature has been lower. However is only observed inside the ultramylonite. Only a small part of the mylonite and ultramylonite is affected by this late overprint which produced only small strain.

5.2 Microstructures and deformation mechanisms in the granite and the polymineralic matrix

The granite consists largely of quartz aggregates, K-feldspar porphyroclasts, biotite, white mica and fine grained plagioclase aggregates. With increasing strain the amount of fine grained material increases as biotite and K-feldspar recrystallize. The fine grained material will be treated as matrix.

Plagioclase:

Plagioclase occurs in fine grained (20-40 μm) aggregates in low and high strain regions of the granite (Fig. 8). Dynamic recrystallization has been proposed as a mechanism responsible for the plagioclase grain size decrease (Marquer et al., 1994). However, grain size reduction of plagioclase by dynamic recrystallization can be excluded for the follwing reasons.

(1) Original magmatic plagioclase is preserved in K-feldspar porphyroclasts (Fig14). See also below.

(2) The fine grained plagioclase always occurs associated with white mica$_2$, which is a reaction product together with the more albitic plagioclase (An20).

(3) The fine grained plagioclase also occurs in undeformed and low strain parts of the rock.

The discontinuous change to an albitic plagioclase composition during high pressure metamorphism (e.g Wayte et al., 1989) can result in the static recrystallization. The formation of fine grained plagioclase pseudomorphs is frequently observed in high pressure metamorphism of magmatites (Gran Paradiso: this thesis Capter 1,2; Dora Maira: Lenze & Stöckert, 2007; Allalin gabbro: Bucher & Grapes, 2009). However, this idea contrasts with the plagioclase in the matrix, magmatic relicts, myrmekites and replaced perthites which have an oligoclase (An20) composition while statically recrystallized grains inside the pseudomorphs of magmatic grains show core compositions of An26.

The quartz seams which grow between the K-feldspar hosts and the pseudomorphs can be takes as evidence of silica release during plagioclase equilibration towards more calcic compositions from a previously more sodic plagioclase. The appearance of albite is restricted to rare flame perthites and as seams along some oligoclase-K-feldspar interfaces in replaced coarse perthites. This albite is most likely not related to the early high pressure metamorphism but rather with retrogression (Fig. 14,15).

Coarse perthite albite lamellae are replaced by fine grained oligoclase and quartz (Fig. 13). Myrmekitic plagioclase has the same composition (An20) as grains, which have been interpreted as magmatic relicts (Fig. 14). The identical composition is most likely the result of the reaction producing more albitic plagioclase and white mica, which is always associated with plagioclase. Only in rare cases are more anorthitic plagioclase relicts (An26) preserved (Fig. 14). Three albite occurrences have been observed: (1) Albite exsolved in coarse perthite lamellae in K-feldspar during magmatic cooling, (2) Albite formed during the high pressure metamorphism (only indicated by the quartz segregations), and (3) late albite present in flame and microperthites formed during the retrogressive stage.

K-feldspar:

K-feldspar forms large phenocrysts in the granite and porphyroclasts in the (ultra)mylonite. It may recrystallize and form fine grained (~20-50 μm) tails . The occurrence of K-feldspar porphyroclasts in the (ultra)mylonite can possibly be attributed to their large grain size (10-100 mm) in the granite at the onset of deformation.

There is no direct microstructural evidence for the deformation mechanism active in the feldspar aggregates. However, the small grain size and mixing with white mica and other phases suggests a grain size sensitive diffusion creep deformation mechanism. The only available experimentally derived flow laws are for anorthite (Rybacki & Dresen, 2000). If we assume that the anorthite flow law may yield a first order approximation for feldspar rheology in general, we can apply it to the K-feldspar aggregates. Applying the Rybacki & Dresen (2000) flow law would predict unrealistically low strain rates at differential stresses obtained from quartz grain size piezometer (Shimizu, 2008) (at 650°C and 15 MPa: $10^{-14}s^{-1}$, at 550°C and 12 MPa: $\sim10^{-16}s^{-1}$), whereas diffusion creep at the estimated temperatures and grain sizes yield reasonable estimates (at 650°C and 30 μm: $5*10^{-12}$, at 550°C and 30 μm: $5*10^{-13}$). In addition, fine grained monomineralic aggregates of K-feldspar have been suggested to deform by diffusion creep (Menegon et al., 2008) at similar metamorphic conditions in a similar rock type (chapter 2).

Mica:

Biotite and white mica both occur as magmatic grains. The replacement of magmatic white mica by new biotite is interpreted to occur during the high temperature stages of deformation after high pressure metamorphism. Occasionally, biotite is also found as micron-sized inclusions in recrystallized quartz grains of microstructure (1). The magmatic quartz grains only contain submicron-sized white mica inclusions. This is circumstantial evidence that the reaction of white mica to biotite may be coeval with grain boundary migration recrystallization of quartz.

In both, the low strain domains and the mylonite, recrystallized biotite forms polycrystalline aggregates. In the mylonite biotite appears as single isolated grains with well defined crystal faces. While the formation of continuous layers is interpreted as a result of crystal plasticity (Kronenberg et al., 1990; Mares & Kronenberg, 1993; Holyoke & Tullis, 2006) by glide perpendicular to [001], the dispersion and mixing of grains is attributed to diffusion creep (e.g. Fliervoet et al, 1997; Kruse & Stünitz 1999; Herwegh & Jenni. 2001).

5.3 Microstructures and deformation mechanisms in the polyphase mixture

In the mylonitic parts of the shear zones, phases are mixed. Fine grained phases of the mixture result from recrystallization of the former perthitic K-feldspar, K-feldspar and biotite precipitation between disintegrating quartz aggregates, myrmekites and reacted plagioclase and white mica aggregates. The mixing increases with increasing shear strain. This behavior is very similar to the observations in the shear zones in the Gran Paradiso metagranodiorite (chapter 1-3).

Mineral precipitation, a high phase boundary mobility, as well as the phase mixture at the small grain size can be regarded as characteristic for flow by a diffusion creep mechanism (Boullier & Gueguen, 1975; Behrmann & Mainprice, 1987; Stünitz & Fitz Gerald, 1993; Fliervoet et al., 1997, Kruse & Stünitz 1999). The phase redistribution by precipitation and growth and exchange reactions like the formation of myrmekite suggest a high mobility of the involved chemical components.

The replacement of biotite by white mica and in few cases also chlorite inside the polymineralic mixture is spatially associated with the smallest dynamically recrystallized quartz grains size and small K-feldspar grains with flame perthites (Fig. 15). This is in accordance with the interpretation that subgrain rotation - bulging quartz microstructures are the latest to form and that they are probably associated with a late stage deformation at lower temperatures and higher differential stresses.

5.4 Quartz deformation in the polyphase mixture

Dispersed quartz grains in the fine grained phase mixture originate either from disintegrated quartz aggregates or from reaction (Fig. 13, 17b, 20). In the latter case, quartz grains are found together with oligoclase derived from either myrmekites or former albitic perthite lamellae. While in microstructure (3) both origins can be separated, in microstructure (4) this is not possible.

The interpretation that the phase mixture deforms by diffusion creep is based on the small grains size, the phase boundary mobility and the precipitation microstructures. Granular materials deforming by diffusion creep often lack a CPO (e.g. Edington et al., 1976; Schmid, 1982; Fliervoet et al., 1997). However, dissolution-precipitation has been suggested as potentially capable of producing a CPO (Bons & den Brok, 2000). Also it has been suggested that a previously established CPO can be retained under certain conditions, e.g. at low grain rotation rates with respect to grain growth rates (Wheeler, 2009).

The bulk quartz CPO measured in microstructures (3) and (4) are very weak but distinct from random for their c-axis distribution (Fig. 20,21). However, the uncorrelated misorientation distribution derived from the full crystal orientation in microstructure (4) is close to random (Fig. 21). The low angle peak between 5-10° in the correlated misorientation distribution points to the presence of low angle boundaries. The origin of these low angle boundaries is caused by the formation of subgrains which may result from the overprint at higher differential stresses. To evaluate the nature and possibly the origin of this weak CPO the shape dependent CPOs and the CPO dependent shapes have been analyzed.

The particle and surface fabrics for grains with orientations inside and outside the [c]-axis maxima are indistinguishable (Fig. 28,29). This is interpreted to be an effect of the weak CPO. Only a small fraction of grains contribute to the CPO maximum while a larger fraction has a random CPO but contribute to the particle and surface preferred orientation. On the other hand, it is shown in microstructure (3) that there is a difference in the CPO elements of grains within a certain range of size, axial ratio and long axis orientation (Fig. 22,23,24). Microstructure (4) does not show any shape dependence of the CPO (Fig. 25,26,27).

The results of the shape dependent CPOs are that large grains, with low axial ratios and an inclined orientation, show a [c]-axis maximum at a small angle to the lineation (175°). The low axial ratios and a preferred grain long axis orientation of 20-30° to the lineation indicate deformation of individual grains, either achieved by intracrystalline plasticity or by grain-scale diffusive mass transfer. The pole figure is compatible with prism-[c] slip (Mainprice et al., 1986). The geometry and distribution of those large grains which typically form quartz - K-feldspar layers imply that they are derived by disintegration of former quartz aggregates.

Monomineralic quartz aggregates usually show CPOs compatible with prism-<a> and basal-<a> slip systems but relict prism [c] CPOs have not been observed in type (3) microstructures. Therefore, either temperatures were high enough for prism-[c] slip to be dominant or dissolution-precipitation creep may have played a role. Dissolution-precipitation is interpreted to produce c-axis orientations sub-parallel to the stretching direction but are only observed in low grade rocks (Hippertt 1994; Stallard & Shelley, 1995; Takeshita & Hara, 1998). Thus, the origin of the "prism [c] slip" pole figures is unclear.

The smaller grains, grains with high axial ratios, and grains which are oriented between 60-180° show the peripheral [c]-axis concentration at ~130°. This is also the CPO typically associated with microstructure (4) which does not show a change with grain size, axial ratio or grain orientation (Fig. 25,26,27). The fact that number and area weighted pole figures for the different groups of axial ratios and grain orientations do not differ significantly suggests that there is no dependence on grain size within the individual groups.

The [c]-axis maximum which is inclined against the shear sense at ~130° can not easily be explained with the common quartz slip systems and a simple shear kinematic framework in the shear zone. In simple shear pure basal-<a> slip system activity is expected to produce a peripheral [c]-axis maximum perpendicular to slightly inclined with respect to the flow plane (e.g. Schmid & Casey, 1986). The synthetic inclination can alternatively be attributed to a deviation from simple shear or an additional contribution of rhomb-<a> slip (Schmid & Casey; 1986; Mancktelow, 1987; Law et al., 1990). The prism-<a> slip system produces [c]-axis polefigures with a Y-maximum and the expected rotation axis is the [c]-axis itself (Schmid & Casey, 1986; Stipp et al., 2002). Prism-[c] slip which is reported for very high temperature deformation tends to result in [c]-axes aligned parallel to slightly inclined to the lineation. The observed [c]-axis inclination of about 130-140°

(counter-clockwise for a dextral shear sense) suggests that the prism plane resolves rather a minimum of the shear stress in the case of simple shear. The same applies to the basal <a> slip system.

Little information is available on the effect of the deviation from simple shear in natural rocks on the geometry of CPOs. This is most probably due to the difficulties in determining the kinematic framework, therefore assuming that material in shear zones experiences simple shear flow (Price, 1985; Schmid & Casey, 1986; Law et al., 1990; Schmid, 1994;). Numerical models as well as experiments (Dell'Angelo & Tullis, 1989) provide insights in deviations from simple shear. While in the pure shear kinematic framework and dominant basal <a> slip the c-axis is expected to rotate towards or in a small circle centered around the shortening direction (Tullis et al., 1973), in flattening shear zones the c-axis evolves between the shear zone boundary and the inferred instantaneous shortening direction (Dell'Angelo & Tullis, 1989). However there is no data which involve other slip systems.

The CPOs observed in microstructure (2) do not deviate distinctly from those typically observed in simple shear kinematics (e.g. Schmid & Casey, 1985). However, one cannot strictly exclude a stretching or thinning component in the shear zone. The CPO can be assumed to form during flow in the shear zone and is not related to a heterogeneous overprint of a later deformation phase. The later and heterogeneous overprint is not related to the CPO forming mechanisms in the microstructure (4) because the samples in which microstructure (4) is observed do not show the oblique mica foliation, lower temperature mineral reactions but kinematically consistent microstructures of type (2), (3) and (4).

Possible processes which can generate a weak CPO in a polyphase material are anisotropic dissolution-precipitation or a combination of grain boundary sliding and crystal plasticity. As stated earlier, diffusion creep is the deformation mechanism in the polymineralic matrix and the ultramylonite. The weakness of the CPO can generally be related with a high fraction of grain rotation (rigid body rotation). Diffusive processes must accommodate heterogeneous strain at the grain scale (Ashby & Verrall, 1973). The effect of dissolution-precipitation on CPO development has been suggested by Bons & denBrok (2000) and shown in numerical models. Dissolution-precipitation creep at low grade conditions is thought to produce quartz c-axis orientations close or in a small circles around the lineation (Hippertt 1994; Stallard & Shelley, 1995; Takeshita & Hara, 1998). The process involved in the formation of the (residual) CPOs is a preferential precipitation or growth of the c-axis parallel to the stretching direction (Cox & Etheridge, 1983; Tullis & Yund, 1989). This is not the case in the shear zones of the present study as the c-axes tend to concentrate in the inferred shortening direction. Unless there is a change in the surface energy anisotropy from low grade conditions to amphibolite facies conditions, a dissolution-precipitation process cannot account for the weak CPO at ~130° in the Truzzo ultramylonite.

An alternative possibility is that to some extent intracrystalline plasticity in quartz grains takes place concomitant with diffusion creep in the phase mixture.
However grains of microstructure (3) which preferentially show the 130° [c]-axis maximum have high axial ratios or long axis orientations between 60-180° which both is not likely to result from crystal plasticity in response to the kinematic imposed kinematic framework. In microstructure (4) no dependency of the CPO with the axial ratio or long axis orientation was found.

In deformation, the grain interior can be considered to be subjected to lower stresses than the grain boundary region, and especially during grain boundary sliding, grain rotation is common. In diffusion creep aggregates, grain boundaries are expected to have the lowest viscosity. Therefore shear induced vorticity may cause grain rotation (spinning) while internal lattice rotation can be independent on the finite rotation but may be related to the instantaneous stretching axes (Turner, 1962; Hobbs et al., 1976, Lister & Williams, 1979). Grain boundaries experience non-coaxial flow while grain interiors have a higher viscosity and therefore experience a coaxial component of flow.

If for example basal <a> slip controls the internal (high viscosity), [c]-axes would tend to rotate towards the instantaneous shortening direction (e.g. Tullis et al., 1973). Rigid body rotation of grains is a competing process and therefore a dynamic equilibrium must be established between external grain spinning (related to the rate of diffusion creep) and internal lattice rotation (related to the rate of glide on the slip system) to produce a stable CPO.

This is a speculative explanation and it depends on many factors e.g. grain size, axial ratio of grains, the degree of mechanical decoupling (boundary viscosity), rates of the competing processes. Additionally it remains unresolved why basal <a> should be the slip system with the lowest critical resolved shear stress as the larger grains in microstructure (3) could potentially indicate the activity of prism-[c] slip. However, the above described process provides an theoretically valid process for the weak CPO which is otherwise incompatible with the usual (common slip systems in simple shear) and unusual (dissolution-precipitation) CPO forming processes.

Microstructure (4) can be regarded as more evolved due to a higher strain causing more extensive phase mixing and grain size reduction. Therefore microstructure (3) represents a transient stage between continuous polycrystalline quartz aggregates (microstructure (2)) and dispersed single grains in a complete phase mixture. However, the possibility exists that within the high temperature metamorphic conditions a decrease in temperature took place but is beyond the sensibility of the mineral assemblage.

5.5 FTIR

5.5.1 Water content

The FTIR spectra of the recrystallized as well as in the unrecrystallized quartz grains record water contents of dry quartz and are close to the detection limit of the FTIR method (Kronenberg & Wolf, 1990). A higher water concentration was only calculated from spectra with a broad absorption band related to molecular water in fluid inclusions.

The intragranular water content of clear grains is between 2-260 H/Si*1e6 with most grains below 100 H/Si*1e6. Kronenberg et al. (1990) report values of 60 - 2000 H/Si*1e6 in an undeformed granite and aplite and 4000 to 11000 H/Si*1e6 in the equivalent deformed rocks. Gleason & DeSisto (2007) report mean values of 30 H/Si*1e6 in an undeformed pegmatite and around 300 H/Si*1e6 in a granitic mylonite. Generally, studies which did not publish the integral molar absorbance and use different calibration coefficients based on different types of absorbance spectra or flawed conversion coefficients are therefore difficult to compare (e.g. Bambauer, 1961; Brunner et al., 1961; Stipp et al., 2006). Absolute values in H/Si*1e6 using the factor 6670 to convert from ppm (wt) H2O are between 170 and 450 H/Si*1e6 (Stipp et al., 2006) in experimentally deformed quartzites.

Generally, values reported in literature for natural quartz range between several 100s to 1000s of H/Si*1e6 (e.g. Kronenberg 1994) with broad absorbance bands related to molecular water. On the other hand, natural clear (Brazil) dry quartz single crystals have water concentrations of 10s to a maximum of 100 H/Si*1e6 (Kronenberg & Wolf, 1990) and show discrete absorbance bands related to structural water in the form of H+/OH-. Therefore, from the quantitative point of view the grains with high water content in the Truzzo granite are comparable with clear natural (Brasil) quartz. Such crystals have been demonstrated to be mechanically very strong (e.g. Griggs & Blacic 1964).

5.5.2 FTIR spectra

The flat spectra indicate that grains are practically free of water (Fig. 30,31,34). Spectra with discrete peaks have normalized absorbances smaller 0.1 cm-1 but the position of peaks can be determined reliably for most of them. The 3195, 3205, 3375 and 3380 cm-1 peaks are not clearly assigned (Katz, 1962; Aines & Rossmann, 1984). The 3205 cm-1 peak has been reported in natural clear quartz (Katz, 1962). The 3375 and the 3380 cm-1 peaks are measured at 78 K (Katz, 1962; Chakraborty & Lehmann, 1976a,b) and are not assigned. A 3371 cm-1 peak at 78 K shifts to 3383 cm-1 at room temperature and is assigned with an SI-Al exchange and the associated charge compensation by H+ (Katz, 1962). Nevertheless this peak is expected to be paired with a 3435 cm-1 peak which has not been observed in the case of the Truzzo quartz grains.

The 3305 cm-1 peak is observed in natural clear quartz and related to a H+ defect (Katz, 1962). The 3485 cm-1 peak is observed at 78 K and associated with an H+ interstitial but is also reported at room temperature related to an Li+ defect, both in natural clear quartz (Katz, 1962). It is not known if the H+ assigned 3485 cm-1 peak undergoes a peak shift at room temperature. The 3596 cm-1 peak is observed in natural and experimentally annealed quartz and assigned an H+ compensation for a structurally controlled, thermally stable, Al point defect (Niimi et al., 1999).

Al-exchange charge compensation, interstitial alkali and proton point defects are reported in natural clear and undeformed quartz and the corresponding absorbances are usually higher than in the Truzzo granite (Katz, 1962).

Spectra of quartz in the Truzzo granite which show the broad band absorbance have always been acquired from regions containing fluid inclusions or grain boundaries. The distribution of primary fluid inclusions is highly heterogeneous. Fluid inclusions in recrystallized grains belong to fluid inclusion trails which cross-cut grain boundaries and are therefore considered as late features. As the clear quartz in the vicinity of fluid-inclusion-rich areas does not show water related absorbance bands, fluid inclusions appear not to affect the water content of the quartz.

It was possible to extract water from grain boundaries at 120°C. The water could have been introduced at any point from metamorphism to sample preparation. Water must have been present along grain boundaries during deformation and metamorphism as fluid inclusions are drained during grain boundary migration because recrystallized grains are free of primary fluid inclusions

(Craw & Norris 1993). Additionally, many microstructures in the Truzzo granite are indicative of processes requiring mass transfer in a fluid, e.g. myrmekites, biotite and K-feldspar precipitation. FTIR spectra of K-feldspar (Fig. 35) also suggest that molecular water is present in fluid inclusions and potentially voids related to perthitic exolutions. The compositional equilibration of plagioclase and white mica inclusions inside K-feldspar phenocrysts during high temperature metamorphic conditions requires a penetrative mass transfer. Lattice diffusion rates are usually far too slow even at high temperatures and instead transport in a fluid phase is considered to be essential in many non-isochemical mineral reactions (e.g. Wayte et al. 1989; Farver & Yund, 1995). Therefore, it is reasonable to assume that water was present during metamorphism and deformation of the Truzzo granite.

5.5.3 Why does quartz remain dry?

The question arises why quartz remains dry, although it is reported that water uptake takes place during deformation (Kronenberg et al., 1990; Nakashima et al., 1995; Gleason & DeSisto, 2008). Studies, which compare the water content in quartz with strain have been conducted on rocks deformed at greenschist facies conditions (<450°C: Nakashima et al., 1995; ~ 400°C: Gleason & DeSisto, 2008) or close to the brittle ductile transition of quartz (Kronenberg et al., 1990). Due to the low temperatures and high differential stresses during deformation the recrystallized grain size in the studied rocks is too small to measure water inside single crystals. The increasing water content reported in these studies increases with strain but also correlates with a decrease in grain size. The study of Gleason & DeSisto (2008) report an increased water content based on an average of their measurements which show a bimodal distribution. Their statement that water was measured inside single grains in an ultramylonite of ~120-160 μm grain size(their highest water content) contradicts with their illustration (their figure 6) as well as with any known deformation mechanism active in ultramylonites of such a grain size at 400°C. Many of their measurements in a granitic gneiss, pegmatite grains and quartz ribbon grains yield a low water content <100 H/Si1e6. The high values reported by Gleason & DeSisto (2008) in the ultramylonite possibly originate from measurements incorporating grain boundaries.

Water in experimentally deformed quartzites, where recrystallization is dominated by grain boundary migration and subgrain rotation has also been determined from polycrystals (Stipp et al. 2006). The water content of quartz schists is reported to decrease with increasing metamorphic grade from lower greenschist to amphibolite facies (Nakashima et al., 1995) accompanied with an increase in grain size. Granulite facies quartz of chert origin is reported to have very low water contents (e.g. Nakashima et al., 1995) measured inside mm-sized, undeformed quartz grains.

Therefore it is likely that the measured water content in previous studies on deformed quartz rocks is largely measuring grain boundary and inclusion water. It is not clear whether the reported correlation of strain and water content (Kronenberg et al., 1990; Nakashima et al., 1995; Gleason & DeSisto, 2008) is indeed related to an uptake of water into the quartz or to grain boundary water. Our result, however, does not dispute that natural quartz is weakened by water in some form as is known from experiments (Griggs & Blacic, 1964; Kekulawala et al., 1978,1981; Kronenberg & Tullis, 1984).

Suggested deformation related processes which contribute to water uptake are (micro)fracturing (Kronenberg et al., 1990) or diffusion, most probably along subgrain boundaries or dislocation cores (Post & Tullis, 1998). It has been speculated (Gleason & DeSisto, 2008) that grain boundary migration contributes to water uptake into quartz during deformation arguing that oxygen diffusion and hence hydroxyl diffusion is enhanced at higher dislocation densities (Post & Tullis, 1998) and that therefore deformation should enhance water uptake. This argument does not seem reasonable as strain induced grain boundary migration reduces the dislocation density. The data of the Truzzo granite also does not confirm this speculation.

Grain boundary migration is the dominant recrystallization mechanism during the formation of microstructure (1) with an increasing contribution of subgrain rotation recrystallization towards microstructure (2). Newly formed grains do not show the white mica related absorbance as well as truncate primary fluid inclusion clouds in relict magmatic grains. Fluid contained in the fluid inclusions must have been expelled into the grain boundary region and is not in included into the newly formed grains. The white mica is either trapped on grain boundaries, reacts and forms coarse biotite inclusions, or it may dissolve and be transported to another reaction site. Grain boundary fluid inclusion in metamorphic rocks have been reported as CO_2 enriched due to the capability of water escape along grain boundaries (Craw & Norris, 1993).

A potential reason why water was not taken up by quartz can be related to deformation at low differential stresses. The grain size piezometer calibration of Stipp & Tullis (2003) is suggested to be independent on the water content (Stipp et al., 2006). However the modified piezometer relation (Shimizu, 2008) incorporates a temperature dependent grain growth component. Grain growth and grain boundary migration have been demonstrated to occur at a higher rate at water present conditions (Tullis & Yund, 1982; Urai et al, 1986; Schenk et al., 2005). As pointed out earlier water was present during quartz recrystallization in the Truzzo shear zones. Therefore it is assumed that the grain size piezometers can be applied. The large recrystallized grain size in microstructure (1) and (2) indicates differential stresses as low as ~5 -15 MPa (Stipp & Tullis, 2003; Shimizu, 2008) rendering fracturing unlikely as a mechanism for water uptake. The low differential stresses also imply low dislocation densities and hence little pathways provided by pipe diffusion trough dislocation cores.

It is suggested that water uptake during deformation did not take place because grain boundary migration and only minor subgrain rotation do not promote water incorporation into the lattice at high temperature. Furthermore, grain boundary migration cleans the quartz grains by expelling inclusions. The observation of dry quartz is consistent with other studies of high temperature rocks where intragranular water was determined (Nakashima et al., 1995).

5.5.4 Implications on the strength of quartz

Experimental deformation of quartz suggests a decrease in strength at water present conditions (Griggs & Blacic, 1964: Kekulawala et al., 1978,1981; Kronenberg & Tullis, 1984). Assuming that the stress estimates by grain size piezometers are in the correct order of magnitude, strain rates predicted by experimental flow laws (e.g Hirth et al., 2001) yield reasonable results which are in the range of predictions for a fine grained feldspar matrix deforming by diffusion creep (for a detailed discussion see Chapter 5) (Fig. 36) at the low differential stresses related to the large grain size of microstructure (1). Hirth et al. (2001) introduce a factor to explain the pressure dependence observed in experimental deformation of quartzites (e.g. Kronenberg & Tullis, 1984) and relate that factor to the water fugacity. Water fugacities cover the range of 100-1000 MPa in normal crustal conditions, therefore contributing about 2-3 orders of magnitude to the calculated strain rates. If one would assume that the contribution of water to the strength of quartz is related to an effect of intragranular water, strain rates would be about many times lower (e.g 700 for 600°C and 0.8 GPa). However, the fact that quartz aggregates deform inside the fine grained feldspathic matrix suggests that quartz is unlikely to flow several orders of magnitude slower than the matrix.

Because quartz in the Truzzo shear zones does not contain intracrystalline water but deform at low differential stress, fluid present conditions, it must be considered that weakening related to water during deformation of polycrystalline quartz is not necessarily related to intracrystalline processes. As pointed out earlier, water measured in previous studies (Kronenberg et al, 1990; Nakashima et al, 1996; Gleason & DeSisto, 2008) can be contained in grain boundaries.

Mancktelow and Pennacchioni (2004) observe a limited grain boundary mobility in water-deficient quartz mylonites and recrystallization by high stress processes (bulging and subgrain rotation), pointing out the importance of grain boundary fluids required for low stress recrystallization. This bears the potential that the weakening effect in polycrystalline quartz is rather related to the enhancement of grain boundary processes (e.g. grain boundary migration, diffusion accommodated grain boundary sliding during dislocation creep).

Following the above reasoning that water weakening in polycrystalline aggregates is related to grain boundary processes, a construction of a stress-strain rate relation based on a “wet” flow law (Hirth et al., 2001) is eligible (Fig. 36).

It has to be pointed out that the water weakening processes observed in (synthetic) single quartz crystals that were experimentally deformed by dislocation glide (e.g. Kekulawala et al., 1978, 1981; Kirby & McCormick, 1979) are unrelated to the processes considered in this study.

5.6 Shear zones

Deformation mechanisms, relative timing, conditions during deformation and rheological inferences can be interpreted from microstructures. Additionally macroscopic structures provide information about the geometry of deformation relative timing and rheology.

5.6.1 Evolution and rheology

The evolution of microstructures in the Truzzo granite samples suggests a change of deformation and temperature conditions during the entire structural history (Fig. 18,19, 12,15). The subsequent development of the quartz microstructures in combination with the stability and the changes in the matrix minerals is used to suggest a sequence of events during shear zone development and deformation.

The quartz microstructures (1) and (2) indicate high temperature deformation at low differential stresses. The matrix minerals and microstructures (3) and (4) are the same as (1) and (2) so that high temperature flow is also inferred. The weakening of the CPO and phase mixing both indicate diffusion creep deformation. The residual CPO could be produced by prism [c] glide in combination with basal <a> glide and grain boundary sliding, or dissolution precipitation processes. In both cases temperature must have remained high based on the plagioclase composition (> 550°). Biotite is stable in all associations and forms at the expense of white mica during grain boundary migration related to microstructure (1).

A later overprint causes quartz recrystallization by subgrain rotation causing a local grain size decrease. The latest, very localized overprint results in quartz recrystallizing by a combination of subgrain rotation and bulging recrystallization associated with a breakdown of biotite to white mica and or chlorite. Therefore this is inferred to happen at somewhat lower temperatures. Taken altogether this records a history of quartz recrystallization starting at high temperature - low differential stress conditions followed by a later higher differential stress overprint at finally lower temperature.

The grain size decrease from more than >500 μm to ~110 μm in pure quartz aggregates is associated with a change in the recrystallization mechanism from dominantly grain boundary migration recrystallization to rotation recrystallization and down to ~25 μm for rotation/bulging recrystallization. As different recrystallization mechanism are involved and the temperatures are not well known results of the quartz grain size piezometers have to be treated with caution (Stipp & Tullis, 2003; Shimizu, 2008). Based on the earlier discussion it is assumed that the grain size piezometers can be used to derive differential stresses. Using the the calibration of Stipp & Tullis (2003) and ignoring that it yields possibly slightly lower stresses for large grain sizes formed by grain boundary migration recrystallization, the stresses are in a range of 5 to 50 MPa.

The feldspar matrix records a similar evolution. The presence of a constant plagioclase composition in the different microstructures suggests that there is no major change in temperature during development of the quartz microstructures (3) and (4). A higher differential stress interpretation at lower temperatures during the later overprint is consistent with the formation of late flame perthites in matrix K-feldspar grains as well as in K-feldspar porphyroclasts. A late temperature decrease is also indicated by the localized biotite breakdown.

Combining the inferred PT-development with the deformation mechanisms identified from microstructures provides a rough estimate of the rheologic evolution of the shear zones and may provide possible explanations for the formation of macroscopic structures (Fig. 36).

The switch to a higher differential stress and in the very last stages also to a lower temperature is attempted to be correlated with the macroscopic structures of the shear zones. The steep strain gradient between the undeformed rock and the ultramylonite and the local thinning of the shear zones into shear bands (Fig. 5c,d) indicate at first a high viscosity ratio and possibly relative strain hardening of the shear zones.

A true strain profile in the shear zones could not be established due to the lack of passive markers. Nevertheless, most broad shear zones typically show an abrupt transition from a weakly deformed granite in the host rock to a highly deformed (ultra)mylonite. The (ultra)mylonite is either homogeneous across the shear zone or more fine grained parts with less porphyroclasts are close to the contact with the wall rock. This is suggestive for type 1 shear zones (Hull, 1988; Means 1995) which grow in width with time and show a hardening behavior with respect to the pristinely deformed material. Nevertheless this is speculative as no passive foliation has been observed.

The relative stress - strain rate estimate is based on the quartz microstructure and the grain sizes. Quartz aggregates form porphyroclasts embedded inside the feldspar-mica matrix. As a first approximation one can assume a Reuss-bound (iso-stress) system. In that iso-stress system polycrystalline quartz aggregates deform by dislocation creep while the feldspar-mica matrix deforms by diffusion creep. Based on the observation that quartz forms low aspect ratio porphyroclasts but also from the extrapolation of experimentally derived flow laws (see Chapter 3,5) the polymineralic phase mixture deforms at a higher rate than the monomineralic quartz aggregates. The strain rate ratio between the two materials (deformed simultaneously by dislocation and diffusion creep) decreases with increasing differential stress below the equiviscous point, where strain rate and differential stress are equal.

Above the equiviscous point the power law material with the higher stress exponent should deform for a given differential stress at a higher rate. However if the power law material is embedded inside the lower viscous material, the system is Voight-bound (iso rate). This is comparable with a transition from an interconnected weak layer to a load bearing framework model (Handy, 1990, 1994) due to an inversion of the effective viscosity ratio.

An increase in the differential stress is indicated in the quartz grain size decrease from microstructure (1) to (2) and the subsequent overprint. The presence of elongate grains and grain substructures indicate crystal plasticity of single quartz grains inside the polymineralic matrix. The coeval activity of crystal plasticity in quartz and diffusion creep in the polymineralic mixture indicates a differential stress level close to the equiviscous point. The latest structures developed in quartz consist of small grains formed by subgrain rotation and bulging recrystallization together with the biotite breakdown. If the differential stress and strain rate in that situation are higher than at the equiviscous point (at a lower temperature) the system should be Voight-bound as single quartz grains occurred isolated in the feldspar-mica matrix. Quartz can deform by intracrystalline plasticity while there is no indication for that mechanism in the feldspar matrix. Above the equiviscous point (Fig. 36) quartz must be regarded as a lower viscous inclusion. As long as newly recrystallizing quartz aggregates do not coalesce the differential stress indicated by the quartz grains size corresponds with a quartz strain rate which should be the strain rate of the entire system (Voight bound). This, however, implies that the required differential stresses in the polymineralic matrix rise to values higher then the assumed confining pressure (Fig. 36).

Instead of forming embedded inclusions in a load-bearing framework, low viscosity inclusions tend to coalesce towards forming interconnected weak layer structures (Jordan, 1987; Holyoke & Tullis, 2006). The latest quartz and biotite-breakdown structures are observed in thin layers parallel to the mylonitic foliation. These structures are interpreted from exactly such a coalescence process. Therefore, above the equiviscous point the differential stresses in the matrix might not have differed much from the differential stresses in the quartz if coalescence of the weak layers took place subsequent to increased loading.

Broad shear zones show locally thinned parts with an adjacent deformation in the hostrock. Shear bands accommodate the displacement at the shear zone - low strain interface and connect the shear zones (Fig. 5c,d). The geometry resembles asymmetric boudinage. Despite the fact that a boudinaged shear zone is at fist instance a paradox, a change in the rheology of the hostrock, the shear zone or both can account for the phenomenon.

The transition to a differential stress higher than the equiviscous point, or alternatively a lowering of the equiviscous point both can serve as an explanation for the hardening behavior of the shear zones. Assuming that grain growth in the polymineralic mixture is inhibited by pinning it might not be easily possible to undergo a switch to dislocation creep. The less deformed granite consists of large mineral grains or monomineralic aggregates. Therefore deformation by dislocation creep can be expected to be more efficient in the granite (large grains, higher grain boundary - phase boundary ratio). This may serve as a possible explanation of the relative hardening of the shear zones with respect to the granite and for the necking of the mature shear zones.

The previous discussion is based on the rheological implications of the microstructures and assumes that the sequence of differential stress - strain rate - temperature belong to a single deformation phase in an approximately constant kinematic framework. However there is no good reason to rule out that the overprinting quartz microstructures and the lower temperature, high stress structures did develop in a separate kinematic framework. The anisotropy of the shear zone foliation may still accommodate differential movement, but possibly in a different loading geometry. While this cannot explain the enigmatic high temperature quartz CPO in the polyphase ultramylonite (microstructure (3) and (4)) it could account for the shear zone necking.

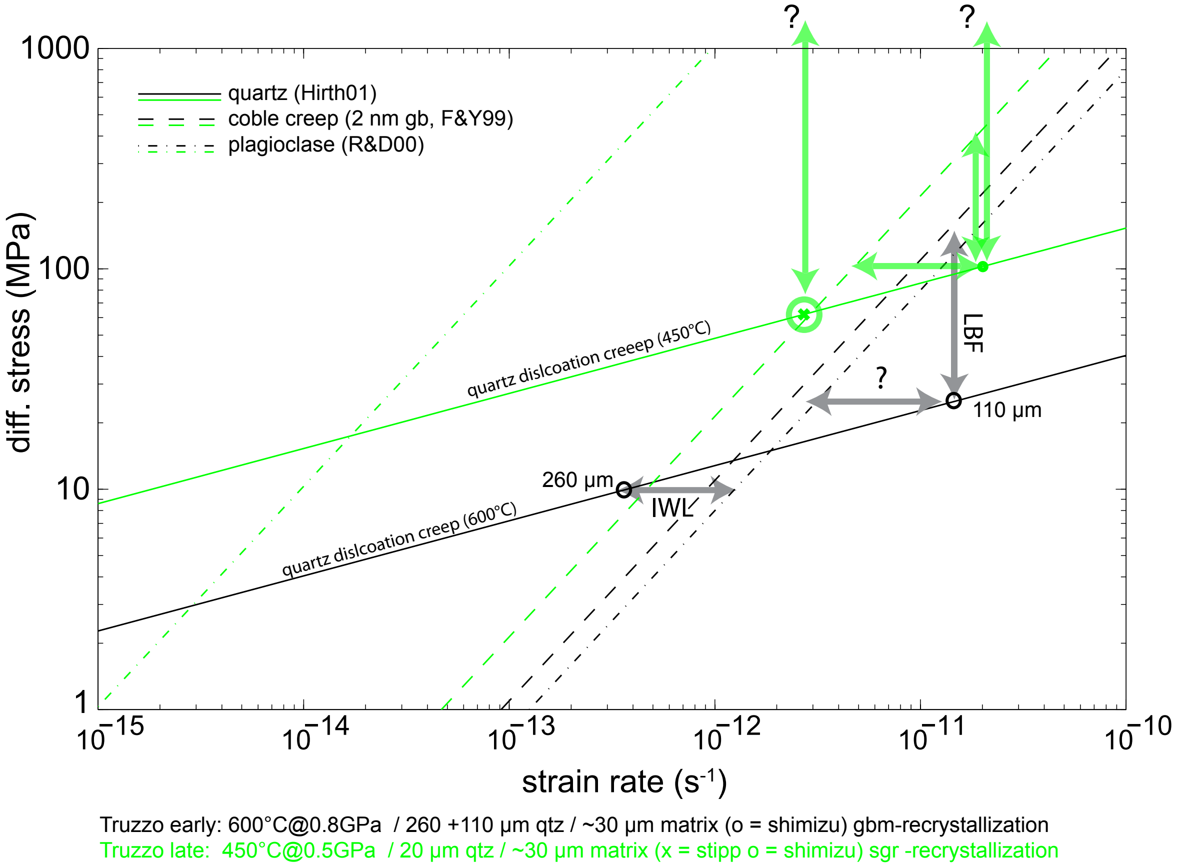

Figure 36: Rheological scheme and possible evolution of the Truzzo granite shear zones: Curves for experimentally derived dislocation creep flow law for quartz (Hirth01: Hirth et al., 2001) and diffusion creep law for plagioclase (R&D00: Rybacki & Dresen, 2000) and theoretical Coble-creep law with experimentally derived parameters for oxygen diffusion in a natural ultramylonite (F&Y99: Farver & Yund, 1999) for 600°C at 0.8 GPa and 450°C at 0.5 GPa assuming a grain boundary width of 2 nm.
The decreasing recrystallized quartz grains size indicates an increasing differential stress and strain rate. Interconnected weak layer structures (IWL) can be approximated by iso-stress conditions (grey arrows) while a load bearing framework structure (LBF) enforces iso-rate conditions (green arrows). The decreased quartz grains size found in late microstructures predicts stresses higher than the equiviscous point. See text for discussion.

5.6.2 Localization and propagation

First the localization mechanism, and then the potential propagation of the shear zones will be discussed:

Plagioclase aggregates and tails of recrystallized K-feldspar deform readily at the margins of broader shear zones and in more homogeneously deformed volumes inside the low strain domain. Thin and crack-like shear zones are not associated with the extensive feldspar deformation and crosscut K-feldspar grains. Two alternatives can account for this situation. (a) Weak feldspar aggregates result in the formation and localization of the shear zones and the subsequent propagation is promoted by a fracture-like mechanism. (b) Alternatively, broad shear zones can accommodate more deformation in volumes with weak feldspar aggregates and highly localized, crack-like shear zones form in volumes of strong feldspar aggregates. While in possibility (b) both processes may happen simultaneously, possibility (a) predicts that the fracture-like tips are the precursors during propagation and follow the viscous shear zone nucleation.

Mesoscopically, it is impossible to decide whether one or the other is the case. However, as the crack-like ends of shear zones only accommodate little displacement they probably are not the kinematic equivalent of the broader shear zones.

Assuming that the fracture-like tips of the shear zones present some kind of spatial or temporal precursor (Pennacchioni, 2005, Pennacchioni et al., 2006), cracks could be either relicts of an unactivated precursor (temporal precursor) or a crack formed during propagation of the yet established shear zone (spatial precursor).

The crack-like tips cut through K-feldspar phenocrysts while in the homogeneously deformed areas C and C’ shear bands form around K-feldspar porphyroclasts (Fig. 7, 6). This suggests that the crack-like structures have at least not been penetratively present in the more homogeneously deformed regions. Based on the FTIR results it can be assumed that microfracturing and water infiltration did not play a significant role for strain localization, like proposed in other cases of brittle precursors (e.g. Kronenberg et al., 1990). From this point of view it does not seem reasonable that the fracture and its wall rock was weaker. Therefore, it is assumed that the shear zones did not initiate along a preexisting fracture but that the fracture formed during propagation of the already established shear zone.

Shear zones which join more homogeneously deformed areas join into C or C’ shear bands defined by fine grained recrystallized feldspar and mica. The coalescence of weak aggregates has been shown to contribute essentially to shear zone formation (Holyoke & Tullis, 2006). Once established, processes like phase mixing may further contribute to weakening of the evolving shear zone.

Once a shear zone is established and accommodates displacement it can propagate in different ways. Brittle fractures have been suggested to propagate at the tip of a ductile shear zone related to stress concentrations (Mancktelow & Pennacchioni, 2005; Fusseis & Handy, 2008). Shear zones may also propagate by the formation of a ductile shear band (Hutchinson & Tvergaard, 1981) and both modes may be present and interact (e.g. Misra et al., 2010). Either mode depends on the rheology and whether temperature and state of stress favor brittle fracturing or the formation of ductile shear bands. Another less investigated process causing a transition from viscous to brittle structures is ductile failure (Kassner & Hayes, 2003; Chokshi, 2005; Rybacki et al., 2008; Rybacki et al., 2010). Ductile failure is used to describe the strain dependent failure caused by the coalescence of creep induced cavitation in materials deforming by grain boundary sliding. Despite it is argued that cavities are difficult to maintain at high confining pressures (Paterson, 1990), cavities are observed in natural high temperature mylonites (Geraud et al., 1995; Fusseis et al., 2008) and high temperature - high pressure experiments on synthetic feldspar aggregates (Rybacki et al., 2008), and fluid or melt rich experiments on quartz (Schmocker et al., 2003) or olivine (Holtzman et al., 2003).
As outlined earlier, stresses during the the onset of deformation are relatively low (~< 5 MPa) as inferred from the grain size of microstructure (1). The deformation mechanism in the polymineralic, strain accommodating matrix is inferred to be diffusion creep with grain boundary sliding. The total shear shear strain accommodated in the mature parts of the shear zones is not well established but at least γ larger than 10. Therefore requirements for coalescence of creep cavitation are potentially met (Rybacki et al., 2008). In the Truzzo granite grain boundary sliding and the accommodation of heterogeneous strain at the grain scale is associated with the precipitation of K-feldspar and biotite. As the growth rate is at least as high as the opening rate of cavities it is not clear whether the opening between grains behaves mechanically similar to cavities. However if strain dependent coalescence of opening sites takes place, it could potentially account for a temporarily increased strain rate which in the continuation of the shear zone can propagate as a brittle fracture.

Both, stress concentrations caused by the shear zone propagation or temporal slip events due to ductile failure could potentially explain the observed crack-like structures at the tips of shear zones. Which mechanism actually is responsible for this structure cannot be decided.

An increasing differential stress is interpreted from quartz microstructures and modeling of flow lows indicates a potential inversion of the effective viscosity ratio (Fig. 36). As mentioned earlier this switch would be related with a highly increased loading of the matrix due to the transition to a Voight-bound system if the microstructure does not change instantly by coalescence of the weak phase forming again an interconnected weak layer. Depending on the flow law assumptions differential stresses can easily reach values larger than the inferred confining pressure (Fig. 36) as long as no coalescence occurs or the system returns in some other way to Reuss-bound conditions. However the thin shear zone tips do not record the lower temperature metamorphic assemblage related to the smallest quartz grain size.

5.6.3 Relative timing and tectonic implications

The metamorphic development of the Truzzo granite can be summarized in the following way: Initial high pressure - high temperature metamorphism leads to the development of fine grained plagioclase. The initial deformation may have initiated as well during high pressure conditions. The main deformation in the shear zones takes place at high temperature conditions. The late overprint is only associated with very minor movements of the shear zone and took place at slightly lower temperatures.

The PT-path presented by other workers suggest similar stages of an early high pressure - high temperature metamorphism, peak metamorphism during decompression and retrogression at lower pressure (Marquer et al., 1994; Huber & Marquer, 1998; Engi et al., 2004). The first deformation phase D1 was suggested to initiate during high pressure conditions and the second deformation phase D2 commencing during decompression towards peak metamorphic conditions (Baudin et al., 1993). However, despite both D1 and D2 are attributed to different tectonic phases (Schmid et al. , 1990; Marquer, 1991; Baudin et al., 1993), the significance of the shear zones in the low strain domain in the southernmost Truzzo granite is unclear. The associated stretching lineation pointing ~E-W is consistent with the described E-W stretching component during nappe stretching (D2). Nevertheless, that kinematic interpretation of D2 is inferred from the neighboring Suretta nappe (Huber & Marquer, 1996; Marquer et al., 1996). Baudin et al. (1993) even consider that some shear zones could have been developed during nappe stacking D1 and reactivated during nappe stretching D2. It is unclear whether these authors refer to the small scale shear zones in the low strain domain or to the mylonitic orthogneiss as a whole.

Shear zones that extend over low strain domain do not clearly cut the foliation in the orthogneiss that surrounds the low strain domains nor does the main foliation in the orthogneiss clearly overprint the shear zones. While the foliation of the orthogneiss wraps around the low strain domain, stretching lineations in the orthogneiss and of the shear zones plunge moderately to E - ESE (Fig. 4). Most shear zones are in an intermediate orientation with respect to the main foliation in the orthogneiss. The geometrical and overprinting aspects permit the possibility of a coeval formation of the shear zones and the main foliation in the orthogneiss.

As pointed out in the introduction, the shear zones in the low strain domain may either represent a precursor stage to the orthogneiss or the shear zones result from the heterogeneous mechanical response due to a displacement field subjected of the low strain domain. In such a case, the low strain domain would have the properties of a porphyroclast inside the orthogneiss. In the latter case the shear zone orientation and kinematics might be of only limited regional significance. The observation that shear zones localize from C and C' shear bands of a slightly more homogeneously deformed granite inside the low strain domain and propagate into undeformed granite is in favor of the latter possibility. This also implies that shear localization is more favorable at the conditions of shear zone formation than deformation distribution.

Despite high pressure is only recorded indirectly in the Truzzo granite and shear zones and most synkinematic minerals are equilibrated at high temperatures the possibility that shear zones already nucleated at high pressure conditions cannot be excluded. Nevertheless the presence of the fine grained plagioclase aggregates which formed statically and during or after high pressure metamorphism is regarded to be essentially enhancing strain localization. Therefore it is more likely that the shear zones formed during decompression towards peak metamorphism and during initial retrogression.

6. Conclusions

1) Quartz microstructures in the shear zones in a low strain domain of the Truzzo granite record a history of increasing differential stress during deformation, which started at high temperatures.
2) Quartz recrystallizes at high temperature by dominantly grain boundary migration recrystallization. A strong CPO is not developed. During later stages of deformation rotation recrystallization becomes the dominant recrystallization mechanism in highly deformed parts of the mylonite. At the latest stage and probably during lower temperatures, thin micro-shear-zones develop in the existing “coarse” ultramylonitic microstructure showing a smaller recrystallized quartz grain size and recrystallization by rotation/bulging recrystallization.
3) A fine grained phase mixture forms at high strain and high temperature and deforms by a diffusion creep with a minor component of dislocation creep.
4) The shear zones show a hardening behavior which can be explained within the deformation history of a later overprint involving an increase in the differential stress. The shear zones and the host rock most likely undergo an inversion of the viscosity contrast.
5) The formation of fine grained feldspar promotes shear zone localization. Fine grained plagioclase is formed by various processes: replacement of perthites, myrmekites, static recrystallization of magmatic plagioclase. Fine grained K-feldspar form by recrystallization of large magmatic porphyroclasts and precipitation in dilatant sites; preferentially between quartz grains.
6) Fracture-like terminations of shear zones probably formed during shear zone propagation. There is no evidence of a late brittle reactivation of the entire shear zone. Fracture-like terminations are interpreted as the propagating tip of the shear zone, advancing either by ductile failure or due to stress concentrations.
7) FTIR spectra of clear quartz grains indicate that neither unrecrystallized nor recrystallized grains contain a significant amount of water. Broad band absorbance is related to fluid inclusion rich areas in magmatic quartz grains.
8) Recrystallization does not contribute to the uptake of water in quartz but eliminates primary fluid inclusions.
9) Magmatic quartz grains contain (submicron) white mica inclusions which react to biotite or are extracted during recrystallization by grain boundary migration.
10) A high water content in fluid inclusions in K-feldspar, stable biotite and myrmekite and leaking of primary fluid inclusions suggest water present conditions during deformation.

Water incorporation into quartz does not take place during recrystallization by grain boundary migration.

11) Quartz recrystallizes at low differential stresses in the absence of intracrystalline water during the main shear zone forming event. The microstructure does not indicate that quartz deforms many orders of magnitude slower than the matrix and can be adequately approximated by a "wet" flow law. The Truzzo granite shear zones can be an example of the effect of grain boundary water on the strength of dry, polycrystalline quartz. In that case, weakening must be related to grain boundary processes.

Chapter 5

Application of flow laws for naturally deformed polyphase rocks

Abstract

Small scale shear zones formed in the Gran Paradiso metagranodiorite under lower amphibolite facies conditions. Based on detailed microstructural work the deformation mechanisms of the different rheological phases have been identified. Polycrystalline quartz aggregates deform by dislocation creep, whereas the polymineralic matrix deforms by diffusion creep.

The geometry of quartz aggregates shows some pinch and swell structures within the matrix, and little coalescence suggesting that quartz represents the more viscous phase in a somewhat lower viscous matrix, at least at low strain. At high strain quartz is completely recrystallized and forms parallel layers with the matrix but almost no boudinage.

Independently derived experimental flow laws for quartz and feldspar as well as the theoretically derived flow law for Coble creep with the appropriate parameters can reproduce the observed relation between quartz aggregates and matrix suggesting a strain rate ratio below 1 order of magnitude.

At the highest strain quartz aggregates disintegrate and single quartz grains become mixed with the polymineralic matrix. They deform with the matrix by grain boundary sliding (diffusion creep). The diffusion creep rate has to be higher than the rate of crystal plastic deformation (dislocation creep) to fit the observations. Though it is possible to determine the scaling factor A for a modified rate law for diffusion accommodated grain boundary sliding it is not possible to apply that rate law to different medium to high grade granitic rocks.

A comparison of data from different granitic rocks deformed between 450° to ~ 600° shows that in combination with a quartz creep law, a Coble creep law is better suited for extrapolation at various natural conditions.

1. Introduction

Quartzo-feldspathic rocks are very common in the earth's crust. Their rheology controls the deformational behavior of a large part of the crust under a wide range of pressure and temperature conditions. Commonly strain localization in these rocks involves reaction or recrystallization of feldspars (Kerrich et al., 1980; Stünitz & FitzGerald, 1993; Tsurumi et al., 2003; Ree et al., 2005; Menegon et al., 2006) and develop monomineralic quartz aggregates embedded in a polymineralic mixture, which tends to be mechanically weaker than the quartz aggregates (Stünitz & FitzGerald 1993; Menegon et al. 2006). As the mechanically stronger quartz typically does not exceed 70 % of the whole rock composition, the rock rheology is not controlled by quartz but by the feldspar-dominated weaker matrix.

While rheological data for quartz exists (derived from laboratory experiments and a combination of laboratory data and observations of naturally sheared quartzites; Luan & Paterson 1990; Paterson & Luan 1992; Gleason & Tullis 1995, Hirth et al. 2001; Rutter & Brodie 2004), there is only limited data for feldspar (Rybacki & Dresen 2000, Rybacki et al. 2006). In addition, data for feldspar-dominated polymineralic mixtures does not exist. As this type of material controls the rheology of a large part of quartzo-feldspathic rocks, it is desirable to obtain rheological information about such polymineralic mixtures.

We will test the applicability of experimentally and theoretically derived flow laws on the rheology in an amphibolite facies shear zone developed in a metagranodiorite.

2. Observations on shear zones in Gran Paradiso metagranodiorite

2.1 Geological setting

The studied metagranodiorite of the Gran Paradiso nappe in the Piantonetto valley, Western Alps, preserves low strain domains which are internally cut by small scale shear zones (Callegari et al, 1969; Dal Piaz et al.,1972; Menegon & Pennacchioni, 2009). Samples (32T0371382/5037194, 32T0371554/5037041,32T0371389/5037047, Alpe Drosa) contain a strain gradient from protomylonites to mylonites to ultamylonites within several millimeters (Fig. 1a). These rocks have been studied in great detail (Le Goff & Ballevre; Brouwer et al., 2002; Menegon et al., 2006/2008; Menegon & Pennacchioni, 2009) for their metamorphic and structural evolution.

The quartz content in the metagranodiorite of about 30% (+/-3) remains constant throughout the strain gradient (Kilian et al., b) as well as the bulk chemical composition (Menegon et al., 2006). The polymineralic matrix consists of fine grained plagioclase (a static high pressure recrystallization product, e.g. Lenze & Stöckert, 2007; Bucher & Grapes, 2009), minor myrmekite-derived fine grained oligoclase and quartz (Menegon et al., 2006), K-feldspar, recrystallized and/or precipitated K-feldspar, biotite, recrystallized and precipitated biotite, and minor clinozoisite and white mica (Fig. 2a,b).

Shear zones:

The shear zones developed during lower amphibolite facies conditions of about 500-550°C and 0.6-0.7 GPa (Brouwer et al., 2002) after an earlier static high pressure event at 550±50°C at 1.0-1.6 GPa (LeGoff & Ballevre,1990) or, as newer data revealed more precisely, at 500-550°C and 1.2-1.4 GPa (Brouwer et al., 2002).

Recrystallized quartz grain sizes in the monomineralic aggregates were obtained from segmentation of CIP-derived misorientation images, from EBSD-derived data, and, with increasing phase mixing, from EBSD and SEM-BSE-images. For the detailed procedures see Chapter 2,3. The grain sizes of the matrix phases and the finest grained phase mixtures are obtained from SEM BSE images. All grain sizes are given as diameter of spheres calculated from the equivalent area.

Quartz layers:

The recrystallized quartz grains have a mean diameter of around 60 μm (number weighted 3D, 70 μm in 2D) and 110 μm (volume weighted 3D). It is constant across the strain gradient (Fig. 3,4). Quartz subgrains in the recrystallized grains are extremely rare as obtained from EBSD data. Subgrain sizes were measured in areas bound by at least two subgrain boundaries (< 7.5° misorientation) and by non-migrated phase or grain boundaries. The sizes range between 20 and 65 μm with a mean and a median at about 40 μm (Fig. 3). These are considered to be formed by subgrain rotation recrystallization as part of maintaining a dynamic steady state grain size.

Matrix layers:

The matrix grain size has been measured on recrystallized K-feldspar and matrix plagioclase grains (e.g. Fig. 2 a,b). Their grain size remains constant throughout the strain gradient smaller 25 μm with a mean of ~10 μm (15 μm volume weighted) (Fig. 5).

In the shear zone center, where the aggregates disintegrate, the quartz grain size is decreased to 20 μm, approaching the matrix grain size. This grain size reduction is the product of a.) pinning of the dynamically recrystallized grains by second phase particles and b.) by subsequent dissolution (Kilian et al., 2011a).

Dislocation creep in quartz layers (mylonite):

Quartz aggregates show a homogeneous microstructure, implying that conditions of differential stress and temperature did not change significantly during deformation.

The development of a homogeneous microstructure, a strong CPO, recrystallization by progressive subgrain rotation, combined with grain boundary migration, development of an asymmetric fabric, and a constant grain size indicate dislocation creep being the dominant deformation mechanism in the quartz aggregates.

Diffusion creep in layered matrix:

The matrix is composed of a polymineralic mixture of plagioclase, biotite, K-feldspar and minor white mica. It is concluded to deform by diffusion creep, inferred from microstructures of albite core - elongate oligoclase rim grains (Fig. 2b), the K-feldspar distribution perpendicular to previously “pure” K-feldspar layers, the biotite phase distribution, absence of interconnected biotite layers, and a dispersed distribution of all phases. The initially small grain size remains constant throughout the strain gradient interpreted to represent a grain size stabilized by second phase particle pinning.

Diffusion creep in polyphase mixture (ultramylonite):

In the center of the shear zone, quartz aggregates are disintegrated along dilatant grain boundaries (i.e. not boudinaged) involving grain boundary sliding (Fig. 1c). The quartz grain is size progressively decreased with increasing shear strain. There is strong evidence that quartz no longer deforms by dislocation- but by diffusion creep (Kilian et al. b), and the grain size reduction occurs through dissolution and precipitation of SiO2 in other dilatant sites. Single quartz grains do not show signs of internal crystal plastic deformation.

Microstructural observations relating to shear zone development:

The microstructural and geometrical development of the shear zone has been studied in (Chapter 2/3) providing detailed data on grain sizes, deformation mechanisms and the geometrical evolution of different layers with increasing strain (Fig. 1a). The studied rock can be simplified to a system

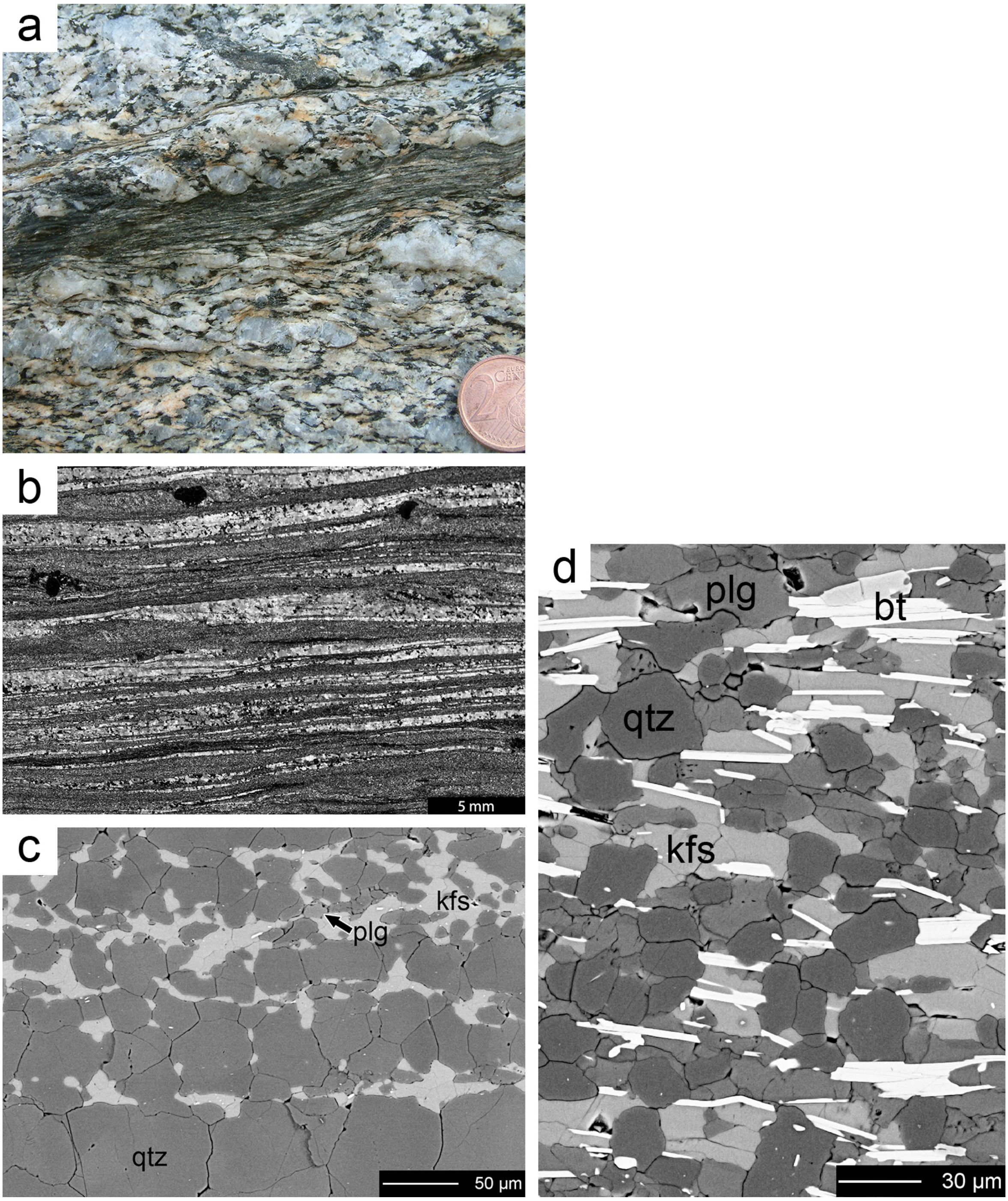

Figure 1: Overview: (a) Shear zone in slightly deformed metagranodiorite. Diameter of coin is 9 mm. (b) Micrograph of the highly deformed mylonite. Quartz aggregates form parallel layers with the matrix. Cross-polarized light. (c) SEM/BSE image of quartz layers which disintegrates during the precipitation of K-feldspar. Plagioclase has a very similar grey value to quartz. It is preferentially found in the K-feldspar layer, has a smaller grain size than quartz, lobate boundaries and is sometimes inclusion rich. (d) Phase mixture in the ultramylonite. Quartz occurs as isolated grains mixed with K-feldspar, biotite and plagioclase.

consisting of original magmatic quartz grains which dynamically recrystallize to monophase quartz aggregates with a constant recrystallized grain size across the shear zone.The quartz aggregates are embedded in a polymineralic, fine grained matrix consisting of feldspar and small amounts of mica. With increasing strain quartz aggregates rotate towards the shear plane and may stretch up to highly elongated, up to one single grain thick layers (Kilian et al., 2011a, Chapter 2) (Fig. 1b).

Coalescence of quartz aggregates is absent and boudinage is rare and related to the propagation of C‘ shear bands or other heterogeneities, so that the pure quartz aggregates and the polymineralic matrix can be suspected to deform at vaguely similar strain rates (at constant differential stress). The monomineralic quartz aggregates deform by dislocation creep demonstrated by extensive subgrain rotation and grain boundary migration recrystallization, a strong CPO, and a narrow grain size distribution (Chapter 2,3).

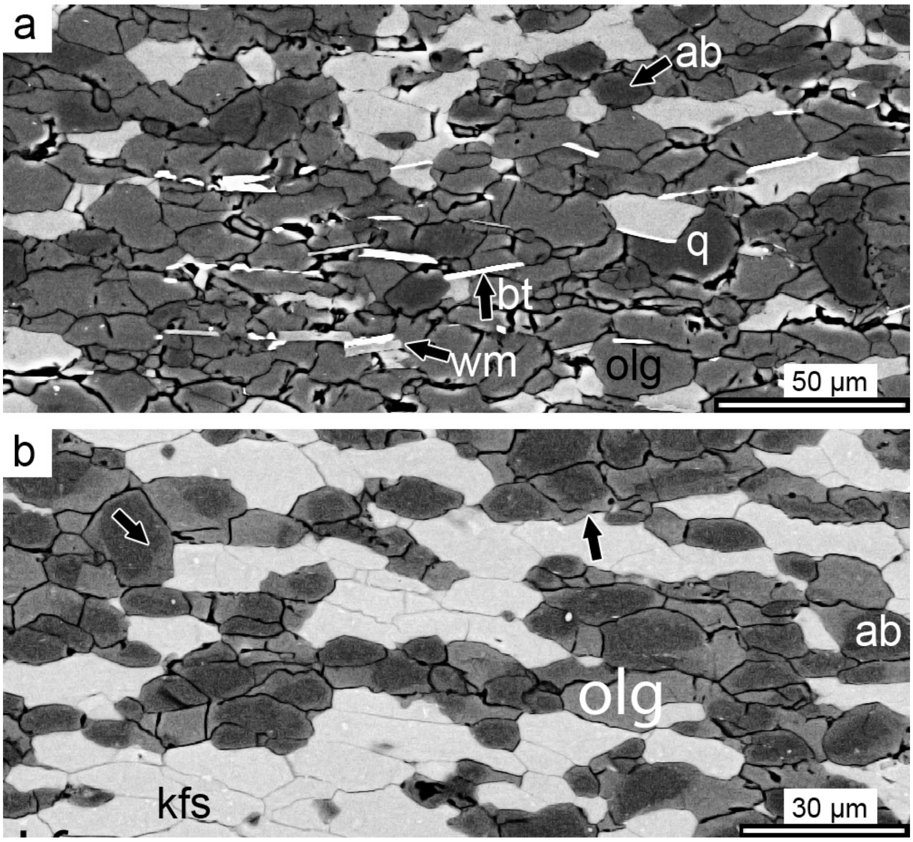

Figure 2: Matrix microstructures: (a) Oligoclase (olg), albite (ab), biotite (bt), white mica (wm) and a few single quartz (q) grains of the matrix. (b) Plagioclase grains composed of albite cores and oligoclase rims. Rims grow preferentially in the direction of the foliation (horizontal). Rims are occasionally truncated against phase or grain boundaries (arrows).

The polymineralic matrix (Fig 2 a,b) and the complete phase mixture (Fig. 1d) deform by diffusion creep as demonstrated by a small grain size, a very weak or absent CPO in quartz, a complete phase dispersion and absence of an internally layered structure.

In the central part of the shear zones representing the highest finite strains, quartz aggregates disintegrate at dilatant grain boundaries, associated with the precipitation of matrix phases (Fig 1c). The quartz grain size is decreased concomitantly with the precipitation of matrix phases and quartz aggregate disintegration (Fig. 3). The processes involved in the continuous grain size reduction are pinning of boundaries (suppression of grain boundary migration) and local phase boundary migration/dissolution-precipitation (Kilian et al., 2011a, Chapter 2).

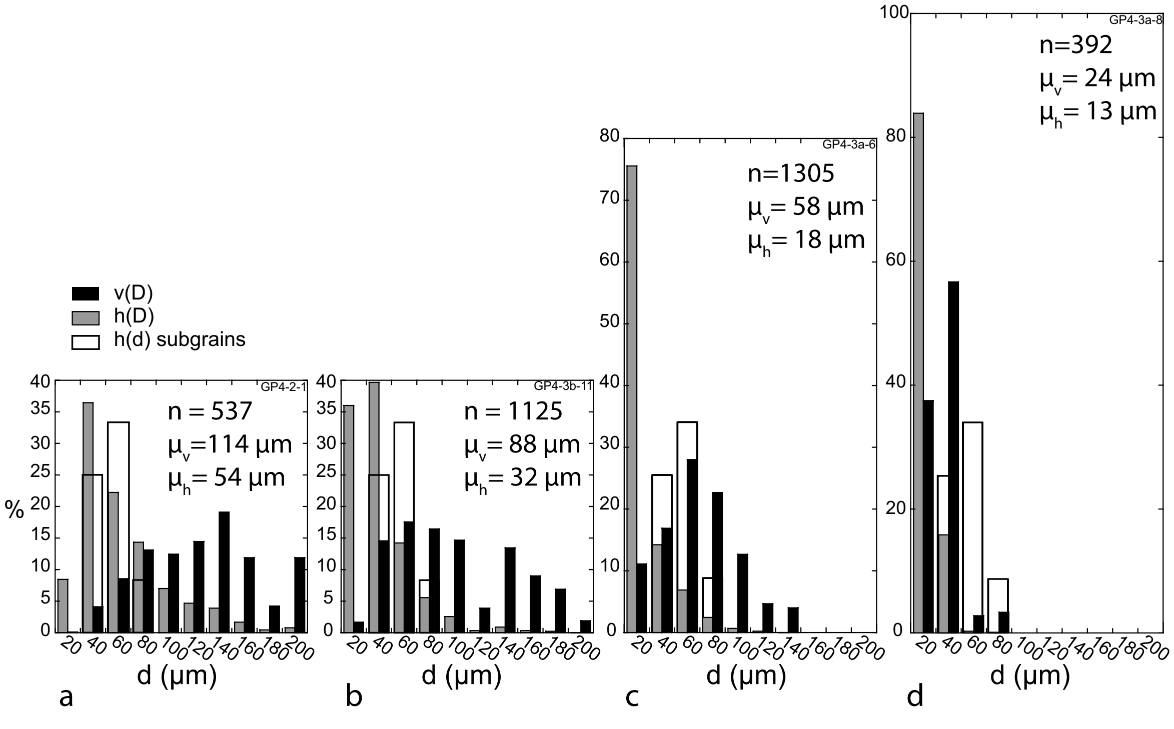

Figure 3: Evolution of the quartz grain size distributions. v(D) is the volume weighted, h(D) the number weighted distribution of diameters of spheres. μ_v and μ_h are the arithmetic mean values of the volume weighted and number weighted distribution. h(d) is the number weighted diameter of subgrains in recrystallized grains (equivalent area). The data is obtained from segmented EBSD maps. Grain sizes of: (a) a quartz aggregate in the most highly strained mylonite, (b), (c) partially disintegrated aggregates in the transition zone and (d) in the complete phase mixture. The subgrain sizes are superposed on each histogram.

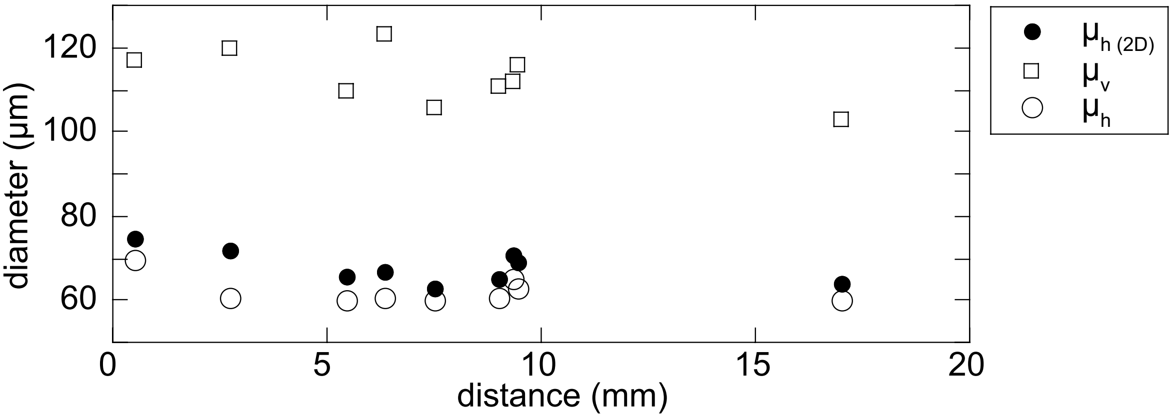

Figure 4: Mean dynamically recrystallized grain sizes throughout the strain gradient measured in monophase quartz aggregates in the mylonite. μ_v and μ_h are the number and the frequency weighted arithmetic mean values of the diameter of the 3D grain size. $\mu_{h(2D)}$ is is number weighted arithmetic mean value of the diameter of the 2D grain size. Distance 0 is at the transition to the ultramylonite.

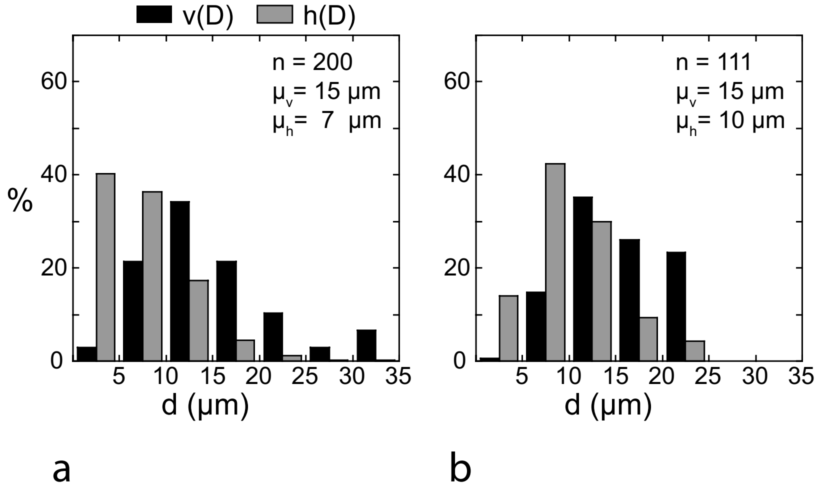

Figure 5: Matrix grain size: (a) Plagioclase and (b) K-feldspar in the polymineralic matrix. v(D) is the volume weighted, h(D) the number weighted distribution of diameters of spheres. μ_v (volume weighted) and μ_h (number weighted) are the arithmetic mean values of the distribution.

3. A mechanical model of shear zone development

Quartz aggregates deform by a different deformation mechanism than the polymineralic matrix but are embedded within the matrix, which forms an interconnected network. Quartz aggregates change their shape from equant magmatic single grains to highly elongate lenses of recrystallized material and they do not coalesce. The coalescence and formation of an interconnected weak layer

(Jordan 1987; Handy, 1990) has been reported as a major weakening mechanism during shear zone formation (Holyoke & Tullis, 2006a) even at volume fractions below 30% (Jordan, 1987; Gilotti, 1992; Holyoke & Tullis 2006b). It has been suggested that the formation of an interconnected weak layer (Handy, 1990) results in a bulk weakening. This has also been observed in various experiments (Jordan, 1987; Holyoke et al., 2006b) and nature (e.g. Park et al., 2006). In the case of the Gran Paradiso mylonites, at low strain the matrix forms the interconnected strain accommodating network and at the highest strains further matrix coalescence is achieved by disintegration of the quartz aggregates. In our analysis, only the fully recrystallized monophase quartz aggregates are considered, rotated parallel to the shear zone forming a laminar microstructure with alternating layers of quartz and polymineralic matrix (Fig. 1b).

The absence of coalescence indicates a somewhat higher effective viscosity of the quartz aggregates with respect to the matrix. Furthermore, the quartz aggregates´ long axes always show a greater angle of rotation and a lower aspect ratio for a given finite shear strain value (Kilian et al. a). These observations also indicate a slower strain rate in quartz aggregates than in the matrix. However, boudinage of quartz aggregates is largely absent – the quartz layers form parallel bands within the matrix at high strains (Kilian et a. a).

The presence of quartz layers that do not boudinage can either indicate that the effective viscosities of both materials are not very different (e.g. Neurath & Smith, 1982; Schmalholz et al, 2008) or that no necking instability arises. The lack of boudinage sets an upper limit for the viscosity ratio (e.g. Schmalholz et al., 2008). Based on numerical modeling Schmalholz et al. (2008) suggest that a power law layer with a stress exponent of 5 and a 100 times higher initial effective viscosity embedded in a linear viscous medium would not necessarily develop a necking instability below a total extension of 80%. In the Gran Paradiso mylonites in the most highly strained part aggregate reach extensions in excess of 500% (maintaining the same area) without boudinage. Thus, as necking is subordinate in the Gran Paradiso mylonites, we assume an effective viscosity ratio of considerably less than 100.

Across the shear zone, as a first approximation, the differential stress should be constant at a given instant of time (e.g. Means, 1979) so that the system can be described as a Reuss-bound (iso-stress) system of stronger layers embedded in a weaker matrix (e.g. Handy, 1990; 1994, Tullis et al. 1991). This implies that if constituting phases differ in their rheology, each phase is required to deform at different strain rates. This may be an oversimplification (e.g. Handy 1994; Ji et al., 2003; Takeda &

Griera, 2006) as the mechanical properties of the interface or strain dependent changes in rheology should be taken into account. However, as the rheology of the total aggregate must lie within the bounds of uniform stress and uniform strain rate, the assumption of uniform stress for a layered rock, practially without boudinage, appears to be reasonable in order to obtain strain rates of different layers and to test the rheological data available.

The strain rates of the individual components - quartz and matrix - can be estimated using experimentally or theoretically derived flow laws at a constant differential stress. Assuming the differential stress is constant across the shear zone, it is possible to calculate the strain rate ratio between the two constituent components if their individual flow laws are known and differential stresses used in the flow laws can be obtained from recrystallized grain size piezometers (Twiss, 1977; Stipp & Tullis, 2003; Shimizu, 2008). A similar approach has been taken by Mehl & Hirth (2008), but assuming that adjacent layers deform at a similar rate.

3.1 Grain size piezometry

The piezometric relationship obtained by Twiss (1977) assumes that the recrystallized grain size relates to a static equilibrium of the free dislocation energy and the (sub)grain boundary energy. An experimental calibration for quartz (Stipp & Tullis, 2003) was carried out at 800 – 1100° C where quartz underwent dominant bulging recrystallization and progressive subgrain rotation. In the experiments used for the calibration (Stipp & Tullis, 2003) grain boundary migration in the very low strain rate - high temperature samples is only subordinate. The largest grain size the piezometer was calibrated with, has a mean of 18 μm (Stipp & Tullis, 2003, 10-6/1100°C/1.2GPa), producing regime 3 (Hirth & Tullis, 1994) microstructures. Regime 3 microstructures rather correspond with subgrain rotation recrystallization with minor grain boundary migration than with grain boundary migration dominated recrystallization in nature (Stipp et al., 2002). Stipp & Tullis (2003) speculate to expect a different piezometric relation just below their experimental stresses. One has to keep in mind that the grain size is outside the calibrated range, the individual contribution of the processes which produced the grain size is different in the experiments and in the Gran Paradiso rocks and the natural grain size range is broader than the range obtained in the experiments.

Shimizu (2008) presented a model for dynamic recrystallization where new grains are nucleated by subgrain rotation and the grains subsequently grow during grain boundary migration. This model suggested a temperature dependence of the dynamically recrystallized grain size as already proposed by De Bresser et al. (2001). At temperatures below the α-β transition the stress values are at 550° C 31 MPa and at 500°C 34 MPa for 70 μm mean grain size (2D-number weighted mean grain size, according to the original calibration by Stipp & Tullis, 2003). These numbers is higher than those obtained from the piezometer of Stipp & Tullis (2003), which are about 23 MPa (exactly:11-57 MPa, including the specified error). The reason for the higher stresses is likely due to the consideration of grain boundary migration contributing to grain growth in the Shimizu (2008) model. As the piezometer of Stipp & Tullis (2003) needs to be extrapolated to obtain data for our measured grain sizes, and Stipp & Tullis (2003) suggest care in the application of the piezometer to grain boundary migration recrystallization microstructures, it appears that the Shimizu (2008) piezometer is more applicable for our data set, because we observe the same sequence of recrystallization stages envisaged by Shimizu (2008): nucleation of new grains by progressive subgrain rotation, followed by growth during grain boundary migration. Therefore, we consider the higher differential stress estimate (31 MPa) as more accurate for the observed conditions.

4. Basic concepts

4.1 Flow laws for dislocation creep in quartz

Dislocation creep flow laws in the form of equation (1) have been derived from experimentally deformed quartz (e.g. Parish et al., 1976; Koch et al., 1989; Luan & Paterson, 90; Gleason & Tullis, 1995, Rutter & Brodie, 2004). Some of the flow laws (Luan & Paterson 1990, Paterson & Luan 1992, Gleason & Tullis 1995) have been calibrated with naturally deformed quartz rocks by Hirth et al., (2001).

(1)

$$\dot{\epsilon} = A\sigma^{n}\, d^{m}\, exp\left(\frac{-Q}{RT}\right)$$

The grain size exponent m is generally believed to be 0 and values for the factor A, the activation energy Q, the stress exponent n are those listed in table 1.

4.2 Flow laws for diffusion creep in feldspar

The polymineralic matrix consists largely of feldspar (50-65 %; Kilian et al. b) and deforms by diffusion creep. Flow data only exists for plagioclase (Rybacki & Dresen 2000; Rybacki et al.

2006), not for K-feldspar. However, natural observations and earlier experimental work suggest that there does not seem to be a large difference in the mechanical behavior between K-feldspar and plagioclase (Tullis 1983). The diffusion parameters of polymineralic mixtures may be different from monophase materials (see below), so that a new diffusion creep law will have to be fitted. For the important comparison with existing experimental data, the plagioclase data of Rybacki & Dresen, (2000) and Rybacki et al., (2006) will be used.

Rybacki & Dresen (2000) produced parameters (Table 1) for linear viscous, grain-size-sensitive (m = 3) and power-law, grain-size-insensitive (m = 0) flow laws of fine grained anorthite in experiments at 300 MPa in the form of equation (1).

4.3 General flow laws for grain boundary sliding during diffusion creep

The transition zone between the mylonite and the ultramylonite yields important information for deriving the flow law of the polymineralic aggregate: The monophase quartz layers become thinned to one or a few grain diameters' thickness (without necking), the disintegration of the layers occurs by grain boundary sliding, cavitation and precipitation processes while deforming in dislocation creep, and the grain size of the quartz is reduced to approximately the size of the subgrains by pinning at the phase boundaries resulting from the precipitation of other phases (Kilian et al. a).

Langdon (1994) derived a rate law (2) for grain boundary sliding as a main kinematic contribution to deformation and linked to deformation of the grain interior (Rachinger sliding ;Rachinger, 1953, Cahn 1996, Langdon 1994, 2006); in contrast to sliding as an accommodation during diffusion creep, (Lifshitz sliding; Lifshitz, 1963; Raj & Ashby, 1971).

(2)

$$\dot{\epsilon}_{gbs} = \frac{A_{gbs}G\mathbf{b}}{kT}\left(\frac{\mathbf{b}}{d}\right)^{m}\left(\frac{\sigma}{G}\right)^{n} D_{GB} exp\left(\frac{-Q_{GB}}{RT}\right)$$

In equation (2) A_{gbs} is numerical factor , G is the shear modulus, b the burgers vector, k the Boltzmann constant, d the subgrain size (L), D_{gb} the diffusion coefficient for grain boundary diffusion and Q_{GB} the activation energy for grain boundary diffusion.

Strain rates for grain boundary sliding can be derived based for on the division between sliding at grain sizes larger than the subgrain size (L) - during dislocation creep, or smaller than the subgrain size - during diffusion creep (Langdon 1994, 2006). The form of the rate law depends on which of the two deformation mechanisms is dominant: dislocation or diffusion creep (Langdon 1993, 1994, 2006; he distinguishes dislocation creep from superplasticity in metals. We assume here that superplasticity is the equivalent deformation process in metals comparable to diffusion creep in silicates). Langdon's model assumes that the switch in the form of the governing relation is only dependent on the change in grain size: if the grain size is smaller than the subgrain size L, no new grains can form by progressive subgrain rotation and deformation takes place by diffusion creep. If the grain size is larger than the subgrain size, the deformation takes place by dislocation creep.

5. Application of flow laws to natural sample

5.1 Application to mylonitic quartz layers

Extrapolation of these flow laws to nature is possible, though that might be problematic due to differences between the experimental and the natural state of stress affecting the pre-exponential factor (e.g. Paterson, 2001). Out of the wide range of flow law results, some do not need to be considered: as the observed deformation occurred with the concomitant precipitation of hydrous phases (white mica, biotite), the presence of an aqueous fluid is required and all dry flow laws are excluded in the further analysis. Only flow law data based on gas or liquid medium technology has been employed.

Figure 6 shows a comparison for some experimentally derived flow laws (Paterson & Luan, 1990; Luan & Paterson 1992; Gleason & Tullis, 1995; Rutter & Brodie, 2004) and flow laws fitted to natural strain rates (Hirth et al., 2001). As the flow laws are obtained in axial compression, the strain rates are corrected for simple shear conditions using 2^(1/n)*3^-(1+1/n)/2 as a factor (e.g. Nye, 1953; Schmid et al., 1987).

The pressure dependence (Kronenberg & Tullis, 1984, Post et al., 1996) of the pre-exponential factor has been corrected for the flow law parameters following Hirth et al. (2001) who introduced a dependency on water fugacity, which allows to compare experimental results obtained at different pressures.

Pressure estimates for the fugacity correction in the Hirth et al. 2001 quartz flow law are taken from the matrix oligoclase which is expected to be stable at 550°C below 0.7 GPa (Maruyama,

1983) or 0.85 GPa (re-calculated for the bulk mylonite composition taken from Menegon et al. (2006) with THERIAK (de Capitani & Brown, 1987)). As an average value, water fugacities for 550°C/0.8 GPa have been used and are calculated using Pfitzer & Sterner (1994). Therefore, calculated strain rates present an upper limit because earlier pressure estimates range from 0.6-0.7 GPa (Brouwer at al.,2002).

5.2 Application to matrix layers

At the observed grain size of the polymineralic mixture (10 μm number weighted as a conservative mean value) the flow law for “wet” grain size sensitive flow of anorthite (Rybacki &Dresen, 2000) is presented in Figure 6, together with dislocation creep data for anorthite for comparison. Although there is no measurement of the water content in the matrix during deformation, the presence and precipitation of hydrous phases is taken as evidence of sufficiently high water contents to apply “wet” flow law data.

The polymineralic nature of the matrix may be a reason that strain rates can even expected to be higher than predicted by the pure plagioclase data, because diffusion (being the rate limiting factor in diffusion creep) may be faster. Farver & Yund (1999) have measured highly increased oxygen grain boundary diffusivities in a natural fine grained mica-bearing ultramylonite. The obtained diffusion coefficient for oxygen is several orders of magnitude larger than that for feldspar or feldspar-quartz aggregates (Farver & Yund, 1999; 1995a/b). At the estimated temperatures of the Gran Paradiso shear zone, the oxygen diffusion coefficient in the natural ultramylonite (Farver & Yund, 1999) and that in a quartz/feldspar mixture and albite (Farver & Yund , 1995a/b) differ only by 2 orders of magnitude.

K-feldspar is seen to be highly mobile at the grain scale in the Gran Paradiso metagranodiorite. Cation transport, at least of K-cations, must have taken place to achieve this mobility, and, in addition, Ca and Na for the formation of the calcic plagioclase. Wether “wet” interconnected grain boundaries existed and transport took place in an interconnected fluid film or by grain boundary diffusion cannot be decided. Diffusion coefficients of potassium and calcium (Farver & Yund, 1995a) in a film of aqueous fluid or in grain boundary channels are high, even compared to the oxygen diffusion coefficient in mica bearing ultramyonite (Farver & Yund, 1999). The precipitation of hydrous phases is taken as an indication that material transport took place in an aqueous grain boundary fluid.

Given the conditions above, it has been attempted to use a flow law (equ. 3) for the polymineralic matrix using the form of Coble creep (Coble, 1963).

(3)

$$\dot{\epsilon}_c = \frac{A\Omega\delta\sigma}{kTd^3} D_{GB} exp\left(\frac{-Q_{GB}}{RT}\right)$$

In equation (3) A is a factor based on the grain geometry (141), Ω the molecular volume of the diffusing species, δ the grain boundary width, k the Boltzmann constant, d the grain size, D_{GB} the grain boundary diffusion coefficient and Q_{GB} the activation energy for grain boundary diffusion.

Oxygen grain boundary diffusion coefficients taken from Farver & Yund (1999; natural micaceous ultramylonite) and Farver & Yund, (1995; synthetic quartz - feldspar aggregates) (table 1) and effective grain boundary widths of 1, 2 and 10 nm have been used (Fig. 7). These grain boundary thickness values cover the range commonly described in literature and are consistent with those found during the determination of the grain boundary diffusion coefficients (Farver & Yund, 1995, 1999, 2000). In the case of oxygen diffusion Farver & Yund (1991) suggest that the actively diffusing species is H2O, so that the molecular volume of water (Pfitzer & Sterner 1994) at the specified condition was used as the volume for the diffusing species.

Strain rates obtained at 500-550°C for the grain size of the polymineralic matrix are very close to those determined from the extrapolation of the plagioclase diffusion creep flow law (Rybacki & Dresen, 2000) (Fig. 7). Despite the sensitivity on the assumed grain boundary width, values of 1-10 nm yield reasonable results.

The activation energy for grain boundary self diffusion is 30 kJ/mol (Farver & Yund, 1999) which is smaller than 135 kJ/mol derived by Rybacki & Dresen (2000) resulting in a smaller temperature dependence. Regarding the polymineralic nature of the matrix, using the coefficients obtained from the natural ultramylonite seems to be the most appropriate for a comparison. This result is reasonable because diffusion appears to be faster in polymineralic aggregates than in monophase ones (Farver & Yund 1995, 2000). One has to keep in mind that the experiments of Rybacki & Dresen (2000) were done with monomineralic anorthite. Thus, the monomineralic anorthite appears to be a fairly good analogues for the polymineralic matrix.

5.3 Application to ultramylonitic phase mixture

The derived rate obtained from Langdon (1994) depend on a dimensionless constant A, a stress exponent n, a diffusion coefficient D and an activation energy for grain boundary sliding Qbs and a grain size exponent. In metals the values of Qbs are similar to those of lattice self diffusion and (Fazan et al., 1954; Davis et al., 1966), and n and m are both assumed to be equal to two for Rachinger sliding in grain boundary sliding dominated flow (d < L) and verified experimentally (Langon, 1994) in several metals (Langdon 2006). These values assume that the rate limiting step of grain boundary sliding is dislocation climb. The value of A depends on the individual assumption on the dislocation process involved during sliding (length of the dislocation pile-up and the climb distance) and is in the range roughly around 10 for sliding during diffusion creep (12: Ball & Hutchinson, 1969; 2: Mukherjee, 1971; 10: Langdon, 1994) and around 1000 for sliding during dislocation creep (Langdon, 1994, assuming Weertman creep (Weertman, 1975)).

Strain rates calculated for the case of Rachinger sliding (d < L) from the flow law derived by Langdon (1994) and grain boundary diffusion coefficients for various diffusing species obtained by Farver & Yund (1991,1995, 1999, 2000) (see table 1) and silica volume diffusion in quartz (Bejina & Jaoul, 1996; Cherniak, 2003) are geologically not reasonable. Sliding rates are either unrealistically high (e.g. oxygen diffusion (Farver & Yund 1995) yield strain rates > 10-6) or negligible low (e.g. silicate bulk diffusion (Cherniak, 2003) yield strain rates < 10-20). One shortcoming is that the grain boundary sliding rate laws are obtained for metals and one has to bear in mind that ambipolar diffusion may be significant in silicates (Gordon, 1973; Langdon & Mohamed, 1978). The second problem arises from the fact that dislocation processes seem to contribute to grain boundary sliding in metals (e.g. Ashby & Verrall, 1973).

However, in silicates the experimental evidence so far indicates diffusion accommodation as the rate limiting step in diffusion creep, and values of m= 3 and n=1 have usually been found for such creep laws (Karato et al. 1986; Wang et al., 1996; Dimanov et al., 1999; Farver & Yund 2000; Xiao et al, 2002; DellePiane et al., 2008). Observations in metals deformed in the transition between dislocation and diffusion creep yield that at small strains at the grain scale the stress exponent approaches 1 while at large strains (“superplasticity”) an n >1 is found to result from a contribution of both, dislocation creep and diffusion creep (Ashby & Verrall, 1973). Therefore, values of m=3 and n=1 seem to be the most appropriate values in the attempt to fit a rate law for diffusion creep (diffusion accommodated grain boundary sliding) in the polymineralic matrix. If m=3 and n=1 are inserted into equ. 2, it reduces to equ. 3 (Coble creep), if the A-values are properly chosen. Thus, we will use a law in the form of Coble creep to fit the diffusion creep of the polymineralic matrix to the dislocation creep law of the monophase quartz layers at the threshold grain size (d = L). As the order of magnitude of A is highly sensitive to the chosen n and m, an appropriate A-value has to be fitted for the case of m=3 and n=1.

A value for A can be fitted for a geologically realistic strain rate e.g. obtained by the experimental flow law for dislocation creep (Hirth et al, 2001), a corresponding differential stress (Shimizu, 2008), a grain boundary diffusion parameter (e.g. Farver & Yund, 1995) and a subgrain size (d=L).

The A-value for the flow law lies in the range of 1e-2 to 4e-1 using oxygen diffusion in quartz - feldspar aggregates (Farver & Yund,1995), a temperature range of 500-550° and the subgrain size range of 20-60 μm. At the subgrain size of 40 μm A is ~ 1e-1. A increases slightly with an increasing temperature used for the fit. Using for example oxygen or silica diffusion in quartz (Farver & Yund, 1991, 1999), A is in the the range of 5e-1 to 2e1 and decreases with increasing temperature.

The resulting flow laws with different values of A can be seen in Figure 8. Derived diffusion creep rates (diffusion accommodated grain boundary sliding rates) are larger than the dislocation creep strain rates (Hirth et al. ,2001) for the case of grain sizes (d < L) smaller than the size (d=L) used to obtain A as well as for lower differential stresses (Fig. 8).
The usefulness of such a fit will be evaluated in the discussion.

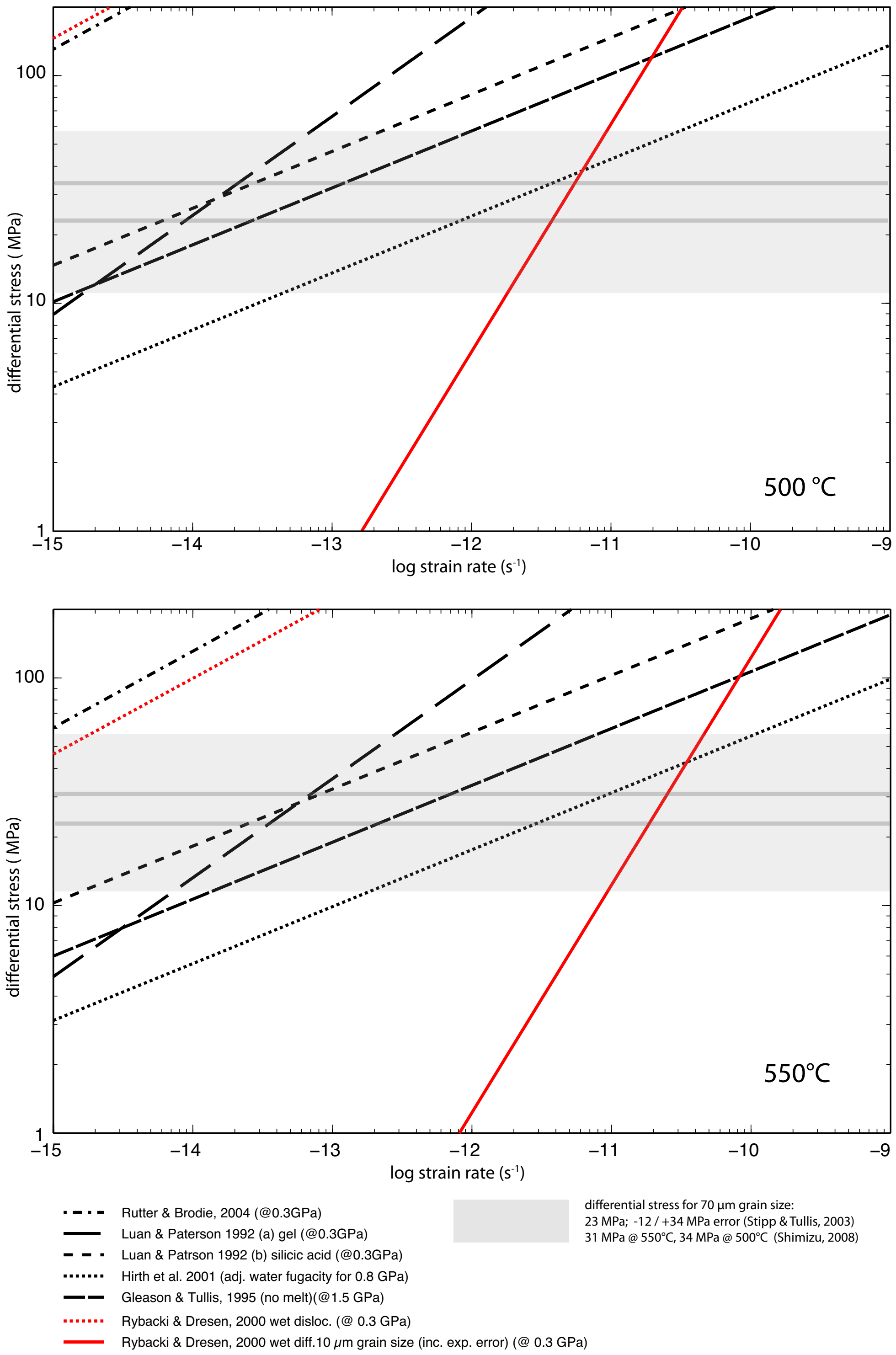

Figure 6: Experimentally derived flow laws for quartz (black) and plagioclase (red) at 500 and 550°C. Differential stresses for the Grain Paradiso mylonite obtained from grain size piezometers are indicated. The broad grey band indicates the error range of the experimental calibration of Stipp & Tullis (2003).

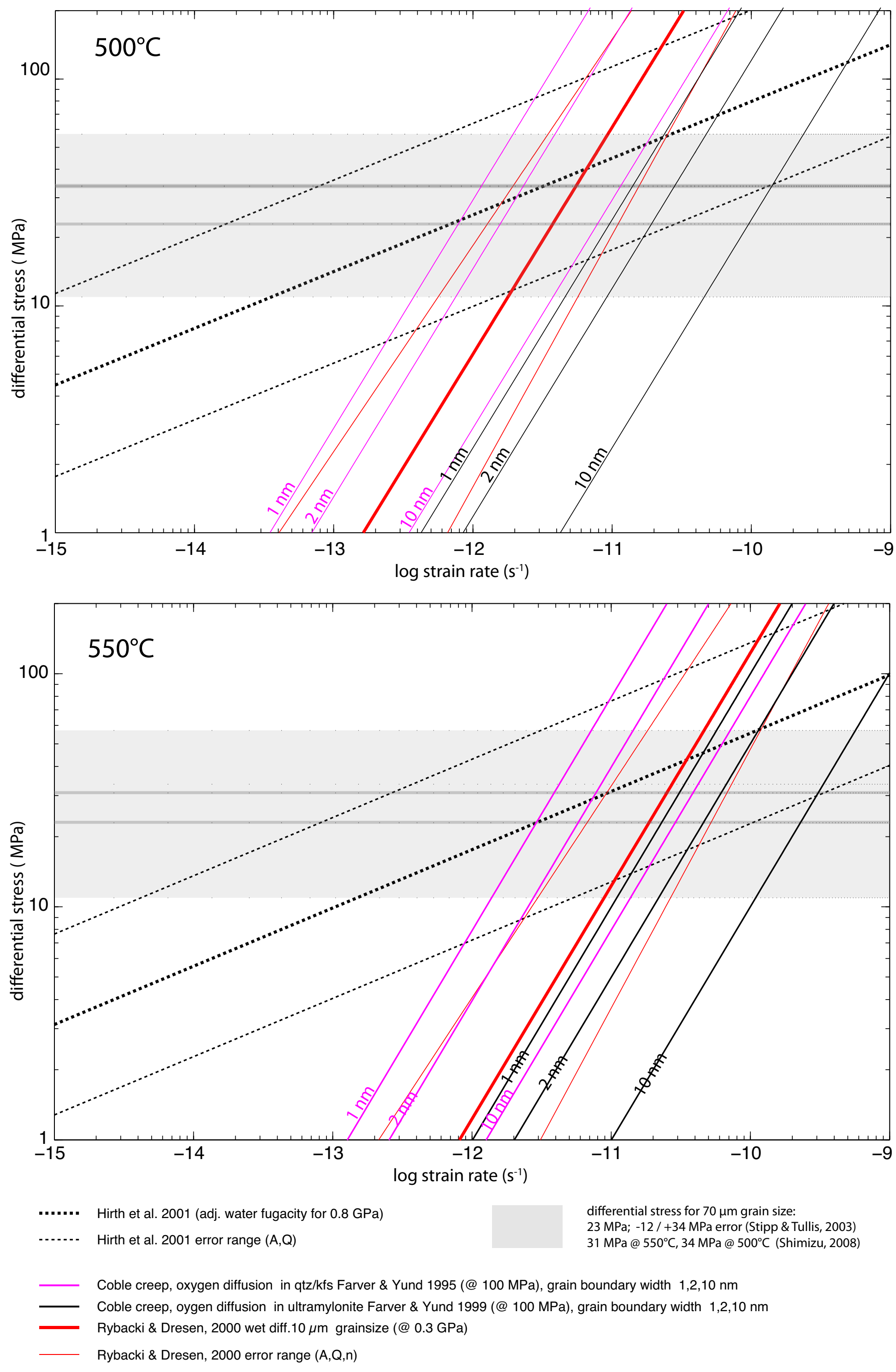

Figure 7: Coble creep law (eq. 3) for oxygen diffusion in quartz- feldspar aggregates (Farver & Yund, 1995) and oxygen diffusion in a natural ultramylonite (Farver & Yund, 1999) at 500 and 550°C for grain boundary widths of 1, 2, 10 nm. For comparison a dislocation creep flow law quartz (Hirth et al., 2001) and a diffusion creep law for plagioclase (Rybacki & Dresen, 2000) are shown, including the error ranges of A, Q and n.

mineral	**A** (MPa^{-n}/s)	**Q** (kJ/mol)	**n**	**reference**
quartz	- 6.5E-08	148 ± 46 135	2.3 ± 0.3 3.1	Paterson & Luan 1990 (gel), Luan & Paterson 1992
quartz	- 4E-10	152 ± 71 135	4 ± 0.8 4	Paterson & Luan, 1990 (sil. acid), Luan & Paterson, 1992
quartz	6.3(+12 -4.7)E-12	135 ± 15	4.0	Hirth et al., 2001
quartz	1.1E-04(± 2)	223 ± 56	4.0 ± 0.9	Gleason & Tullis, 1995
quartz	1.20E-05	242	2.97	Rutter & Brodie, 2004 dislocation creep
plagioclase	4.0(-2 +4)E+02	356 ± 9	3.0 ± 0.2	Rybacki & Dresen 2000, dislocation creep, “wet”
plagioclase	5.0(-2 +3)E+1	170 ± 6	1.0 ± 0.1	Rybacki & Dresen 2000, diffusion creep “wet”

diffusing element	D_{GB} (m^2/s)	**Q** (kJ/mol)	**reference**
oxygen in ultramylonite	2E-11 (channel?)	30 ± 6	Farver & Yund, 1999, 100 MPa
oxygen in quartz/K-feldspar	1.8E-09* (3.6E-18, D’∂)	75 ± 13	Farver & Yund, 1995b, 100 MPa
silica in quartz	5.4E-07** (3.7E-10, Dbulk)	137±18	Farver & Yund, 2000, 150 MPa
oxygen in quartz	1.3E-08* (3.4E-17, D’∂)	113 ± 5	Farver & Yund, 1991, 100 MPa (as used in F&Y 2000)
oxygen in albite	5.5E-10* (1.1E-18, D’∂)	68 ± 12	Farver & Yund, 1995a, 100 MPa
	D_{Vol} (m^2/s)	**Q** (kJ/mol)	
silica in quartz	2.90E+03	746 ± 125	Bejina & Jaoul, 1996, 2.0 GPa
silica in quartz	8.00E-06	447 ± 31	Cherniak, 2003, 0.1 MPa

* assuming 2nm grain boundary width

** assuming 2nm grain boundary width and 5 μm grain size, tortuosity 1.7

Table 1: flow law parameters and diffusion coefficients

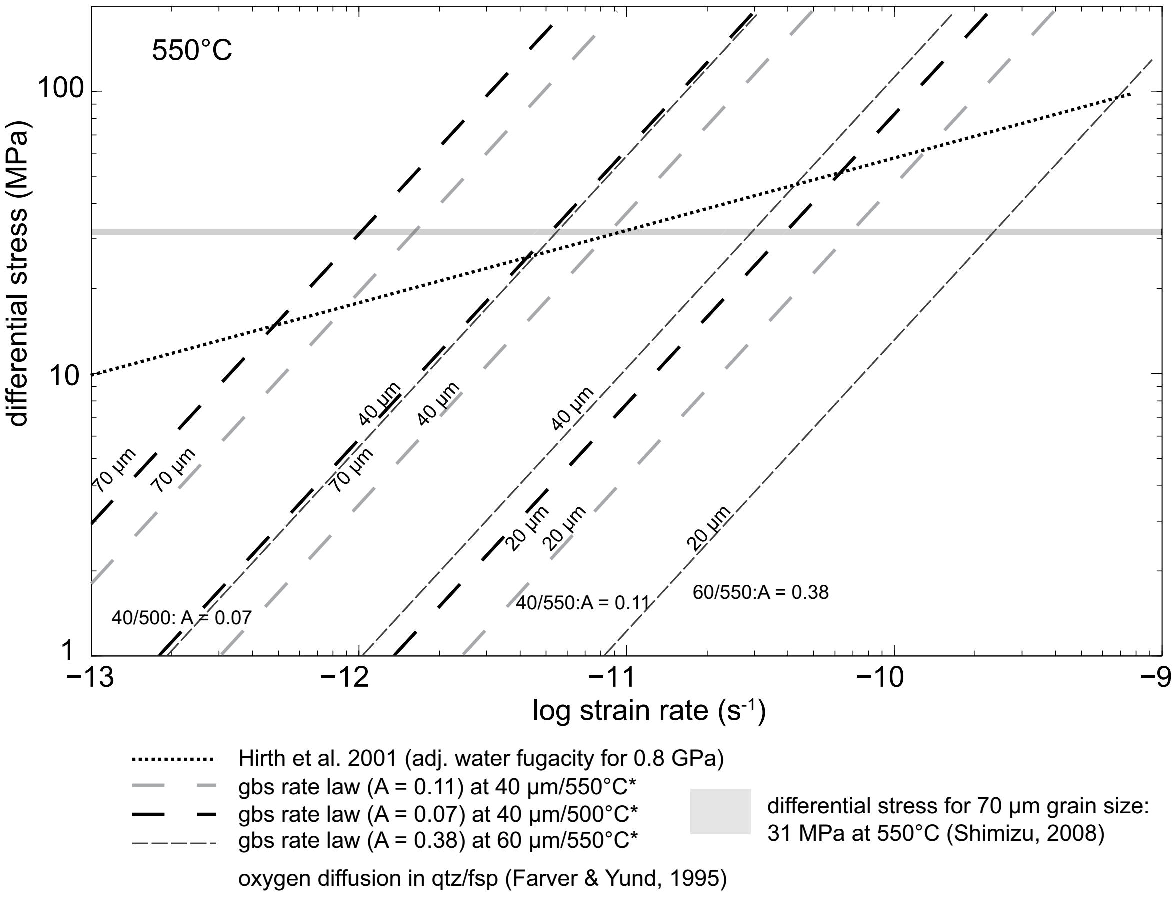

Figure 8: Comparison of the flow law for diffusion accommodated grain boundary sliding (Coble creep - form, eq. 3) at 550°C with a fitted parameter A for oxygen diffusion in quartz-feldspar aggregates (Farver & Yund, 1995). A was fitted for a subgrain size of 40 μm at 500°C (A = 0.07) and 550°C (A=0.11) and 60 μm at 550°C (A=0.38). The dislocation creep flow law (Hirth et al., 2001) provides minimal strain rates. It is obvious that A is not universally applicable.

5.4 Comparison with other data

Figure 9. shows a comparison of of various granitic rocks in which quartz aggregates deform in a fine grained feldspar dominated matrix. In all rocks quartz forms clast in a fine grained, feldspar rich matrix, so iso-stress conditions can be assumed.

The data of the Truzzo granite is obtained from shear zones (see chapter 3) which formed in a low strain domain, similar to the situation of the Gran Paradiso shear zones. The temperature is not well constrained between 550° and 650° (Huber & Marquer, 1998). Differential stresses are plotted for a grain size with μ_h(d) = 650 μm and μh(d) = 110 μm, both are interpreted be related to dynamic recrystallization at roughly the same temperature. Data for the Vepor Unit is taken from Jerabek et al., (2007) who infer deformation temperatures between 450 and 480°C. Dynamically recrystallized quartz aggregates have grain sizes between 70 and 80 μm and deform inside an albitic matrix with a grain sizes of ~ 20 to 30 μm.

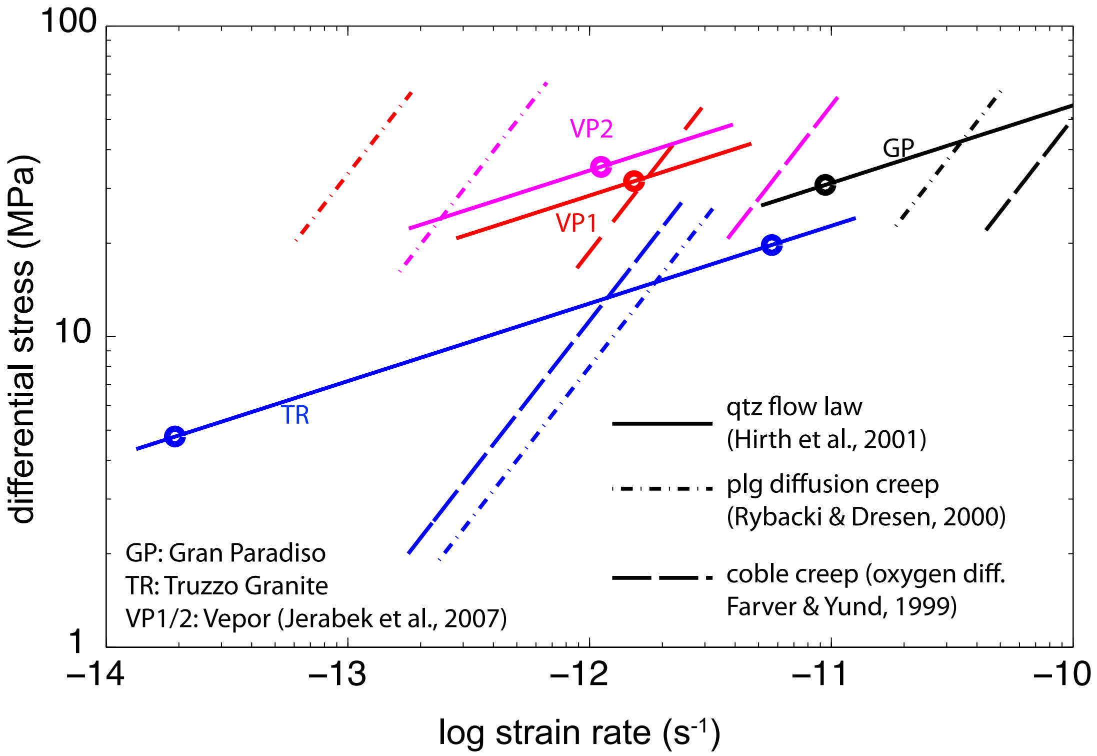

Figure 9: Comparison of data from the Gan Paradiso shear zones with shear zones in the Truzzo granite and data for the Vepor Unit (Jerabek etal., 2007). GP: 70 μm quartz and 10 μm matrix grain size, 550°C, 0.8 GPa; TR: 650 and 110 μm quartz and 30 μm matrix grain size, 600°C, 0.8 GPa; VP1: 80 μm quartz and 30 μm matrix grain size, 480°C, 0.85 GPa; VP2: 70 μm quartz and 20 μm matrix grain size, 450°C, 0.65 GPa. Curves for quartz are calculated using the Hirth et al, 2001 flow law. The curves for the matrix are calcuated using the Coble creep law and the anorthite flow law for wet diffusion creep (Rybacki & Dresen, 2000). Coble creep curves are calculated for 2nm grain boundary width and for oxygen diffusion in a natural ultramylonite (Farver & Yund, 1999).

6. Discussion

6.1 Dislocation creep of quartz

A comparison of the flow laws for quartz (dislocation creep) and anorthite (diffusion creep) at the parameters inferred for the Gran Paradiso shear zone is shown in Fig. 6. The range of the differential stresses predicted by the recrystallized grain size piezometer relations (Stipp & Tullis, 2003; Shimizu, 2008) is also indicated.

The flow law by Rutter & Brodie (2004) yields strain rates which are geologically not realistic at the inferred differential stress. The two flow laws by Paterson & Luan (1990; Laun & Paterson, 1992) yield virtually indistinguishable results at the stress estimates given (Fig. 6), but it yields about 2 orders of magnitude slower strain rates than the Hirth et al. (2001) flow law. The Hirth et al. (2001) flow law is similar to the Gleason & Tullis (1995) one, but includes the pressure correction. Furthermore, both error limits given for A, n and Q in the Hirth et al. (2001) flow law yield geologically reasonable strain rates (Fig. 7). In addition, it appears to be the most robust and reasonably well-tested law, so that we will use this flow law in the further analysis.

Interestingly, the strain rates for a grain size of 10 μm in diffusion creep of anorthite from the flow law of Rybacki & Dresen (2000) at the specified conditions are very similar to those of the Hirth et al. (2001) flow law at the given stress estimates (Fig. 7). This result is also consistent with the observation that the feldspar-dominated matrix is slightly weaker than the monophase quartz aggregates. The plagioclase flow law has been derived at 300 MPa (Rybacki & Dresen, 2000) and has not been corrected for a higher pressure as the pressure dependence is not known (Rybacki et al., 2006). This provides a lower limit for the derived strain rates. The experiments by Rybacki & Dresen (2000) were conducted on pure anorthite aggregates, while for the above mentioned considerations, grain boundary diffusion can be expected as much higher in a polyphase aggregate containing mica and other phase boundaries (e.g. Wheeler, 1992, Farver & Yund, 1999). Therefore one can expect higher strain rates than obtained from the plagioclase flow law when extrapolating to the higher natural pressures and higher grain boundary diffusion coefficients at the inferred differential stresses.

Experimentally derived flow laws (Rybacki & Dresen, 2000) as well as theoretical considerations (Coble creep) suggest an at least up to several times larger strain rate in the matrix than in the quartz at the considered constant differential stresses. This has to be evaluated with respect to the observed behaviour of quartz aggregates (no coalescence, predominant absence of boudinage as long as strain is not exceedingly high,finite rotation behavior of quartz aggregates).

6.2 Modified flow law

The formulation for grain sizes smaller than the subgrain size provides strain rates for grain boundary sliding during diffusion creep. In the studied rocks the subgrain size is measured to be between 20 and 65 μm with a mean of about 40 μm. This grain size is attained by a combination of pinning (by the growth of K-feldspar and biotite) and subsequent phase boundary migration.

Contrary to Langdon (1994) we assume that grain boundary sliding is accommodated by diffusion rather than dislocation processes. During aggregate disintegration dislocation creep ceases therefore we interpret that at the given stress level strain is accommodated by grain boundary sliding at a much higher rate.

As in our case quartz aggregates disintegrate with the concomitant introduction of phase boundaries, the diffusion coefficient for quartz - feldspar rocks (Farver & Yund, 1995) is reasonable. The uncertainty in temperature between 500 and 550°C has only a very minor influence on the value of A. An influence much larger than temperature is the choice of the subgrain size (Fig. 8). The larger the subgrain size used to calculate A, the higher the resulting strain rates.

Despite the rate law will provide a lower limit for the strain rate of the polyphase mixture it is not universally applicable (Fig. 8).
Its application is restricted by the variation of the parameters used for the calculation of A. For example, if the rock has a different relation between the recrystallized grain size and the subgrain size than the rock used for the calculation of A, the result is incorrect.

Therefore a fit based on a single natural “experiment” can not be used to infer stress - strain rate relations in other rocks that have e.g. a different matrix grain size, subgrain size - grain size ratio or deformation temperature.

6.3 Comparison of inferred flow laws with natural microstructures

The strain rate ratio derived from the flow laws is below one order of magnitude. Does this correspond with the behavior of the quartz aggregates in the matrix? Quartz aggregates do not coalesce nor boudinage.

Two situations must then be compared: 1) the structures indicate that the two components, quartz and matrix deform at approximately the same strain rate and the flow laws or the piezometer relation or the assumption of pure end member flaw laws is inaccurate. 2) the calculated strain rates are correct but the developed structures are also dependent on finite strain or other factors and are insensitive to the present strain rate ratio.

Situation 1: The flow laws or the piezometric relationship is inaccurate as both components deform at the same strain rate.

The assumption that the quartz aggregate deform by dislocation creep is based on the development of a CPO, an SPO and a constant dynamically recrystallized grain size via subgrain rotation and grain boundary migration recrystallization. There is evidence from metallurgical tests that during dislocation creep up to 15% of the finite strain is accommodated by grain boundary sliding during dislocation creep (e.g. Kottada & Chokshi, 2007). Grain boundary sliding has also been suggested as one consequence of heterogeneous strain at the grain scale due to a limited number of available slip systems (Zhang et al., 1994). Though diffusion creep is not expected to govern quartz deformation at the measured grain sizes (Rutter & Brodie, 2004), grain boundary sliding can be an additional process contributing to the total quartz strain rate. Microstructural evidence for a contribution of grain boundary sliding in the monomineralic quartz aggregates of the Gran Paradiso metagranodiorite is reported in Kilian et al. (2011a). Therefore as a potential possibility of the misfit between the quartz and plagioclase data, it can be considered that quartz is deforming with an additional contribution of grain boundary sliding, larger than the fraction that has to be assumed to take place during experimental quartz deformation in the dislocation creep regime.

The differential stress estimation is based on the grain size piezometer relation. The piezometer relation based on theoretical considerations of subgrain rotation recrystallization and grain boundary migration (Shimizu, 2008) includes a temperature dependence due to a contribution of grain growth. Provided differential stresses are higher compared to the piezometer calibration of Stipp & Tullis (2003). The higher differential stresses are closer to the linear - power law crossover. Taking the error of the experimental calibration (Stipp & Tullis, 2003) into account, the resulting stress estimate ranges between 11 and 57 MPa at 70 μm grain size. This translates for most power-law flow laws to a difference in strain rates of about 3 orders of magnitude, rendering the entire consideration of experimental flow laws or piezometry questionable if no additional information is available. Within the range of the experimental errors it is not possible to decide whether both materials should deform at different strain rates or not.

Situation 2: The actual strain rate ratio calculated from the experimentally derived flow laws is correct and correspond with the observed structures.

Numerical modeling (Schmalholz et al., 2008) predicts that necking is not necessarily occurring in a power law layer embedded in a linear viscous matrix at 100 times higher effective viscosities. Nevertheless finite stretches of the quartz aggregates (~500%) in the Gran Paradiso rocks are much higher than stretches considered in the numerical model (80%). The effective viscosity ratio used by Schmalholz et al. (2008) assumes a constant displacement rate while we assume Reuss bound behavior. Despite these differences, the absence of boudinage does not contradict with a slightly higher effective viscosity in the quartz aggregates.

An explanation for the absence of boudinage could be a laminar, non-coaxial flow with a sufficiently decoupled interface. Layers parallel to the flow plane experience zero stretch. As suggested above, grain boundary sliding rates or Coble creep between quartz and matrix can be considered higher as the bulk strain rate in the quartz aggregate and matrix; possibly providing a low viscosity of the phase boundary layer between the aggregates and matrix. This fits well with the observation of initial quartz aggregate disintegration along its periphery associated with viscous sliding along the boundary.

Coalescence of a weak phase even at low volume fractions has been shown experimentally (e.g. Jordan, 1978; Holyoke & Tullis, 2006b). Phase strength contrasts (peak strength) about 45 result in a strain rate difference of up to 2 orders of magnitude during localization (Holyoke & Tullis, 2006b). A phase strength contrast of about 10 seems not to produce any recognizable strain rate differences in the experiments (Holyoke & Tullis, 2006b). However, it is probably not possible to translate these results to our situation.

The difference of the finite rotation angle between the quartz aggregates and the matrix foliation (Chapter 2) is interpreted in the way that the aggregates rotate more and flatten less than it would be expected for a passive marker. This relationship can be interpreted to result form a non-unique viscosity ratio between aggregates and matrix (e.g. Gay, 1968; Schmid & Podladchikov, 2003, Mulchrone & Walsh, 2006; Mancktelow & Pennacchioni, 2010). Nevertheless a similar particle behavior could be produced by a deviation from plane strain simple shear.

Therefore the structural record does not contradict the strain rate ratio between quartz aggregates and the matrix. However the calculated strain rate ratio of around one order of magnitude cannot be confirmed by the structural information.

6.4 Deformation of ultramylonite

The strain rate of the entire phase mixture with the 30 % quartz diluted inside the former matrix could be predicted by a law in the form of Coble creep assuming that grain boundary sliding is accommodated by grain boundary diffusion. Additional remarks will be made.

Quartz grains in the ultramylonite still preserve an isometric shape different from the plagioclase, K-felspar and mica grains but the grain size is decreased towards the range of the matrix grains (Chapter 2). This possibly indicates that strain accommodation by neighbor switching between quartz and plagioclase becomes geometrically possible.

In the ultramylonite K-feldspar continuous to precipitates preferentially adjacent to quartz grains. This indicates that they provide low pressure dilatant sites and thus still have a higher viscosity than the surrounding grains. It can be argued that the dilution of the relatively rigid quartz grains in the polymineralic matrix should support the formation of dynamic porosity (e.g. Fusseis et al., 2009). This can be caused by the pressure differences on a particle surface embedded in a flowing matrix (e.g. Masuda & Ando, 1988; Schmid & Podladchikov, 2003); the higher the effective viscosity ratio between the particle and the matrix, the higher the pressure gradient along the particle surface. The pressure gradient is proportional to the gradient of the chemical potential and therefore to the diffusive flux or reaction (dissolution/precipitation) rates. The minerals precipitation at the inferred "low" pressure site can be interpreted in that previous context. Increasing phase mixing creates new phase boundaries. The increase in phase boundaries that experience the increased chemical potential gradient around dispersed quartz grains can be expected to lead to an increase in the bulk diffusion in the ultramylonite.

6.5 Comparison with other data

The comparison of data from the Truzzo granite shear zones and from the gneisses of the Vepor Unit (Jerabek et al., 2007) (Fig. 9) suggests a more universal applicability of the combination of the quartz flow law of Hirth et al. (2001) and the Coble creep flow law using the parameters of Farver & Yund (1999).

The diffusion creep law for anorthite (Rybacki & Dresen, 2000) however shows a much stronger temperature dependence. Matrix strain rates in the rocks of the Vepor Unit (450-480°C) are predicted to be lower than the quartz strain rates using the Rybacki & Dresen (2000) flow law. However Jerabek et al. (2007) report microstructures for quartz aggregates that suggest that quartz also forms a higher viscous inclusion in a lower viscous matrix.

The lower differential stress in theTruzzo granite is derived from the dynamically recrystallized grains size in quartz aggregates which clearly form little deformed clasts embedded in a feldspar matrix. The higher differential stress is derived from grains in an aggregate which forms a highly stretched layer parallel with the matrix foliation, rather suggestive of small strain rate differences. However the temperature estimate in the Truzzo granite is as good as in the Gran Paradiso or in the Vepor Unit rocks. In both cases also the determination of the matrix grain size is not as systematical as for the Gran Paradiso. The non-linear dependence of the strain rate on the grain size during diffusion creep requires a careful and consistent grains size determination.

7. Conclusions

By using experimentally derived flow laws with parameters measured in the naturally deformed Gran Paradiso metagranodiorite, the rheology of the bulk and the components in the mylonites and ultramylonites can be adequately estimated.

Structures suggest that monophase quartz layers behave as a slightly higher viscous material embedded in a less viscous matrix, and boudinage at the aggregate scale does not occur.

The extrapolated strain rates derived from experimental flow laws result in most cases in strain rate ratio values lower one order of magnitude.

Experimental diffusion creep flow laws (Rybacki &Dresen 2000) were derived on monomineralic plagioclase and at lower pressures, though that the calculated strain rates mark a lower limit. Using experimentally derived diffusion coefficients (e.g.Farver & Yund,1999) for Coble creep suggest that the matrix should have deformed at a higher rate, than predicted by the experimentally derived laws. Regarding this point, the existence of a low viscosity phase boundary between quartz and matrix by a theoretically derived rate law for grain boundary sliding (Langdon, 1994) helps to explain the absence of boudinage.

We suggest that a careful application of theoretically and experimentally derived flow laws can yield valuable information, though regarding the error associated with extrapolation, uncertainties and measurements, the interpretation incorporation of all available structural information.

How tempting it seems, it is not possible to extrapolate a single flow law fitted with the data of the Gran Paradiso to other conditions encountered in granitic medium to high grade rocks.

The combination of the quartz flow law (Hirth et al., 2001) and the Coble creep flow law using the diffusion parameters of Farver & Yund (1999) explains more satisfactorily the quartz- matrix relation in the considered examples. Different, well constrained examples that cover a broader grain size and temperature range are needed to establish a combined flow law for quartz-feldspar rocks at medium to high grade conditions.

Chapter 6

Summary and general conclusions

1. Quartz deformation mechanism in polyphase rocks

In both studied granitoids, quartz deforms at the onset of deformation by dislocation creep. Recrystallization happens by subgrain rotation and grain boundary migration. The recrystallized grain size is dynamically stable, caused by a grain size reduction by subgrain rotation and grain growth realized during grain boundary migration.

With increasing strain it is observed that quartz aggregates disintegrate and form grain scale polyphase mixtures with the matrix with a decreased quartz grain size. In the case of the Gran Paradiso shear zones it is shown that the disintegration is caused by intergranular dilatancy and K-feldspar and biotite precipitation. The quartz grain size decrease results from the combination of two processes: (1) by pinning of grain boundaries by the precipitated phases which impedes the contribution of synkinematic grain growth and the grain size is arrested at the subgrain size and (2) by dissolution and precipitation of quartz which enables a grain size decrease below the subgrain size.

The absence of grain boundaries, as well as a grain size that is smaller than the subgrain size, require that quartz deforms together with the matrix by diffusion creep. In the case of the ultramylonites of the Gran Paradiso shear zones, single dispersed quartz grains show a random CP and isotropic shapes. Quartz grains still form the higher viscous particles and no signs of intracrystalline deformation are observed. In the Truzzo shear zones, single dispersed quartz grains in the ultramylonite show an anisotropic shape and a very weak CPO which can be interpreted to result from a contribution of intracrystalline deformation during bulk diffusion creep in the polymineralic mixture. However, the exact process responsible for the CPO formation is not know.

The combination of processes responsible for the disintegration of the quartz aggregates (intergranular dilatancy associated with grain boundary sliding, precipitation of second phases and pinning of the dynamic grain size) highlight the importance of the contribution of grain boundary sliding and synkinematic grain growth during dislocation creep.

Synkinematic grain growth has consequence on the applicability of grain size piezometers. If the recrystallization processes during the experiments used for calibration (Stipp & Tullis, 2003) do not support grain growth, differential stresses obtained from large grain sizes are likely to be underestimated. Grain growth is additionally a function of temperature and it is therefore reasonable to include a temperature dependence in the grain size piezometer (Shimizu, 2008). Microstructures indicative of grain boundary sliding are not restricted to the disintegrating quartz aggregates. Aligned grain boundaries and diamond shaped grains in entirely recrystallized quartz aggregates in the mylonite can also be interpreted to originate from grain boundary sliding during dislocation creep. The contribution of grain boundary sliding during dislocation creep has been known from metallurgy (e.g. Gifkins, 1976; Kottada & Chokshi, 2007), but was rarely proposed for quartz (Luan & Paterson, 1992; Zhang et al., 1996, Pauli et al., 1996).

2. Water in quartz

FTIR measurements of intraganular water in magmatic and recrystallized grains of the Truzzo granite shear zones reveal that both are basically free of intracrystalline water. Magmatic grains contain primary fluid inclusions, which are absent in the recrystallized grains. The dominant recrystallization mechanism is grain boundary migration at relatively high temperature (~550 - 650°C). This suggests, that in spite of water present conditions and the high degree of strain localization in the feldspar, neither pre-kinematic water weakening affected quartz, nor water was incorporated into quartz during deformation. It is concluded that grain boundary migration does not serve as a process contributing to the uptake of water in quartz during amphibolite facies conditions. Primary fluid inclusions and primary, sub-micron white mica are expelled from magmatic grains during grain boundary migration.

Deformation of the quartz aggregates takes place at water present conditions (grain boundaries), low differential stresses and geologically reasonable strain rates. This is based on the assumption that the diffusion creep laws used for the feldspathic matrix in the Gran Paradiso rocks also apply for the matrix in the Truzzo granite and that quartz aggregates are unlikely to deform several orders of magnitude slower than the matrix. Because the deformation behavior of quartz in the Truzzo granite is inconsistent with the mechanical behavior of dry quartz deformed at water absent conditions, it is suggested that grain boundary processes play a role in the weakening effect of water on polycrystalline quartz. A rate increase in grain boundary migration or grain boundary sliding can be considered to depend on the presence of an intergranular fluid.

The relation of strain and water incorporation in naturally deformed rocks has been based on FTIR measurements on polycrystalline aggregates which all incorporate grain boundaries (Kroneneberg et al., 1990; Nakashima et al., 1995; Gleason & DeSisto, 2008). It is likely that at least a part of the water measured in those previous studies is grain boundary water. However, this cannot be clearly proven as long as it is not possible to measure intragranular water at small grain sizes without the contribution of grain boundaries.

3. Quartz as a proxy for polyphase rocks

The applicability of quartz rheology as a proxy for the bulk rock rheology is very limited.

Based on the analysis of small scale shear zones, it is concluded that quartz frequently forms porphyroclasts embedded in a lower viscous matrix. A constant and dynamically recrystallized grain size at steady state deformation is associated with iso-differential stress conditions in such a system, which is can be approximated by Reuss-bound conditions. As long as these porphyroclasts consist of polycrystalline quartz and deform by dislocation creep, grain size piezometers can be used to obtain an estimate on the differential stress. However the strain rate of the entire rock can not be derived and the quartz flow laws set only a lower limit for the strain rate as long as quartz aggregates do not disintegrate. The formation of quartz porphyroclasts that are embedded in a weaker feldspar matrix is observed in both case studies.

One explanation for that behavior can be that quartz does not support localization at the encountered temperature (~500-650°C) and boundary conditions (loading rate or displacement rate). Feldspars form fine grained aggregates, which readily deform by diffusion creep at low stresses which controls the localization. In the Gran Paradiso mylonites which do not show a later overprint, following observations of quartz aggregates are consistent with a higher viscous clast - lower viscous matrix system: absence of coalescence, porphyroclast kinematics, constant differential stress.

The inversion of the viscosity contrast between shear zones and the Truzzo granite is interpreted to result from a change of the boundary conditions resulting in a higher differential stress. The coarse grained granite deforms more easily than the fine grained phase mixture.

In the ultramylonitic Truzzo granite, the formation of newly recrystallized, fine grained layers of quartz and white mica, is interpreted to display the coalescence of the lower viscous phase at now even higher differential stress - lower temperature conditions. If the differential stresses in the grain scale polymineralic mixture rises higher than the equiviscous point of quartz (deforming by dislocation creep) and the polyphase mixture (deforming by diffusion creep), quartz grains will suddenly occupy the position of a weak phase in a load bearing framework. This is a consequence of the higher stress-dependence of dislocation creep. Feldspars are not observed to recrystallize dynamically at the high stress conditions, maybe due to a small, pinned grain size or already temperature which are too low to activate dislocation creep in feldspar. Feldspar forms in this situation the load bearing framework (Voight -bound) which is subject to extremely high differential stresses unless new interconnected weak layers form by coalescence of the low viscosity phase.

The small scale shear zones in the both studied granitoids developed due to an efficient localization mechanism. Both granitoids have in common that they underwent a static high pressure metamorphism, which causes a static plagioclase grain size reduction. Fine grained plagioclase aggregates are present before the onset of deformation. The conditions and the small grain size favor diffusion creep in the feldspar-mica matrix. Further localization is associated with increase in phase mixing and an increase of the volume fraction of the fine grained phase (K-feldspar incorporation). If the feldspars does not provide a low viscosity matrix (e.g. magmatic plagioclase remains stable and does not form small grains), stresses must be higher. Feldspar based localization would not occur as quartz is the weaker phase at high stress conditions.

The observation that quartz does not support localization in quartz-feldspar rocks at low differential stress conditions but localizes deformation at high differential stresses, complies well with the inferred deformation mechanisms. Despite rare exceptions, monophase quartz aggregates are not very keen to support diffusion creep at the conditions realized in the earth’ s crust (e.g.Behrmann, 1985; Rutter & Brodie, 2004) and usually deform with a power-law behavior. At the other hand, dynamic recrystallization of feldspar requires large grain sizes and high stresses (Rybacki & Dresen; 2004) whereas fine grained feldspar readily deforms by linear viscous behavior (Tullis & Yund, 1991). Therefore quartz should control the strain rate at high stresses while felspar at low stresses in a Reuss-bound system. In an ideal Reuss-bound system, the bulk strain rate is the sum of the strain rates of the individual phases.

Quartz as the lower viscous phase phase (deforming by dislocation creep) in homogeneously deformed granitoids (e.g Vernon et al., 1983) implies high differential stresses. The high differential stress in a rock can be regarded as an expression of the failure to localize deformation, e.g. by a mechanism that decreases the grain size of feldspar.

4. The relation of fabrics and crystallographic preferred orientations

Fabrics and crystallographic preferred orientations develop independently of the global kinematic framework of the shear zone but with respect to a local kinematic framework. That local kinematic framework is defined by the quartz aggregate and its position inside the matrix. Flow partitioning between the matrix and polycrystalline quartz aggregates is suggested to be responsible for the development of a local shear sense, which can be opposite to the global shear sense, even at aggregate orientations of 15° with respect to the shear zone boundary.

[c]-axis polefigures have dominantly orthorhombic geometries with peripheral single maxima. A strong CPO develops already at relatively small aggregate strains and reaches a stable orientation of about 70° with respect to the local flow pane.

The particle and surface fabric depends on the CPO. The surface orientation distribution functions develop a monoclinic geometry at high grain boundary mobilities, and a monoclinic geometry at low grain boundary mobilities. The maxima of the surface orientation distribution functions consistently show a synthetic rotation with respect to the inferred sense of slip in the basal plane of the quartz crystals.

Bulk CPOs that incorporate recrystallized grains of different aggregates across the strain gradient are comparable to CPOs measured in monophase, non-domainal quartz rocks.

The inversion of shear senses and the deviation from a stable position with respect to the global kinematic framework has an impact on the reliability of shear senses determined from single aggregate measurements in polyphase rocks. It is suggested that multiple aggregates should be measured, which do not spin with respect to the shear zone boundary.

References

Adams, B., 1993. Orientation imaging microscopy. Electron Microscopy and Analysis 1993 (138), 489-494.

Aines, R., Rossman, G., 1984. Water in minerals - a peak in the infrared. Journal of Geophysical Research 89 (NB6), 4059-4071.

Arzi, A., 1978. Critical phenomena in rheology of partially melted rocks. Tectonophysics 44 (1-4), 173-184.

Ashby, M., Verrall, R., 1973. Diffusion-accommodated flow and superplasticity. Acta Metallurgica 21 (2), 149-163.

Auer, F., Berckhemer, H., Oehlschlegel, G., 1981. Steady-state creep of fine-grain granite at partial melting. Journal of Geophysics-Zeitschrift Fur Geophysik 49 (2), 89-92.

Ayensu, A., Langdon, T., 1996. The inter-relationship between grain boundary sliding and cavitation during creep of polycrystalline copper. Metallurgical and Materials Transactions A-Physical Metallurgy and Materials Science 27 (4), 901-907.

Baeta, R., Ashbee, K., 1969. Slip systems in quartz .2. interpretation. American Mineralogist 54 (11-1), 1574-1582.

Baker, D., Wenk, H., 1972. Preferred orientation in a low-symmetry quartz mylonite. Journal of Geology 80 (1), 80-81.

Ball, A., Hutchison, M., 1969. Superplasticity in the aluminum-zinc entectoid. Metal Sci J. 3, 1-7.

Bambauer, H., 1961. Spurenelementgehalt und gamma-Farbzentren in Quarzen aus Zerrklüften der Schweizer Alpen. Schweiz. Min. Pet. Mitt. 41, 335-369.

Barreiro, J. G., Lonardelli, I., Wenk, H. R., Dresen, G., Rybacki, E., Ren, Y., Tome, C. N., 2007. Preferred orientation of anorthite deformed experimentally in newtonian creep. Earth and Planetary Science Letters 264 (1-2), 188-207.

Baudin, T., Marquer, D., 1993. Metamorphism and deformation in the tambo nappe (swiss central alps) - evolution of the phengite substitution during alpine deformation. Schweizerische Mineralogische Und Petrographische Mitteilungen 73 (2), 285-299.

Baudin, T., Marquer, D., Peroz, F., 1993. Basement cover relationships in the tambo nappe (central alps, switzerland) - geometry, structure and kinematics. Journal of Structural Geology 15 (3-5), 543-553.

Becker, J. K., Bons, P. D., Jessell, M. W., 2008. A new front-tracking method to model anisotropic grain and phase boundary motion in rocks. Computers & Geosciences 34 (3), 201-212.

Behrmann, J., 1985. Crystal plasticity and superplasticity in quartzite - a natural example. Tectonophysics 115 (1-2), 101-129.

Behrmann, J., Mainprice, D., 1987. Deformation mechanisms in a high-temperature quartz feldspar mylonite - evidence for superplastic flow in the lower continental-crust. Tectonophysics 140 (2-4), 297-305.

Behrmann, J., Platt, J., 1982. Sense of nappe emplacement from quartz c-axis fabrics - an example from the Betic cordilleras (Spain). Earth and Planetary Science Letters 59 (1), 208-215.

Bejina, F., Jaoul, O., 1996. Silicon self-diffusion in quartz and diopside measured by nuclear micro-analysis methods. Physics of the Earth and Planetary Interiors 97 (1-4), 145-162.

Berger, A., Rosenberg, C., Schmid, S., 1996. Ascent, emplacement and exhumation of the bergell pluton within the southern steep belt of the central alps. Schweizerische Mineralogische Und Petrographische Mitteilungen 76 (3), 357-382.

Berthe, D., Choukroune, S., Gapasi, D., 1979a. Quartz fabrics and progressive gneissification of granites by simple shear - example of the south armerican shear zone. Bulletin De Mineralogie 102 (2-3), 265-272.

Berthe, D., Choukroune, S., Jegouzo, P., 1979b. Orthogneiss, mylonite and non coaxial deformation of granites - example of the South-Armorican-Shear-Zone. Journal of Structural Geology 1 (1), 31-42.

Bertrand, J.-M., Paquette, J.-L., Guillot, F., 2005. Permian zircon U-Pb ages in the Gran Paradiso massif: revisiting post-Variscan events in the Western Alps. Schweizerische Mineralogische und Petrographische Mitteilungen 85 (1), 15-29.

Bestmann, M., Prior, D., Veltkamp, K., 2004. Development of single-crystal sigma-shaped quartz porphyroclasts by dissolution-precipitation creep in a calcite marble shear zone. Journal of Structural Geology 26 (5), 869-883.

Blacic, J., 1975. Plastic-deformation mechanisms in quartz - effect of water. Tectonophysics 27 (3), 271-294.

Bons, P., Urai, J., 1994. Experimental deformation of 2-phase rock analogs. Materials Science and Engineering A-Structural Materials Properties Microstructure and Processing 175 (1-2), 221-229.

Bons, P. D., den Brok, B., 2000. Crystallographic preferred orientation development by dissolution-precipitation creep. Journal of Structural Geology 22 (11-12), 1713-1722.

Bons, P. D., Urai, J., 1992. Syndeformational grain-growth - microstructures and kinetics. Journal of Structural Geology 14 (8-9), 1101-1109.

Bouchez, J., 1977. Plastic-deformation of quartzites at low-temperature in an area of natural strain gradient. Tectonophysics 39 (1-3), 25-50.

Bouchez, J., Duval, P., 1982. The fabric of polycrystalline ice deformed in simple shear - experiments in torsion, natural deformation and geometrical interpretation. Textures and Microstructures 5 (3), 171-190.

Boullier, A., Gueguen, Y., 1975. SP-mylonites - origin of some mylonites by superplastic flow. Contributions To Mineralogy and Petrology 50 (2), 93-104.

Brouwer, F., Vissers, R., Lamb, W., 2002. Structure and metamorphism of the Gran Paradiso massif, western Alps, Italy. Contributions To Mineralogy and Petrology 143 (4), 450-470.

Bruhn, D., Olgaard, D., Dell'Angelo, L., 1999. Evidence for enhanced deformation in two-phase rocks: Experiments on the rheology of calcite-anhydrite aggregates. Journal of Geophysical Research-Solid Earth 104 (B1), 707-724.

Brunner, G., Wondratschek, H., Laves, F., 1961. Ultrarotuntersuchungen uber den Einbau von H in naturlichem Quarz. Zeitschrift Fur Elektrochemie 65 (9), 735-750.

Bucher, K., Grapes, R., 2009. The eclogite-facies allalin gabbro of the zermatt-saas ophiolite, western alps: a record of subduction zone hydration. Journal of Petrology 50 (8), 1405-1442.

Bunge, H., 1989. Advantages of neutron-diffraction in texture analysis. Textures and Microstructures 10 (4), 265-307.

Burg, J., Laurent, P., 1978. Strain analysis of a shear zone in a granodiorite. Tectonophysics 47 (1-2), 15-42.

Callegari, E., Compagnoni, R., Piaz, G. D., 1969. Relitti di strutture intrusive erciniche e scisti a sillimanie nel Massicio del Gran Paradiso. Boll Soc Geol Ital 88, 59-69.

Carreras, J., Estrada, A., White, S., 1977. Effects of folding on c-axis fabrics of a quartz mylonite. Tectonophysics 39 (1-3), 3-24.

Carter, R., Norris, R., 1976. Cainozoic history of southern new-zealand - accord between geological observations and plate-tectonic predictions. Earth and Planetary Science Letters 31 (1), 85-94.

Chakraborty, D., Lehmann, G., 1976a. Distribution of oh in synthetic and natural quartz crystals. Journal of Solid State Chemistry 17 (3), 305-311.

Chakraborty, D., Lehmann, G., 1976b. Structures and orientations of hydrogen defects in natural and synthetic quartz crystals. Physica Status Solidi A-Applied Research 34 (2), 467-474.

Cherniak, D., 2003. Silicon self-diffusion in single-crystal natural quartz and feldspar. Earth and Planetary Science Letters 214 (3-4), 655-668.

Chokshi, A., 2005. Cavity nucleation and growth in superplasticity. Materials Science and Engineering A-Structural Materials Properties Microstructure and Processing 410, 95-99.

Coble, R., 1963. A model for boundary diffusion controlled creep in polycrystalline materials. Journal of Applied Physics 34 (6), 1679.

Cox, S., Etheridge, M., 1983. Crack-seal fiber growth mechanisms and their significance in the development of oriented layer silicate microstructures. Tectonophysics 92 (1-3), 147-170.

Craw, D., Norris, R., 1993. Grain-boundary migration of water and carbon-dioxide during uplift of garnet-zone alpine schist, new-zealand. Journal of Metamorphic Geology 11 (3), 371-378.

Crossman, F., Ashby, M., 1975. Nonuniform flow of polycrystals by grain-boundary sliding accommodated by power-law creep. Acta Metallurgica 23 (4), 425-440.

Dal Piaz, G., Hunziker, J., Martinotti, G., 1972. La zona sesia-lanzo e l'evoluzione tettonico-metamorfica delle alpi nordoccidentali interne. Mem Soc Geol Ital 11, 433-466.

Davies, P., Stevens, R., Wilshire, B., 1966. Grain-boundary sliding in polycrystalline aluminium. Journal of the Institute of Metals 94 (2), 49-&.

de Bresser, J., Ter Heege, J., Spiers, C., 2001. Grain size reduction by dynamic recrystallization: can it result in major rheological weakening? International Journal of Earth Sciences 90 (1), 28-45.

de Ronde, A., Stünitz, H., Tullis, J., Heilbronner, R., 2005. Reaction-induced weakening of plagioclase-olivine composites. Tectonophysics 409 (1-4), 85-106.

DeCapitani, C., Brown, T., 1987. The computation of chemical-equilibrium in complex-systems containing nonideal solutions. Geochimica Et Cosmochimica Acta 51 (10), 2639-2652.

DellAngelo, L., Tullis, J., 1988. Experimental deformation of partially melted granitic aggregates. Journal of Metamorphic Geology 6 (4), 495-515.

DellAngelo, L., Tullis, J., 1989. Fabric development in experimentally sheared quartzites. Tectonophysics 169 (1-3), 1-21.

Delle Piane, C., Burlini, L., Kunze, K., Brack, P., Burg, J. P., 2008. Rheology of dolomite: Large strain torsion experiments and natural examples. Journal of Structural Geology 30 (6), 767-776.

Derby, B., 1990. The mechanism of internal-stress superplasticity. In: Mayo, M., Kobayashi, M., Wadsworth, J. (Eds.), Superplasticity in metals, ceramics and intermetallics. Vol. 196 of Materials Research Society Symposium Proceedings. Materials Research Soc, pp. 115-120.

Dimanov, A., Dresen, G., 2005. Rheology of synthetic anorthite-diopside aggregates: Implications for ductile shear zones. Journal of Geophysical Research-Solid Earth 110 (B7).

Dimanov, A., Dresen, G., Xiao, X., Wirth, R., 1999. Grain boundary diffusion creep of synthetic anorthite aggregates: The effect of water. Journal of Geophysical Research-Solid Earth 104 (B5), 10483-10497.

Drury, M., Urai, J., 1990. Deformation-related recrystallization processes. Tectonophysics 172 (3-4), 235-253.

Drury, M. R., Humphreys, F., 1988. Microstructural shear criteria associated with grain-boundary sliding during ductile deformation. Journal of Structural Geology 10 (1), 83-89.

Ebert, A., Herwegh, M., Evans, B., Pfiffner, A., Austin, N., Vennemann, T., 2007. Microfabrics in carbonate mylonites along a large-scale shear zone (helvetic alps). Tectonophysics 444 (1-4), 1-26.

Edington, J., Melton, K., Cutler, C., 1976. Superplasticity. Progress In Materials Science 21 (2), 63-170.

Engi, M., Bousquet, R., Berger, A., 2004. Explanatory notes to the map: Metamorphic structure of the Alps Central Alps. Mitteil. Oesterr. Mineral. Gesell. 149 (157-173).

Etchecopar, A., 1977. Plane kinematic model of progressive deformation in a polycrystalline aggregate. Tectonophysics 39 (1-3), 121-139.

Etchecopar, A., Vasseur, G., 1987. A 3-d kinematic model of fabric development in polycrystalline aggregates - comparisons with experimental and natural examples. Journal of Structural Geology 9 (5-6), 705-717.

Etheridge, M., Wilkie, J., 1979. Grain-size reduction, grain-boundary sliding and the flow strength of mylonites. Tectonophysics 58 (1-2), 159-178.

Evans, B., Renner, J., Hirth, G., 2001. A few remarks on the kinetics of static grain growth in rocks. International Journal of Earth Sciences 90 (1), 88-103.

Farver, J., Yund, R., 1991. Measurement of oxygen grain-boundary diffusion in natural, fine-grained, quartz aggregates. Geochimica Et Cosmochimica Acta 55 (6), 1597-1607.

Farver, J., Yund, R., 1995a. Grain-boundary diffusion of oxygen, potassium and calcium in natural and hot-pressed feldspar aggregates. Contributions To Mineralogy and Petrology 118 (4), 340-355.

Farver, J., Yund, R., 1995b. Interphase boundary diffusion of oxygen and potassium in k-feldspar/quartz aggregates. Geochimica Et Cosmochimica Acta 59 (18), 3697-3705.

Farver, J., Yund, R., 1999. Oxygen bulk diffusion measurements and tem characterization of a natural ultramylonite: implications for fluid transport in mica-bearing rocks. Journal of Metamorphic Geology 17 (6), 669-683.

Farver, J., Yund, R., 2000. Silicon diffusion in a natural quartz aggregate: constraints on solution-transfer diffusion creep. Tectonophysics 325 (3-4), 193-205.

Fazan, B., Shreby, O., Dorn, J., 1954. Some observations on grain boundary shearing during creep. Journal of Metals 6 (8), 919-921.

Fitz Gerald, J., Stünitz, H., 1993. Deformation of granitoids at low metamorphic grade .1. reactions and grain-size reduction. Tectonophysics 221 (3-4), 269-297.

Fliervoet, T., White, S., 1995. Quartz deformation in a very fine-grained quartzo-feldspathic mylonite - a lack of evidence for dominant grain-boundary sliding deformation. Journal of Structural Geology 17 (8), 1095-1109.

Fliervoet, T., White, S., Drury, M., 1997. Evidence for dominant grain-boundary sliding deformation in greenschist- and amphibolite-grade polymineralic ultramylonites from the Redbank Deformed Zone, Central Australia. Journal of Structural Geology 19 (12), 1495-1520.

Fossen, H., Tikoff, B., 1993. The deformation matrix for simultaneous simple shearing, pure shearing and volume change, and its application to transpression transtension tectonics. Journal of Structural Geology 15 (3-5), 413-422.

Freeman, B., 1987. The behavior of deformable ellipsoidal particles in 3-dimensional slow flows - implications for geological strain analysis. Tectonophysics 132 (4), 297-309.

Fusseis, F., Handy, M. R., 2008. Micromechanisms of shear zone propagation at the brittle-viscous transition. Journal of Structural Geology 30 (10), 1242-1253.

Fusseis, F., Regenauer-Lieb, K., Liu, J., Hough, R. M., De Carlo, F., 2009. Creep cavitation can establish a dynamic granular fluid pump in ductile shear zones. Nature 459 (7249), 974-977.

Fynn, G. W., Powell, W. J. A., 1979. The cutting and polishing of electro-optic materials. Adam Hilger, Bristol, Eng.

Garcia-Celma, A., 1983. C-axis and shape fabrics in quartz-mylonites of Cap de Creus (Spain); their properties and development. Ph.D. thesis, University of Utrecht.

Gay, N., 1968a. Pure shear and simple shear deformation of inhomogeneous viscous fluids .1. theory. Tectonophysics 5 (3), 211-&.

Gay, N., 1968b. Pure shear and simple shear deformation of inhomogeneous viscous fluids .2. determination of total finite strain in a rock from objects such as deformed pebbles. Tectonophysics 5 (4), 295-&.

Geraud, Y., Caron, J., Faure, P., 1995. Porosity network of a ductile shear zone. Journal of Structural Geology 17 (12), 1757-&.

Gifkins, R., 1976. Grain-boundary sliding and its accommodation during creep and superplasticity. Metallurgical Transactions A-Physical Metallurgy and Materials Science 7 (8), 1225-1232.

Gilotti, J., 1992. The rheologically critical matrix in arkosic mylonites along the Särv thrust, Swedish Caledonides. J. Hopkins University Press, pp. 145-160.

Gleason, G., Tullis, J., 1995. A flow law for dislocation creep of quartz aggregates determined with the molten-salt cell. Tectonophysics 247 (1-4), 1-23.

Gleason, G. C., DeSisto, S., 2008. A natural example of crystal-plastic deformation enhancing the incorporation of water into quartz. Tectonophysics 446 (1-4), 16-30.

Goetze, C., Kohlsted, D., 1973. Laboratory study of dislocation climb and diffusion in olivine. Journal of Geophysical Research 78 (26), 5961-5971.

Goldsby, D., Kohlstedt, D., 2001. Superplastic deformation of ice: Experimental observations. Journal of Geophysical Research-Solid Earth 106 (B6), 11017-11030.

Gower, R., Simpson, C., 1992. Phase-boundary mobility in naturally deformed, high-grade quartzofeldspathic rocks - evidence for diffusional creep. Journal of Structural Geology 14 (3), 301-313.

Griggs, D., Blacic, J., 1964. The strength of quartz in the ductile regime. Eos. Trans. Am. geopys. Union 45, 102-103.

Griggs, D., Blacic, J., 1965. Quartz - anomalous weakness of synthetic crystals. Science 147 (3655), 292-&.

Grimmer, H., 1979. Distribution of disorientation angles if all relative orientations of neighboring grains are equally probable. Scripta Metallurgica 13 (2), 161-164.

Groves, G., Kelly, A., 1969. Change of shape due to dislocation climb. Philosophical Magazine 19 (161), 977-986.

Guermani, A., Pennacchioni, G., 1998. Brittle precursors of plastic deformation in a granite: an example from the mont blanc massif (helvetic, western alps). Journal of Structural Geology 20 (2-3), 135-148.

Guillope, M., Poirier, J. P., 1979. Dynamic recrystallization during creep of single-crystalline halite - experimental-study. Journal of Geophysical Research 84 (NB10), 5557-5567.

Halfpenny, A., Prior, D. J., Wheeler, J., 2006. Analysis of dynamic recrystallization and nucleation in a quartzite mylonite. Tectonophysics 427 (1-4), 3-14.

Handy, M., 1990. The solid-state flow of polymineralic rocks. Journal of Geophysical Research-Solid Earth and Planets 95 (B6), 8647-8661.

Handy, M., 1994. Flow laws for rocks containing 2 nonlinear viscous phases - a phenomenological approach. Journal of Structural Geology 16 (3), 287-301.

Hanmer, S., 2000. Matrix mosaics, brittle deformation, and elongate porphyroclasts: granulite facies microstructures in the Striding-Athabasca mylonite zone, Western Canada. Journal of Structural Geology 22 (7), 947-967.

Hansen, F., Carter, N., 1982. Creep of selected crustal rocks at 1000 MPa. Eos. Trans. Am. geopys. Union 63, 437.

Heilbronner, R., 2000. Automatic grain boundary detection and grain size analysis using polarization micrographs or orientation images. Journal of Structural Geology 22 (7), 969-981.

Heilbronner, R., 2002. Analysis of bulk fabrics and microstructure variations using tesselations of autocorrelation functions. Computers & Geosciences 28 (4), 447-455.

Heilbronner, R., 2010. Mapping texture domains in quartzite microstructures. Journal of the Geological Society of India 75 (1), 160-170.

Heilbronner, R., Bruhn, D., 1998. The influence of three-dimensional grain size distributions on the rheology of polyphase rocks. Journal of Structural Geology 20 (6), 695-705.

Heilbronner, R., Keulen, N., 2006. Grain size and grain shape analysis of fault rocks. Tectonophysics 427 (1-4), 199-216.

Heilbronner, R., Pauli, C., 1993. Integrated spatial and orientation analysis of quartz c-axes by computer-aided microscopy. Journal of Structural Geology 15 (3-5), 369-382.

Heilbronner, R., Tullis, J., 2006. Evolution of c axis pole figures and grain size during dynamic recrystallization: Results from experimentally sheared quartzite. Journal of Geophysical Research-Solid Earth 111 (B10), B10202.

Herwegh, M., Jenni, A., 2001. Granular flow in polymineralic rocks bearing sheet silicates: new evidence from natural examples. Tectonophysics 332 (3), 309-320.

Hielscher, R., Schaeben, H., 2008. A novel pole figure inversion method: specification of the mtex algorithm. Journal of Applied Crystallography 41, 1024-1037.

Hippertt, J., 1994. Microstructures and c-axis fabrics indicative of quartz dissolution in sheared quartzites and phyllonites. Tectonophysics 229 (3-4), 141-163.

Hippertt, J., Hongn, F., 1998. Deformation mechanisms in the mylonite/ultramylonite transition. Journal Of Structural Geology 20 (11), 1435-1448.

Hirth, G., Teyssier, C., Dunlap, W., 2001. An evaluation of quartzite flow laws based on comparisons between experimentally and naturally deformed rocks. International Journal of Earth Sciences 90 (1), 77-87.

Hirth, G., Tullis, J., 1992. Dislocation creep regimes in quartz aggregates. Journal of Structural Geology 14 (2), 145-159.

Hirth, G., Tullis, J., 1994. The brittle-plastic transition in experimentally deformed quartz aggregates. Journal of Geophysical Research-Solid Earth 99 (B6), 11731-11747.

Hobbs, B. E., 1985. The geological significance of microfabric. Vol. Preferred orientation in deformed metals and rocks. Academic Press, New York.

Hobbs, B. E., Means, W., Williams, P. F., 1976. An Outline of Structural Geology. Wiley.

Hofmeister, A., Rossman, G., 1985. A model for the irradiative coloration of smoky feldspar and the inhibiting influence of water. Physics and Chemistry of Minerals 12 (6), 324-332.

Holtzman, B., Groebner, N., Zimmerman, M., Ginsberg, S., Kohlstedt, D., 2003. Stress-driven melt segregation in partially molten rocks. Geochemistry Geophysics Geosystems 4.

Holyoke, C., Tullis, J., 2006a. Formation and maintenance of shear zones. Geology 34 (2), 105-108.

Holyoke, C., Tullis, J., 2006b. Mechanisms of weak phase interconnection and the effects of phase strength contrast on fabric development. Journal of Structural Geology 28 (4), 621-640.

Honnef, H., Mecking, H., 1978. In: Gottstein, C., Lücke, K. (Eds.), Proc. 5th Int. Conf. Texture of Materials. Vol. 5. Springer-Verlag, Berlin.

Huber, R., Marquer, D., 1998. The tectonometamorphic history of the peridotitic chiavenna unit from mesozoic to tertiary tectonics: a restoration controlled by melt polarity indicators (eastern swiss alps). Tectonophysics 296 (1-2), 205-223.

Hudleston, P., 1977. Progressive deformation and development of fabric across zones of shear in glacial ice. Vol. Energetics of Geological Processes. Springer Verlag, New York.

Hudleston, P., 1980. The progressive development of inhomogeneous shear and crystallographic fabric in glacial ice. Journal of Structural Geology 2 (1-2), 189-196.

Hull, J., 1988. Thickness displacement relationships for deformation zones. Journal of Structural Geology 10 (4), 431-435.

Hutchinson, J., 1976. Bounds and self-consistent estimates for creep of polycrystalline materials. Proc. R. Soc. Lond., Ch. A 348, p. 101.

Hutchinson, J., Tvergaard, V., 1981. Shear band formation in plane-strain. International Journal of Solids and Structures 17 (5), 451-470.

Ishii, K., 1992. Partitioning of noncoaxiality in deforming layered rock masses. Tectonophysics 210 (1-2), 33-43.

Ishii, K., Kanagawa, K., Shigematsu, N., Okudaira, T., 2007. High ductility of k-feldspar and development of granitic banded ultramylonite in the ryoke metamorphic belt, sw japan. Journal of Structural Geology 29 (6), 1083-1098.

Jerabek, P., Stuenitz, H., Heilbronner, R., Lexa, O., Schulmann, K., 2007. Microstructural-deformation record of an orogen-parallel extension in the vepor unit, west carpathians. Journal of Structural Geology 29 (11), 1722-1743.

Jessell, M., 1987. Grain-boundary migration microstructures in a naturally deformed quartzite. Journal of Structural Geology 9 (8), 1007-1014.

Jessell, M., Lister, G., 1990. A simulation of temperature dependence of quartz fabrics. Vol. 54. Geol Soc Lond Spec Publ, pp. 353-362.

Ji, S., Xia, B., 2002. Rheology of polyphase earth materials. Polytechnic International Press.

JI, S., Zhao, P., 1994. Strength of 2-phase rocks - a model-based on fiber-loading theory. Journal of Structural Geology 16 (2), 253-262.

Ji, S., Zhao, P., Xia, B., 2003. Flow laws of multiphase materials and rocks from end-member flow laws. Tectonophysics 370 (1-4), 129-145.

Jiang, D., 1994. Flow variation in layered rocks subjected to bulk flow of various kinematics vorticities - theory and geological implications. Journal Of Structural Geology 16 (8), 1159-1172.

Johnson, E., Rossman, G., 2003. The concentration and speciation of hydrogen in feldspars using FTIR and H-1 MAS NMR spectroscopy. American Mineralogist 88 (5-6), 901-911.

Johnson, S., Vernon, R., Upton, P., 2004. Foliation development and progressive strain-rate partitioning in the crystallizing carapace of a tonalite pluton: microstructural evidence and numerical modeling. Journal of Structural Geology 26 (10), 1845-1865.

Jordan, P., 1987. The deformational behavior of bimineralic limestone halite aggregates. Tectonophysics 135 (1-3), 185-197.

Jordan, P., 1988. The rheology of polymineralic rocks - an approach. Geologische Rundschau 77 (1), 285-294.

Kanagawa, K., Shimano, H., Hiroi, Y., 2008. Mylonitic deformation of gabbro in the lower crust: A case study from the Pankenushi gabbro in the Hidaka metamorphic belt of central Hokkaido, Japan. Journal Of Structural Geology 30 (9), 1150-1166.

Karato, S., Paterson, M., FitzGerald, J., 1986. Rheology of synthetic olivine aggregates - influence of grain-size and water. Journal of Geophysical Research-Solid Earth and Planets 91 (B8), 8151-8176.

Kassem, K., 2005. Finite-strain analysis in orthogneiss of the gran paradiso massif, western alps, italy. Ph.D. thesis, University Mainz.

Kassner, M., Hayes, T., 2003. Creep cavitation in metals. International Journal of Plasticity 19 (10), 1715-1748.

Katz, A., 1962. Hydrogen in alpha-quartz. Phillips Res. Rep. 17, 1-31, 133-279.

Kekulawala, K., Paterson, M., Boland, J., 1978. Hydrolytic weakening in quartz. Tectonophysics 46 (1-2), T1-T6.

Kekulawala, K., Paterson, M., Boland, J., 1981. An experimental study of the role of water in quartz deformation. Vol. 24. AGU Geophys.Monogr., pp. 49-60.

Kenkmann, T., Dresen, G., 2002. Dislocation microstructure and phase distribution in a lower crustal shear zone - an example from the ivrea-zone, italy. International Journal of Earth Sciences 91 (3), 445-458.

Kerrich, R., Allison, I., Barnett, R., Moss, S., Starkey, J., 1980. Microstructural and chemical-transformations accompanying deformation of granite in a shear zone at Mieville, Switzerland - with implications for stress-corrosion cracking and superplastic flow. Contributions To Mineralogy and Petrology 73 (3), 221-242.

Khayutin, S., 1974. Deformation of polycrystals connected with grain-boundaries migration. Fizika Metallov I Metallovedenie 37 (5), 1072-1080.

Kilian, R., Heilbronner, R., Stünitz, H., 2011a. Quartz grain size reduction in a granitoid rock and the transition from dislocation to diffusion creep. Journal of Structural Geology, 33, 1265-1284.

Kilian, R., Heilbronner, R., Stünitz, H., 2011b. Quartz microstructures and crystallographic preferred orientations: which shear sense do they indicate?. Journal of Structural Geology,33, 1446-1466.

Kirby, S., McCormick, J., 1979. Creep of hydrolytically weakened synthetic quartz crystals oriented to promote (2110) less-than-0001-greater-than slip - brief summary of work to date. Bulletin De Mineralogie 102 (2-3), 124-137.

Kleinschrodt, R., 1994. Textures of geological materials: Competing crystal-plastic and grain size sensitive deformation mechanisms in a peridotite mylonite from the Finero complex Ivrea Zone, Italy. DGM, Informationsgesellschaft, pp. 203-219.

Knipe, R., Law, R., 1987. The influence of crystallographic orientation and grain-boundary migration on microstructural and textural evolution in an S-C mylonite. Tectonophysics 135 (1-3), 155-169.

Koch, P., Christie, J., Ord, A., George, R., 1989. Effect of water on the rheology of experimentally deformed quartzite. Journal of Geophysical Research-Solid Earth and Planets 94 (B10), 13975-13996.

Kohlstedt, D., Evans, B., Mackwell, S., 1995. Strength of the lithosphere - constraints imposed by laboratory experiments. Journal of Geophysical Research-Solid Earth 100 (B9), 17587-17602.

Kottada, R. S., Chokshi, A. H., 2007. Grain boundary sliding during diffusion and dislocation creep in a Mg-0.7 pct Al alloy. Metallurgical and Materials Transactions A-Physical Metallurgy and Materials Science 38A (8), 1743-1749.

Kretz, R., 1969. On the spatial distribution of crystals in rocks. Lithos 2 (1), 39 - 65.

Kretz, R., 2006. Shape, size, spatial distribution and composition of garnet crystals in highly deformed gneiss of the otter lake area, quebec, and a model for garnet crystallization. Journal of Metamorphic Geology 24 (6), 431-449.

Kronenberg, A., 1994. Hydrogen speciation and chemical weakening of quartz. Silica: Physical Behavior, Geochemistry and Materials Applications 29, 123-176.

Kronenberg, A., Kirby, S., Aines, R., Rossman, G., 1986. Solubility and diffusional uptake of hydrogen in quartz at high water pressures - implications for hydrolytic weakening. Journal of Geophysical Research-Solid Earth and Planets 91 (B12), 2723-2744.

Kronenberg, A., Kirby, S., Pinkston, J., 1990a. Basal slip and mechanical anisotropy of biotite. Journal of Geophysical Research-Solid Earth and Planets 95 (B12), 19257-19278.

Kronenberg, A., Segall, P., Wolf, G., 1990c. Hydrolitic weakening and penetrative deformation within a natural shear zone. No. 56. Am Geophys. Union, pp. 21-36.

Kronenberg, A., Tullis, J., 1984. Flow strengths of quartz aggregates - grain-size and pressure effects due to hydrolytic weakening. Journal of Geophysical Research 89 (NB6), 4281-4297.

Kronenberg, A., Wolf, G., 1990. Fourier-transform infrared-spectroscopy determinations of intragranular water-content in quartz-bearing rocks - implications for hydrolytic weakening in the laboratory and within the earth. Tectonophysics 172 (3-4), 255-271.

Kruhl, J., 1996. Prism- and basal-plane parallel subgrain boundaries in quartz: A microstructural geothermobarometer. Journal of Metamorphic Geology 14 (5), 581-589.

Kruhl, J., Peternell, M., 2002. The equilibration of high-angle grain boundaries in dynamically recrystallized quartz: the effect of crystallography and temperature. Journal of Structural Geology 24 (6-7), 1125-1137.

Kruse, R., Stünitz, H., 1999. Deformation mechanisms and phase distribution in mafic high-temperature mylonites from the jotun nappe, southern norway. Tectonophysics 303 (1-4), 223-249.

Kuntcheva, B., Kruhl, J. H., Kunze, K., 2006. Crystallographic orientations of high-angle grain boundaries in dynamically recrystallized quartz: First results. Tectonophysics 421 (3-4), 331-346.

Lagoeiro, L., Fueten, F., 2008. Fluid-assisted grain boundary sliding in bedding-parallel quartz veins deformed under greenschist metamophic grade. Tectonophysics 446 (1-4), 42-50.

Langdon, T., 1993. The role of grain-boundaries in high-temperature deformation. Materials Science and Engineering A-Structural Materials Properties Microstructure and Processing 166 (1-2), 67-79.

Langdon, T., 1994. A unified approach to grain-boundary sliding in creep and superplasticity. Acta Metallurgica Et Materialia 42 (7), 2437-2443.

Langdon, T., 2006. Grain boundary sliding revisited: Developments in sliding over four decades. Journal of Materials Science 41 (3), 597-609.

Law, R., 1986. Relationships between strain and quartz crystallographic fabrics in the roche maurice quartzites of plougastel, western brittany. Journal of Structural Geology 8 (5), 493-515.

Law, R., Schmid, S., Wheeler, J., 1990. Simple shear deformation and quartz crystallographic fabrics - a possible natural example from the torridon area of nw scotland. Journal of Structural Geology 12 (1), 29-45.

Law, R., Searle, M., Simpson, R., 2004. Strain, deformation temperatures and vorticity of flow at the top of the Greater Himalayan Slab, Everest Massif, Tibet. Journal of Geological Society of London 161, 305-320.

Le Bayon, B., Pitra, P., Ballevre, M., Bohn, M., 2006. Reconstructing P-T paths during continental collision using multi-stage garnet (Gran Paradiso nappe, Western Alps). Journal of Metamorphic Geology 24 (6), 477-496.

LeGoff, E., Ballevre, M., 1990. Geothermobarometry in albite-garnet orthogneisses - a case-study from the Gran-Paradiso nappe (Western Alps). Lithos 25 (4), 261-280.

LeHazif, R., 1978. Plastic-deformation of 2-phase fe-ag system containing phases of equal volume. Acta Metallurgica 26 (2), 247-257.

Lenze, A., Stoeckhert, B., 2007. Microfabrics of uhp metamorphic granites in the dora maira massif, western alps - no evidence of deformation at great depth. Journal of Metamorphic Geology 25 (4), 461-475.

Libowitzky, E., Rossman, G., 1997. An ir absorption calibration for water in minerals. American Mineralogist 82 (11-12), 1111-1115.

Lifshitz, I., 1963. On the theory of diffusion-viscous flow of polycrystalline bodies. Soviet Physics Jetp-Ussr 17 (4), 909-920.

Lister, G., Dornsiepen, U., 1982. Fabric transitions in the saxony granulite terrain. Journal of Structural Geology 4 (1), 81-92.

Lister, G., Hobbs, B., 1980. The simulation of fabric development during plastic-deformation and its application to quartzite - the influence of deformation history. Journal of Structural Geology 2 (3), 355-370.

Lister, G., Paterson, M., Hobbs, B., 1978. Simulation of fabric development in plastic-deformation and its application to quartzite - model. Tectonophysics 45 (2-3), 107-158.

Lister, G., Snoke, A., 1984. S-c mylonites. Journal of Structural Geology 6 (6), 617-638.

Lister, G., Williams, P., 1979. Fabric development in shear zones - theoretical controls and observed phenomena. Journal of Structural Geology 1 (4), 283-297.

Lister, G., Williams, P., 1983. The partitioning of deformation in flowing rock masses. Tectonophysics 92 (1-3), 1-33.

Llana-Funez, S., 2002. Quartz c-axis texture mapping of a variscan regional foliation (Malpica-Tui Unit, NW Spain). Journal of Structural Geology 24 (8), 1299-1312.

Lloyd, G., 1987. Fabric analysis using sem electron channeling. In: Journal of the Geological Society. Vol. 144. Geological Soc Publ House, pp. 678-678.

Lloyd, G., Farmer, A., Mainprice, D., 1997. Misorientation analysis and the formation and orientation of subgrain and grain boundaries. Tectonophysics 279 (1-4), 55-78.

Luan, F., Paterson, M., 1992. Preparation and deformation of synthetic aggregates of quartz. Journal of Geophysical Research-Solid Earth 97 (B1), 301-320.

Mackenzie, J. R., Egozcue, J. J., Heilbronner, R., Hielscher, R., Müller, A., Schaeben, H., 2008. Quantifying rock fabrics - a test of independence of the spatial distribution of crystals. CoDaWork08:Girona http://hdl.handle.net/10256/719.

Mainprice, D., Bouchez, J., Blumenfeld, P., Tubia, J., 1986. Dominant-c slip in naturally deformed quartz - implications for dramatic plastic softening at high-temperature. Geology 14 (10), 819-822.

Mancktelow, N., 1987. Quartz textures from the Simplon fault zone, southwest Switzerland and north Italy. Tectonophysics 135 (1-3), 133-153.

Mancktelow, N., Pennacchioni, G., 2004. The influence of grain boundary fluids on the microstructure of quartz-feldspar mylonites. Journal of Structural Geology 26 (1), 47-69.

Mancktelow, N., Pennacchioni, G., 2005. The control of precursor brittle fracture and fluid-rock interaction on the development of single and paired ductile shear zones. Journal of Structural Geology 27 (4), 645-661.

Mancktelow, N. S., Pennacchioni, G., 2010. Why calcite can be stronger than quartz. Journal of Geophysical Research-Solid Earth 115.

Mares, V., Kronenberg, A., 1993. Experimental deformation of muscovite. Journal of Structural Geology 15 (9-10), 1061-1075.

Marquer, D., 1991. Structures and kinematic history of alpine deformation in the truzzo granite (Tambo Nappe Central Alps Switzerland). Eclogae Geologicae Helvetiae 84 (1), 107-123.

Marquer, D., Baudin, T., Peucat, J., Peroz, F., 1994. Rb-sr mica ages in the alpine shear zones of the Truzzo granite - timing of the tertiary alpine p-t-deformations in the Tambo Nappe (Central Alps, Switzerland). Eclogae Geologicae Helvetiae 87 (1), 225-239.

Marquer, D., Challandes, N., Baudin, T., 1996. Shear zone patterns and strain distribution at the scale of a Penninic nappe: The Suretta Nappe (Eastern Swiss Alps). Journal of Structural Geology 18 (6), 753-&.

Marques, F., Taborda, R., Antunes, J., 2005. 2d rotation of rigid inclusions in confined bulk simple shear flow: a numerical study. Journal of Structural Geology 27 (12), 2171-2180.

Maruyama, S., Suzuki, K., Liou, J., 1983. Greenschist-amphibolite transition equilibria at low-pressures. Journal of Petrology 24 (4), 583-604.

Massonne, H., Schreyer, W., 1987. Phengite geobarometry based on the limiting assemblage with k-feldspar, phlogopite, and quartz. Contributions To Mineralogy and Petrology 96 (2), 212-224.

Masuda, T., Ando, S., 1988. Viscous-flow around a rigid spherical body - a hydrodynamical approach. Tectonophysics 148 (3-4), 337-346.

Means, W., 1979. Stress and strain. Springer, Berlin Heidelberg New York.

Means, W., 1981. The concept of steady-state foliation. Tectonophysics 78 (1-4), 179-199.

Means, W., Jessell, M., 1986. Accommodation migration of grain-boundaries. Tectonophysics 127 (1-2), 67-86.

Means, W. D., 1995. Shear zones and rock history. Tectonophysics 247 (1-4), 157-160.

Mehl, L., Hirth, G., 2008. Plagioclase preferred orientation in layered mylonites: Evaluation of flow laws for the lower crust. Journal of Geophysical Research-Solid Earth 113 (B5), B05202.

Menegon, L., 2006. Ductile deformation of granitic rocks: Selected examples from the western alps. Ph.D. thesis, Univ. Padova,Dip di Geologia., Paleontologia e Geofisica.

Menegon, L., Pennacchioni, G., 2009. Local shear zone pattern and bulk deformation in the Gran Paradiso metagranite (NW Italian Alps). International Journal of Earth Sciences.

Menegon, L., Pennacchioni, G., Heilbronner, R., Pittarello, L., 2008a. Evolution of quartz microstructure and c-axis crystallographic preferred orientation within ductilely deformed granitoids (arolla unit, western alps). Journal of Structural Geology 30 (11), 1332-1347.

Menegon, L., Pennacchioni, G., Spiess, R., 2008b. Dissolution-precipitation creep of k-feldspar in mid-crustal granite mylonites. Journal of Structural Geology 30 (5), 565-579.

Menegon, L., Pennacchioni, G., Stuenitz, H., 2006. Nucleation and growth of myrmekite during ductile shear deformation in metagranites. Journal of Metamorphic Geology 24 (7), 553-568.

Mercier, J., 1980. Magnitude of the continental lithospheric stresses inferred from rheomorphic petrology. Journal of Geophysical Research 85 (NB11), 6293-6303.

Mises von, R., 1928. Mechanics of the ductile form changes of crystals. Zeitschrift fur Angewandte Mathematik und Mechanik 8, 161-185.

Misra, S., 2010. Deformation localization at the tips of shear fractures: An analytical approach. Tectonophysics doi: 10.1016/j.tecto.2010.09.030.

Mukherjee, A., 1971. Rate controlling mechanism in superplasticity. Materials Science and Engineering 8 (2), 83-89.

Mulchrone, K., Walsh, K., 2006. The motion of a non-rigid ellipse in a general 2d deformation. Journal of Structural Geology 28 (3), 392-407.

Mulchrone, K. F., 2007. An analytical solution in 2d for the motion of rigid elliptical particles with a slipping interface under a general deformation. Journal of Structural Geology 29 (6), 950-960.

Nakashima, S., Matayoshi, H., Yuko, T., Michibayashi, K., Masuda, T., Kuroki, N., Yamagishi, H., Iito, Y., Nakamura, A., 1995. Infrared microspectroscopy analysis of water distribution in deformed and metamorphosed rocks. Tectonophysics 245 (3-4), 263-276.

Neurath, C., Smith, R., 1982. The effect of material properties on growth-rates of folding and boudinage - experiments with wax models. Journal of Structural Geology 4 (2), 215-&.

Niimi, N., Aikawa, N., Shinoda, K., 1999. The infrared absorption band at 3596 cm(-1) of the recrystallized quartz from mt. takamiyama, southwest japan. Mineralogical Magazine 63 (5), 693-701.

Nye, J. F., 1953. The flow law of ice from measurements in glacier tunnels, laboratory experiments and the Jungfraufim borehole experiment. Proceedings of the Royal Society, London 219, 477-489.

Olgaard, D., 1990. The role of 2nd phase in localizing deformation. In: Knipe, R., Rutter, E. (Eds.), Deformation Mechanisms, Rheology and Tectonic. Vol. 54 of Geol. Soc. Spec. Pub. Geol. Soc. Spec. Pub., pp. 175-181.

Olgaard, D., Evans, B., 1986. Effect of 2nd-phase particles on grain-growth in calcite. Journal of the American Ceramic Society 69 (11), C272-C277.

Olgaard, D., Evans, B., 1988. Grain-growth in synthetic marbles with added mica and water. Contributions To Mineralogy and Petrology 100 (2), 246-260.

Padmanabhan, K., Davis, G., 1980. Superplasticity. Springer, Berlin.

Panozzo, R., 1983. Two-dimensional analysis of shape-fabric using projections of digitized lines in a plane. Tectonophysics 95 (3-4), 279-294.

Panozzo, R., 1984. Two-dimensional strain from the orientation of lines in a plane. Journal of Structural Geology 6 (1-2), 215-221.

Panozzo, R., Hurlimann, H., 1983. A simple method for the quantitative discrimination of convex and convex-concave lines. Microscopica Acta 87 (2), 169-176.

Park, Y., Yoo, S.-H., Ree, J.-H., 2006. Weakening of deforming granitic rocks with layer development at middle crust. Journal of Structural Geology 28 (5), 919-928.

Parrish, D., Krivz, A., Carter, N., 1976. Finite-element folds of similar geometry. Tectonophysics 32 (3-4), 183-207.

Passchier, C. W., 1983. The reliability of asymmetric c-axis fabrics of quartz to determine sense of vorticity. Tectonophysics 99 (1), T9-T18.

Passchier, C. W., 1987. Stable positions of rigid objects in noncoaxial flow - a study in vorticity analysis. Journal of Structural Geology 9 (5-6), 679-&.

Passchier, C. W., Trouw, R. A. J., 1996. Microtectonics. Springer Verlag,Berlin.

Paterson, M., 1982. The determination of hydroxyl by infrared-absorption in quartz, silicate-glasses and similar materials. Bulletin De Mineralogie 105 (1), 20-29.

Paterson, M., 1989. The interaction of water with quartz and its influence in dislocation flow--an overview. Rheology of Solids and of the Earth, Oxford Science Publications, Oxford, pp. 107-142.

Paterson, M., 1990. Superplasticity in geological-materials. In: Mayo, M., Kobayashi, M., Wadsworth, J. (Eds.), Superplasticity in metals, ceramics, and intermetallics. Vol. 196 of Materials Research Society Symposium Proceedings. Materials Research Soc, pp. 303-312.

Paterson, M., 1995. A theory for granular flow accommodated by material transfer via an intergranular fluid. Tectonophysics 245 (3-4), 135-151.

Paterson, M., 2001. Relating experimental and geological theology. International Journal of Earth Sciences 90 (1), 157-167.

Paterson, M., Luan, F., 1990. Quartzite rheology under geological conditions. Vol. 54 of Deformation mechanisms, rheology and tectonics. Geological Society of London, London, pp. 299-307.

Pauli, C., Schmid, S., Heilbronner, R., 1996. Fabric domains in quartz mylonites: Localized three dimensional analysis of microstructure and texture. Journal of Structural Geology 18 (10), 1183-1203.

Pennacchioni, G., 2005. Control of the geometry of precursor brittle structures on the type of ductile shear zone in the adamello tonalites, southern alps (italy). Journal of Structural Geology 27 (4), 627-644.

Pennacchioni, G., Di Toro, G., Brack, P., Menegon, L., Villa, I. M., 2006. Brittle-ductile-brittle deformation during cooling of tonalite (adamello, southern italian alps). Tectonophysics 427 (1-4), 171-197.

Pennacchioni, G., Mancktelow, N. S., 2007. Nucleation and initial growth of a shear zone network within compositionally and structurally heterogeneous granitoids under amphibolite facies conditions. Journal of Structural Geology 29 (11), 1757-1780.

Pilling, J., Ridley, N., 1988. Cavitation in superplastic alloys and the effect of hydrostatic-pressure. Res Mechanica 23 (1), 31-63.

Pitzer, K., Sterner, S., 1994. Equations of state valid continuously from zero to extreme pressures for H2O and CO2. Journal of Chemical Physics 101 (4), 3111-3116.

Platt, J., Behrmann, J., 1986. Structures and fabrics in a crustal-scale shear zone, Betic Cordillera, SE Spain. Journal of Structural Geology 8 (1), 15-&.

Platt, J., Behrmann, J., Martinez, J., Vissers, R., 1984. A zone of mylonite and related ductile deformation beneath the Alpujarride nappe complex, Betic Cordilleras, Southern Spain. Geologische Rundschau 73 (2), 773-785.

Poirier, J., 1980. Shear localization and shear instability in materials in the ductile field. Journal of Structural Geology 2 (1-2), 135-142.

Poirier, J., 1985. Creep of crystals: high-temperature deformation processes in metals, ceramics and minerals. Cambridge Univ Press, Cambridge.

Poirier, J., Guillope, M., 1979. Deformation induced recrystallization of minerals. Bulletin De Mineralogie 102 (2-3), 67-74.

Pollard, D, Fletcher, R., 2005. Fundamentals of Structural Geology. Cambridge University Press.

Post, A., Tullis, J., 1998. The rate of water penetration in experimentally deformed quartzite, implications for hydrolytic weakening. Tectonophysics 295 (1-2), 117-137.

Post, A., Tullis, J., Yund, R., 1996. Effects of chemical environment on dislocation creep of quartzite. Journal of Geophysical Research-Solid Earth 101 (B10), 22143-22155.

Price, G., 1985. Preferred orientation in quartzites. Preferred Orientation in Deformed Metals and Rocks: an Introduction to Modern Texture Analysis, Academic Press, Orlando, pp. 385-406.

Rachinger, W., 1952. Relative grain translations in the plastic flow of aluminium. Journal of the Institute of Metals 81 (1), 33-41.

Raj, R., Ashby, M., 1971. Grain boundary sliding and diffusional creep. Metallurgical Transactions 2 (4), 1113-&.

Ramsay, J. F., Huber, M. I., 1983. The techniques of modern structural geology. Academic Press, London.

Ree, J., 1991. An experimental steady-state foliation. Journal of Structural Geology 13 (9), 1001-1011.

Ree, J., 1994. Grain-boundary sliding and development of grain-boundary openings in experimentally deformed octachloropropane. Journal of Structural Geology 16 (3), 403-418.

Regenauer-Lieb, K., Yuen, D., 2003. Modeling shear zones in geological and planetary sciences: solid- and fluid-thermal-mechanical approaches. Earth-Science Reviews 63 (3-4), 295-349.

Regenauer-Lieb, K., Yuen, D. A., 2006. Quartz rheology and short-time-scale crustal instabilities. Pure and Applied Geophysics 163 (9), 1915-1932.

Renner, J., Siddiqi, G., Evans, B., 2007. Plastic flow of two-phase marbles. Journal of Geophysical Research-Solid Earth 112 (B7).

Rubie, D., 1983. Reaction-enhanced ductility - the role of solid-solid univariant reactions in deformation of the crust and mantle. Tectonophysics 96 (3-4), 331-352.

Rutter, E., Brodie, K., 2004a. Experimental grain size-sensitive flow of hot-pressed brazilian quartz aggregates. Journal of Structural Geology 26 (11), 2011-2023.

Rutter, E., Brodie, K., 2004b. Experimental intracrystalline plastic flow in hot-pressed synthetic quartzite prepared from brazilian quartz crystals. Journal of Structural Geology 26 (2), 259-270.

Rutter, E., Neumann, D., 1995. Experimental deformation of partially molten westerly granite under fluid-absent conditions, with implications for the extraction of granitic magmas. Journal of Geophysical Research-Solid Earth 100 (B8), 15697-15715.

Rybacki, E., Dresen, G., 2000. Dislocation and diffusion creep of synthetic anorthite aggregates. Journal of Geophysical Research-Solid Earth 105 (B11), 26017-26036.

Rybacki,E., Dresen, G.,2004. Deformation mechanism maps for feldspar rocks. Tectonophysics, 382(3-4):173–187.

Rybacki, E., Gottschalk, M., Wirth, R., Dresen, G., 2006. Influence of water fugacity and activation volume on the flow properties of fine-grained anorthite aggregates. Journal of Geophysical Research-Solid Earth 111 (B3).

Rybacki, E., Wirth, R., Dresen, G., 2008. High-strain creep of feldspar rocks: Implications for cavitation and ductile failure in the lower crust. Geophysical Research Letters 35 (4), L04304.

Sander, B., 1934. Petrofabrics (gefugekunde der gesteine) and orogenesis. American Journal of Science 28 (163), 37-50.

Schenk, O., Urai, J., Evans, B., 2005. The effect of water on recrystallization behavior and grain boundary morphology in calcite-observations of natural marble mylonites. Journal of Structural Geology 27 (10), 1856-1872.

Schmalholz, S. M., Schmid, D. W., Fletcher, R. C., 2008. Evolution of pinch-and-swell structures in a power-law layer. Journal of Structural Geology 30 (5), 649-663.

Schmid, D., Podladchikov, Y., 2003. Analytical solutions for deformable elliptical inclusions in general shear. Geophysical Journal International 155 (1), 269-288.

Schmid, S., 1982. Microfabric studies as indicators of deformation mechanisms and flow laws operative in mountain building. Academic Press, London.

Schmid, S., 1994. Textures of geological materials. DGM, Informationsgesellschaft, pp. 279-301.

Schmid, S., Boland, J., Paterson, M., 1977. Superplastic flow in finegrained limestone. Tectonophysics 43 (3-4), 257-291.

Schmid, S., Casey, M., 1986. Complete fabric analysis of some commonly observed quartz c-axis patterns. Vol. 36 of Geophysical Monograph. American Geophysical Union, pp. 263-286.

Schmid, S., Rück, P., Schreurs, G., 1990. The significance of the Schams nappes for the reconstruction of the paleotectonic and orogenic evolution of the Pennine zone along the NFP 20 East traverse (Grisons, eastern Switzerland). Deep Structure of the Alps. Mém. Soc. Géol. France.

Schmid, S. M., Panozzo, R., Bauer, S., 1987. Simple shear experiments on calcite rocks - rheology and microfabric. Journal of Structural Geology 9 (5-6), 747-778.

Schmocker, M., 2002. Rheology and micro fabrics of quartz: Experimental deformation in torsion. Ph.D. thesis, ETH Zürich.

Schmocker, M., Bystricky, M., Kunze, K., Burlini, L., Stünitz, H., Burg, J., 2003. Granular flow and riedel band formation in water-rich quartz aggregates experimentally deformed in torsion. Journal of Geophysical Research-Solid Earth 108 (B5).

Segall, P., Pollard, D., 1983. Nucleation and growth of strike slip faults in granite. Journal of Geophysical Research 88 (NB1), 555-568.

Segall, P., Simpson, C., 1986. Nucleation of ductile shear zones on dilatant fractures. Geology 14 (1), 56-59.

Serratosa, J., Bradley, W., 1958. Determination of the orientation of oh bond axes in layer silicates by infrared absorption. Journal of Physical Chemistry 62 (10), 1164-1167.

Sheltono, G., Tulis, J., Tullis, T., 1981. Experimental high-temperature and high-pressure faults. Geophysical Research Letters 8 (1), 55-58.

Shimizu, I., 1998. Stress and temperature dependence of recrystallized grain size: A subgrain misorientation model. Geophysical Research Letters 25 (22), 4237-4240.

Shimizu, I., 2008. Theories and applicability of grain size piezometers: The role of dynamic recrystallization mechanisms. Journal Of Structural Geology 30 (7), 899-917.

Simpson, C., 1980. Oblique girdle orientation patterns of quartz c-axes from a shear zone in the basement core of the Maggia-Nappe-Ticino, Switzerland. Journal of Structural Geology 2 (1-2), 243-247.

Simpson, C., 1985. Deformation of granitic-rocks across the brittle ductile transition. Journal of Structural Geology 7 (5), 503-511.

Simpson, C., Schmid, S., 1983. An evaluation of criteria to deduce the sense of movement in sheared rocks. Geological Society of America Bulletin 94 (11), 1281-1288.

Simpson, C., Wintsch, R., 1989. Evidence for deformation-induced K-feldspar replacement by myrmekite. Journal of Metamorphic Geology 7 (2), 261-275.

Skemer, P., Katayama, B., Jiang, Z., Karato, S., 2005. The misorientation index: Development of a new method for calculating the strength of lattice-preferred orientation. Tectonophysics 411 (1-4), 157-167.

Song, W. J., Ree, J. H., 2007. Effect of mica on the grain size of dynamically recrystallized quartz in a quartz-muscovite mylonite. Journal of Structural Geology 29 (12), 1872-1881.

Stallard, A., Shelley, D., 1995. Quartz c-axes parallel to stretching directions in very low-grade metamorphic rocks. Tectonophysics 249 (1-2), 31-40.

Stipp, M., Stünitz, H., Heilbronner, R., Schmid, S., 2002. The eastern tonale fault zone: a 'natural laboratory' for crystal plastic deformation of quartz over a temperature range from 250 to 700 degrees C. Journal of Structural Geology 24 (12), 1861-1884.

Stipp, M., Tullis, J., 2003. The recrystallized grain size piezometer for quartz. Geophysical Research Letters 30 (21).

Stipp, M., Tullis, J., Behrens, H., 2006. Effect of water on the dislocation creep microstructure and flow stress of quartz and implications for the recrystallized grain size piezometer. Journal of Geophysical Research-Solid Earth 111 (B4).

Stolper, E., 1982. Water in silicate-glasses - an infrared spectroscopic study. Contributions To Mineralogy and Petrology 81 (1), 1-17.

Stünitz, H., 1991. Folding and shear deformation in quartzites, inferred from crystallographic preferred orientation and shape fabrics. Journal of Structural Geology 13 (1), 71-86.

Stünitz, H., Fitz Gerald, J., 1993. Deformation of granitoids at low metamorphic grade .2. granular flow in albite-rich mylonites. Tectonophysics 221 (3-4), 299-324.

Sundberg, M., Cooper, R. F., 2008. Crystallographic preferred orientation produced by diffusional creep of harzburgite: Effects of chemical interactions among phases during plastic flow. Journal of Geophysical Research-Solid Earth 113 (B12), B12208.

Takeda, Y.-T., Griera, A., 2006. Rheological and kinematical responses to flow of two-phase rocks. Tectonophysics 427 (1-4), 95-113.

Takeshita, T., 1996. Estimate of physical conditions for deformation based on c-axis transitions in naturally deformed quartzite. Journal of the Geological Society of Japan 102 (3), 211-222.

Takeshita, T., Hara, I., 1998. C-axis fabrics and microstructures in a recrystallized quartz vein deformed under fluid-rich greenschist conditions. Journal of Structural Geology 20 (4), 417-431.

Tapponnier, P., Molnar, P., 1977. Active faulting and tectonics in China. Journal of Geophysical Research 82 (20), 2905-&.

Trepied, L., Doukhan, J., Paquet, J., 1980. Subgrain boundaries in quartz - theoretical-analysis and microscopic observations. Physics and Chemistry of Minerals 5 (3), 201-218.

Trimby, P., Prior, D., Wheeler, J., 1998. Grain boundary hierarchy development in a quartz mylonite. Journal of Structural Geology 20 (7), 917-935.

Tsurumi, J., Hosonuma, H., Kanagawa, K., 2003. Strain localization due to a positive feedback of deformation and myrmekite-forming reaction in granite and aplite mylonites along the Hatagawa shear zone of NE Japan. Journal of Structural Geology 25 (4), 557-574.

Tullis, J., 1977. Preferred orientation of quartz produced by slip during plane strain. Tectonophysics 39 (1-3), 87-102.

Tullis, J., 1983. Deformation of feldspars. Min. Soc. Amer., Reviews in Mineralogy - Feldspar Mineralogy, pp. 297-323.

Tullis, J., Christie, J., Griggs, D., 1973. Microstructures and preferred orientations of experimentally deformed quartzites. Geological Society of America Bulletin 84 (1), 297-314.

Tullis, J., DellAngelo, L., Yund, R., 1990. Ductile shear zones from brittle precursors in feldspathic rocks: the role of dynamic recrystallization. No. 56. AGU Geophys.Monogr., pp. 67-81.

Tullis, J., Yund, R., 1977a. Deformation-behavior of quartz and feldspar in experimentally deformed granite. In: Transactions-American Geophysical Union. Vol. 58. Amer. Geophys. Union, pp. 513-513.

Tullis, J., Yund, R., 1977b. Experimental deformation of dry westerly granite. Journal of Geophysical Research 82 (36), 5705-5718.

Tullis, J., Yund, R., 1982. Grain-growth kinetics of quartz and calcite aggregates. Journal of Geology 90 (3), 301-318.

Tullis, J., Yund, R., 1985. Dynamic recrystallization of feldspar - a mechanism for ductile shear zone formation. Geology 13 (4), 238-241.

Tullis, T., Horowitz, F., Tullis, J., 1991. Flow laws of polyphase aggregates from end-member flow laws. Journal of Geophysical Research-Solid Earth 96 (B5), 8081-8096.

Tullis, J., Yund, R., 1991. Diffusion creep in feldspar aggregates - experimental-evidence. Journal of Structural Geology, 13(9):987–1000.

Turner, F., 1962. Rotation of crystal lattice in kink bands, deformation bands, and twin lamellae of strained crystals. Proceedings of the National Academy of Sciences of the United States of America 48 (6), 955.

Twiss, R., 1977. Theory and applicability of a recrystallized grain-size paleopiezometer. Pure and Applied Geophysics 115 (1-2), 227-244.

Urai, J., Spiers, C., Zwart, H., Lister, G., 1986. Weakening of rock salt by water during long-term creep. Nature 324 (6097), 554-557.

Vandermolen, I., Paterson, M., 1979. Experimental deformation of partially-melted granite. Contributions To Mineralogy and Petrology 70 (3), 299-318.

vanRoermund, H., Lister, G., Williams, P., 1979. Progressive development of quartz fabrics in a shear zone from monte-mucrone, sesia-lanzo-zone, italian alps. Journal of Structural Geology 1 (1), 43-52.

Venables, J., Harland, C., 1973. Electron backscattering patterns - new technique for obtaining crystallographic information in scanning electron-microscope. Philosophical Magazine 27 (5), 1193-1200.

Vernon, R., Flood, R., 1988. Contrasting deformation of s-type and i-type granitoids in the Lachlan fold belt, eastern Australia. Tectonophysics 147 (1-2), 127-143.

Vernon, R., Williams, V., Darcy, W., 1983. Grain-size reduction and foliation development in a deformed granitoid batholith. Tectonophysics 92 (1-3), 123-145.

Wang, Z., Dresen, G., Wirth, R., 1996. Diffusion creep of fine-grained polycrystalline anorthite at high temperature. Geophysical Research Letters 23 (22), 3111-3114.

Wayte, G., Worden, R., Rubie, D., Droop, G., 1989. A tem study of disequilibrium plagioclase breakdown at high-pressure - the role of infiltrating fluid. Contributions To Mineralogy and Petrology 101 (4), 426-437.

Weertman, J., Weertmann, J., 1975. High-temperature creep of rock and mantle viscosity. Annual Review of Earth and Planetary Sciences 3, 293-315.

Wellman, H., 1984. The alpine fault, new-zealand, near milford sound and to the southwest. Geological Magazine 121 (5), 437-441.

Wenk, H., Canova, G., Molinari, A., Kocks, U., 1989. Viscoplastic modeling of texture development in quartzite. Journal of Geophysical Research-Solid Earth and Planets 94 (B12), 17895-17906.

Wheeler, J., 1992. Importance of pressure solution and coble creep in the deformation of polymineralic rocks. Journal of Geophysical Research-Solid Earth 97 (B4), 4579-4586.

Wheeler, J., 2009. The preservation of seismic anisotropy in the earth's mantle during diffusion creep. Geophysical Journal International 178 (3), 1723-1732.

Wheeler, J., Prior, D., Jiang, Z., Spiess, R., Trimby, P., 2001. The petrological significance of misorientations between grains. Contributions To Mineralogy and Petrology 141 (1), 109-124.

White, S., 1973. Syntectonic recrystallization and texture development in quartz. Nature 244 (5414), 276-278.

White, S., 1976. The role of dislocation processes during tectonic deformation with special reference to quartz. Vol. The Physics and Chemistry of minerals and rocks. Wiley, london, pp. 75-91.

Wintsch, R., Yi, K., 2002. Dissolution and replacement creep: a significant deformation mechanism in mid-crustal rocks. Journal of Structural Geology 24 (6-7), 1179-1193.

Xiao, X., Wirth, R., Dresen, G., 2002. Diffusion creep of anorthite-quartz aggregates. Journal of Geophysical Research-Solid Earth 107 (B11).

Zelin, M., Krasilnikov, N., Valiev, R., Grabski, M., Yang, H., Mukherjee, A., 1994. On the microstructural aspects of the nonhomogeneity of superplastic deformation at the level of grain groups. Acta Metallurgica Et Materialia 42 (1), 119-126.

Zhang, Y., Hobbs, B., Jessell, M., 1994. The effect of grain-boundary sliding on fabric development in polycrystalline aggregates. Journal of Structural Geology 16 (9), 1315-1325.

Zhang, Y., Jessell, M. W., Hobbs, B. E., 1996. Experimental and numerical studies of the accommodation of strain incompatibility on the grain scale. Journal of Structural Geology 18 (4), 451-460.

Zhao, Y., ZhongYan, W., Kohlstedt, D. I., 2009. Grain boundary sliding in compressed olivine aggregates. Acta Petrologica Sinica 25 (3), 708-712.

Appendix

Appendix A: Sample localities

Sample localities for the Truzzo granite and the Gran Paradiso granodiorite. Sample numbers, locations, orientations of shear zones (shz) or foliations S_x(blank), lineations L_x and type of lineation (bt=biotite, wm =white mica, ma=mineral aggregate)

Name	**E**	**N**	**Sx**			**Lx**			**Description**
			dip dir	**dip**	**type**	**trend**	**plunge**	**type**	
Truzzo granite (CH1903)									
TR1	748888	133092	357	49	shz	270	17	bt	incipient shear zone. mag.fab. und mag.lin? , (shz. L measured from sample)
TR2	748897	133049	85	35	shz	102	21	wm	shear zone, magfab ~ENE/WSW/ host rock Lin (118/11) Lm 76/20, plane
TR3	748894	133050	54	44	shz	116	25	bt	anastom. mm-scale shear zone
TR3a	748894	133050							mag. fab ~ENE/WSW steil
TR4	748894	133046	64	43		125	22		def. granite
TR5	748911	133007	42	62	shz				anastom shz, SC , mag. fab. E/W
TR6	748912	133011	46	42	shz				shz core of 8 cm wide (ultra)mylonite, next to D.Marquer cores ?
TR7	748950	132924	29	60	shz				incip. shear zone, offset of mafic xenolith, mag. fab. 280/steep, same shear zone as TR8
TR8	748950	132925	29	60	shz				thin diskrete shear zone with local SC, same shear zone as TR7, mag. fab.
TR9	748918	132952	91	20		107	16		strongly def. granite outside low stran domain, D2(?) , crenulated Sm, anastom. mm-scale shear zone
TR10	748917	132948	36	66		75	28	bt	weakly def. granite, adjacent to TR9
TR12	748944	132923	31	46	shz	90	35		shear zone core (ultra)mylonite, strong mag. fab.
TR13	749252	132553	357	60		78	9	wm	strongly def. granite outside low strain domin, large fold, bridge
TR14	749252	132553	18	48		88	10	bt	-""-'
TR15	749247	132541	10	50		94	21	wm	-""-', S of TR13
TR16	749266	132556	358	41					-""-', E of TR13
BTR1	746426	135238	258	13		87	10	wm	weakly def granite, parallel layering, weak SC (top E)
BTR2/3	747420	134461							int. def. granite, qrz-fsp layering and large fsp. clasts, large wm/bt

Name	**E**	**N**	**Sx**			**Lx**			**Description**
			dip dir	**dip**	**type**	**trend**	**plunge**	**type**	
Gran Paradiso /Lago Teleccio/ Val Soana (UTM, Rome40)									
GP2	32T 0371831	5037022							unoriented, mylonitic granodiorite
GP3	32T 0371554	5037041	166	28	shz	126	25		shearzone in weakl. def. granodiorite
GP4	32T 0371554	5037041	158	33	shz	84	21	bt	def. granodiorite (3 samples), thick ulltramylonite, strongly foliated granite, 2nd shearzone
GP5	Road N of Locana		88	36	shz	91	15	ma	shearzone with strain marker (48 cm/ 5.5 cm)
GP6	Parking at Lago Telecci		350	19	shz	255	2	bt	slightly foliated granodiorite, sets of small small shear zones
GP7	Parking at Lago Telecci		345	25	shz	72	2		slightly foliated granodiorite, sets of int. shearzones
GP8	32T 0373284	5039425	64	18		98	8		mylonitic granodiorite, with transposed qtz-fsp veins
GP9	32T 0372881	5038395			shz			ma	foliated granodiorite, mylonitic shear zone, unor.
GP10	32T 0372881	5038395							shear zone in coarse grained, undef. granodiorite, unor.
GP11	32T 0371389	5037047	136	21	shz	132	16	bt	weakly def. granodiorite to mylonitic granodiorite, shear zone w. strain markers (42cm/1cm)
GP12	32T 0371389	5037047	110	19	shz	114	18		anastom shearzones ub weakly def. granodioriti
GP13	32T 0371382	5037194							mylonitic granodioraite with mylonitic aplite (2x)
GP14	32T 0371382	5037194	136	25	shz	143	23	wm	aplitic dike sandwiched between shear zones
GP15	32T 0371382	5037194						bt	weakly def. granodiorite
GP16	32T 0371382	5037194							SC granodiorite, sandwiched between shear zones
GP17	32T 0371382	5037194						ma	weakly def. granodiorite, grading to mylonitic granodiorite
GP18	32T 0371589	5037047	222	32	shz	20	9		shear zones in granodiorite
GP18			180	15	Sm				
GP19	32T 0371589	5037047	130	30	shz	73	20		shear zone in weakly def. granodiorite, thin core
GP20									shear zone in granodiorite, unor. sample
GP21	ValSoera, western side of the lake								L-Type granite

Appendix B: Maxima of Random Polefigures

a.

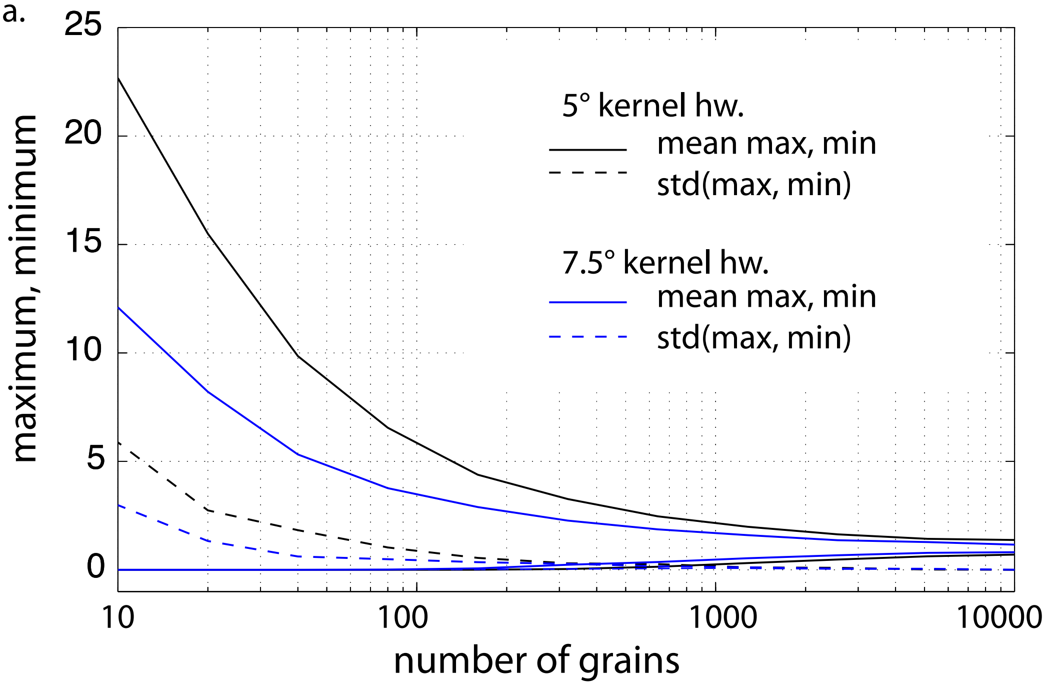

b.

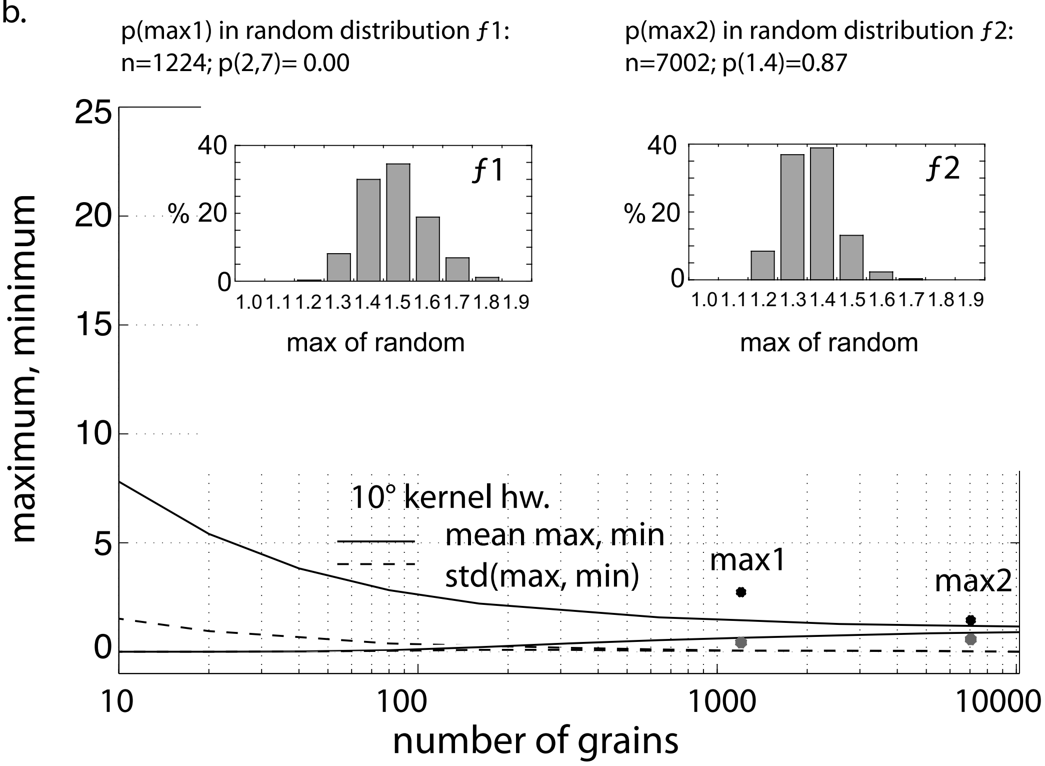

Test for maxima of polefigures against randomness:

Values of the distribution of maxima and minima of random [c]-axis polefigures are a function of the number of individual, independent measurements (number of grains). Random points are selected out of an uniform orientation density function (ODF), and a new ODF' is calculated with the specified kernel width. Pole density functions (PDF) are calculated from ODF' and values of maxima and minima determined. The curves are based on 100 random polefigures. The ODFs and PDFs are calculated with the Mtex toolbox (Hielscher & Schäben, 2008)

(a) Mean and standard deviation of distributions of maxima and minima of [c]-axis polefigures as a function of the number grains (independent measurements). Black curve is for 5° kernel halfwidth (comparable to CIP). Blue curve for 7.5° kernel halfwidth. (b) Histograms of the distributions of maxima for random [c]-axis polefigures at 1224 grains ($f1$) and 7002 grains ($f2$). 260 random polefigures were simulated. The measured maxima (max1 = 2.7 at 1224 grains and max2 = 1.4 at 7002 grains) of real polefigures are taken from Figure 14, Chapter 2. Maxima and minima are indicated as black and grey points in the lower plot, respectively, together with curves of the mean values of the random distributions of [c]-axis polefigure maxima and minima as a function of the number grains for a 10° kernel halfwidth.

The probability p(max) is determined with a modified z-test for a screwed distribution. The probabilities that the measured values max1 and max2 are elements of the distributions $f1$ and $f2$, respectively, are 0.00 and 0.87.

Appendix C: Supplemental data GP11

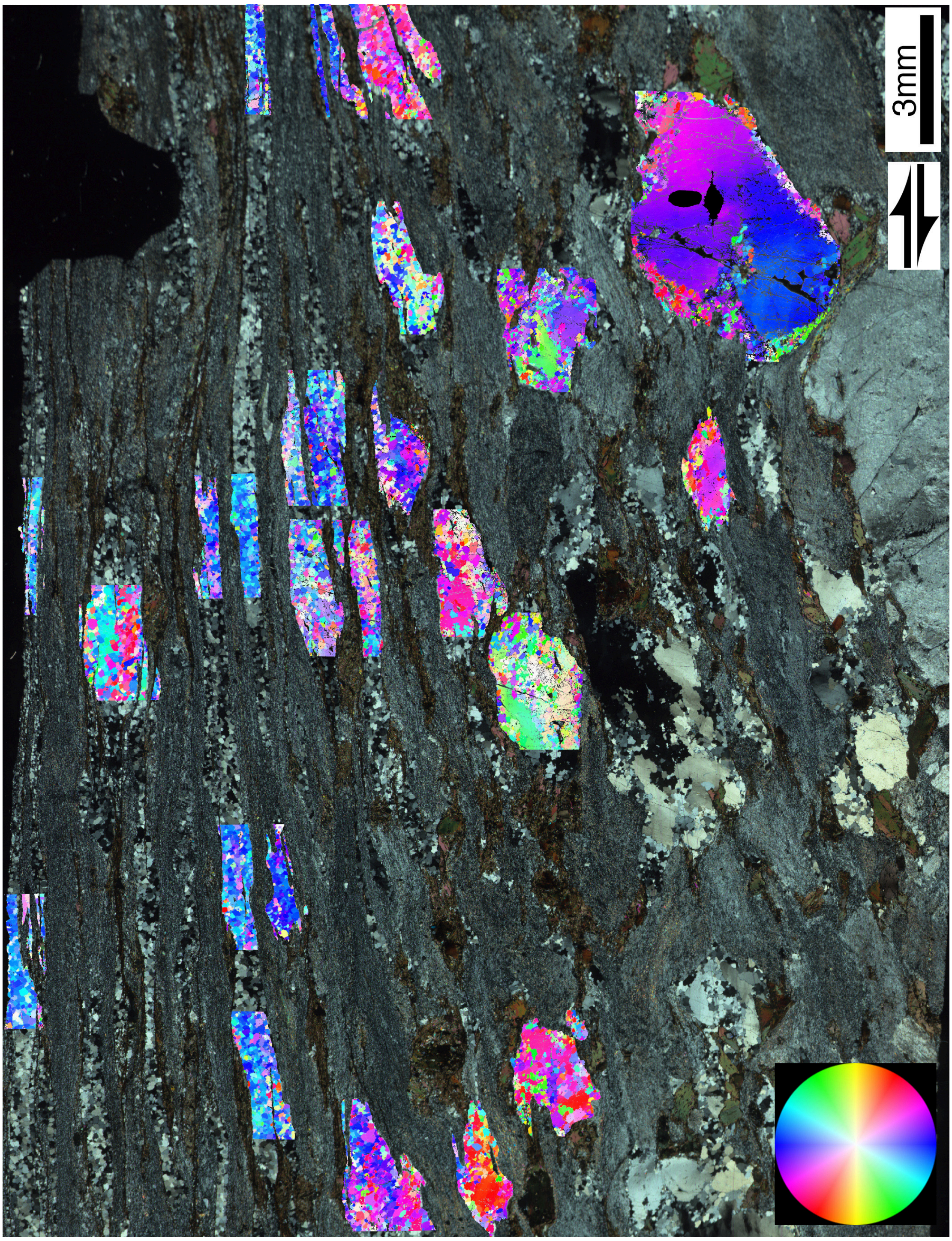

CIP derived [c]-axis orientation image of quartz aggregates in GP11. Parent grains are included. See Chapter 3, Figure 8 for the corresponding sites and polefigures of the recrystallized grains.

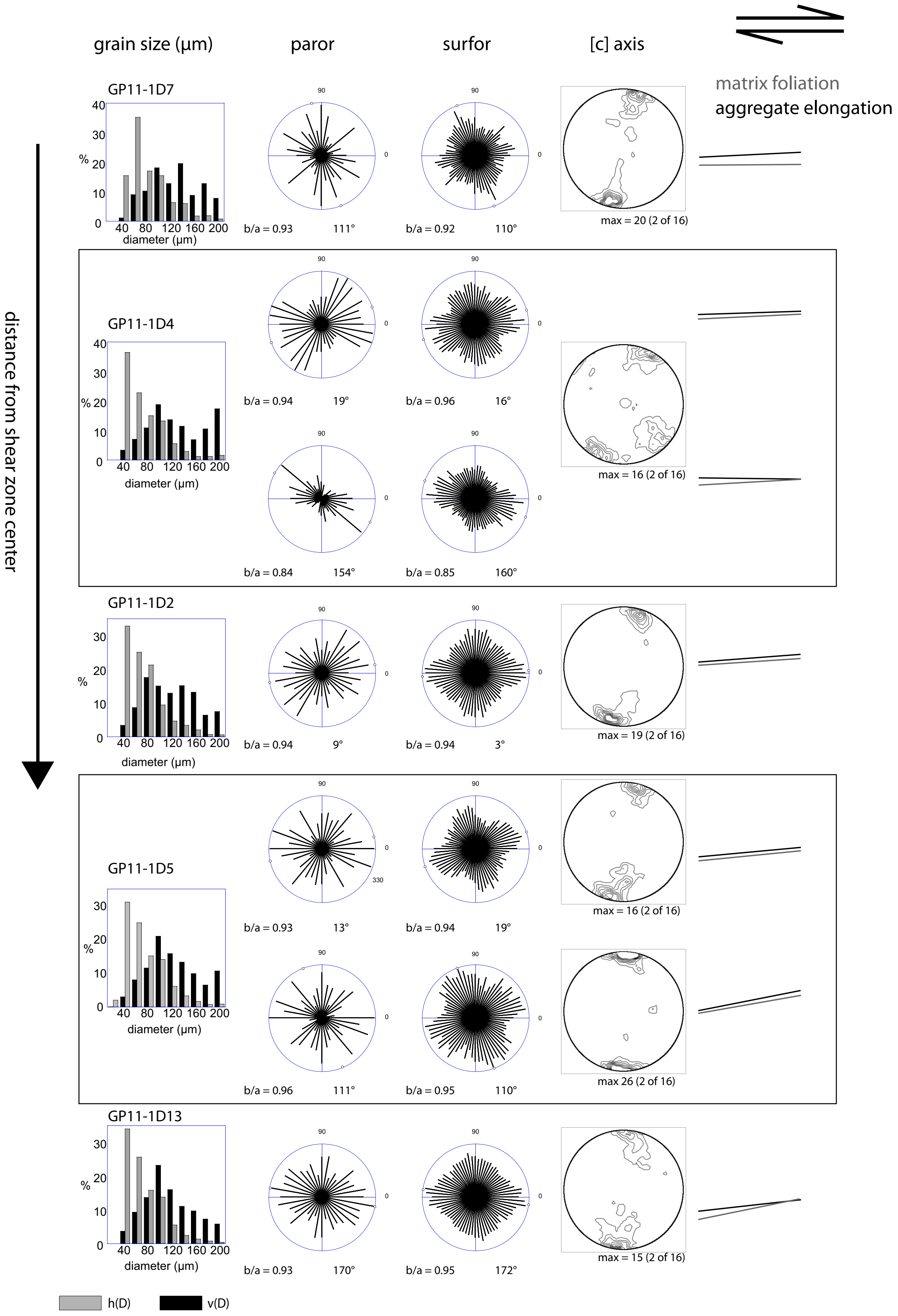
grain size (μm)
paror
surfor
[c] axis
matrix foliation
aggregate elongation
distance from shear zone center
GP11-1D7
b/a = 0.93
111°
b/a = 0.92
110°
max = 20 (2 of 16)
GP11-1D4
b/a = 0.94
19°
b/a = 0.96
16°
max = 16 (2 of 16)
b/a = 0.84
154°
b/a = 0.85
160°
GP11-1D2
b/a = 0.94
9°
b/a = 0.94
3°
max = 19 (2 of 16)
GP11-1D5
b/a = 0.93
13°
b/a = 0.94
19°
max = 16 (2 of 16)
b/a = 0.96
111°
b/a = 0.95
110°
max 26 (2 of 16)
GP11-1D13
b/a = 0.93
170°
b/a = 0.95
172°
max = 15 (2 of 16)
%
diameter (μm)
40
80
120
160
200
0
10
20
30
40
90
0
330
h(D)
v(D)

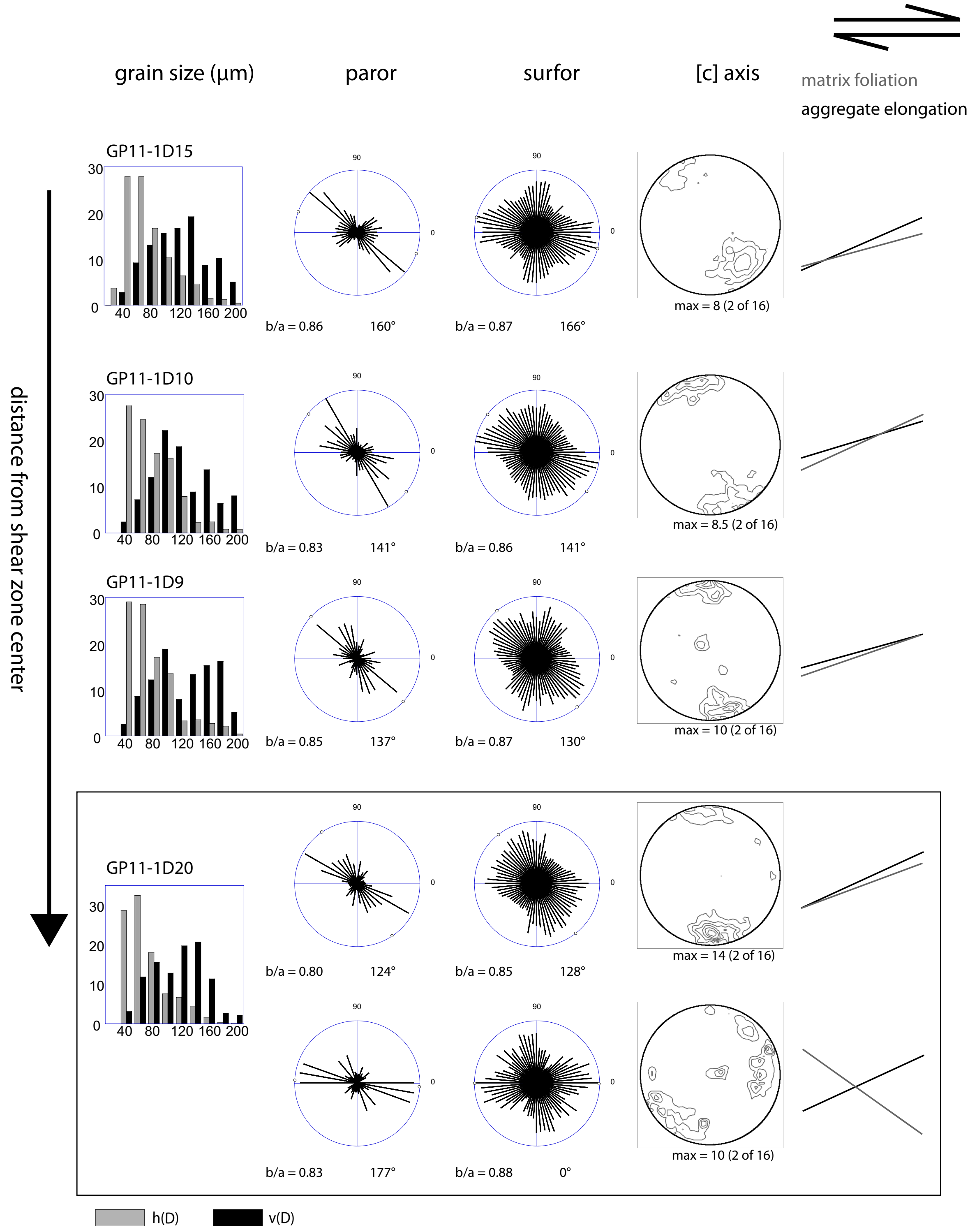

Grain size histograms, PAROR and SURFOR rose diagrams and [c]-axis polefigures of selected sites of GP11, ordered with a decreasing distance from the shear zone center (distance not to scale). See Chapter 3, Figure 8 for details. Grain sizes are given as diameters of μ_h(D) and μ_v(D). b/a_{bulk} and orientation of the maximum of the projection functions indicated with each rose diagram.

Appendix D: Supplemental data GP9

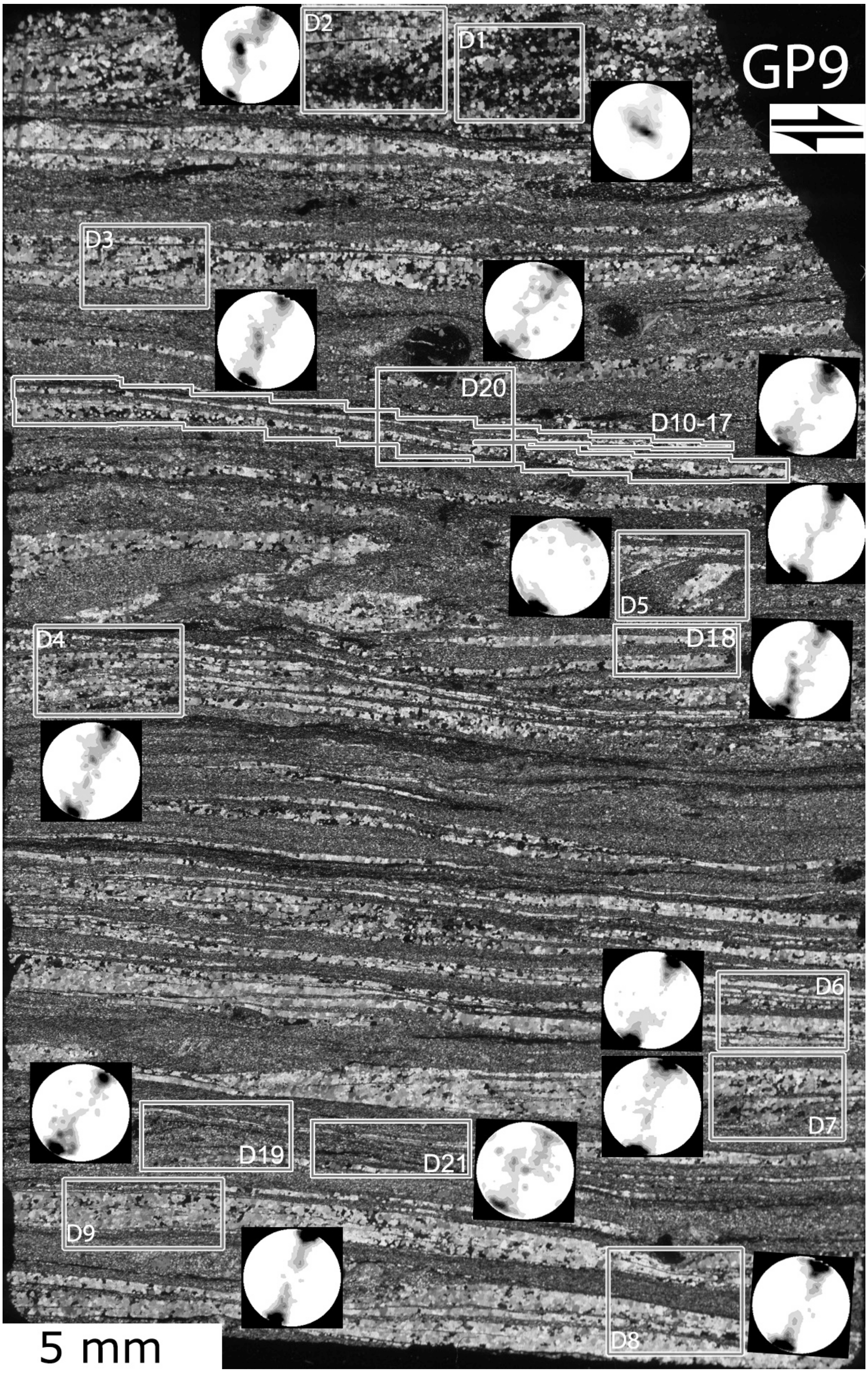

CIP derived [c]-axis polefigures of fully recrystallized, sub-parallel quartz layers in GP9. See Chapter 3, Figure 13, 16, 17 for details of the microstructure and orientation images.

Appendix E: FTIR calibration coefficients

Author	integral molar absorption coefficient ϵ ($L\ cm^{-2}\ mol^{-1}\ H_2O$)	calibration factor f ($cm^2\ H/10^6Si$)	comment
Quartz Stipp et al., 2006	24100 ± 1800	1.881	broad band bulk absorption
Quartz Libowitzky & Rossmann, 1997	~ 30800* 246.6(3753-v)	1.473*	* as apparently used by Stipp et al., 2006
Quartz Paterson, 1982	~33000 - 45000* γ150(3780-v)** 78000	1.375-1.008*	* as apparently used by Stipp et al., 2006 **$cm^{-2}\ mol^{-1}$ H/l
Quartz Katz, 1962	56200***	0.812***	***as used by Kronenberg & Wolf, 1990; Post & Tullis, 1998; Gleason & DeSisto, 2008
Feldspar Johnson & Rossman (2003)	107000	0.51	assuming per $AlSi_3$ for molar ppm

Kronenberg & Wolf (1990) give a calibration factor derived from Katz (1962) in cm^2 mol to derive a concentration by multiplication with the integral absorption. Gleason & DeSisto (2008) use this coefficient but provide $cm^{-2}\ mol^{-1}$ as units.

* Values for the integral molar absorption coefficient and the calibration factor are derived from the concentrations provided in Stipp et al. (2006)

The relation of the calibration factor f with the integral molar absorption coefficient ϵ is $f = 6670 * M_{H2O} * \epsilon^{-1} * \varrho^{-1}$ with the density ϱ of quartz or feldspar in g cm^{-3} and the molecular weight of H_2O M_{H2O} in g mol^{-1}.

** The integral molar absorption coefficient derived from Paterson (1982) would be for the integral absorption from 3780cm^{-1} to wavenumber v times an orientation factor γ=⅓ (for unpolarized beam assuming an isotropic broad band). Note that it is provided per mol H/l and not H2O. For a broad band from 3000 to 3780 cm^{-1} ϵ = 78000 L cm^{-2} mol^{-1} H, and respectively smaller for a narrower absorption band. As the absorption coefficient is a function of the wavelength, water content derived from other calibrations can only be compared if the complete spectra are available.

Appendix F: FTIR white mica

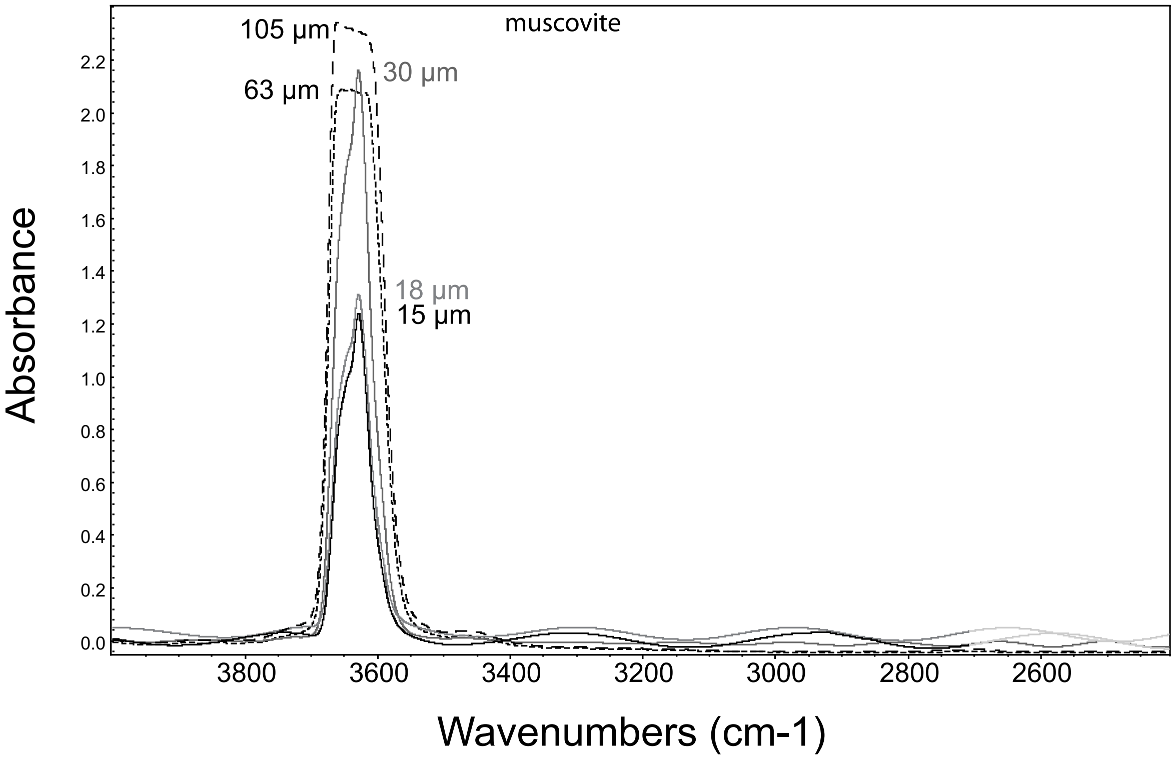

Spectra of muscovite sheets perpendicular [001] with variable thickness have been measured (Methuen muscovite: Mares & Kronenberg, 1993) in order to determine the white mica content inside quartz grains. Sheets with 105 and 63 μm thickness show a peak saturation and sheets of 30, 18,15 μm thickness were the thinnest obtained by manual cleaving. An integral molar absobance coefficient of about 7000 cm-2 has been derived from the integral absorbance of the 3629 cm-1 peak. 15, 18 and 30 μm thick sheets were used for the calculation of the integral molar absorbance coefficient.

Appendix G: White mica compositions

Cations:	1	2	3	4
Si	5.93	6.38	6.48	6.41
Al(IV)	2.07	1.62	1.52	1.59
Al(VI)	3.82	3.42	3.46	3.62
Fe	0.27	0.28	0.26	0.20
Mg	0.01	0.24	0.24	0.22
Ti	0.01	0.08	0.08	0.04
K	1.75	1.90	1.74	1.72
Na	0.27	0.08	0.08	0.05

White mica compositions: cations pfu

1: Methuen muscovite (Mares & Kronenberg, 1993)

2: mylonitc Truzzo granite (Marquer et al., 1994)

3: Truzzo granite (Marquer et al., 1994)

4: Truzzo granite: this study

Appendix H: FTIR CH-peak

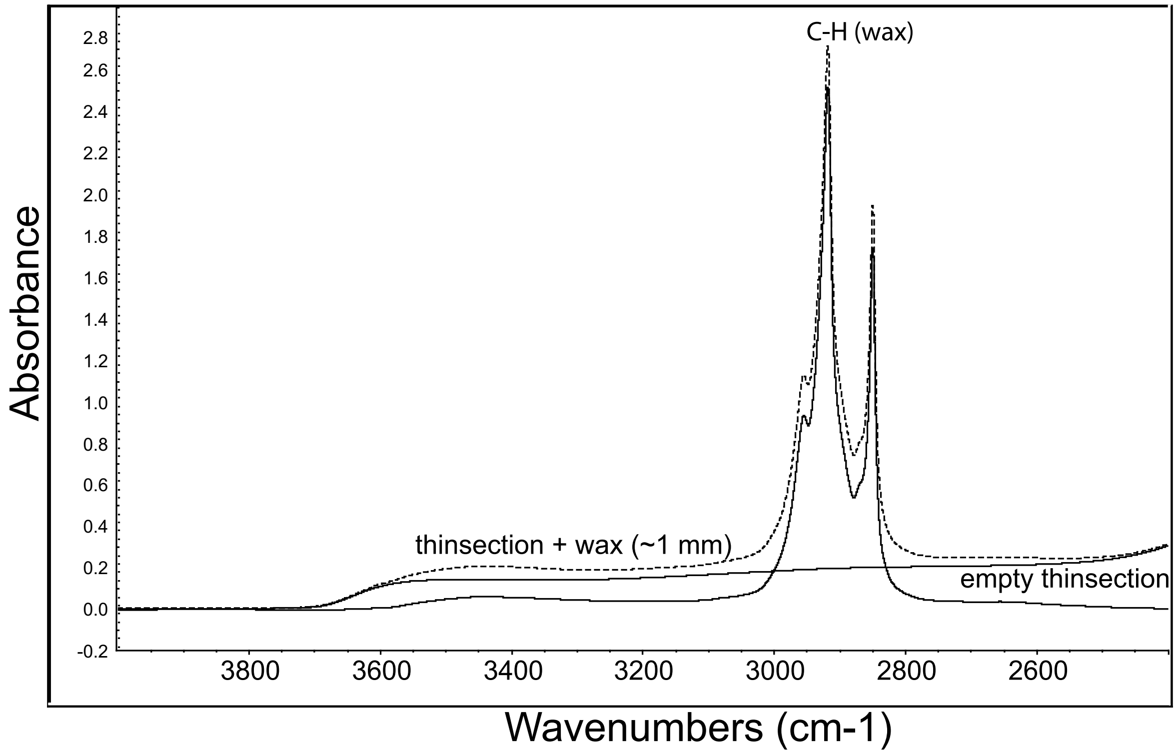

C-H peaks in FTIR spectra are usually related to epoxy or some kind of binder which are known to contain variable amounts of water, usually rendering those spectra unusable for the quantitative determination of water.

For the preparation of the FTRI thick sections Deiberit 502 dental wax was used. FTIR spectra for a thin section including ~1 mm of Deiberit 502 dental wax, used for preparation and for an empty glass slide, and the subtracted spectrum of the pure wax. The wax shows basically no absorbance peaks between 3000 and 3800 cm-1. Therefore spectra with C-H peaks can be used nonetheless for the water quantification.

Appendix I: FTIR data of the Truzzo granite

Site	thickness (cm)	wm. int. absorbance (cm^{-2})	int.absorbance 3000-3800 (cm^{-2})*	H/ Si*1e6 (Stipp et al, 2006)	H/ Si*1e6 (Katz, 1962)	H/ Si*1e6(Paterson, 1982)	wt % muscovite	comment
Tr3-1n_1	0.0190	0.00	6.71	665	287	205	0.00	crack
Tr3-1n_10	0.0190	0.13	0.41	41	18	13	0.01	
Tr3-1n_11	0.0190	0.00	0.46	46	20	14	0.00	
Tr3-1n_12	0.0190	0.00	2.10	208	90	64	0.00	
Tr3-1n_2	0.0185	0.49	1.25	127	55	39	0.06	
Tr3-1n_3	0.0190	0.18	1.98	196	85	61	0.02	gb
Tr3-1n_4	0.0195	0.23	2.38	230	99	71	0.03	broad
Tr3-1n_5	0.0190	0.27	2.49	247	107	76	0.03	
Tr3-1n_6	0.0195	0.13	0.10	10	4	3	0.01	
Tr3-1n_7	0.0195	0.17	0.58	56	24	17	0.02	
Tr3-1n_8	0.0180	0.00	3.84	401	173	124	0.00	incl.
Tr3-1n_9	0.0180	0.00	0.51	53	23	16	0.00	
Tr3-1n_T2	0.0195	0.31	0.56	54	23	17	0.03	dried,gbs
Tr3-1n_T3	0.0180	0.50	4.16	434	187	134	0.06	ht,cracks
Tr3-3_1	0.0130	0.73	0.33	48	21	15	0.12	
Tr3-3_10	0.0140	0.96	2.29	308	133	95	0.15	
Tr3-3_11	0.0135	0.95	2.55	355	153	110	0.15	
Tr3-3_11_2nd	0.0135	0.65	0.47	65	28	20	0.10	
Tr3-3_12	0.0120	0.00	1.12	176	76	54	0.00	gbs
Tr3-3_16	0.0140	0.20	0.64	86	37	27	0.03	
Tr3-3_17	0.0140	0.09	0.39	53	23	16	0.01	
Tr3-3_18	0.0140	0.00	6.81	915	395	283	0.00	incl
Tr3-3_18_2nd	0.0140	0.00	5.52	742	320	229	0.00	incl
Tr3-3_18_3rd	0.0140	0.00	7.63	1026	443	317	0.00	incl.
Tr3-3_19	0.0135	0.00	3.28	457	197	141	0.00	incl.
Tr3-3_2	0.0130	0.00	1.37	198	85	61	0.00	
Tr3-3_20	0.0165	0.47	1.36	155	67	48	0.06	crack,gb
Tr3-3_25	0.0135	0.89	2.05	286	123	88	0.14	incl.
Tr3-3_26	0.0135	0.54	1.02	142	61	44	0.09	

Site	thickness (cm)	wm. int. absorbance (cm^{-2})	int.absorbance 3000-3800 (cm^{-2})*	H/Si*1e6 (Stipp et al, 2006)	H/Si*1e6 (Katz, 1962)	H/Si*1e6(Paterson, 1982)	wt % muscovite	comment
Tr3-3_29	0.0130	0.00	0.61	88	38	27	0.00	
Tr3-3_3	0.0130	0.11	0.27	39	17	12	0.02	sgr
Tr3-3_31	0.0150	0.32	0.75	95	41	29	0.05	gb
Tr3-3_32	0.0135	0.00	0.63	88	38	27	0.00	
Tr3-3_33	0.0140	0.81	0.02	3	1	1	0.12	
Tr3-3_34	0.0145	0.44	0.60	78	34	24	0.07	
Tr3-3_4	0.0130	0.00	0.44	64	27	20	0.00	
Tr3-3_5	0.0130	0.33	0.20	28	12	9	0.05	
Tr3-3_6	0.0130	0.11	0.22	31	13	10	0.02	
Tr3-3_7	0.0135	0.68	1.89	264	114	82	0.11	incl.
Tr3-3_8	0.0130	0.81	1.00	144	62	45	0.13	crack
Tr3-3_T2	0.0165	0.78	3.67	418	180	129	0.10	ht, gbs
Tr3-3_T3	0.0130	0.02	4.32	626	270	193	0.00	ht, incl., gb
Tr3-3_T4	0.0125	0.00	0.68	102	44	32	0.00	ht, cracks, gbs
Tr3-3_T5	0.0120	0.00	1.06	166	72	51	0.00	ht, gbs
Tr3-3_T6	0.0135	0.61	2.40	335	145	104	0.10	ht, incl.,gbs
Tr3-3_T7	0.0135	0.86	6.07	846	365	261	0.14	ht,incl.
Tr4-1a_10	0.0170	1.49	7.79	862	372	266	0.19	incl.
Tr4-1a_11	0.0170	0.00	7.00	775	334	239	0.00	crack
Tr4-1a_11_2nd	0.0170	0.00	2.18	241	104	75	0.00	
Tr4-1a_12	0.0170	0.08	1.35	150	65	46	0.01	
Tr4-1a_13-2nd	0.0175	0.71	1.62	174	75	54	0.09	
Tr4-1a_15_2nd	0.0170	0.00	0.75	83	36	26	0.00	
Tr4-1a_17	0.0170	0.00	2.91	322	139	100	0.00	gb
Tr4-1a_17-2nd	0.0170	0.00	0.70	77	33	24	0.00	
Tr4-1a_18	0.0170	0.00	7.26	804	347	248	0.00	incl.
Tr4-1a_19	0.0175	0.00	0.47	51	22	16	0.00	
Tr4-1a_1_2nd	0.0165	1.13	0.31	36	15	11	0.15	sgr
Tr4-1a_2	0.0165	0.00	52.30	5965	2574	1843	0.00	incl.
Tr4-1a_20	0.0175	0.00	4.13	444	192	137	0.00	

Site	thickness (cm)	wm. int. absorbance (cm^{-2})	int.absorbance 3000-3800 (cm^{-2})*	H/ Si*1e6 (Stipp et al, 2006)	H/ Si*1e6 (Katz, 1962)	H/ Si*1e6(Paterson, 1982)	wt % muscovite	comment
Tr4-1a_20_2nd	0.0175	0.00	2.94	316	136	98	0.00	
Tr4-1a_21_2nd	0.0175	0.00	0.47	51	22	16	0.00	
Tr4-1a_21_3rd	0.0175	0.00	3.09	332	143	103	0.00	incl.
Tr4-1a_22_2nd	0.0175	0.00	1.38	148	64	46	0.00	
Tr4-1a_23	0.0175	0.00	0.71	76	33	24	0.00	
Tr4-1a_24a	0.0180	1.38	10.75	1124	485	347	0.16	incl.
Tr4-1a_25	0.0180	1.58	4.09	428	185	132	0.19	
Tr4-1a_26	0.0180	1.32	14.28	1493	644	461	0.16	incl.
Tr4-1a_27	0.0180	0.00	12.20	1276	550	394	0.00	incl.
Tr4-1a_27_2nd	0.0180	0.00	0.58	61	26	19	0.00	
Tr4-1a_28	0.0175	0.00	9.59	1031	445	319	0.00	incl.
Tr4-1a_29_2nd	0.0170	0.00	0.50	55	24	17	0.00	
Tr4-1a_3	0.0165	0.88	1.10	125	54	39	0.11	sgr,incl.
Tr4-1a_30	0.0170	0.00	0.46	51	22	16	0.00	
Tr4-1a_31	0.0170	0.00	2.78	308	133	95	0.00	
Tr4-1a_32_2nd	0.0170	0.00	0.55	61	26	19	0.00	
Tr4-1a_33	0.0175	1.03	1.26	136	58	42	0.13	sgr,incl.
Tr4-1a_34	0.0170	0.00	1.71	189	82	58	0.00	
Tr4-1a_35_2nd	0.0170	1.25	0.83	92	40	28	0.16	gb
Tr4-1a_36_2nd	0.0170	0.00	2.54	281	121	87	0.00	
Tr4-1a_38	0.0175	0.00	0.49	53	23	16	0.00	
Tr4-1a_43	0.0170	0.00	0.92	102	44	32	0.00	
Tr4-1a_6	0.0175	1.49	2.06	222	96	68	0.18	
Tr4-1a_7	0.0170	1.55	1.23	136	59	42	0.20	
Tr4-1a_8	0.0170	1.00	2.77	307	132	95	0.13	
Tr4-1a_9	0.0170	1.69	1.68	186	80	57	0.21	

Site refers to the frame indicated in figure 8. “wm. int. absorbance” is the integral absorption of the white mica peak. “int absorbance” is the integral absorbance from the wavenumber 3000 to 3800 cm-1. The white integral absorbance of the white mica peak is subtracted.Comments: incl. = inclusion, gb(s) = grain boundary, sgr = grain is suspected to have formed by subgrain rotation, ht = heat treated for 24 hours at 120°C.

All FTIR spectra, normalized for the indicated section thickness:

Sample Tr3-1: all spectra

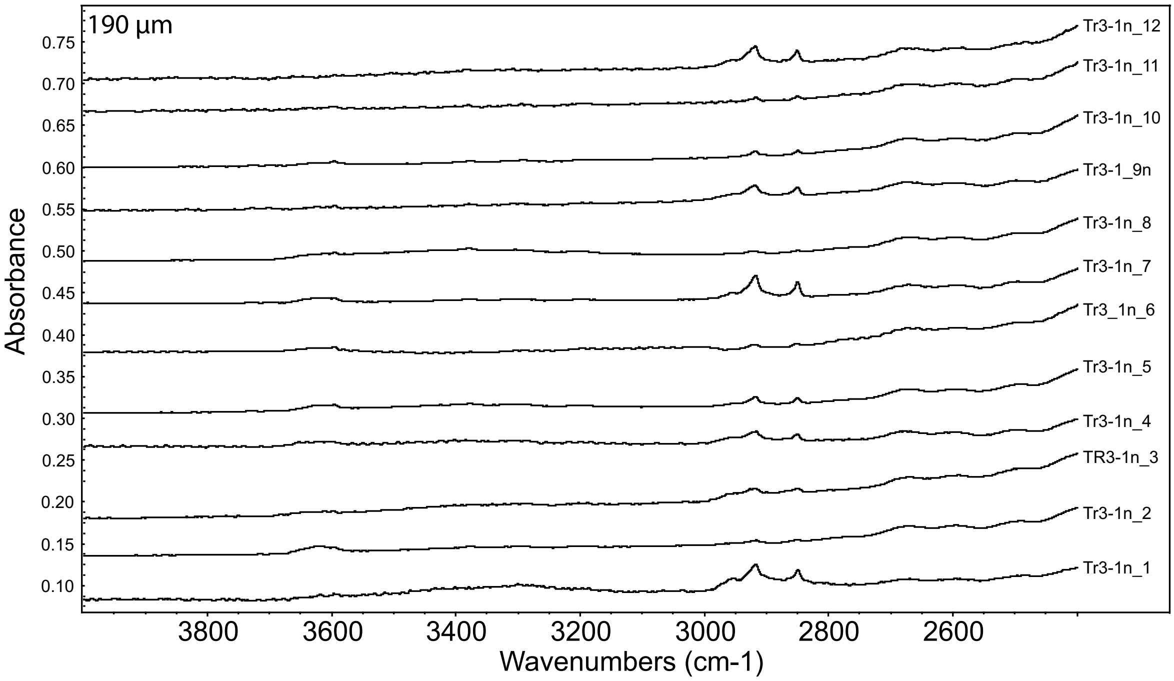

Sample Tr3-3: magmatic, unrecrystallized grains

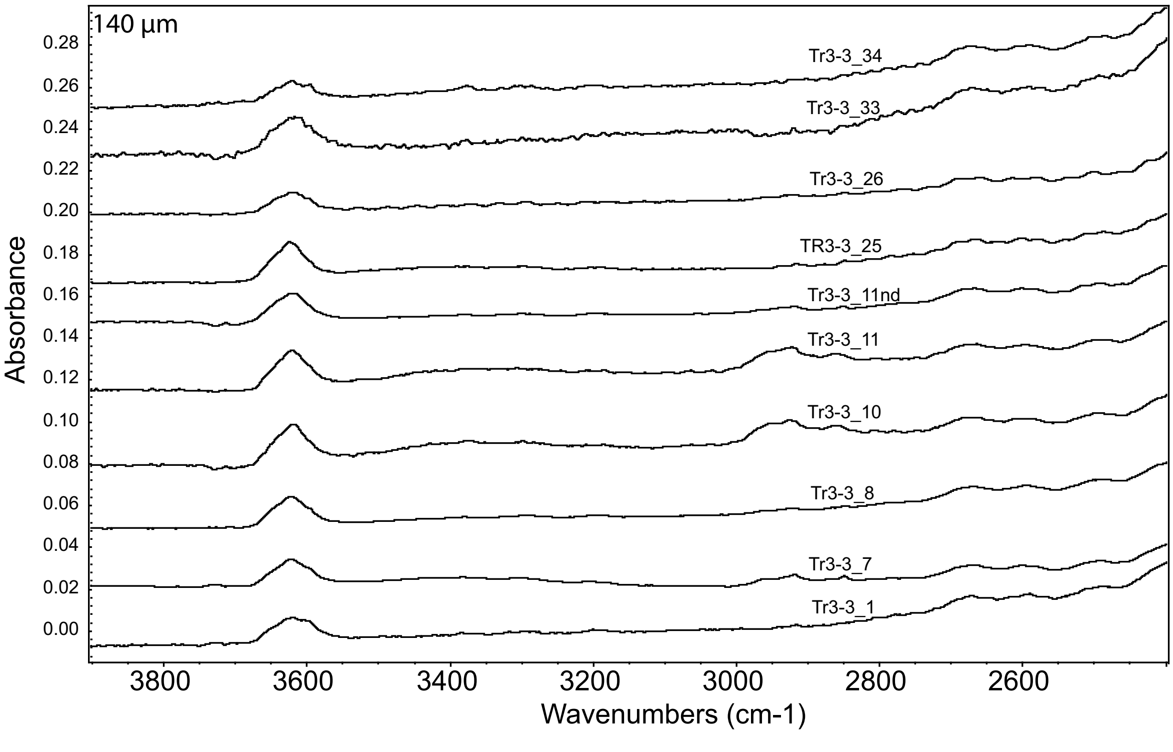

Sample Tr3-3: recrystallized grains

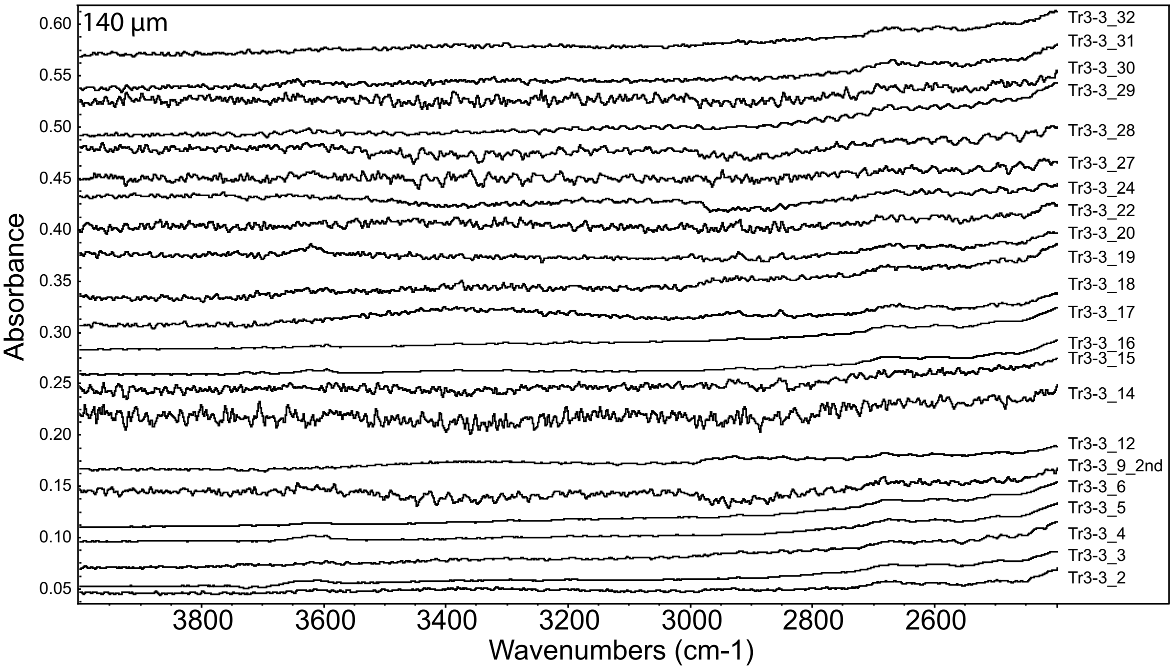

Sample Tr1-4a: magmatic, unrecrystallized grains

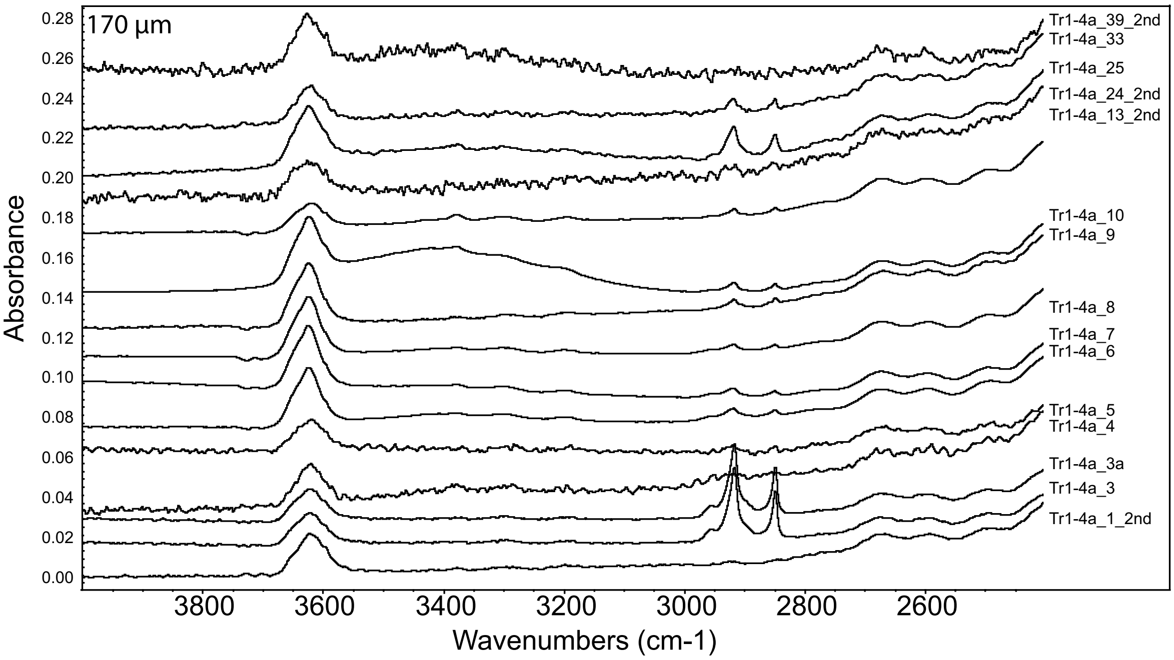

Sample Tr1-4a: recrystallized grains

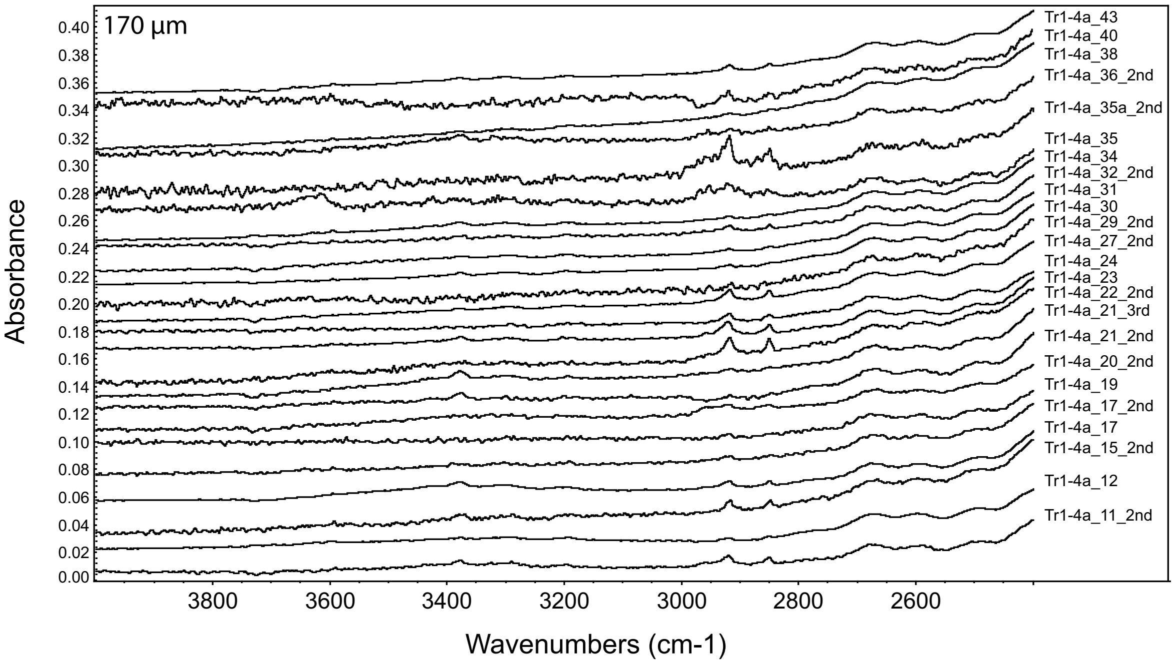

Samples Tr3-1, Tr3-3 heat treated 24h at 120°C

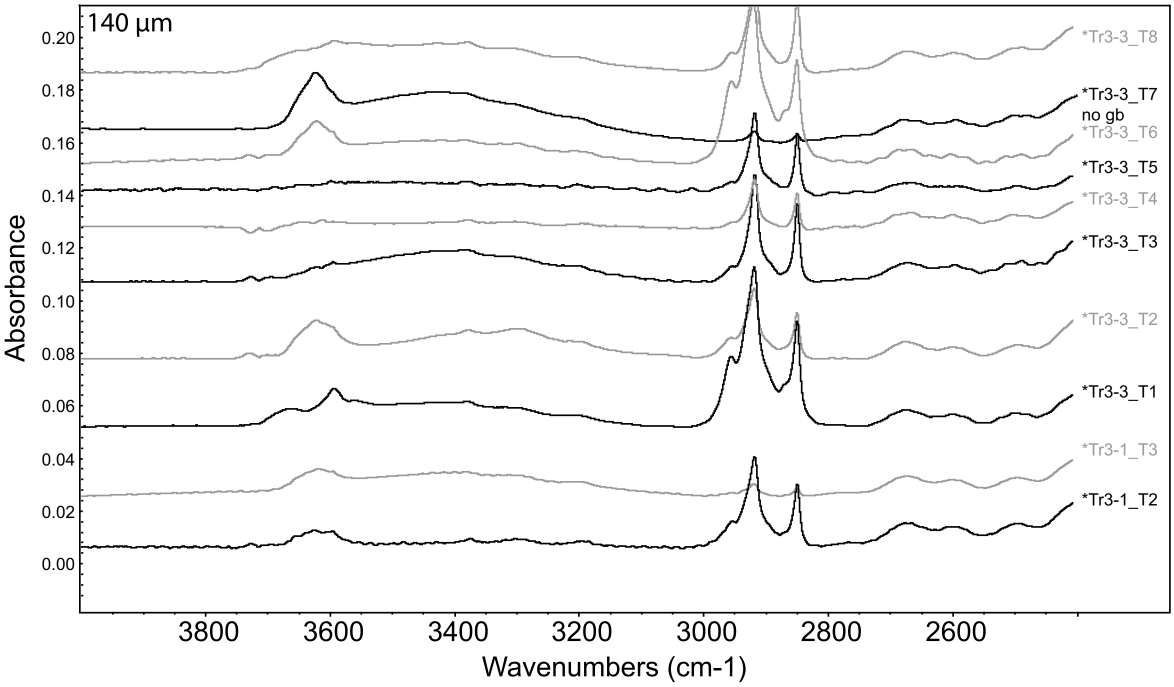

For the position see frame numbers in figure 8, main text. Spectra labelled _T% are acquired from heat treated samples.

Appendix J: EBSD at FTIR sites

EBSD derived [c]-axis orientation image of quartz aggregate in the mylonitic Truzzo granite incl. FTIR sites

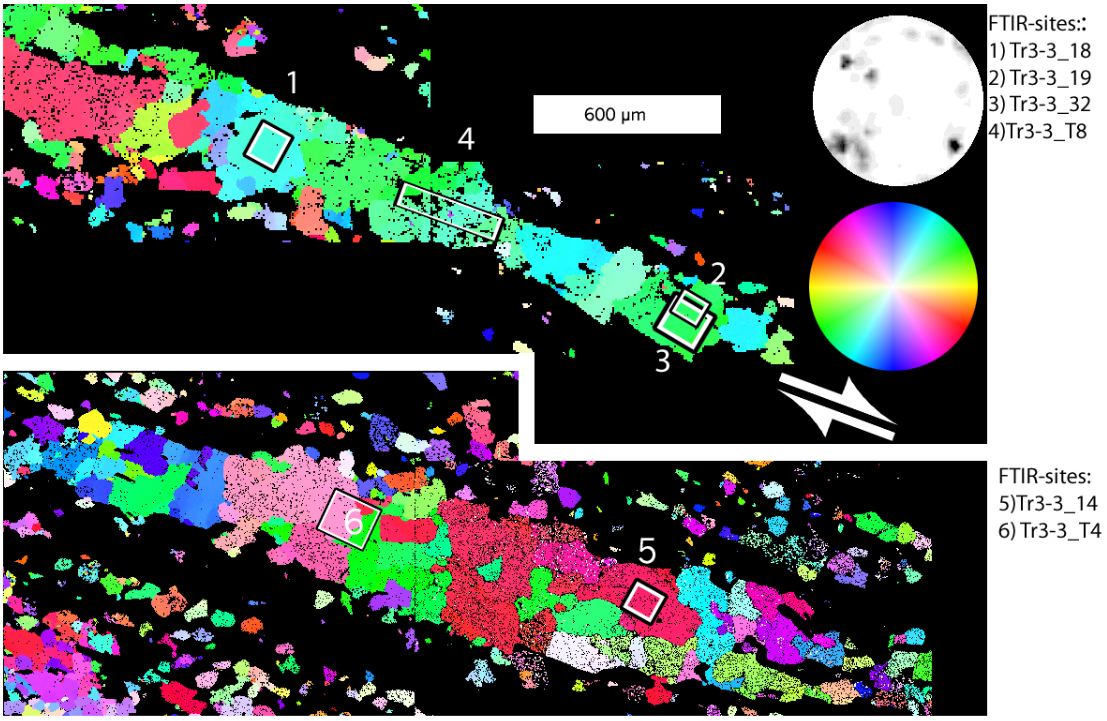

EBSD derived [c]-axis orientation maps of quartz aggregates in the mylonitic part of TR3-3. FTIR sites indicated The polefigure incorporates orientations of both aggregates. See Chapter 4, Figure 8a for location.

Appendix K: Microprobe data of the Truzzo granite

Plagioclase inclusion in K-feldspar:

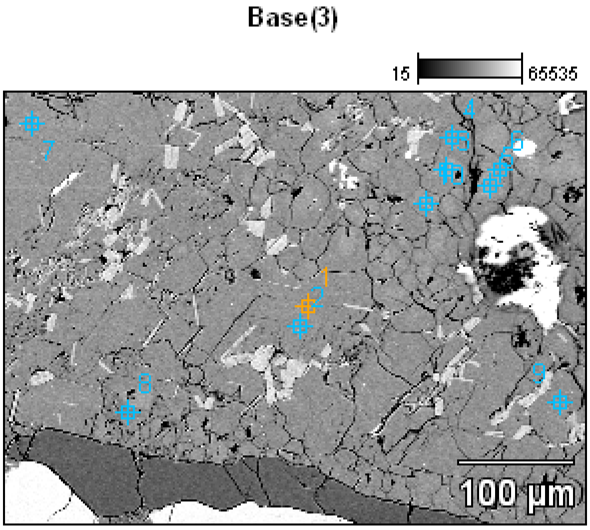

Compound %

	Na2O	*Al2O3*	*SiO2*	*K2O*	*CaO*
Base(3)_pt1	9.30	22.73	63.70	0.03	4.24
Base(3)_pt2	9.25	22.66	63.74		4.35
Base(3)_pt3	8.44	23.93	62.01		5.62
Base(3)_pt4	8.96	22.89	63.31		4.84
Base(3)_pt5	8.63	23.74	62.40		5.24
Base(3)_pt6	9.11	22.79	63.74		4.36
Base(3)_pt7	9.15	22.62	63.82		4.41
Base(3)_pt8	9.93	21.60	65.84		2.63
Base(3)_pt9	9.23	22.80	63.50		4.46
Base(3)_pt10	8.62	23.59	62.63		5.17

Cations

	Na-K	*Al-K*	*Si-K*	*K-K*	*Ca-K*	**mineral**
Base(3)_pt1	0.80	1.18	2.81	0.00	0.20	plg
Base(3)_pt2	0.79	1.18	2.81		0.21	plg
Base(3)_pt3	0.73	1.25	2.75		0.27	plg
Base(3)_pt4	0.77	1.19	2.80		0.23	plg
Base(3)_pt5	0.74	1.24	2.76		0.25	plg
Base(3)_pt6	0.78	1.19	2.81		0.21	plg
Base(3)_pt7	0.78	1.18	2.82		0.21	plg
Base(3)_pt8	0.85	1.12	2.89		0.12	plg
Base(3)_pt9	0.79	1.19	2.81		0.21	plg
Base(3)_pt10	0.74	1.23	2.77		0.25	plg

Plagioclase inclusion in Feldspar:

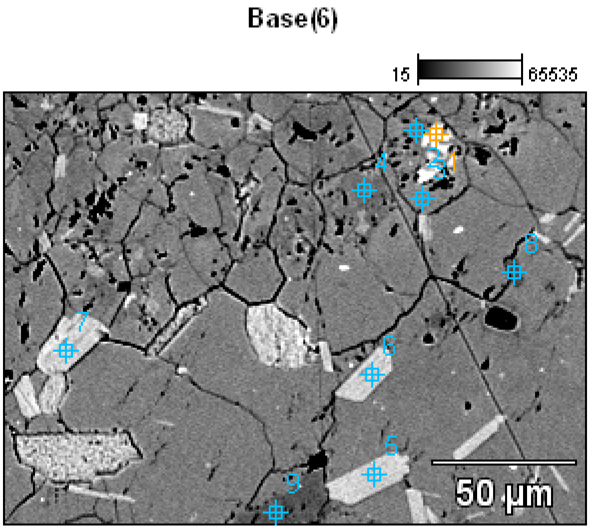

Compound %

	Na2O	***MgO***	***Al2O3***	***SiO2***	***K2O***	***CaO***	***TiO2***	***FeO***
Base(6)_pt1	0.73		18.71	65.91	14.55		0.10	
Base(6)_pt2	10.50		20.55	67.32		1.63		
Base(6)_pt3	9.21		22.90	63.63		4.27		
Base(6)_pt4	10.34		21.01	66.54		2.11		
Base(6)_pt5	0.20	1.00	35.67	50.49	10.42		0.25	1.97
Base(6)_pt6		0.87	35.06	50.42	10.69		0.91	2.06
Base(6)_pt7		1.04	34.81	51.10	10.57			2.47
Base(6)_pt8			0.61	99.39				
Base(6)_pt9	11.40		19.61	68.57		0.43		

Cations

	Na-K	***Mg-K***	***Al-K***	***Si-K***	***K-K***	***Ca-K***	***Ti-K***	***Fe-K***	**mineral**
Base(6)_pt1	0.07		1.01	3.01	0.85		0.00		kfs
Base(6)_pt2	0.89		1.06	2.94		0.08			plg
Base(6)_pt3	0.79		1.19	2.81		0.20			plg
Base(6)_pt4	0.88		1.09	2.92		0.10			plg
Base(6)_pt5	0.05	0.19	5.30	6.37	1.68		0.02	0.21	wm
Base(6)_pt6		0.16	5.22	6.37	1.72		0.09	0.22	wm
Base(6)_pt7		0.20	5.18	6.46	1.70			0.26	wm
Base(6)_pt8			0.08	10.94					qtz
Base(6)_pt9	0.96		1.01	2.99		0.02			plg

K-feldspar:

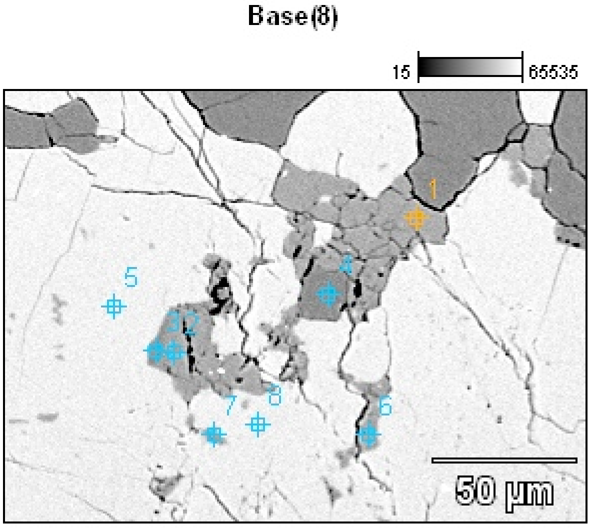

Compound %

	Na_2O	***Al_2O_3***	***SiO_2***	***K_2O***	***CaO***
Base(8)_pt1	9.35	22.62	63.36		4.67
Base(8)_pt2	9.38	22.79	63.71		4.11
Base(8)_pt3	11.59	19.31	68.61		0.49
Base(8)_pt4		0.07	99.93		
Base(8)_pt5	0.96	18.38	65.92	14.74	
Base(8)_pt6	9.46	22.38	64.44		3.72
Base(8)_pt7	8.98	21.93	64.27	1.38	3.45
Base(8)_pt8	0.74	18.37	66.04	14.85	

Cations

	Na-K	***Al-K***	***Si-K***	***K-K***	***Ca-K***	**mineral**
Base(8)_pt1	0.80	1.18	2.80		0.22	plg
Base(8)_pt2	0.80	1.19	2.81		0.19	plg
Base(8)_pt3	0.98	0.99	3.00		0.02	plg
Base(8)_pt4		0.00	4.00			qtz
Base(8)_pt5	0.09	0.99	3.02	0.86		kfs
Base(8)_pt6	0.81	1.16	2.84		0.18	plg
Base(8)_pt7	0.77	1.15	2.85	0.08	0.16	plg
Base(8)_pt8	0.07	0.99	3.02	0.87		kfs

Matrix around K-feldspar:

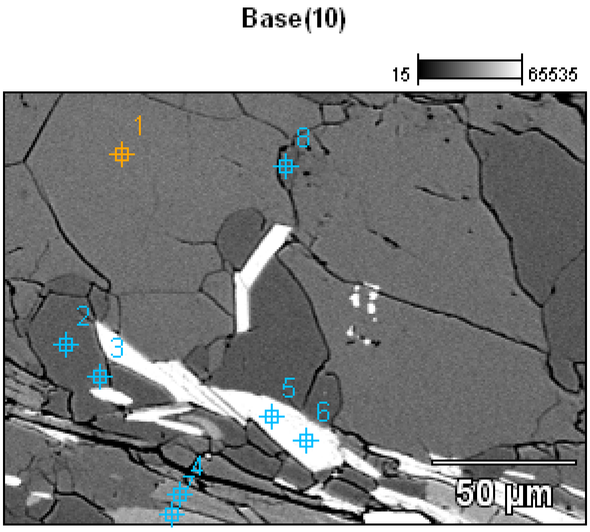

Compound %

	Na2O	*MgO*	*Al2O3*	*SiO2*	*K2O*	*CaO*	*TiO2*	*FeO*
Base(10)_pt1	9.03		23.26	63.24		4.47		
Base(10)_pt2-No Data.								
Base(10)_pt3	9.57		22.27	64.34		3.82		
Base(10)_pt4		1.22	34.53	51.08	10.37		0.59	2.21
Base(10)_pt5		7.27	18.03	38.74	9.53		2.32	24.12
Base(10)_pt6		7.01	17.45	38.20	9.64		2.37	25.33
Base(10)_pt7	0.64		18.44	65.74	15.18			
Base(10)_pt8-No Data.								

Cations

	Na-K	*Mg-K*	*Al-K*	*Si-K*	*K-K*	*Ca-K*	*Ti-K*	*Fe-K*	**mineral**
Base(10)_pt1	0.77		1.21	2.79		0.21			plg
Base(10)_pt2-No Data.									
Base(10)_pt3	0.82		1.16	2.84		0.18			plg
Base(10)_pt4		0.23	5.13	6.44	1.67		0.06	0.23	wm
Base(10)_pt5		1.59	3.12	5.68	1.78		0.26	2.96	bt
Base(10)_pt6		1.55	3.05	5.66	1.82		0.26	3.14	bt
Base(10)_pt7	0.06		1.00	3.02	0.89				kfs
Base(10)_pt8-No Data.									

mineral abbreviations: plg = plagioclase, wm = white mica, bt = biotite, kfs = K-feldspar, qtz = quartz. Cations in feldspars are calculated for 8 oxygens and 11 oxygens for dry mica

Acknowledgements

I would like to thank a lot of people and most likely I might forget to mention some of them.

First of all I would like to thank my supervisors Renée Heilbronner and Holger Stünitz for the countless good advices, excellent support and for enduring my extensive discussions. And for the meat at the balcony. Many thanks to Luca Mengon who introduced me to the rocks of the Gran Paradiso. I have profited a lot from his detailed knowledge about those rocks and enjoyed a lot the stimulating discussions. Marco Herwegh is thanked for introducing me to the EBSD and for the interesting discussions we had when I visited the basement in Bern. Thanks a lot to Giorgio Pennacchioni who provided many good ideas and samples that unfortunately, but for the sake of the reader, didn't make it into this thesis. I had a good time and fruitful discussions with Caleb Holyoke (III) during my stay at Texas A&M. He helped me a lot with the FTIR work and convinced me that home-brew is not that bad. Thanks to Andreas Kronenberg who provided the FTIR facility and the kind invitation to A&M. Big thanks to Matej and Anja. They should know, for what reason. Big thanks also to all those friends who turned my stay in Basel into a very pleasant time. I enjoy it a lot. Special thanks to my parents for supporting "the rock thing" in my early life. I am very grateful to Isla Ward for the mentoring of that life outside the office during the writing of this thesis.